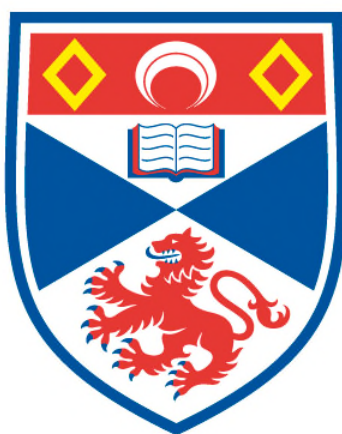


FEPT MAGNETIC NANOPARTICLES: SYNTHESSES, FUNCTIONALISATION AND CHARACTERISATION FOR BIOMEDICAL APPLICATIONS

Shu Chen

**A Thesis Submitted for the Degree of PhD
at the
University of St Andrews**



2011

**Full metadata for this item is available in
St Andrews Research Repository
at:**

<http://research-repository.st-andrews.ac.uk/>

Please use this identifier to cite or link to this item:

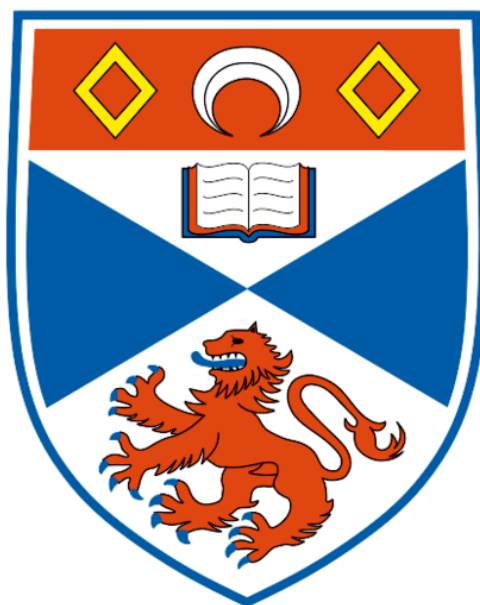
<http://hdl.handle.net/10023/2151>

This item is protected by original copyright

**This item is licensed under a
Creative Commons Licence**

FePt Magnetic Nanoparticles: Syntheses, Functionalisation and Characterisation for Biomedical Applications

Shu Chen



Feb 2011

A thesis submitted for the degree of Doctor of Philosophy
at the University of St Andrews

Declaration

I, Shu Chen, hereby certify that this thesis, which is approximately 50000 words in length, has been written by me, that it is the record of work carried out by me and that it has not been submitted in any previous application for a higher degree.

I was admitted as a research student in Feb, 2007 and as a candidate for the degree of Chemistry and Physics in Feb, 2007; the higher study for which this is a record was carried out in the University of St Andrews between 2007 and 2011.

Feb 2011

Shu Chen (陈澍)

I hereby certify that the candidate has fulfilled the conditions of the Resolution and Regulations appropriate for the degree of Ph.D in the University of St Andrews and that the candidate is qualified to submit this thesis in application for that degree.

Feb 2011

Pascal André

Feb 2011

David J. Cole-Hamilton

In submitting this thesis to the University of St Andrews I understand that I am giving permission for it to be made available for use in accordance with the regulations of the University Library for the time being in force, subject to any copyright vested in the work not being affected thereby. I also understand that the title and the abstract will be published, and that a copy of the work may be made and supplied to any bona fide library or research worker, that my thesis will be electronically accessible for personal or research use unless exempt by award of an embargo as requested below, and that the library has the right to migrate my thesis into new electronic forms as required to ensure continued access to the thesis. I have obtained any third-party copyright permissions that may be required in order to allow such access and migration, or have requested the appropriate embargo below.

The following is an agreed request by candidate and supervisor regarding the electronic publication of this thesis:

Embargo of all of printed copy and electronic publication of the thesis for a period of two years on the following ground: publication would preclude future publication.

Feb 2011 Shu Chen (陈澍)

Feb 2011 Pascal André

Feb 2011 David J. Cole-Hamilton

Acknowledgement

I would like to begin by thanking Prof. Oya Alpar (The School of Pharmacy, University of London) who gave me genuine and helpful advice when I was deciding between a job position in a pharmaceutical company and a Ph.D at St Andrews. I am glad I made the right choice, when I look back I have no regrets.

I would like to thank Dr. Pascal André, Prof. David Cole-Hamilton and Prof. Steve Lee for giving me the opportunity to carry out my Ph.D study and all their support and guidance. Particularly, I would like thank my first supervisor Dr. Pascal André, from him, not only did I learn how to be a scientific researcher, but also I learned more things than a normal Ph.D student could have expected, from setting up a lab to developing collaborations. I am sure in the future, I will appreciate for the experience of working with him over the past four years. I also gratefully acknowledge the James and Enid Nicol Trust and University of St Andrews for studentship funding and the extra financial support provided by Dr. Pascal André during my thesis writing.

Many people have offered their time and help for my study. Without these, I would not have been able to achieve as much as I have. Here I would like to express my sincere appreciation to

- Prof. David Cole-Hamilton's group, particularly Dr. Nicolas Vautravers for precursor and organic ligand synthesis and discussion,
- Prof. Ifor Samuel and Polyopto group for the access of instruments,

- Prof. Peter Bruce and Dr. Robert Armstrong for the access of Fe source XRD,
- Dr. Yuri Andreev, Mr. Ross Blackly and Dr. Philip Lightfoot for training and discussion of XRD,
- Mr. Ross Blackly, Dr. Bo Liu, Prof. Wuzong Zhou and Dr. Zhixue Su for training and help of HRTEM,
- Dr. Sidong Song for his help of impedance spectroscopy,
- Mr. Jimmy Lindsay, Mr. David Steven and Mr. Mark Ross for home made conductivity cell,
- Dr. David Heron, Soumya Ray, Vikash Venkataramana, Dr. Stephen Lister and Dr. Matthew Wismayer for magnetism discussion and helium filling for SQUID experiments,
- Dr. Lorna Eades (University of Edinburgh) who is always helpful for ICP-OES training and measurement,
- Dr. Steve Francis for the FTIR measurements,
- Dr. Suzanne Duce, Mr. Steve Quinn, Dr. Paul Dalgarno, Dr. Donald MacLaren, Dr. Gordon Hedley, Dr. Paul Cruickshank and Mr. Neil Montgomery who contributed to my thesis proof reading.

My Ph.D is an interdisciplinary project which was involved collaborations between different departments in the University of St Andrews and three other universities. Here I would like to express my sincere appreciation to our collaborators, not only for their contribution to the project, but also for their expertise for the advice and discussions,

- University of Glasgow (amphiphilic system): Dr. Donald MacLaren (TEM),
- Department of Chemistry, University of St Andrews (amphiphilic system): Dr. Richard Baker (impedance),
- University of Dundee (biomedical applications): Dr. Lijun Wang (cell

study), Dr. Suzanne Duce (MRI). Here I would like to thank Dr. Suzanne Duce particularly for her suggestions and encouragements.

- University of Belfast (thermal decomposition): Dr. Mark Muldoon, Dr. Kris Anderson (ionic liquids).

Additionally, thanks will go to everyone in the physics department, especially the secretaries (Mrs. Mary Rodger, Mrs. Lee Staniforth and Mrs. Lesley Aitken) and technicians (Mr. Geroge Robb and Mr. Scott Johnston). Also, Many thanks to all my friends here at St Andrews for their encouragement and help all these years.

Last but not least, I would like to thank my parents Mr. Chen Junqiang (陈军强), Mrs. Jiang Lingling (蒋玲玲) and my fiancé Dr. Yang Ying (杨莹) who gave me all their love and support to make my dream come true.

Abstract

Iron platinum (FePt) has attracted growing interest because of its high Curie temperature, magneto-crystalline anisotropy and chemical stability. Nanoparticles (NPs) made of this alloy are promising candidates for a wide range of biomedical applications including magnetic separation, magnetic targeted drug delivery, hyperthermia for cancer therapy and also as magnetic resonance imaging (MRI) contrast agents.

This thesis presents the synthesis, functionalization and characterization of FePt NPs along with a toxicity study and an investigation into their application as MRI contrast agents. Regarding their synthesis, different approaches have been explored including the co-reduction of Fe and Pt precursors in an aqueous media, the thermal decomposition in a conventional high-boiling solvent such as benzyl ether, and in low-melting organic salts (ionic liquids). The data revealed an inhomogeneous composition distribution of Fe and Pt between particles obtained in aqueous media, due to the iron salts hydrolysis, and a mismatch in the co-reduction kinetic of the two metal precursors. While the iron content in the NPs could be increased by using more hydrolytically stable iron precursors or stronger reducing agents, there are remaining limiting parameters which prevent further Fe content increase in NPs. In contrast, by excluding the water from the reaction system and using a Fe^{2+} iron precursor, homogenous 1:1 Fe to Pt ratio NPs can be obtained through a modified thermal decomposition pathway in benzyl ether. Based on the study of synthesis in this conventional chemical, the

potential of ionic liquids (ILs) to be used as novel solvents for FePt NPs synthesis was further explored. It was then demonstrated that ionic liquids (ILs) can not only be used as a solvent for synthesis of FePt NPs, but also can provide an exciting alternative pathway to direct synthesis *fcc*-FePt NPs.

In the context of the bioapplication of FePt NPs, a family of FePt NPs was specifically designed to enhance their MRI contrast agents properties. In contrast with previous reports, this thesis demonstrates that FePt NPs can be made non-toxic and provides the first data on their cellular uptake mechanisms. A six times increase in the FePt based T_2 contrast properties compared to clinical iron oxide NPs is reported. The relationship between the MRI contrast properties and the NPs architecture is explored and rationalised as the basis for the design of NPs as enhanced MRI contrast agents. Finally, the first observations of cellular and *in vivo* MR imaging with FePt NPs is also reported. This study opens the way for several applications of FePt NPs such as regenerative medicine and stem cell therapy, thus providing a bio-platform to develop novel diagnostic and therapeutic agents.

Table of Contents

Chapter 1: Introduction	1
Chapter 2: Nanoparticles and Their Applications.....	7
2.1. Nanoparticles and Their General features.....	7
2.2. Non-magnetic Nanoparticles	8
2.2.1. Semiconductor Nanoparticles.....	8
2.2.2. Noble Metal Nanoparticles.....	11
2.3. Magnetic Nanoparticles	12
2.3.1. Origin of Atomic Magnetic Moment.....	13
2.3.2. Types of Magnetism	13
2.3.2.1. Diamagnetism	14
2.3.2.2. Paramagnetism.....	15
2.3.2.3. Ferromagnetism	15
2.3.2.3.1. Bulk Ferromagnetic Material.....	15
2.3.2.3.2. Single Domain Magnetic Nanoparticle.....	18
2.4. Biomedical Application of Magnetic Nanoparticles	21
2.4.1. Magnetic Separation.....	22
2.4.2. Magnetic Drug Delivery and Targeting	23
2.4.3. Hyperthermia.....	25
2.4.4. MRI Contrast Agents.....	26
2.4.4.1. Introduction of Basic Principles of MRI	26
2.4.4.2. T_1 Contrast Agent	30
2.4.4.3. T_2 Contrast Agent	33
2.5. Conclusion	36
References	38

Chapter 3: Background of FePt Magnetic Nanoparticles 41

3.1. Introduction to FePt Magnetic Nanoparticles	41
3.2. Review of Solution Chemical Syntheses of FePt Nanoparticles	44
3.2.1. High Temperature: Thermal Decomposition and Reduction	45
3.2.1.1. “Conventional” Thermal Decomposition	45
3.2.1.2. Co-reduction of Fe and Pt Precursors.....	52
3.2.2. Low temperature: Co-reduction in Amphiphilic System	57
3.3. FePt NPs Surface Functionalisation for Biomedical Purposes.....	59
3.3.1. Molecular Coating.....	59
3.3.2. Thin Film Coating	61
3.3.2.1. Carbon Coating	62
3.3.2.2. Noble Metal Coating	63
3.3.2.3. Silica Coating.....	64
3.4. Conclusion	66
References	69

Chapter 4: FePt Magnetic Nanoparticles Synthesized at Low Temperature in Aqueous Media..... 77

4.1. Introduction	77
4.2. Experimental Results	78
4.2.1. Amphiphilic System Characterization	78
4.2.2. $\text{N}_2\text{H}_4 \cdot \text{H}_2\text{O}$ as Reducing Agent	80
4.3. Discussion	90
4.3.1. Hypotheses and Strategy Development.....	92
4.3.2. Reaction Time	93
4.3.3. Impact of Pt and Fe precursors.....	95
4.3.4. NaBH_4 as reducing agent.....	98
4.4. Conclusion	102
References	103

Chapter 5: FePt Magnetic Nanoparticles Synthesized through Thermal Decomposition.....	105
5.1. Introduction	105
5.2. Reminder of the Mechanism of NPs Nucleation and Growth	106
5.3. Conventional High-boiling Chemical as a Solvent.....	107
5.3.1. Experiment Protocol.....	107
5.3.2. Experiment Results	108
5.3.3. Discussion and Comparison with Literature.....	110
5.4. Ionic Liquids as Solvents	112
5.4.1. Reaction Time Investigation.....	113
5.4.2. NPs Size Tuning	119
5.4.3. Direct <i>fct</i> -FePt Synthesis.....	122
5.5. Conclusion	128
References.....	131
 Chapter 6: Biomedical Applications of FePt Nanoparticles	 133
6.1. Introduction	133
6.2. Experimental Results and Discussion	138
6.2.1. FePt NPs Characterization	138
6.2.1.1. FTIR.....	138
6.2.1.2. TEM.....	140
6.2.1.3. XRD.....	141
6.2.1.4. SQUID	142
6.2.2. Biomedical Applications	147
6.2.2.1. Cell Toxicity.....	147
6.2.2.2. Cellular Uptake	154
6.2.2.3. <i>In vitro</i> MRI	158
6.2.2.4. <i>In vivo</i> MRI	162
6.3. Conclusion	165
References.....	167

Chapter 7: Conclusion.....	171
Appendix.....	175
Appx. I. Experimental Methods for Chapter 4	175
Appx. I.1. Materials	175
Appx. I.2. FePt Nanoparticles Synthesis	176
Appx. I.3. Characterization Techniques	176
Appx. II. Experimental Methods for Chapter 5	182
Appx. II.1. Materials	182
Appx. II.2. Synthesis	182
Appx. III. Experimental Methods for Chapter 6	183
Appx. III.1. FePt Nanoparticles Preparation	184
Appx. III.2. FePt Nanoparticles Characterization	186
Appx. III.3. Cell culture	188
Appx. III.4. Micro-MRI	192
References.....	194
Publications Arising from This Work.....	195

Chapter 1

Introduction

Nanoparticles (NPs) have attracted considerable research interest as revolutionary diagnostic and therapeutic tools in biomedical fields.¹⁻³ Nanometer size materials can display very different chemical and physical properties compared to corresponding bulk materials due to their high surface to volume ratio and quantum confinement effects.⁴ Their unique properties offer tremendous opportunities for applications in biomedicine. For example, the surface plasmon resonance effect of gold NPs has led to their applications in optical imaging and sensing.² The photoluminescence wavelength of Cd, Pb and Se derived semiconductor nanoparticles, known as quantum dots (QDs), can be controlled over the visible to near infrared range by adjusting their size, enabling their use as fluorophores in a variety of biological investigations.³ Magnetic NPs, which often contain magnetic elements such as iron, cobalt, and nickel, offer unique properties and have applications including magnetic separation, magnetic targeted drug delivery, hyperthermia for cancer therapy and also as MRI contrast agents.⁵

Iron platinum (FePt) metallic alloy NPs are one of the important classes of magnetic materials. Their magnetic properties strongly depend on size, shape and

composition together with their crystalline structure. For example, depending on the size as well as structure, they behave as superparamagnetic when they are in face centred cubic (*fcc*) phase and ferromagnetic when they are in face centred tetragonal (*fcc*) phase. FePt NPs have emerged as promising candidates for a new generation of magnetic nano-material thanks to their high Curie temperature and magneto-crystalline anisotropy.⁶

This thesis presents synthetic pathways, characterization of FePt NPs and their application as MRI contrast agent. It will begin with providing an overview of the development of NPs, especially inorganic NPs, their features and potential for use in biomedicine (Chapter 2). It then focuses on introducing specific elements of magnetism, magnetic NPs and some of their biomedical applications (Chapter 2). A review of the development of chemical synthesis of FePt NPs, functionalization is presented in Chapter 3.

In the context of this PhD study, three main different approaches have been applied to synthesize FePt NPs. In Chapter 4, a detailed investigation of low temperature aqueous solution syntheses, focusing on the stoichiometry and the composition of FePt NPs, is presented. A quaternary system based on water, isooctane, and Brij52 as nonionic surfactant and butanol as a co-surfactant was used. A precise composition analysis of individual NPs was carried out and revealed an inhomogeneous distribution of Fe and Pt between particles. The aim of this work is to understand the limiting parameters on individual NP composition and identify suitable strategies to increase the iron content of NP. The characterization was completed by combining a SQUID magnetometer, Inductively Coupled Plasma Optical Emission Spectrometry (ICP-OES), Wide-angle powder X-ray diffraction (XRD), Transmission Electron Microscopy (TEM) as well as Scanning Transmission Electron Microscope and Energy

Dispersive X-ray analysis (STEM-EDX). The reaction time, precursor ions and choice of reducing agents were used to increase the insertion of the iron in the $\text{Fe}_x\text{Pt}_{100-x}$ NPs.

Based on the knowledge and experience learned from the FePt NPs synthesis in aqueous solution, a modified thermal decomposition method was developed for FePt NPs synthesis, presented in Chapter 5. In contrast to low temperature synthesis, uniform, well dispersed and close 1 to 1 Fe to Pt ratio *fcc*-FePt NP could be obtained, by using a high-boiling organic solvent like benzyl ether, combined with $\text{Na}_2\text{Fe}(\text{CO})_4/\text{Pt}(\text{acac})_2$ in the presence of oleic acid and oleylamine. In addition, the potential of ionic liquids (ILs), as novel solvents for FePt NPs synthesis was explored. ILs are low melting organic salts many of which are liquid over a wide range of temperature and can be used as solvents for numerous inorganic and organic materials.⁷⁻¹¹ The results indicate that ILs can not only be used as a solvent for high temperature synthesis of FePt NPs, but also can provide an exciting alternative pathway to direct synthesis *fcc*-FePt NPs.

Finally, the bioapplication of FePt NPs as MRI contrast agent was investigated and presented in Chapter 6. It describes the fabrication of a family of FePt NPs designed to explore and rationalise both toxicity and MRI contrast agent properties. In contrast with previous reports, this work demonstrated that FePt NPs can be made non-toxic and provides the first data on their cellular uptake mechanisms. A six fold increase in the FePt based T_2 contrast properties compared to clinical iron oxide NPs is reported. The relationship between the MRI contrast properties and the NPs architecture is explored and rationalised as the basis for the design of NPs as enhanced MRI contrast agents. Finally, the first observations of cellular and *in vivo* MR imaging with FePt NPs are also reported. This study opens the way for several applications of FePt NPs such as regenerative medicine and stem cell therapy, in

addition to the enhanced MR diagnostic imaging, thus providing a platform to develop novel diagnostic and therapeutic agents.

References

- (1) Shubayev, V. I.; Pisanic, T. R.; Jin, S. H. *Adv. Drug. Deliver. Rev.* **2009**, 61, 467-477.
- (2) Daniel, M. C.; Astruc, D. *Chem.Rev.* **2004**, 104, 293-346.
- (3) Medintz, I. L.; Uyeda, H. T.; Goldman, E. R.; Mattoussi, H. *Nat. Mater.* **2005**, 4, 435-446.
- (4) Na, H. B.; Song, I. C.; Hyeon, T. *Adv. Mater.* **2009**, 21, 2133-2148.
- (5) Pankhurst, Q. A.; Connolly, J.; Jones, S. K.; Dobson, J. *J. Phys. D-Appl. Phys.* **2003**, 36, R167-R181.
- (6) Sun, S. H. *Adv. Mater.* **2006**, 18, 393-403.
- (7) Li, Z. G.; Jia, Z.; Luan, Y. X.; Mu, T. C. *Curr. Opin. Solid. St. M.* **2009**, 12, 1-8.
- (8) Seddon, K. R.; Stark, A.; Torres, M. J. *Pure. Appl. Chem.* **2000**, 72, 2275-2287.
- (9) Buhler, G.; Zharkouskaya, A.; Feldmann, C. *Solid. State. Sci.* **2008**, 10, 461-465.
- (10) Earle, M. J.; Esperanca, J. M. S. S.; Gilea, M. A.; Lopes, J. N. C.; Rebelo, L. P. N.; Magee, J. W.; Seddon, K. R.; Widegren, J. A. *Nature.* **2006**, 439, 831-834.
- (11) Torimoto, T.; Tsuda, T.; Okazaki, K.; Kuwabata, S. *Adv. Mater.* **2010**, 22, 1196-1221.

Chapter 2

Nanoparticles and Their Applications

2.1. Nanoparticles and Their General features

Nanoparticles (NPs) are part of a class of materials bridging bulk materials and structures with an atomic length scale. All the solid particles in the range of 1 nm to 1 μm in all three dimensions could be called as NPs. However, the particles smaller than 100 nm often show dramatical changes in their physical chemical properties compared to the corresponding bulk materials.¹⁻⁴

Over the past decades, nanomaterials have attracted tremendous attention from researchers from a wide range of disciplines especially in physics, chemistry, and biology, because of their distinct characteristics which include the ultrafine size, large surface to volume ratio and unique physical chemical properties.³⁻⁴ This dissertation focuses on biomedical applications of NPs with domain size comparable or smaller than the biological materials e.g. a cell (10-100 μm), a virus (20-450 nm), or a protein (5-50 nm). As a result the NPs operate at the same microscopic scale as these biological functional subjects. Thus, NPs are expected to be able to provide a new framework for diagnosing, treating and preventing disease.⁵⁻⁶ NP has large surface to volume ratio, which means that relatively there are many more atoms located on the surface of a nano-size particle than a micro-size particle. For example, the fraction of atoms on the surface of a 20 μm

cubic particle is less than 0.01%, but this increases to almost 50% for a 2 nm cubic particle.³ Consequently engineered NPs can have much higher chemical reactivity, and binding efficiency compared to bulk materials. In addition, NPs can display unique physical and chemical properties such as magnetic and photonic behaviours, which set them apart from bulk materials.

Semiconductor quantum dots (QDs), non-magnetic metallic, magnetic nanoparticles, lipid and polymeric particles and carbon-based nanomaterials are major and sometimes overlapping classes of nanomaterials which have emerged over recent decades, and they are being exploited for a large range of applications. Carbons, lipid, polymeric based nanomaterials are appreciated for their high biocompatibility, and have been widely investigated for their drug delivery purposes since 1950s.⁷ In this thesis, this exciting aspect of nanocolloids will be put aside and focused on inorganic NPs. Whereas magnetic NPs, QDs, and non metallic NPs have attracted tremendous attention over the past three decades, due to their special magnetic, optical, and thermal properties, that are appealing for both disease diagnosis and therapy.⁶ Thanks to the development of various inorganic NPs, we are getting closer to the day when the concept of a “magic bullet” as a medical agent with specific biomedical functions, including targeted delivery and multimodal non-invasive imaging, becomes reality. A brief introduction on semiconductor NPs, noble metallic NPs, magnetic NPs are given in the following section.

2.2. Non-magnetic Nanoparticles

2.2.1. Semiconductor Nanoparticles

QDs are defined as semiconductor structures with physical dimensions typically in the range of a few nanometers.⁸ QDs such as CdSe, CdTe, CdS, ZnSe, PbS, PbSe etc. can display unique photoluminescence properties including high emission intensity, superb photostability over conventional organic fluorophores.

In addition, the fluorescence emission of QDs is size and composition tunable therefore it is possible to fabricate QDs with fluorescence emission that ranges from the visible to infrared wavelengths. Furthermore, QDs have large absorption coefficients across a wide spectral range which allows different QD emissions to be excited simultaneously using a single wavelength, i.e. single excitation wavelength for multiple colours.^{6, 9} Therefore, QDs are promising biological optical probes to replace or complement existing organic fluorophores used extensively in biological research.⁹⁻¹⁵

The optical properties of QDs can be described by conventional semiconductor physics and quantum mechanics.^{9, 16-17} In these systems, characterized by valence and conduction bands, the energy difference between the two bands is called the bandgap energy. When a semiconductor is optically or electrically excited, the electrons located in the valence band will move into the conduction band and leave holes behind. After a period of time termed as the lifetime, typically around 20 ns, the electron and hole will recombine. This recombination can be associated with the emission of photons with a high “quantum yield”. The QDs fluorescence emission is dependent upon the bandgap energy; which in turn is related to the QD’s size, shape, and composition due to the quantum confinement effect. Figure 2.1A1-A3 show several vials of QDs of different size illustrating their fluorescence properties,⁹ demonstrating that as the QDs size becomes larger, their optical emission shifts from blue to red. This tunable fluorescence emission property and the microscopic size of the QDs means they play an immense role in the development of biomedical imaging. A typical example is the multi-colour labelling shown in Figure 2.1B, which presents a pseudocoloured image of fixed human epithelial cells stained by five-colour QDs functionalized with different antibodies which selectively binds to specific surface receptors inside the cells.¹¹

A new and exciting avenue of QDs research is their application as optical probes emitting in the near-IR (NIR) emission range (> 650 nm).¹⁸⁻¹⁹ 650–900 and 1025–1150 nm are typical NIR emitting windows,^{9, 11} which have low tissue absorption and scattering effects hence increase the potential of non-invasive *in*

in vivo biological optical imaging as it allows deeper penetration. While there are only a limited amount of organic fluorophores and chemiluminescence probes with NIR emission, it is possible to prepare a series of NIR-emitting QDs suitable for animal imaging, by tuning the optical properties of QDs altering their size and composition. Indeed, CdTe, CdSe-ZnS, CdTeSe, InAs, PbS, and PbSe have already been successfully synthesized with NIR emission.¹⁹⁻²¹

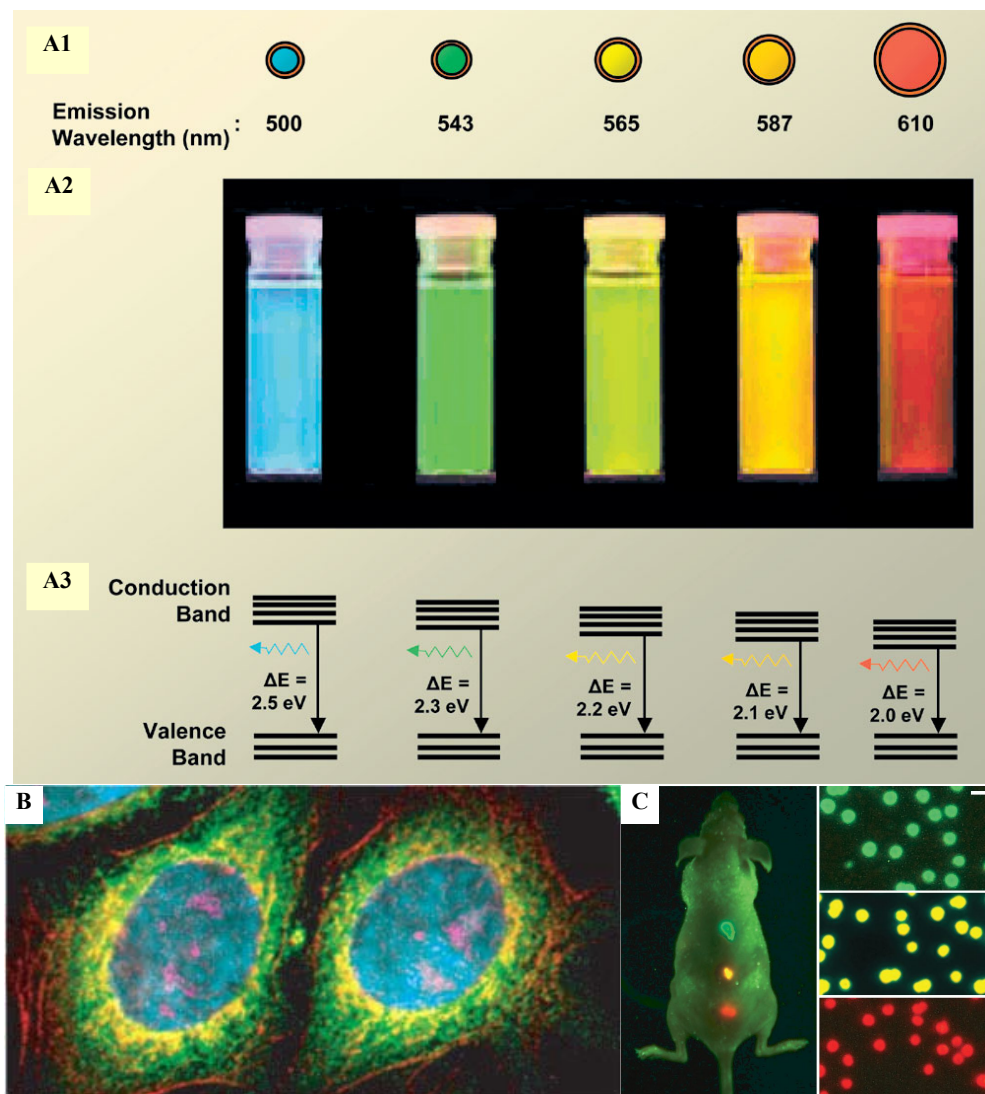


Figure 2.1 (A) Tunable optical properties of QDs: Schematic of the size-dependent optical properties of QDs (A1), their real-color emission, excited by a hand-held UV lamp (A2) and the corresponding bandgap energies (A3).⁹ (Copyright 2006, Wiley-VCH Verlag GmbH & Co. KGaA. Reproduced with permission.) Pseudocoloured image depicting five-colour QD staining of fixed human epithelial cells (B). (Courtesy of Quantum Dot Corp.) Simultaneous *in vivo* imaging of multicolour QD-encoded polymer microbeads (C).¹⁸ (Adapted by permission from Macmillan Publishers Ltd: [Nat. Biotechnol.] (¹⁸), copyright 2004.)

Figure 2.1C illustrates the capability of CdSe-ZnS core-shell QD in high sensitive, multicolour imaging of live animals.¹⁸ An equal number of polymer beads doped with 3 different colour QDs emitting green, yellow and red light respectively, were injected into a host mouse at three adjacent locations. All three colours were observed simultaneously in the mouse with a single light source, thus demonstrating the large potential of NIR QDs as sensitive optical probes for non-invasive, multi-colour *in vivo* imaging.

2.2.2. Noble Metal Nanoparticles

The coherent oscillation of free electrons at metallic surfaces associated with electromagnetic fields is called the surface plasmon resonance (SPR).²²⁻²⁴ When metal NPs are exposed to light radiation, the electric field of the light can cause the collective oscillation of the free electrons at the surface of the NPs. Subsequently, the oscillating electrons radiate electromagnetic radiation with the same frequency as the oscillating electrons. Chemically stable silver and gold NPs have been shown to be efficient at Plasmon scatter. Their SPR-enhanced properties including Mie scattering, surface plasmon absorption, surface-enhanced luminescence and surface enhanced raman scattering (SERS) have been widely investigated for biomedical applications.²²

In this section, gold (Au) NPs are briefly introduced representing non-magnetic metal NPs. When compared with QDs, Au NPs have their own advantages such as dual scattering, fluorescence properties, easier surface functionalization, and low toxicity.²² Most importantly, Au NPs have photothermal property that QDs do not exhibit. The photothermal property of Au NPs is attributed to the strong light absorption as a result of the SPR. The absorbed light can be converted into heat on a picosecond time scale. The highly efficient and localized light-to-heat conversion by Au NPs makes them very promising candidates for cancer photothermal therapies and as a thermal sensitive drug delivery system.²² Recently, a controllable drug releasing system was reported based on photothermal effect of Au nanocages, as illustrated in Figure 2.2. Au nanocages are gold nanostructures

with hollow interiors and porous walls, and have strong light absorption in the near-infrared region, a region in which biological tissue has high transmissivity. In this drug delivery system, these Au nanocages are coated with thermal sensitive polymer which can change conformation in response to small variations in temperature. Therefore, when the heat is generated by Au nanocages through conversion of absorbed light into heat which dissipates into the surroundings, it will cause the polymer chains to collapse. This in turn, exposes the pores on the nanocages resulting in the release of preloaded drug. The drug release can then be stopped by turning off the laser source, reducing the temperature and returning the polymer to its original extended conformation therefore closing the pores of nanocages and stopping drug release.²⁵

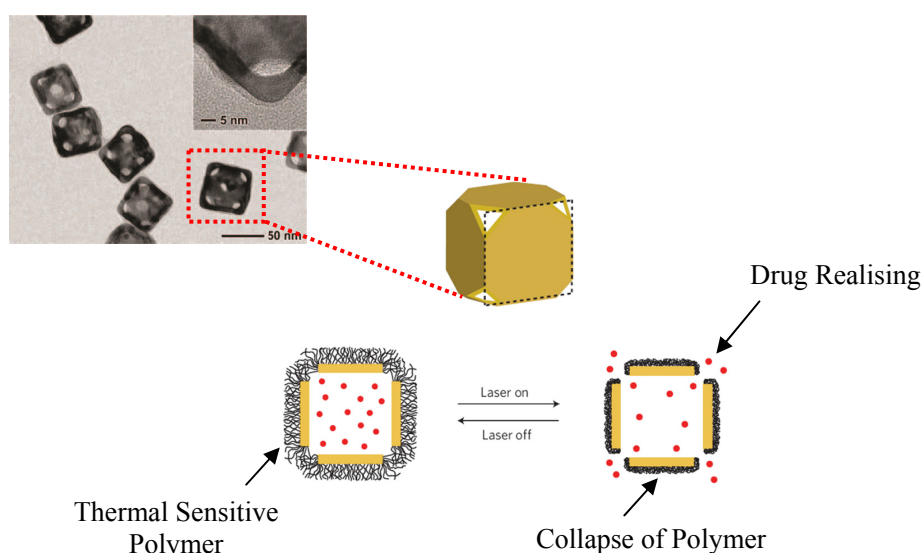


Figure 2.2 Schematic illustration of Au nanocage-smart polymer controlled-drug system. The drug releasing is controlled by triggering the thermal sensitive polymer conformation change through the light-heat conversion by Au nanocage upon exposure to a near-infrared laser.²⁵ (Adapted by permission from Macmillan Publishers Ltd: [Nat. Mater.] (²⁵), copyright 2009.)

2.3. Magnetic Nanoparticles

During the course of this PhD, I have focused on iron platinum alloy magnetic NPs. Thus, the following section will introduce the general rules associated with their magnetic properties.

2.3.1. Origin of Atomic Magnetic Moment

When a current passes through a length of wire, a magnetic field is generated. In the case of an electric current moving in a circular loop, this current loop behaves as a magnetic dipole,²⁶ a schematic drawing is shown in Figure 2.3A. By invoking this concept of electrical charges in motion, the origins of atomic magnetic moment responsible for magnetism in all materials can be explained. The electron spin magnetic moment of an atom originates from the orbital angular momentum of the electrons around the nuclei (Figure 2.3B). If the atom has more than one electron, the total atomic magnetic moment depends on the spin-orbital electron magnetic moment interactions, so called spin-orbit, spin-spin or orbit-orbit coupling between electrons of the atom.²⁷

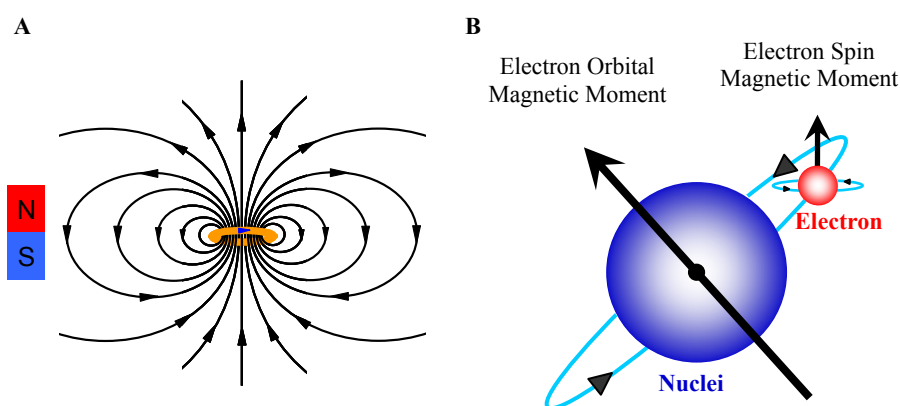


Figure 2.3 Schematic drawing of a magnetic field generated by a current loop (A), an atomic magnetic moment produced by an electron orbiting the nucleus and the spin of the electron.

2.3.2. Types of Magnetism

Materials can be classified into five magnetic categories namely: diamagnetic, paramagnetic, ferromagnetic, ferrimagnetic and antiferromagnetic according to the arrangement and origin of their magnetic moment in the absence and presence of an external magnetic field.^{5, 26-30}

2.3.2.1. Diamagnetism

Diamagnets are materials with no permanent net atomic magnetic moment, for example, copper, silver and gold are typical diamagnetic materials. The diamagnetic atoms have filled sub-electron shells and the magnetic moments of those paired electrons will cancel each other in the absence of a magnetic field resulting in zero net atomic magnetic moment (Figure 2.4)²⁷ When a magnetic field is applied, the atomic magnetic moment with a direction opposing the external field will be generated. This is because the orbital motion of the electrons in the same electron shell will be either accelerated or decelerated simultaneously subject to an applied magnetic field, thereby contribute to a change in the orbital magnetic moment in such a way that the induced moment opposing the applied field.²⁶⁻²⁷

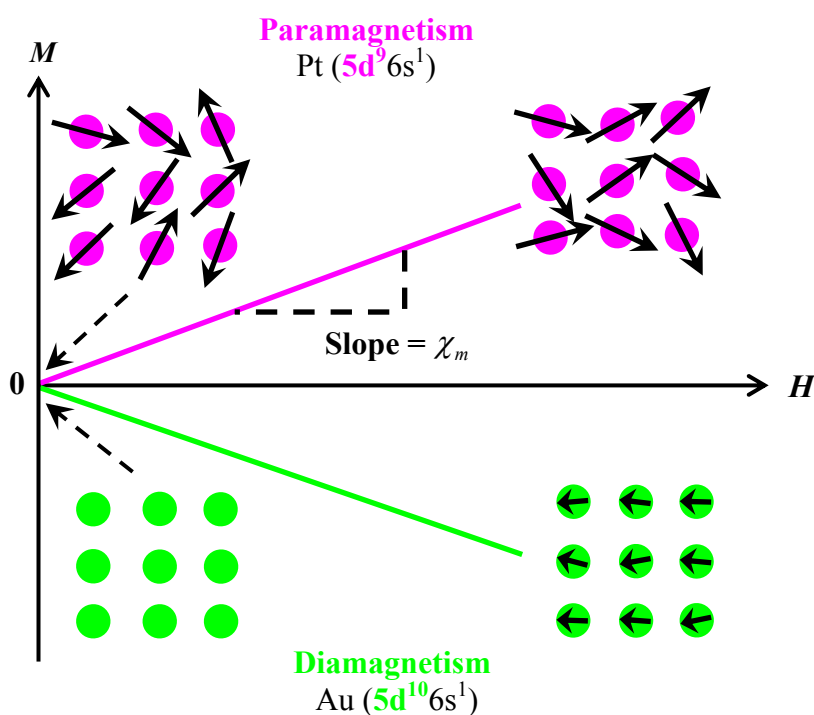


Figure 2.4 Schematic illustrating the arrangements of magnetic dipoles for Diamagnetic and Paramagnetic materials in the absence or presence of an external magnetic field (H).^{5, 28}

The *magnetization* (M) is defined as the magnetic moment per unit volume of a solid and is used to quantify the strength of the magnetic moment. The *magnetic*

susceptibility (χ_m) usually describes the magnetic response of material to an applied magnetic field, and can be defined as the gradient of the M - H curve (Figure 2.4). The χ_m of diamagnetic materials is negative with a very small magnitude typically of about 10^{-5} .²⁶⁻²⁷

2.3.2.2. Paramagnetism

Unlike diamagnets, paramagnetic materials have permanent atomic magnetic moments which do not rely on the presence of an external magnetic field. Paramagnetic atoms, e.g. oxygen and platinum, usually have an odd number of electrons in the sub-electron shell, the unpaired electron spins give rise to a permanent net atomic magnetic moment (Figure 2.4).²⁷ However, normally these atomic magnetic dipoles are not parallel but randomly oriented within a material, the interactions between paramagnetic atomic dipoles are much weaker than the thermal agitation, termed as Boltzmann energy. Under these conditions, for example in the absence of an external magnetic field, the macroscopic or net magnetic moment of the paramagnetic material is zero.

Applying a strong external magnetic field has the effect of making the atomic dipoles line up parallel to the applied field; as a result a positive susceptibility can be obtained (Figure 2.4). However, the fraction of the moments that align with the field is usually very small subject to the thermal agitation, thus the magnitude of the susceptibility (χ_m) typically ranges from 10^{-3} to 10^{-5} .^{27, 31}

2.3.2.3. Ferromagnetism

2.3.2.3.1. Bulk Ferromagnetic Material

Similar to paramagnetic materials, ferromagnetic materials e.g. iron, cobalt, nickel, heavy rare earth elements have permanent atomic magnetic moments due

to unpaired electrons in sub-electron shell. However strong interatomic interaction, the so called Weiss Interaction, induces spontaneous magnetization in ferromagnetic materials. Thus neighbouring atomic magnetic moments tend to align parallel to each other to lower the energy of the system (Figure 2.5A). This can not be explained in classical terms but depends entirely on quantum theory. The overall energy of the system is further decreased in bulk ferromagnetic material, as it forms small magnetic domains which in the absence of an external magnetic field are separated by domain walls (Figure 2.5A). Within each domain, there is a large net magnetic moment (spontaneous magnetization), due to the

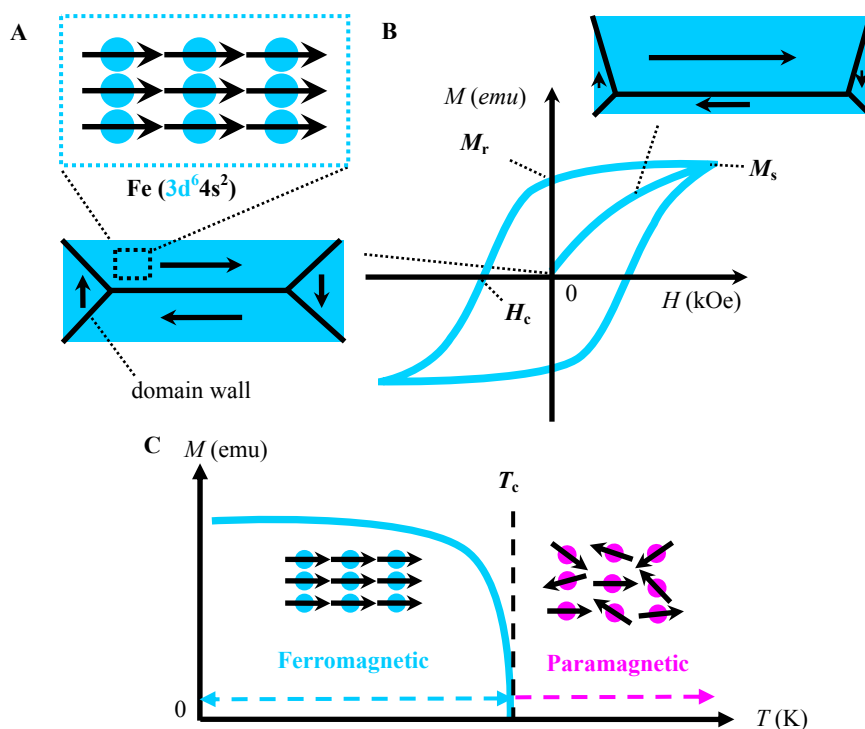


Figure 2.5 Schematic drawing of Ferromagnetism in the bulk material. (A) Multi-domain structure existed in the bulk ferromagnetic material (B) important parameters obtained from a magnetic hysteresis loop: the magnetic saturation (M_s), the remnant magnetization (M_r). The coercivity field (H_c) (C) a typical plot of the Curie temperature T_c .³¹

parallel alignment of the large numbers of atomic magnetic dipoles, typically from 10^{12} to 10^{15} .²⁷ The size and direction of the magnetic moments of each domain however varies with each other, and in the demagnetized state the net magnetic moment of the macroscopic ferromagnetic material is zero. However, the application of even a small magnetic field induces a large magnetization often in

the order of a magnitude greater than the field strength in ferromagnetic material. The magnitude of susceptibility is positive with typical values from about ~ 50 to 10^3 , which is much larger than in the paramagnetic materials.²⁷

The generation of large magnetization is attributed to two processes. One is the rotation of the direction of the domain magnetization along the applied field direction. This generally costs more energy than the motion of domain walls, because it involves rotating the magnetization away from the easy direction being fixed by magnetic anisotropy.³¹ The other is the domain wall motion involving the volumes of domains aligned along the field become greater than the volume of domains aligned against the field (Figure 2.5B).³¹ When these two processes are completed under a sufficiently strong applied magnetic field, the sample is in a state of *magnetic saturation* (M_s). The rotation of magnetization is reversible, therefore on the reduction of the applied magnetic field, the magnetization rotates back toward its easy directions. As the applied field decreases further, domain walls begin moving backwards. However because wall motion is an irreversible, lossy process, the M - H loop opens up, resulting in hysteresis. The induced magnetization remains in the sample even when the applied field is reduced to zero, this is called *remnant magnetization* (M_r). A reverse field called the *coercive field* (H_c) is required to completely demagnetize the remaining magnetization (Figure 2.5B).

Ferromagnetism is highly temperature dependent, as the magnetization of ferromagnetic material arises from the collective net interactions of permanent atomic magnetic moments.²⁸ As temperature increases, thermal energy starts to become large enough to break the parallel alignment of atomic magnetic moments of the ferromagnetic material. When it has risen to above a critical temperature, all the atomic magnetic moments are randomized by thermal agitation, and the spontaneous magnetization of ferromagnetic materials falls rapidly to zero. The result is the ferromagnets behave like a paramagnetic material. This transition temperature from ferromagnetic to paramagnetic behaviour is called the *Curie temperature* (T_c) (Figure 2.5C).²⁷

In addition to ferromagnets, there are two other magnetic materials that are classified as ferrimagnets and antiferromagnets. They also exhibit ordered magnetic states in the absence of an external magnetic field. In a ferrimagnetic material, the magnetic dipoles have an ordered arrangement with one magnetic dipole aligned antiparallel to an adjacent stronger dipole resulting in a weak net magnetic moment (Figure 2.6A). In an antiferromagnetic material, the neighbouring dipoles are aligned antiparallel and of equal magnitude thus they cancel each other (Figure 2.6B).³²⁻³³

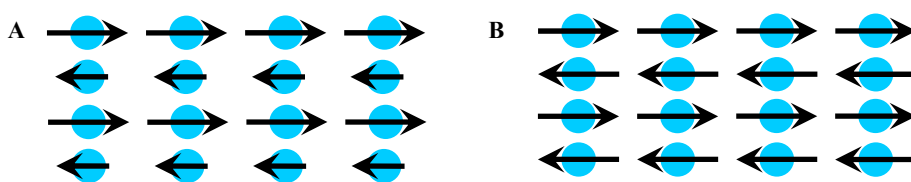


Figure 2.6 Schematic drawing of atomic magnetic moments arrangement in ferrimagnetic material (A) and antiferromagnetic material (B).³²⁻³³

2.3.2.3.2. Single Domain Magnetic Nanoparticle

In addition to temperature, the magnetization of ferromagnetic material is also strongly related to the size of material. In large scale bulk materials, there is presence of magnetic domains where regions of uniform magnetization are separated by domain walls (Section 2.3.2.3.1). When the material size is reduced as in the case of NPs, there is a critical volume below which it costs more energy to create a domain wall than to support the external magnetostatic energy of a single-domain particle. This critical size is called the single-domain size (D_c). Inside each single-domain particle, there is a giant magnetic moment because all the atomic magnetic moments within this particle are aligned parallel along a specific direction (Figure 2.7A).

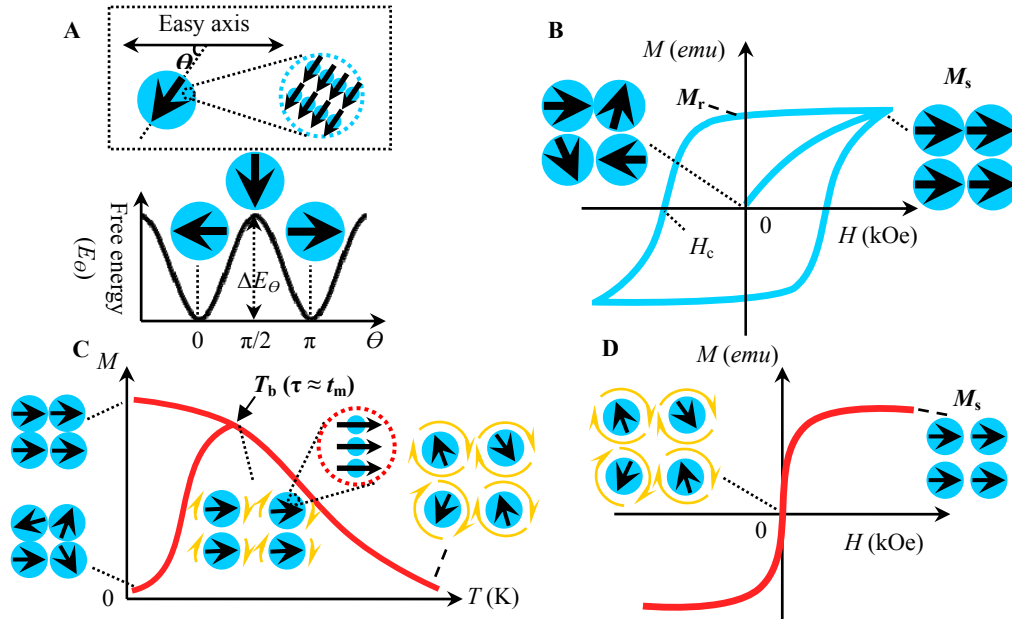


Figure 2.7 Schematic drawing of a single domain ferromagnetic NP, its free energy with uniaxial anisotropy as a function of magnetization direction (A),³⁴ and hysteresis loop of ferromagnetic NPs (B). Schematic drawing of the reversals of a superparamagnetic NP magnetization subject to thermal agitation, ZFC-FC curve of superparamagnetic NPs (C) and hysteresis loop of superparamagnetic NPs (D).

The macroscopic magnetic moment of magnetic NPs can be seen as a collection of giant magnetic dipoles, which thus depends on the directions of individual magnetic nanoparticle magnetization. The magnetic anisotropy is responsible for holding the particle magnetization along a certain direction, and the energy per particle can be expressed as follow:

$$E(\theta) = K_{\text{eff}} V \sin^2 \theta \quad \text{eq.(1)}$$

where K_{eff} is the anisotropy constant depends on magnetocrystalline anisotropy, shape anisotropy, strain anisotropy and surface anisotropy,³⁴ V is the particle volume and θ is the angle between the particle's magnetization and the preferential direction of magnetization known as the easy axis. The energy barrier

$$\Delta E = K_{\text{eff}} V \quad \text{eq.(2)}$$

separates the two energy minima magnetization at $\theta = 0$ and $\theta = \pi$

corresponding to the magnetization aligned parallel or antiparallel along the easy axis (Figure 2.7A).³⁴ Particles are also subjected to thermal energy, $k_B T$, where k_B is the Boltzmann constant, T is the temperature. When $K_{\text{eff}}V > k_B T$, particles manifest ferromagnetic properties as characterized by an irreversible hysteresis loop (Figure 2.7B). The magnetic moments of particles tend to align to the same direction as the applied external magnetic field and finally reach a saturation magnetic moment (M_s) with all the particular magnetic moment aligned in the same direction. Similar to bulk ferromagnetic magnetic material, there is a remnant magnetic moment (M_s) left after the disappearance of the external field, and a magnetic field applied in the opposite direction (H_c) is needed to demagnetize the sample (Figure 2.7B).

The energy barrier $K_{\text{eff}}V$ decreases with the particle size, and below a size limit when the thermal energy $K_B T$ exceeds $K_{\text{eff}}V$, the magnetization of particle, it becomes easily flipped (Figure 2.7C). These particles are said to be superparamagnetic particles. The critical size below which this occurs is called the superparamagnetic limit size (D_s). It needs to be noted that, different to a paramagnetic particle which has no net particulate magnetic moment itself, each superparamagnetic particle is still a permanent magnet because of spontaneous magnetization within the particle; however, the magnetization of each single particle is fluctuating rapidly subject to the thermal agitation (Figure 2.7C), resulting in zero net macroscopic magnetization for a collection of superparamagnetic particles.

This magnetic property of superparamagnetic particles can be characterized by the **ZFC-FC** (Zero-Field Cooled and Field Cooled) curves using SQUID (Superconducting Quantum Interference Devices). The ZFC curve is obtained by cooling down the sample without applying any magnetic field from a high temperature, at which all particles show superparamagnetic behaviour, to a low temperature whilst measuring the magnetization under a small applied field typically 100 Oe and increasing temperatures stepwise. The FC curve is normally obtained by first cooling the system from a high temperature to a low temperature

in the presence of the small applied magnetic field, then measuring the magnetization in the same small applied field while stepwise increasing temperatures.³⁵ The magnetic behaviour of particles is characterized by the so called *blocking temperature* (T_b), at which the relaxation time of NPs becomes comparable to SQUID measurement time (t_m) about 100 s (Figure 2.7C). The *relaxation time* (τ) of the magnetic moment of a particle, is given by the Néel-Brown equation, where $\tau_0 \approx 10^{-10}$ s is the inverse attempt frequency,³⁴ K is the anisotropy constant, V is the particle volume, k_B is the Boltzmann's constant,

$$\tau = \tau_0 \exp\left(\frac{K_{\text{eff}}V}{k_B T}\right) \quad \text{eq. (3)}$$

Below T_b , the particles magnetic moments are said to be 'blocked', they appear frozen on the time scale of the measurement and therefore particles show ferromagnetic properties, as characterized by an open hysteresis loop. Above T_b , particles exhibit paramagnetic properties without any hysteresis. However, in contrast, the collective magnetic moment of superparamagnetic NPs can easily reach saturation under relatively low magnetic field (Figure 2.7D). For a specific sample the blocking temperature is not uniquely defined and depends on the characterization instrument used for the characterisation. However, the blocking temperature can be defined for each applied experimental technique.³⁴

2.4. Biomedical Application of Magnetic Nanoparticles

Due to the unique magnetic properties and their ability to function at the cellular and molecular level of biological interaction, magnetic NPs have attracted tremendous research interest as revolutionary diagnostic and therapeutic tools in biomedical applications.^{5, 28, 33, 36} Major bioapplications of magnetic NPs including magnetic separation, magnetic targeting, hyperthermia, and as MRI contrast agent are introduced in the following sections.

2.4.1. Magnetic Separation

In biology, it is often of interest to separate out specific biological substances from a heterogeneous sample matrix either to purify the sample or to concentrate the desired components for subsequent analysis and usage. Separation using magnetic NPs provides one straightforward and efficient way to achieve this purpose. In general, the separation involves two-steps,

- i) the tagging or labelling of the desired biological objects like bacteria or protein with the magnetic NPs. The labelling is normally made via a linkage between NPs and targeted biological materials such as ligand-receptor interactions.³³
- ii) the magnetically labelled materials can be separated from the native solution, for example, passing the fluid mixture through a region where a magnetic field gradient can immobilize the tagged materials.⁵

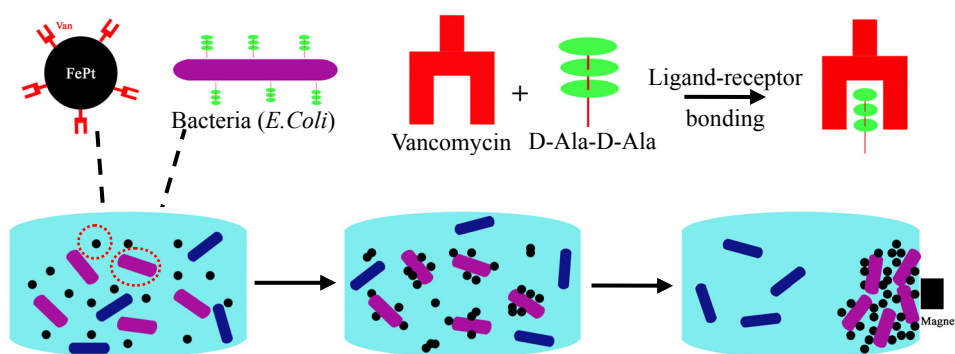


Figure 2.8 A schematic illustration of the capture of bacteria by vancomycin-conjugated FePt magnetic NPs, modified based on ref.³⁷

A typical example is illustrated in Figure 2.8. A broad spectrum antibiotic Vancomycin is attached to the surface of magnetic NPs that targets the terminal peptide, D-Ala-D-Ala, which is located on the cell wall of a Gram-positive bacterium via polyvalent ligand-receptor interaction. The nP-Van conjugates can selectively and efficiently bind to Gram-positive bacteria (within ~10 min), such as *Staphylococcus aureus*, *S. epidermidis*. The bacteria bound with NPs can then be separated by a point magnet (with the tip field strength at ~400 G) from the

solution and allow subsequent identification with optical microscopy or SEM. The sensitivity of this bacteria assay using FePt NPs is impressive as it can purify bacteria at a concentration of ~ 10 cfu mL⁻¹ (cfu: colony forming units), which is more sensitive than the best assays for bacteria detection based on luminescence (detection limit: 180 cfu mL⁻¹).³⁷⁻³⁸

2.4.2. Magnetic Drug Delivery and Targeting

The concept of targeted drug delivery is attractive as the aim is to release the drugs at specific lesions sites in the body. This achieves enhanced drug delivery efficiency, reduces dosage and minimize undesired side effects. In cancer treatment, the traditional chemotherapy is non-specific and the therapeutic drugs are normally administered intravenously leading to general systemic distribution. This results in deleterious side-effects as the drug not only attacks tumour cells but also healthy cells. There are typically two approaches to achieve specific drug delivery to pathological sites.³⁹ The first one is called passive targeting pathway which takes advantages of “natural” process of the body for clearance of drugs. For example, particulate drug carriers tend to be phagocytosed by cells of mononuclear phagocyte system (MPS) sometimes also known as the reticuloendothelial system (RES). This results in the drug accumulation in the major organs such as liver and spleen which have abundance of MPS macrophages and a rich blood supply. This passive targeting is advantageous in a number of situations, e.g. the treatment of macrophage-associated microbial, viral or bacterial diseases and the immunopotential of vaccines, etc.⁴⁰ Passive targeting can also be achieved by enhancing permeability and retention (EPR) effect, this will deliver drugs to the particular pathological sites e.g. tumours, inflammatory where the microvasculature is hyperpermeable, leaky and lack of lymphatic drainage system which leads to the accumulation of macromolecules and small particles to these sites (Figure 2.9).^{18, 40-41} This form of passive targeting, also called ‘selective targeting’, requires the size of the drug carrier system to be larger than the size of normal endothelial fenestrations but also small enough to go through the “leaky” endothelial sites. In addition, the carrier systems have to

“escape” from MPS clearance so they have long enough blood circulation time to accumulate at the desired pathological sites. To reduce the RES clearance, a typical approach is to increase the hydrophilicity of the particles, by for example, coating the particles with hydrophilic polymer like PEG (Figure 2.9).⁴²

The alternative specific drug delivery approach is called “active targeting”. This strategy is to attach a “homing device”, like antibodies or ligands targeting corresponding cell-specific receptors covalently or non-covalently, to the particles surface that allows the drug carriers to identify and bind to a desired target at the pathological sites (Figure 2.9). For example, galactose can be used to target a drug carrier to parenchymal liver cells.⁴⁰

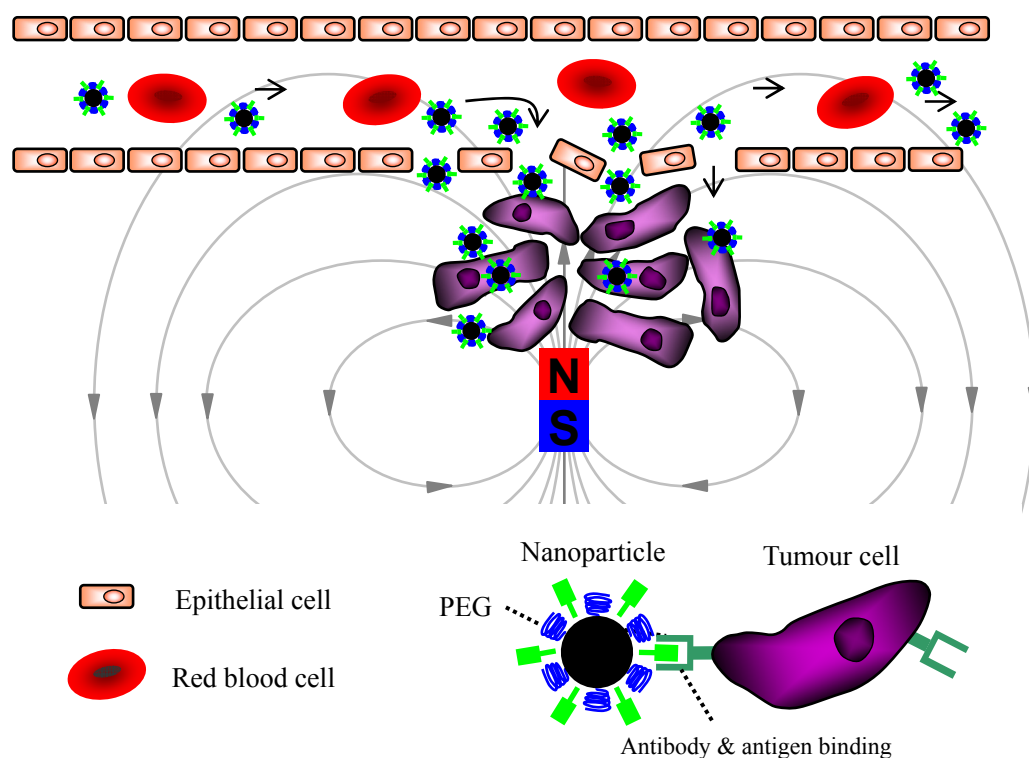


Figure 2.9 Schematic drawing of drug delivery strategies.

The development of magnetic NPs allows an alternative ‘active targeting’ strategy known as magnetic targeting, this guides magnetic drug carriers to a chosen site by an external magnetic force (Figure 2.9).⁴¹ The magnetic targeting strategy is

appealing as it complements existing passive and active drug delivery methods and can improve the effectiveness of drug targeting. FeRx, Inc. produced magnetic particles (MTC-DOX) of size 500 nm – 5 μ m consisting of metallic Fe ground together with activated carbon loaded with an anticancer drug Doxorubicin. Experiments showed that MTC-DOX NPs can be accurately targeted to the regions of interest e.g. liver and lung in a swine model. The development of MTC-DOX NPs went to the Phase II clinical study in patients with primary liver cancer. Although the trial was not successful, it demonstrated the promising capability of magnetic particles for the drug targeting application.⁴³⁻⁴⁴

2.4.3. Hyperthermia

When magnetic NPs are exposed to an alternating magnetic field, heat will be generated. For ferromagnetic NPs, the mechanism of heat generation is due to hysteresis loss, and the amount of heat generated by this mechanism is proportional to the frequency of the oscillating magnetic field and to the area of the magnetic hysteresis loop. For superparamagnetic NPs, two different mechanisms of heat generation are involved: (i) the rotation of magnetic moment across the NPs and (ii) the physical rotation of the particles themselves. The former is referred to as ‘Néel relaxation’ and the latter is termed as the ‘Brownian relaxation’.^{5, 45-46}

Hyperthermia is an attractive cancer therapy as controlled heat release from the magnetic NPs produces apoptosis of cells. The tumour cells are more vulnerable due to the physiological difference between healthy tissues and solid tumours. The low oxygen and low pH environment in tumour due to the insufficient blood perfusion, makes tumour cells more sensitive to temperature rises than healthy tissues. For example, it has been demonstrated that if the temperature can be maintained above the therapeutic threshold of 42 °C for half an hour or more, the tumour cells can be destroyed^{33, 45, 47-48}, while most tissues are undamaged by heating treatment for 1 h at the temperature up to 44 °C.⁴⁷ In addition, the temperature rises are easier in tumour sites because of the insufficient blood flow. Consequently, tumour cells can be selectively killed by hyperthermia treatment. It

is usually used as an additive therapy with standard treatments, such as radiotherapy and chemotherapy.⁴⁹

2.4.4. MRI Contrast Agents

2.4.4.1. Introduction of Basic Principles of MRI

The basic principle of nuclear magnetic resonance (NMR) that underpins magnetic resonance imaging (MRI) is shown in Figure 2.10.⁵⁰⁻⁵² If we consider a hydrogen nucleus, it contains a positively charged proton. The proton has nuclear spin. Thus the positively charged hydrogen nucleus has a magnetic moment due to its self-rotation, and the direction of the magnetic moment is parallel to the axis of self-rotation. In the absence of a field, the protons have their magnetic moments oriented randomly, thus the net magnetic moment of these protons is zero (Figure 2.10A). When an external magnetic field is applied, the spins of the protons nuclei have two potential energy states, which in classical terms can be thought of nuclear magnetic moment aligning either parallel or antiparallel to the applied magnetic field. During their alignment, the spins precess at a specified frequency, known as the *Larmor frequency* (ω_0) or the frequency of precession, which is proportional to the strength external magnetic field,

$$\omega_0 = \gamma B_0 \quad \text{eq.(4)}$$

where γ is the magnetogyric ratio and B_0 is the strength of the applied magnetic field (Figure 2.10B1). The magnetization of proton (M_0) can be considered as two orthogonal components: a longitudinal component or Z component (M_z) and a transverse component lying on the XY plane (M_{xy}) (Figure 2.10B2). Under the external magnetic field, there are more spins aligned with the field (low energy state) than against the field (high energy state). Therefore, the net magnetization or macroscopic magnetization has a longitudinal component aligned with applied magnetic field (Figure 2.10B3).

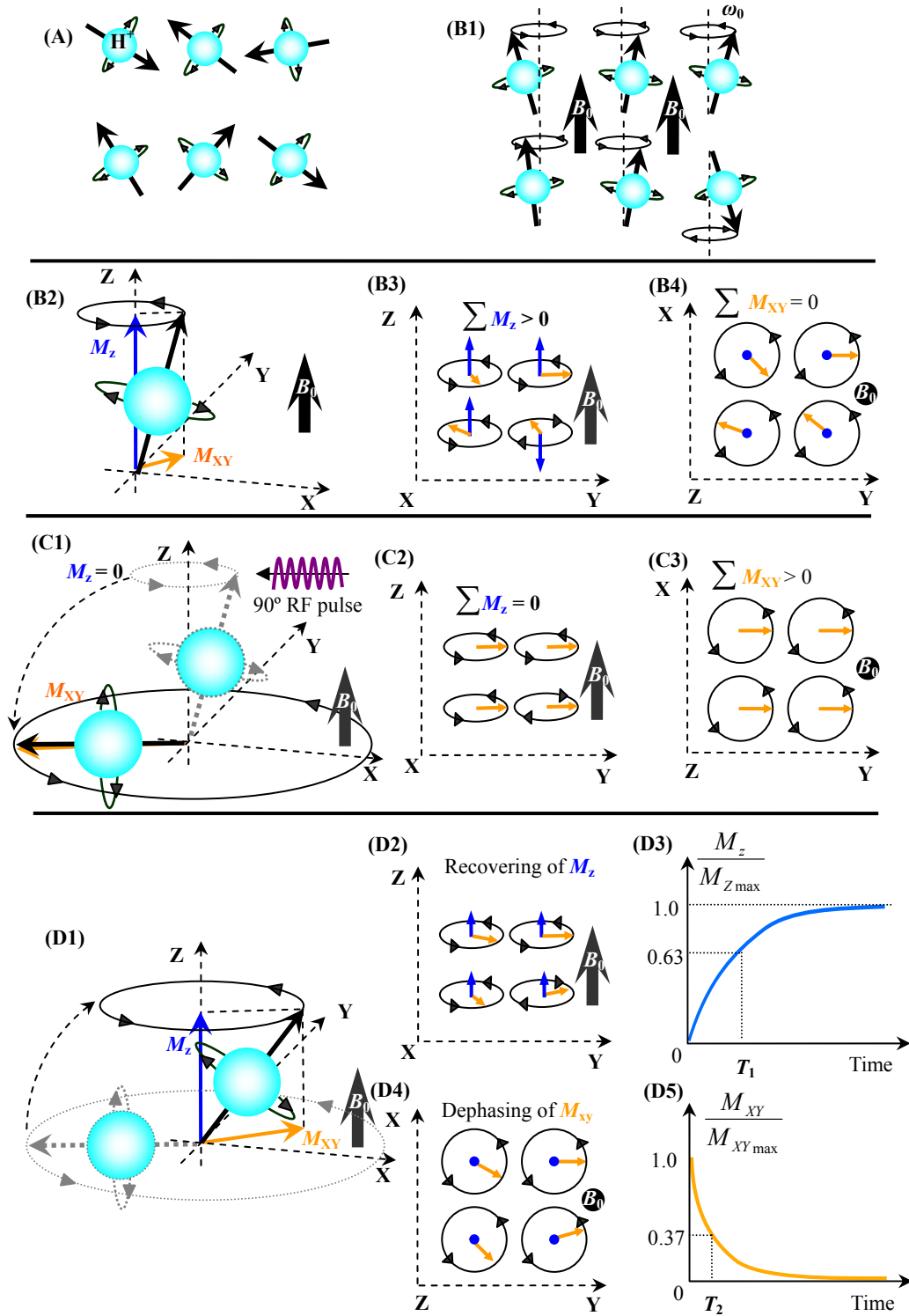


Figure 2.10 Principle of magnetic resonance imaging. (A) Protons have their magnetic moment oriented randomly in the absence of an external magnetic field. (B) Proton spins align parallel or antiparallel to the magnetic field and precess under Larmor frequency (ω_0). (C) Excitation process: after induction of 90° radio-frequency (RF) pulse, protons absorb energy and magnetization rotates into transverse plane. (D) Relaxation process: following a 90° RF pulse, excited spins release their energy through longitudinal and transverse relaxation process. More details are presented in the main text.

At equilibrium, the sum of transverse magnetization is zero as spins and magnetization of proton (M_0) equals M_z (Figure 2.10B4). When a ‘resonance’ frequency in the radio-frequency (RF) range is introduced to the nuclei, the protons absorb energy at resonance frequency and are excited to the higher energy state, i.e. from parallel to antiparallel direction. Depending on the strength of the RF pulse, the magnetization of proton (M_0) can rotate 90-degree into the transverse plane, this is termed as a 90-degree flip angle pulse (Figure 2.10C1). During such excitation process, the longitudinal magnetization disappears gradually due to the decrease of z axis component (M_z) of net magnetization, while transverse magnetization (M_{XY}) increases since the spins have phase coherence. At the end of the 90° RF pulse, when the magnetization of proton are oriented in the transverse plane, the value of M_z will be zero (Figure 2.10C2). By contrast, M_{XY} reaches its maximum because each proton precesses at the same frequency and is synchronized at the same point or phase of its precessional cycle (Figure 2.10C3).

After excitation, the nuclei will undergo the relaxation process, i.e. emit energy and return to their equilibrium state (Figure 2.10D1). There are two different relaxation pathways. The first is called longitudinal relaxation and involves energy loss so that the net magnetization (M_0) returns to its initial equilibrium state along Z axes (Figure 2.10D2). The longitudinal relaxation time (T_1), also called spin-lattice relaxation time, is a consequence of energy transfer between the excited proton (“spin”) transfers its energy to its surroundings (“lattice”) like nearby molecules. It is noticeable that this type energy transfer no longer contributes to the spin excitation.⁵¹ The relaxation time T_1 is defined as the time required for M_z to return to 63% of its original value following an excitation pulse (Figure 2.10D3).⁵¹

Transverse relaxation is the other relaxation pathway and involves the induced magnetization in the perpendicular plane (M_{xy}) and involves the loss of coherence of the proton spins in the XY plane (Figure 2.10D4). Transverse relaxation time T_2 is defined as the time when the transverse magnetization decays to 37% of its

original value after an excitation RF pulse (Figure 2.10D5).⁵¹ Transverse relaxation is also referred as spin–spin relaxation, involving the energy transfer from an excited proton to another nearby proton.⁵¹ Indeed nearby proton of the same type having the same molecular environment and the same ω_0 , can readily absorb the energy that is being released by its neighbour, get excited and then transfer this energy to another neighbouring spin. In a T_2 relaxation process, the absorbed energy remains as spin excitation rather than being transferred to the surroundings in contrast of a T_1 relaxation process. This fluctuation produces a gradual, irreversible loss of phase coherence to the spins as they exchange energy and reduce the magnitude of the transverse magnetization. Another additional mechanism for the loss of phase coherence arises is called T_2^* arises from the fact that a proton never experiences a 100% homogeneous magnetic field. The fluctuating local magnetic field causes a change in ω_0 and a loss in transverse phase coherence. This nonuniformity in B_0 comes from three sources:

- i) main field inhomogeneity related to imperfections in magnet manufacturing.
- ii) sample-induced inhomogeneity, e.g. differences in the magnetic susceptibility or degree of magnetic polarization of adjacent tissues (e.g., bone, air) will distort the local magnetic field near the interface between the different tissues.
- iii) Imaging gradients generated by a technique used for spatial localization generates a magnetic field inhomogeneity that induces proton dephasing.⁵¹

In a T_1 -weight image, the repetition time (T_R) is set short relative to T_1 . Under these conditions, the water hydrogen's with long T_1 are not given time to relax back to equilibrium before the next pulse of radiofrequency energy is applied, therefore the signal get saturated and signal observed is reduced. Thus in an image, water in tissues with short T_1 appears brighter than water in tissues with long T_1 . In a T_2 -weighted image, the echo repetition time (T_E) is set long relative to T_2 . Water protons with short T_2 lead to signal loss and gives dark contrast image. Since there is often little difference in relaxation time between healthy and pathological tissues, additional supplements known as contrast agents are often necessary in order to improve the accuracy of detection and diagnosis.⁵²

2.4.4.2. T_1 Contrast Agent

In practise, all MRI contrast agents alter both T_1 and T_2 . However, T_1 contrast agents alter the longitudinal relaxation rate T_1^{-1} more than transverse relaxation rate T_2^{-1} . The result is that tissue containing contrast agent appears brighter than before (hypointensity). Most intravenous contrast agents currently in clinical use are T_1 relaxation agents. The formulations consist of one or more paramagnetic metal ions, typically gadolinium.

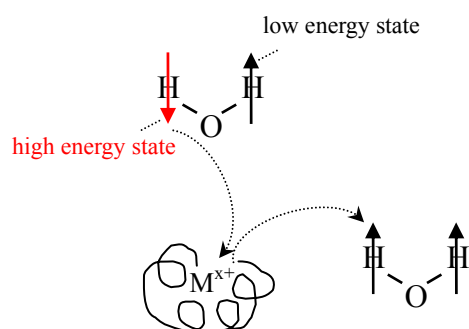


Figure 2.11 Exchange of water molecules in the coordination sphere of a metal ion (M^{x+}) surrounded by ligand. The chelate molecule causes steric hindrance around the metal ion, restricting its access. An excited water molecule is small enough to reach the inner sphere and transfer its energy to the metal ion and becomes unexcited. Modified from ref.⁵¹.

As mentioned above, T_1 relaxation depends upon the “lattice” or surroundings receiving the energy from the protons have absorbed from the RF excitation pulse. The primary mode of operation for T_1 contrast agents can be seen a relaxation sink for the water protons. When an excited water molecule diffuses and gets close to the paramagnetic metal ion, it transfers energy to the metal ion and becomes unexcited (Figure 2.11).⁵¹ The water molecules which gave its absorbed energy to the contrast agent will further exchange energy with other water molecules. This diffusion/exchange occurs very rapidly, $\sim 10^6$ times per second, ideally enabling the bulk tissue water to relaxed back to equilibrium before the subsequent excitation pulse is applied. In addition, the coordinated ligands around metal ions are relatively large and cause a steric hindrance. For this reason, the energy transfer between water molecules and contrast agent occurs most efficiently when the protons are close to the metal ion. This is one of the factors that induce the

contrast between different tissues. For example, it is difficult for the protons of large molecules such as fat to get close to the metal ion for efficient energy transfer. In contrast, protons on water molecule are able to diffuse into the coordination sphere of the metal ion and transfer its energy, after which it can exchange energy with the bulk tissue water molecules, enabling additional water molecules to enter the coordination sphere. The effect is a much more efficient energy transfer than with large hydrocarbon molecules.

Ion	Electron Configuration		Magnetic Moment (μ_B)
	3d	4f	
$^{25}\text{Mn}^{2+}$	$\uparrow \uparrow \uparrow \uparrow \uparrow$		5.92
$^{26}\text{Fe}^{3+}$	$\uparrow \uparrow \uparrow \uparrow \uparrow$		5.92
$^{29}\text{Cu}^{2+}$	$\uparrow\downarrow \uparrow\downarrow \uparrow\downarrow \uparrow\downarrow \uparrow$		1.73
$^{64}\text{Gd}^{3+}$		$\uparrow \uparrow \uparrow \uparrow \uparrow \uparrow \uparrow$	7.94

Figure 2.12 Electron configuration and spin-only effective magneton numbers of metal ions, μ_B is the Bohr magneton, closely equal to the spin magnetic moment of a free electron.^{29, 50}

The Gadolinium (Gd^{3+})-based agents are most widely used T_1 contrast agent because Gd^{3+} has seven unpaired electrons resulting a high magnetic moment and its relatively slow electronic relaxation rate (Figure 2.12).⁵²⁻⁵³ Other transition metal ions are used alternatively as T_1 contrast agents include manganese (Mn^{2+}), iron (Fe^{3+}), and copper (Cu^{2+}) ions. Due to the toxicity of metal ions, the contrast agents are usually in the form of ionic complexes with chelating ligands. For example, Gd-DTPA (Magnevist) is a widely used Gd based T_1 contrast agent and its chemical structure is displayed in Figure 2.13. It is the first contrast agent introduced in clinical practice in which the octa-coordinating DTPA ligand wraps around the Gd^{3+} . The ligand encapsulates the gadolinium, resulting in a high thermodynamic stability and kinetic inertness with respect to metal loss. All commercialized gadolinium compounds exhibit similar features: eight coordinate ligands plus a single water molecule bound to gadolinium. The coordinated water molecule is responsible for a rapid chemical exchange with solvating water

molecules leading to a catalytic effect whereby the Gd complexes are able to effectively shorten the T_1 relaxation times of the bulk solution.

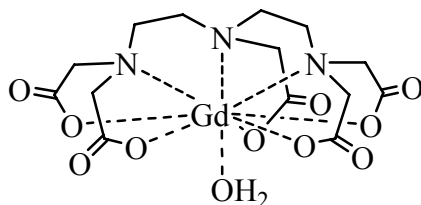


Figure 2.13 The chemical structure of Gd-DTPA compound.⁵³

After administration, the paramagnetic ions complexes based T_1 contrast agents are easily excreted from the patients' body resulting in very short life spans in the body after having worked in a nonspecific manner. Most T_1 contrast agents reside within the extracellular space, and usually interact with the blood. Therefore they have limitations to be used as MRI probes of targeting and long time tracking functions.⁵⁰

Very recently, the nanostructured T_1 contrast agents have attracted intense attention. They are promising candidates as they only retaining the positive contrast function, but have very efficient relaxivity because the surface of the NPs contains a large number of metal ions with high magnetic moment.⁵⁴ In addition, nanostructured size also allows more efficient intracellular uptake and accumulation, as well as having longer circulation time in the body. Furthermore, nanostructured materials have large surface area that is suitable for surface modification and labelling with for example disease-specific biomarker. The nanostructured T_1 contrast agents can be classified into two categories:⁵⁴ the first category is nanostructured materials immobilized with a large number of paramagnetic ions like Gd^{3+} . Such nanostructured materials have been investigated include dendrimers, liposomes, silica and carbon nanotubes, which act as framework to be either loaded or surface conjugated with paramagnetic ions or their complexes.⁵⁵⁻⁵⁶ The other class of nanostructured T_1 contrast agents is inorganic NPs with surface functionalized with biocompatible materials. Typical

examples include Dextran, PEG coated Gd_2O_3 ,⁵⁷ GdPO_4 ,⁵⁸ MnO ,⁵⁹ GdF_3 NPs,⁶⁰ graphitic carbon-PEG coated FeCo NPs.⁶¹

2.4.4.3. T_2 Contrast Agent

In contrast to T_1 contrast agents, T_2 contrast agents increase T_2^{-1} dominantly. The reduction in the water protons T_2 relaxation time is induced by the local magnetic inhomogeneities created by the local magnetic moment of T_2 contrast agents, leading to a rapid dephasing of proton spins in XY plane. Consequently, the presence of T_2 contrast agents in tissues produces a reduction in signal intensity resulting in a dark contrast image (hypointensity). T_2 contrast agents are normally based on magnetic NPs.^{36, 45-46, 50, 62-69} Because of their particulate structure, they have advantages over conventional T_1 paramagnetic complex contrast agent, such as efficient uptake by both macrophage and non-phagocytic cells, and large surface area ready for surface functionalization with biological probes like antibodies, oligonucleotides for targeted imaging purpose. Superparamagnetic iron oxide particles (SPIO) are classic examples of T_2 contrast agents, which have been widely investigated as MRI molecular and cellular imaging probes since their first use as MRI contrast agent about 20 years ago.⁵² Since the size of particles is the main factor that controls their bio-characteristics, such as blood half-life and biodistribution, they can be classified by size into three categories:^{50,}

- i) micro-sized paramagnetic iron oxide NPs (MPIO, > 200 nm),
- ii) superparamagnetic iron oxide NPs (SPIO, < 50 nm),
- iii) ultra small superparamagnetic iron oxide NPs (USPIO, < 50 nm),

Each of them has their main imaging applications.

MPIO are iron oxide particles with a large diameter normally over 200 nm. Their main applications are for exploration of gastrointestinal tract due to their large size.⁷⁰ MPIO NPs convey an amount of iron per particle that is orders of magnitude greater than ultrasmall iron oxide NPs. Therefore they are able to cause a local magnetic field inhomogeneity extending for a distance roughly 50 times their

physical diameter. Advantageously, MPIO NPs are less susceptible to non-specific uptake by endothelial cells than smaller NPs. Finally, MPIO NPs clear rapidly from the blood circulation which results in minimal background contrast. Due to these advantages, MPIO NPs have also been exploited as MRI probes conjugated with antibody for *in vivo* detection endothelial vascular cell adhesion molecule-1 which is one of the key mediators of leukocyte recruitment associated with acute brain inflammation in a mouse model.⁷¹

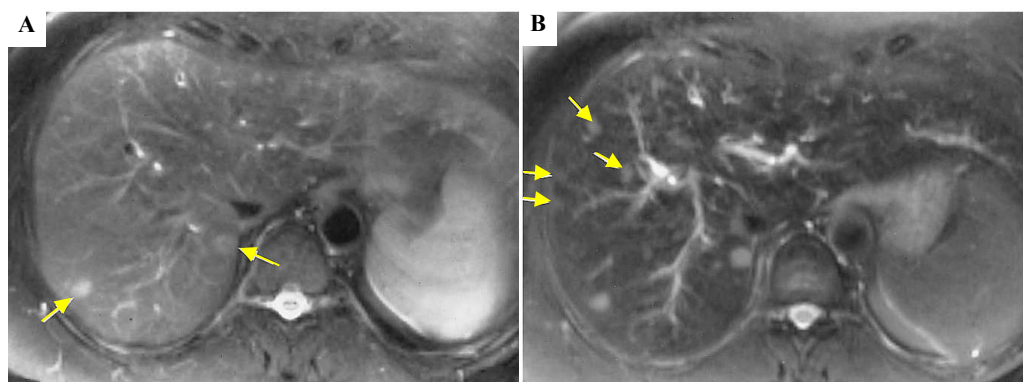


Figure 2.14 MR images of liver metastases: T_2 -weighted MR image without Feridex (A) and with Feridex (B). Lesions are indicated by arrows. (Reproduced with permission from ⁽⁷²⁾. Copyright 2001, Radiological Society of North America.)

The most widely used T_2 contrast agent are SPIO NPs, which are superparamagnetic iron oxide (e.g. Feridex I.V.®, Resovist®) with diameters greater than 50 nm. The usual clinical targets of SPIO have been liver, spleen, bone marrow, because of the efficient phagocytosis of SPIO by the macrophages which are abundantly located in those organs.⁷³⁻⁷⁵ For the instance with the detection of liver disease, the normal liver architecture is destructed by a hepatic disease, such as a primary liver tumour or liver metastasis, this region lacks macrophages known as Kupffer cells. Consequently the pathological tissue takes up less SPIO and therefore in the image appears brighter compared to healthy liver tissues. Typical MR images of liver metastases are presented in Figure 2.14 to illustrate the efficiency of SPIO as a contrast agent. Figure 2.14A shows T_2 -weighted MR image without contrast agent containing two mildly hyperintense focal liver lesions as indicated by arrows. In comparison, Figure 2.14B under the contrast enhancement of Feridex displays additional small metastases that are not

apparent in Figure 2.14A as indicated by arrows. The main disadvantage of SPIO is their rapid clearance by the reticuloendothelial system which leads to a short blood circulation time and limits SPIO's capacity to be used as molecular and cellular targeting MRI probes *in vivo*.

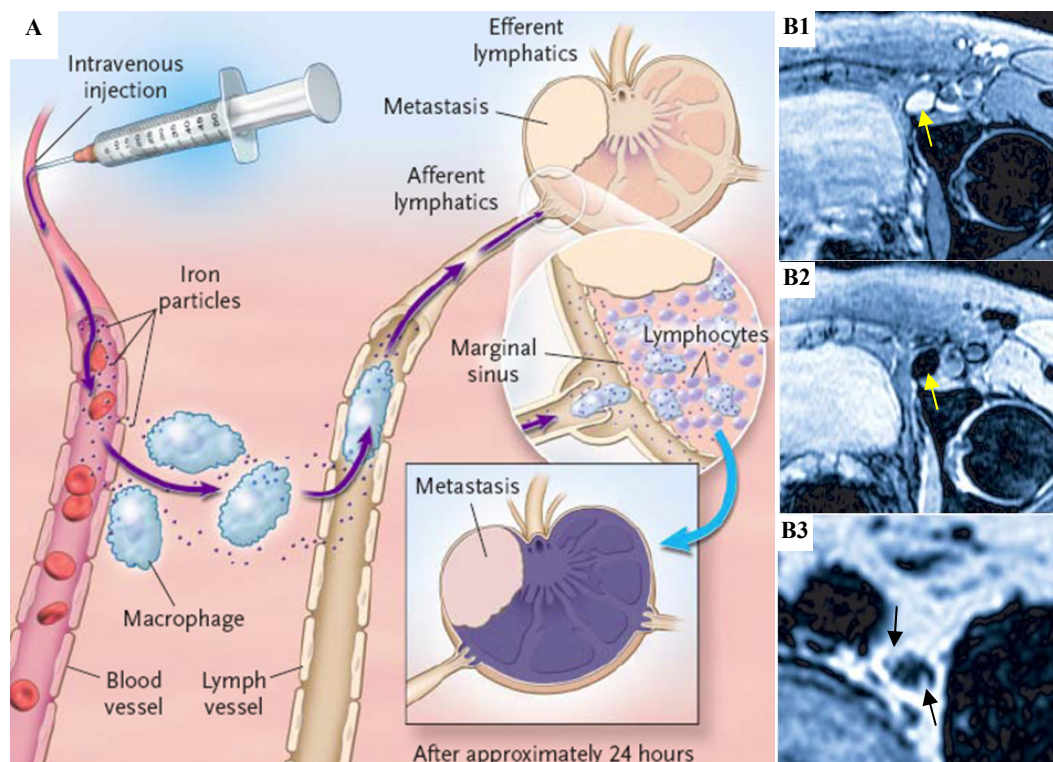


Figure 2.15 Schematic drawing of mechanism of lymph nodes MRI using USPIO NPs (A). (B) Clinic MRI of nodal abnormalities in patients with prostate cancer: as compared with conventional MRI (B1), MRI obtained 24 hours after the administration of USPIO NPs shows a homogeneous decrease in signal intensity due to the accumulation of USPIO NPs in a normal lymph node indicated by arrow (B2), MRI with USPIO NPs demonstrates two hyperintense foci (B3) within the node, corresponding to 2-mm metastases. (Reproduced with permission from ⁽⁷⁶⁾. Copyright 2003 Massachusetts Medical Society.)

USPIO are superparamagnetic iron oxide (e.g. Cambidex®) with size less than 50 nm. Like SPIO, USPIO are also used for macrophage-specific MR imaging since they can be selectively ingested by macrophages which are located in the organs of the mononuclear phagocyte system, i.e. bone marrow, lymph nodes, liver and spleen or by migrating macrophages.⁷⁶⁻⁷⁹ However, USPIO NPs have longer blood circulating life than SPIO NPs, primarily because they accumulate less in the reticulo-endothelial system due to their smaller size than SPIO. This makes them very useful in lymph nodes imaging application. The resulting longer blood

circulating life allows USPIO NPs to be extravasated from the blood vessels into interstitial spaces, from which they are transported to lymph nodes through lymphatic vessels. Within normal lymph nodes tissue, USPIO NPs accumulate through phagocytosis by nodal macrophages and induce a reduction in signal intensity in T_2 weighted image. However, if a lymph node contains metastases, there will be a limited hypointensity within metastases tissue due to the lacks of nodal phagocytosis of USPIO NPs. This produces contrast between normal lymph nodes tissue and metastases (Figure 2.15A).

Weissleder *et al* reported a successful detection of lymph-node metastases in patients with prostate cancer using USPIO. As compared with conventional MRI (Figure 2.15B1), MRI obtained 24 hours after the administration of USPIO NPs shows a homogeneous decrease in signal intensity due to the accumulation of USPIO NPs in a normal lymph node indicated by arrow (Figure 2.15B2). MRI with USPIO NPs demonstrates two hyperintense foci within the node, corresponding to 2-mm metastases (Figure 2.15B3).

2.5. Conclusion

This chapter presented an overview of the general features and unique physical and chemical properties of inorganic nanoparticles (NPs) and their biomedical applications. Quantum dots (QDs) and gold NPs are introduced as representative examples of non-magnetic NPs in the first half of this chapter. QDs, due to their size and composition tunable fluorescence emission (ranging from visible to infrared wavelengths) have been widely investigated as fluorophore probes for optical biological imaging including *in vivo* imaging. They have great potential in non-invasive disease diagnosis application. Gold (Au) NPs have attracted huge attention as optical probes for biological imaging, due to their SPR (surface plasmon resonance) enhance scattering and fluorescence properties. In addition, the photothermal property of Au NPs attributed to the strong light absorption as a result of the SPR, makes them promising candidates for photothermal cancers treatment and as thermal sensitive drug carriers.

This PhD thesis focuses on the synthesis and biomedical application of iron platinum alloy magnetic NPs as MRI contrast agent. Therefore, the second half of this chapter focused on the basic principles of magnetic properties including the origins of magnetism, magnetic properties in the bulk materials and special magnetic features of magnetic NPs. Due to the unique magnetic properties of magnetic NPs and their ability to function at the cellular and molecular level of biological interaction, magnetic NPs have attracted tremendous research interest as revolutionary diagnostic and therapeutic tools in biomedical applications including magnetic separation, magnetic targeting, hyperthermia, and especially as contrast agents for magnetic resonance imaging. MRI contrast agents depend upon altering the longitudinal (T_1) or transverse (T_2) relaxation time of water protons, and can be divided into two general groups i.e. T_1 or T_2 contrast agent depending on which relaxation is the dominate effect. Magnetic NPs can significantly shorten the T_2 relaxation time of water protons by producing local magnetic moment inhomogeneities, resulting in hyperintensity. Magnetic NPs based T_2 contrast agents have advantages over conventional T_1 paramagnetic ionic contrast agent, such as efficient uptake by both macrophage and non-phagocytic cells, and large surface area ready for surface functionalization with biological probes like antibodies, oligonucleotides for targeted imaging purpose.

Iron platinum (FePt) NPs have emerged as an important class of magnetic material with high Curie temperature, saturation magnetic moment and magneto-crystalline anisotropy. FePt NPs are promising candidates for a new generation of magnetic nano-material. Over the course of this PhD thesis, the synthesis, characterization and functionalization of FePt NPs and their application as MRI contrast agent were investigated. In next Chapter, a short literature review of synthesis, characterization, functionalization of FePt magnetic NPs will be presented.

References

- (1) Willard, M. A.; Kurihara, L. K.; Carpenter, E. E.; Calvin, S.; Harris, V. G. *Int. Mater. Rev.* **2004**, 49, 125-170.
- (2) Gao, J. H.; Xu, B. *Nano. Today.* **2009**, 4, 37-51.
- (3) Hosokawa, M.; Kiyoshi, N.; Naito, M.; Yokoyama, T., *Nanoparticle Technology Handbook*. 1st ed.; Elsevier Science: London, 2007.
- (4) Gubin, S. P., *Magnetic Nanoparticles*. 1st ed.; Wiley: London, 2009.
- (5) Pankhurst, Q. A.; Connolly, J.; Jones, S. K.; Dobson, J. *J. Phys. D-Appl. Phys.* **2003**, 36, R167-R181.
- (6) Xia, Y. N. *Nat. Mater.* **2008**, 7, 758-760.
- (7) Petros, R. A.; DeSimone, J. M. *Nat. Rev. Drug. Discov.* **2010**, 9, 615-627.
- (8) Reiss, P.; Protiere, M.; Li, L. *Small.* **2009**, 5, 154-168.
- (9) Klostranec, J. M.; Chan, W. C. W. *Adv. Mater.* **2006**, 18, 1953-1964.
- (10) Han, M. Y.; Gao, X. H.; Su, J. Z.; Nie, S. *Nat. Biotechnol.* **2001**, 19, 631-635.
- (11) Medintz, I. L.; Uyeda, H. T.; Goldman, E. R.; Mattoussi, H. *Nat. Mater.* **2005**, 4, 435-446.
- (12) Wu, X.; Liu, H.; Liu, J.; Naley, K. N.; Treadway, J. A.; Larson, J. P.; Ge, N.; Peale, F.; Bruchez, M. P. *Nat. Biotechnol.* **2003**, 21, 41-46.
- (13) Voura, E. B.; Jaiswal, J. K.; Mattoussi, H.; Simon, S. M. *Nat. Med.* **2004**, 10, 993-998.
- (14) Bakalova, R.; Zhelev, Z.; Aoki, I.; Kanno, I. *Nat. Photonics.* **2007**, 1, 487-489.
- (15) Medintz, I. L.; Clapp, A. R.; Mattoussi, H.; Goldman, E. R.; Fisher, B.; Mauro, J. M. *Nat. Mater.* **2003**, 2, 630-638.
- (16) Brus, L. E. *J. Chem. Phys.* **1984**, 80, 4403-4409.
- (17) Brus, L. *J. Phys. Chem.* **1986**, 90, 2555-2560.
- (18) Gao, X.; Cui, Y.; Levenson, R. M.; Chung, L. W.; Nie, S. *Nat. Biotechnol.* **2004**, 22, 969-976.
- (19) Kim, S.; Lim, Y. T.; Soltesz, E. G.; De Grand, A. M.; Lee, J.; Nakayama, A.; Parker, J. A.; Mihaljevic, T.; Laurence, R. G.; Dor, D. M.; Cohn, L. H.; Bawendi, M. G.; Frangioni, J. V. *Nat. Biotechnol.* **2004**, 22, 93-97.
- (20) Bailey, R. E.; Nie, S. *J. Am. Chem. Soc.* **2003**, 125, 7100-7106.
- (21) Kim, S.-W.; Zimmer, J. P.; Ohnishi, S.; Tracy, J. B.; Frangioni, J. V.; Bawendi, M. G. *J. Am. Chem. Soc.* **2005**, 127, 10526-10532.
- (22) Huang, X. H.; Jain, P. K.; El-Sayed, I. H.; El-Sayed, M. A. *Nanomedicine-Uk.* **2007**, 2, 681-693.
- (23) Kelly, K. L.; Coronado, E.; Zhao, L. L.; Schatz, G. C. *J. Phys. Chem. B.* **2003**, 107, 668-677.
- (24) Aslan, K.; Lakowicz, J. R.; Geddes, C. D. *Curr. Opin. Chem. Biol.* **2005**, 9, 538-544.
- (25) Yavuz, M. S.; Cheng, Y.; Chen, J.; Cobley, C. M.; Zhang, Q.; Rycenga, M.; Xie, J.; Kim, C.; Song, K. H.; Schwartz, A. G.; Wang, L. V.; Xia, Y. *Nat. Mater.* **2009**, 8, 935-939.
- (26) Tipler, P. A., *Physics for Scientists and Engineers*. 4th ed.; W. H. Freeman and Company: New York, NY.

- (27) Jiles, D., *Introduction to Magnetism and Magnetic Materials*. 1st ed.; Chapman and Hall: London, 1991.
- (28) Jeong, U.; Teng, X. W.; Wang, Y.; Yang, H.; Xia, Y. N. *Adv. Mater.* **2007**, 19, 33-60.
- (29) Kittel, C., *Introduction to solid state physics*. 8th ed.; Wiley: 2005.
- (30) Turton, R. J., *The Physics of Solids* 1st ed.; Oxford: New York, 2000.
- (31) O'Handley, R. C., *Modern Magnetic Materials: Principles and Applications*. 1st ed.; Wiley, New York: New York ; Chichester, 2000.
- (32) Chikazumi, S., *Physics of Ferromagnetism*. 2nd ed.; Oxford: New York, 1997.
- (33) Lu, A. H.; Salabas, E. L.; Schuth, F. *Angew. Chem.-Int. Edit.* **2007**, 46, 1222-1244.
- (34) Bedanta, S.; Kleemann, W. *J. Phys. D. Appl. Phys.* **2009**, 42, 013001.
- (35) Hansen, M. F.; Morup, S. *J. Magn. Magn. Mater.* **1999**, 203, 214-216.
- (36) Sun, C.; Lee, J. S. H.; Zhang, M. Q. *Adv. Drug. Deliver. Rev.* **2008**, 60, 1252-1265.
- (37) Gu, H.; Ho, P. L.; Tsang, K. W. T.; Wang, L.; Xu, B. *J. Am. Chem. Soc.* **2003**, 125, 15702-15703.
- (38) Sun, S. H. *Adv. Mater.* **2006**, 18, 393-403.
- (39) Lammers, T.; Hennink, W. E.; Storm, G. *Br J Cancer.* **2008**, 99, 392-397.
- (40) Hillery, A. M.; Lloyd, A. W.; Swarbrick, J., *Drug Delivery and Targeting for Pharmacists and Pharmaceutical Scientists*. ed.; Taylor & Francis: London, 2001.
- (41) Arruebo, M.; Fernandez-Pacheco, R.; Ibarra, M. R.; Santamaria, J. *Nano Today.* **2007**, 2, 22-32.
- (42) Otsuka, H.; Nagasaki, Y.; Kataoka, K. *Adv. Drug. Deliv. Rev.* **2003**, 55, 403-419.
- (43) Goodwin, S.; Peterson, C.; Hoh, C.; Bittner, C. *J. Magn. Magn. Mater.* **1999**, 194, 132-139.
- (44) Goodwin, S. C.; Bittner, C. A.; Peterson, C. L.; Wong, G. *Toxicol. Sci.* **2001**, 60, 177-183.
- (45) Figuerola, A.; Di Corato, R.; Manna, L.; Pellegrino, T. *Pharmacol. Res.* **2010**, 62, 126-143.
- (46) Mornet, S.; Vasseur, S.; Grasset, F.; Duguet, E. *J. Mater. Chem.* **2004**, 14, 2161-2175.
- (47) van der Zee, J. *Ann. Oncol.* **2002**, 13, 1173-1184.
- (48) Hergt, R.; Dutz, S.; Muller, R.; Zeisberger, M. *J. Phys-Condens. Mat.* **2006**, 18, S2919-S2934.
- (49) Maenosono, S.; Saita, S. *Ieee. T. Magn.* **2006**, 42, 1638-1642.
- (50) Na, H. B.; Song, I. C.; Hyeon, T. *Adv. Mater.* **2009**, 21, 2133-2148.
- (51) Brown, M. A.; Semelka, R. C., *MRI: Basic Principles and Applications*. 3rd ed.; Wiley: Hoboken, 2005.
- (52) Modo, M. M. J.; Bulte, J. W. M., *Molecular and Cellular MR Imaging*. 1st ed.; CRC Press: London, 2007.
- (53) Caravan, P. *Chem. Soc. Rev.* **2006**, 35, 512-523.
- (54) Na, H. B.; Hyeon, T. *J. Mater. Chem.* **2009**, 19, 6267-6273.
- (55) Sipkins, D. A.; Cheresch, D. A.; Kazemi, M. R.; Nevin, L. M.; Bednarski, M. D.; Li, K. C. P. *Nat. Med.* **1998**, 4, 623-626.

- (56) Rieter, W. J.; Kim, J. S.; Taylor, K. M. L.; An, H. Y.; Lin, W. L.; Tarrant, T.; Lin, W. B. *Angew. Chem. Int. Edit.* **2007**, 46, 3680-3682.
- (57) Bridot, J. L.; Faure, A. C.; Laurent, S.; Riviere, C.; Billotey, C.; Hiba, B.; Janier, M.; Josserand, V.; Coll, J. L.; Vander Elst, L.; Muller, R.; Roux, S.; Perriat, P.; Tillement, O. *J. Am. Chem. Soc.* **2007**, 129, 5076-5084.
- (58) Hifumi, H.; Yamaoka, S.; Tanimoto, A.; Citterio, D.; Suzuki, K. *J. Am. Chem. Soc.* **2006**, 128, 15090-15091.
- (59) Na, H. B.; Lee, J. H.; An, K.; Park, Y. I.; Park, M.; Lee, I. S.; Nam, D. H.; Kim, S. T.; Kim, S. H.; Kim, S. W.; Lim, K. H.; Kim, K. S.; Kim, S. O.; Hyeon, T. *Angew. Chem. Int. Ed. Engl.* **2007**, 46, 5397-5401.
- (60) Evanics, F.; Diamante, P. R.; van Veggel, F. C. J. M.; Stanisiz, G. J.; Prosser, R. S. *Chem. Mater.* **2006**, 18, 2499-2505.
- (61) Seo, W. S.; Lee, J. H.; Sun, X. M.; Suzuki, Y.; Mann, D.; Liu, Z.; Terashima, M.; Yang, P. C.; McConnell, M. V.; Nishimura, D. G.; Dai, H. *J. Nat. Mater.* **2006**, 5, 971-976.
- (62) Weinstein, J. S.; Varallyay, C. G.; Dosa, E.; Gahramanov, S.; Hamilton, B.; Rooney, W. D.; Muldoon, L. L.; Neuwelt, E. A. *J. Cerebr. Blood. F. Met.* **2010**, 30, 15-35.
- (63) Corot, C.; Robert, P.; Idee, J. M.; Port, M. *Adv Drug Deliver Rev.* **2006**, 58, 1471-1504.
- (64) Gupta, A. K.; Gupta, M. *Biomaterials.* **2005**, 26, 3995-4021.
- (65) Frey, N. A.; Peng, S.; Cheng, K.; Sun, S. H. *Chem. Soc. Rev.* **2009**, 38, 2532-2542.
- (66) Tartaj, P. *Curr. Nanosci.* **2006**, 2, 43-53.
- (67) Wang, Y. X. J.; Hussain, S. M.; Krestin, G. P. *Eur. Radiol.* **2001**, 11, 2319-2331.
- (68) Berry, C. C.; Curtis, A. S. G. *J. Phys. D-Appl. Phys.* **2003**, 36, R198-R206.
- (69) Veiseh, O.; Gunn, J. W.; Zhang, M. Q. *Adv. Drug. Deliver. Rev.* **2010**, 62, 284-304.
- (70) Yan, G.; Robinson, L.; Hogg, P. *Radiography.* **2007**, 13, e5-e19.
- (71) McAteer, M. A.; Sibson, N. R.; von zur Muhlen, C.; Schneider, J. E.; Lowe, A. S.; Warrick, N.; Channon, K. M.; Anthony, D. C.; Choudhury, R. P. *Nat. Med.* **2007**, 13, 1253-1258.
- (72) Semelka, R. C.; Helmberger, T. K. G. *Radiology.* **2001**, 218, 27-38.
- (73) Gandhi, S. N.; Brown, M. A.; Wong, J. G.; Aguirre, D. A.; Sirlin, C. B. *Radiographics.* **2006**, 26, 1621-1636.
- (74) Mahfouz, A. E.; Hamm, B.; Taupitz, M. *Eur. Radiol.* **1997**, 7, 507-513.
- (75) Kim, S. H.; Lee, J. M.; Han, J. K.; Lee, J. Y.; Kang, W. J.; Jang, J. Y.; Shin, K. S.; Cho, K. C.; Choi, B. I. *Eur. Radiol.* **2006**, 16, 1887-1897.
- (76) Harisinghani, M. G.; Barentsz, J.; Hahn, P. F.; Deserno, W. M.; Tabatabaei, S.; van de Kaa, C. H.; de la Rosette, J.; Weissleder, R. *New Engl. J. Med.* **2003**, 348, 2491-U2495.
- (77) Daldrup-Link, H. E.; Henning, T.; Link, T. M. *Eur. Radiol.* **2007**, 17, 743-761.
- (78) Schramm, N. *Radiologe.* **2010**, 50, 205-207.
- (79) Azoulay, R.; Olivier, P.; Baud, O.; Verney, C.; Santus, R.; Robert, P.; Gressens, P.; Sebag, G. *J. Magn. Reson. Imaging.* **2008**, 28, 1046-1052.

Chapter 3

Background of FePt Magnetic Nanoparticles

3.1. Introduction to FePt Magnetic Nanoparticles

The 2nd chapter presented the main characteristics of nanoparticles and then provided an introduction to magnetic nanoparticles together with their main properties and applications. This 3rd chapter aims at introducing the reader to FePt nanoparticles which, over the course of this PhD, has been the key-material used in view of developing a platform for biomedical applications. After having justified the choice of FePt as a starting material, this chapter will briefly review the main “wet” chemistry pathways used to synthesize FePt NPs, followed by the main coating options available to use FePt nanoparticles for biomedical applications. Advantages and drawbacks of each approach will be briefly discussed in each section.

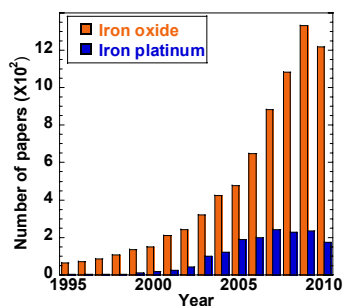


Figure 3.1 Number of publications on iron oxide and iron platinum from year 1995 to 2010. This search was carried out through ISI web of Science.¹

Interest in FePt nanocolloids is fairly recent as compared with iron oxide or cobalt for instance. Potentially more challenging to prepare than the above mentioned materials along with including the more expensive platinum, it has nonetheless seen a surge of activities over the past 10 to 15 years, which can nicely be illustrated by a straightforward search on ISI web of Science (Figure 3.1) with a simple set of keywords.¹

Table 3.1 Some intrinsic magnetic properties for selected materials. T_c : Curie temperature, M_s : saturated magnetization, K : magnetocrystalline anisotropy and D_c : estimated or reported single domain particle diameter, D_p is the thermally stable grain diameter over 10 years storage time at 300 K.

Material	Crystal Symmetry	T_c (K) (bulk)	M_s (emu/cm ³) bulk	K (1*10 ⁶ J/m ³)	D_c (nm)	D_p (nm)	Ref
Fe	<i>bcc</i>	1043	~ 1700	~1	15	--	2-3 4
Co	<i>hcp</i>	1390	~ 1400	0.45	~ 35-60	8.0	2-3, 5-7 4
Ni	<i>fcc</i>	631	~ 510	~ 0.08	55	--	2-3 4
FePt	<i>fcc, fct</i>	585 (<i>fcc</i>) 750 (<i>fct</i>)	-- 1140	-- 6.6-10	-- ~340	-- 2.8-3.3	2-3, 5-6, 8
CoPt	<i>fcc, fct</i>	840	~ 800	4.9	~610	3.6	2-3, 5-6
γ -Fe ₂ O ₃	<i>fcc</i>	848	~ 450-490	~ 0.035	30	--	2, 7
Fe ₃ O ₄	<i>fcc</i>	858	~ 480-520	~ 0.1	128	--	2-3
Fe ₁₄ Nd ₂ B	tetragonal	585	1270	4.6	~ 230	3.7	6
SmCo ₅	<i>hcp</i>	1000	910	11-20	~ 710-960	2.2-2.7	6-7

-- Values could not be found in the literature.

FePt is a bimetallic alloy material comprised of both iron and platinum. It has relatively high Curie temperature, T_c : 750 K (Table 3.1), which is much higher than room temperature. The saturated magnetization M_s is comparable to Fe and Co and about 3 times higher than iron oxides. The magnetocrystalline anisotropy K is one of the highest among hard magnetic materials of the order of ~1–10 10⁶ J/m³ (Table 3.1). This large K value observed for FePt alloys is explained by Fe and Pt interactions originating from spin-orbit coupling and the hybridization between Fe 3*d* and Pt 5*d* states.⁹ The grain diameter, D_p can go down to ~2.8 nm at 300 K.⁶ This makes FePt a promising candidate for ultra-high density recording media with the potential to reach an areal density as high as 10 Tbits/in² and above,¹⁰ if NP magnetic interactions at such a small length scale can be controlled

to guarantee the integrity of the stored information. In addition, FePt is thought to have higher chemical stability as compared to single metallic material like Fe and Co, as well as the other large coercive materials like SmCo_5 and $\text{Nd}_2\text{Fe}_{14}\text{B}$, which makes it attractive for biomedical applications.⁹ While the chemical stability will be discussed further in chapter 6, selected intrinsic magnetic properties of some of the most common magnetic materials are shown in Table 3.1 for comparison purposes.

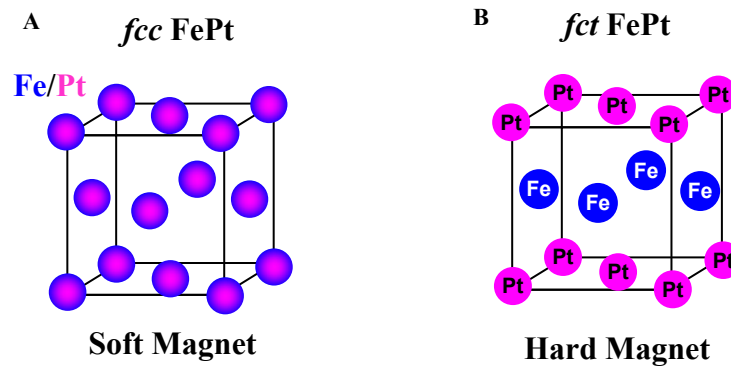


Figure 3.2 Schematic drawing of (A) face centered cubic (*fcc*) crystal phase FePt and face centered tetragonal (*fct*) FePt.

Depending upon the Fe to Pt elemental ratio, iron-platinum materials can display a complex phase diagram including chemically disordered face centered cubic (*fcc*) phase or chemically ordered phases, such as $L1_2$ for Fe_3Pt , face centered tetragonal (*fct*) phase ($L1_0$) for FePt and $L1_2$ for FePt_3 . While these crystalline structures can be influenced by the fabrication methods, they present dramatic variations in the magnetic properties of the alloys. For example, the $L1_2$ Fe_3Pt material is ferromagnetic, the *fcc* FePt is superparamagnetic, the $L1_2$ FePt_3 is antiferromagnetic, while the *fct*- $L1_0$ structured FePt shows strong ferromagnetic properties. Among these, the most investigated FePt crystal phase are *fcc* and *fct* phase FePt (Figure 3.2).

In the *fcc* phase, iron and platinum atoms are chemically disordered (Figure 3.2A), the material is a magnetically soft alloy, which means that it has very small coercivity and remanence, when the size of the material is decreased it becomes

superparamagnetic at room temperature. In contrast, the *fcc*-structured FePt is chemically ordered and can be viewed as alternating atomic layers of Fe and Pt stacked along the *c* axis direction (Figure 3.2B). The *fcc* FePt is a hard magnetic material, and its coercivity can reach values as high as ~ 2 T.⁶ The *fcc* crystalline structure can be obtained after annealing of *fcc*-FePt material and is consequently the thermodynamically stable phase; however both phases of FePt have great potential for biological applications.

3.2. Review of Solution Chemical Syntheses of FePt Nanoparticles

The preparation of homogenous colloidal nanoparticles with desired composition, size, and crystal phase is a key-concern for researchers using wet chemistry methods and this has consequently received tremendous attention for a wide range of nanocolloids. There are various techniques for producing colloidal nanoparticles and generally they are classified as either physical or chemical-synthetic methods. Larger volumes of product could potentially be produced by physical methods, the ball milling method¹¹ or pulsed plasma chemical vapor synthesis for example,¹² which would be commercially attractive. However, chemical routes often provide better control over the particle size, shape, composition and crystallinity; all of which in return impact on researchers abilities to tune the NP properties. In addition, surface modifications of the particles during or after synthesis is relatively easily achievable and provides numerous opportunities to combine additional but essential functionalities to fit specific applications.

The chemical synthesis of FePt NPs can be divided into two main classes for the sake of argumentation. The first one normally requires the reaction to be completed at a high temperature of the order of ~ 300 °C if not above (thermal decomposition pathway), while the 2nd is carried out at temperatures close to room temperature (amphiphilic method). It is however noticeable that these approaches generally lead to *fcc* crystalline structures; whereas the direct synthesis of well dispersed *fcc*-FePt is still rather challenging at present.¹³⁻¹⁴ A compensatory protocol is to subsequently

anneal *fcc*-FePt NPs which can be obtained directly through most solution synthesis protocols to induce a phase transfer towards the *fct* crystalline phase at temperatures normally above 500 °C.^{9, 15-17} In addition to the high temperature, the composition of the initial alloy is an essential factor to achieve *fcc-fct* phase transfer, which requires $40 < x < 60$ in $\text{Fe}_x\text{Pt}_{100-x}$.¹⁸⁻²⁰ Over the past few years, the annealing methods of FePt nanomaterials have gone through tremendous evolution, including for instance the use of a salt matrix,²¹⁻²⁴ or the use of a doping agent to reduce the annealing temperature.²⁵⁻³⁰ However for this review chapter to remain concise, FePt nanocolloids obtained after annealing will not be described in depth and the reader will be referred to the relevant literature.^{14, 18, 31-45} Instead, it will be focused on the nanoparticle syntheses themselves.

3.2.1. High Temperature: Thermal Decomposition and Reduction

3.2.1.1. “Conventional” Thermal Decomposition

The first very successful synthesis of monodispersed FePt NPs was reported by Sun et al in 2000,⁴⁶ potentially triggering further interest for this material. This synthesis is based on the reduction of platinum acetylacetonate $\text{Pt}(\text{acac})_2$ by a mild reducing agent 1,2-hexadecanediol and the thermal decomposition of iron pentacarbonyl, $\text{Fe}(\text{CO})_5$ in a high boiling point solvent such as benzyl ether and octyl ether (Figure 3.3A). The synthesis was carried out at ~300 °C, in the presence of stabilizers such as oleic acid and oleylamine. To describe the interplay between the precursors and the ligands, the general consensus is that carboxylate groups tend to bind to Fe atoms as a chelate ligand via monodentate or bidentate configuration, whereas amine molecules interact primarily with Pt atoms (Figure 3.3B).⁹ The long alkyl chains from both capping agents provide a steric blocking effect to stabilize FePt NPs. A typical TEM image of synthesized 6 nm FePt NPs is shown in Figure 3.3C. The composition of NPs is controlled by changing initial molar ratio of Fe to Pt precursors, e.g. a 2:1 molar ratio yielded $\text{Fe}_{52}\text{Pt}_{48}$, and a 4:1 ratio produced $\text{Fe}_{70}\text{Pt}_{30}$.⁴⁶ These parameters (precursors, ligands, solvents,

temperatures) have mostly become standards with little variation from one research group to another.^{41, 47-49} Oleic acid and oleylamine are now the ligands used as standards in several syntheses completed in non-polar, alkyl media including benzyl ether and octyl ether.

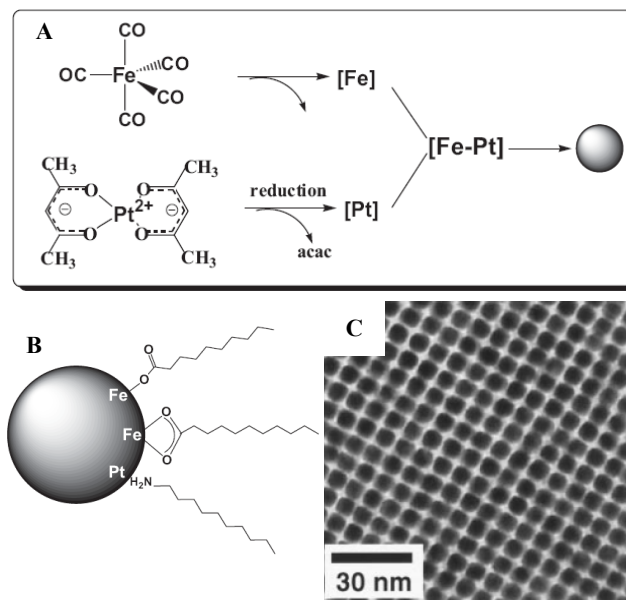


Figure 3.3 Schematic illustration of FePt nanoparticle formation through the decomposition of Fe(CO)_5 and reduction of Pt(acac)_2 (A). The schematic of binding of alkyl carboxylate and alkylamine molecules to a FePt nanoparticle (B).⁹ (Copyright 2006, Wiley-VCH Verlag GmbH & Co. KGaA. Reproduced with permission.) TEM micrograph of a 3D assembly of 6 nm $\text{Fe}_{50}\text{Pt}_{50}$ sample (C).¹⁶ (From ⁽¹⁶⁾, reprinted with permission from AAAS.)

The main disadvantage of this protocol is the broad composition distribution of individual NPs. An EDX study on the composition of individual FePt NPs showed that only 29.0% of the NPs were within the composition range of $40 < x < 60$ ($\text{Fe}_x\text{Pt}_{100-x}$), whereas 40.5% NPs were Pt rich, and 30.5% were Fe rich.¹³ The NPs nucleation and growth mechanism along with their broad composition distribution was investigated by a systematical study on this $\text{Fe(CO)}_5/\text{Pt(acac)}_2/1,2$ -hexadecanediol system.⁵⁰ It showed that Pt rich nuclei with a composition of $\sim\text{Fe}_4\text{Pt}_{96}$ (4% of Fe) formed as early as $\sim 160^\circ\text{C}$, and their formation could have been assisted by 1,2-hexadecanediol acting as a reducing agent (Figure 3.4A1). In contrast, a significant amount of Fe(CO)_5 could be found in vapor phase because of its low boiling point of 108°C . Whereas the decomposition temperature of

$\text{Fe}(\text{CO})_5$ is around 298 °C,⁵¹ the decomposition can be catalyzed by the Pt nuclei, as suggested by the Fe increase in NP, e.g. the iron content reached 15% ($\text{Fe}_{15}\text{Pt}_{85}$) at 175 °C (Figure 3.4A2). While the temperature further increased up to 200 °C, ~4 nm NPs with an individual NP composition varying from ~ $\text{Fe}_{14}\text{Pt}_{86}$ to ~ $\text{Fe}_{54}\text{Pt}_{46}$ were formed (Figure 3.4A3). After 30 min refluxing, the composition distribution of individual NPs was reported to be narrowed from ~ $\text{Fe}_{38}\text{Pt}_{62}$ to ~ $\text{Fe}_{66}\text{Pt}_{34}$, which was concomitant with a further size increase up to ~4.5 nm (Figure 3.4A4).

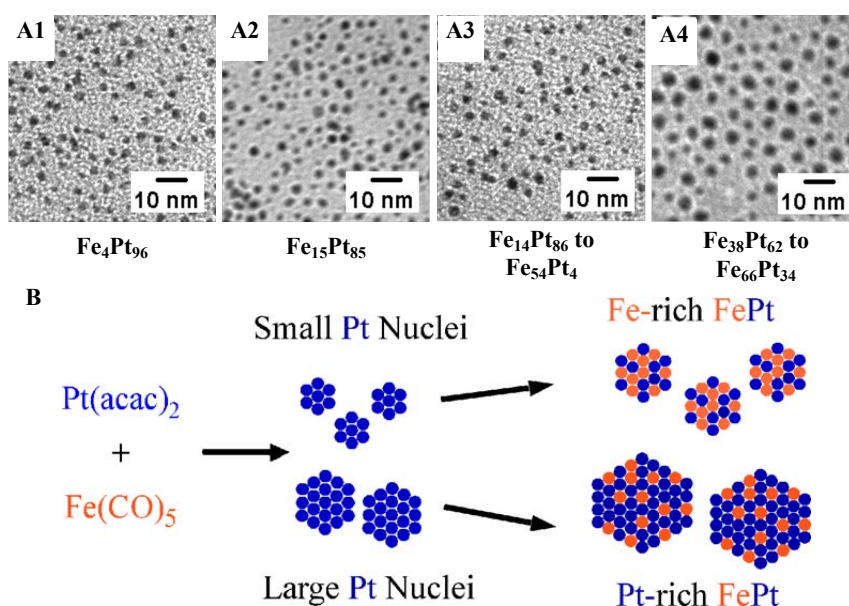


Figure 3.4 TEM images of FePt NPs withdrawn at 160 °C (A1), 175 °C (A2), 200 °C (A3), 256 °C, 30 min (A4), and a schematic of the suggested particle growth mechanism used to explain the wide composition distribution from particle to particle (B). (Adapted with permission from ⁽⁵⁰⁾, copyright 2007, American Institute of Physics.)

The broad composition distribution from particle to particle is attributed to the significant size distribution of Pt rich nuclei initially formed at 160 °C (Figure 3.4A1). Indeed, since small Pt nuclei have a larger surface area per Pt atom compared to the large nuclei, the smaller Pt nuclei would become richer in Fe (Figure 3.4B).⁵⁰ A later report provided further evidence showing that smaller NPs are indeed richer in Fe than larger ones.⁵² A later numerical study completed by Monte Carlo free energy perturbations pointed towards a thermodynamic preference for iron to be incorporated into the subsurface of a platinum rich

cluster,⁵³ this work has however to be considered carefully as the ligands are not included in the simulation and these molecules are known to have a strong impact on the growth of the NPs as illustrated for instance in the QD research field.⁵⁴⁻⁵⁶ Nonetheless as a consequence of the thermodynamic preference, the initial iron rich clusters could experience a restricted growth compared to Pt rich ones and end up as small iron rich NPs. This may explain the composition and size distribution of the NPs synthesized through this synthetic pathway.⁵⁷ An extension of the refluxing time however allows the eventual narrowing of the composition likely resulting from the Fe rich clusters attaching to the larger Pt richer NPs probably via an Oswald ripening kind of growth.⁵²

By excluding the reducing agent 1,2-alkaediol from the reaction system, NPs size was increased to 6 nm, without compromising the low size polydispersity of the product.⁵⁸ This can be attributed to a slower Pt rich nucleation in the absence of diol, which leads to a slower consumption of metal precursors at the nucleation stage.⁵⁸ Illustrating the efforts made to control this relatively new nanomaterial, along with its challenges, it is noticeable that the NPs size can be further tuned by controlling not only the ratio of stabilizers to metal precursors and the growth temperature, but also the interim heating temperature steps and heating rate. High stabilizers to precursor's ratio, low interim heating temperature steps or slow heating rate apparently slow down the nucleation rate and consequently favor the formation of larger size NPs.^{20, 58-60} For example, a molar ratio of at least 8:1, and a 15 °C/min heating rate, and a 240 °C interim heating temperature before reaching refluxing at 300 °C was required to make 6 nm size NPs. In contrast, a slower 5 °C/min heating rate and a lower heating temperature 225 °C lead to 9 nm size FePt NPs.⁵⁸

Noticeably, there are very few studies focusing on controlling the shape of FePt nanocrystals, however Fe(CO)₅/Pt(acac)₂/1,2-hexadecanediol system has been successfully used for this purpose; and by adjusting ligand concentration, or ligand adding sequence, nanowires, nanorods, hexagonal, oval-shaped and cubic NPs could then be obtained.⁶¹⁻⁶⁷ These opportunities to control the NP

morphology is very exciting, however falls beyond the scope of the present short review.

Due to the high toxicity and low boiling point of $\text{Fe}(\text{CO})_5$, less toxic and nonvolatile iron precursors, such as $\text{Fe}(\text{acac})_3$,^{37, 68-70} and $\text{Fe}(\text{OEt})_3$,^{20, 40, 71} were investigated for the synthesis of FePt NPs. When $\text{Fe}(\text{acac})_3$ is used as a precursor, ~2 nm NPs can be obtained by using a similar experimental protocol as described with $\text{Fe}(\text{CO})_5$ / $\text{Pt}(\text{acac})_2$ / 1,2-hexadecanediol system,⁶⁹⁻⁷⁰ and size can be further increased to ~6 nm NPs in presence of a large excess of ligands,⁶⁸ as very likely the complexes they form with the iron and platinum atoms decrease the NPs nucleation rate.

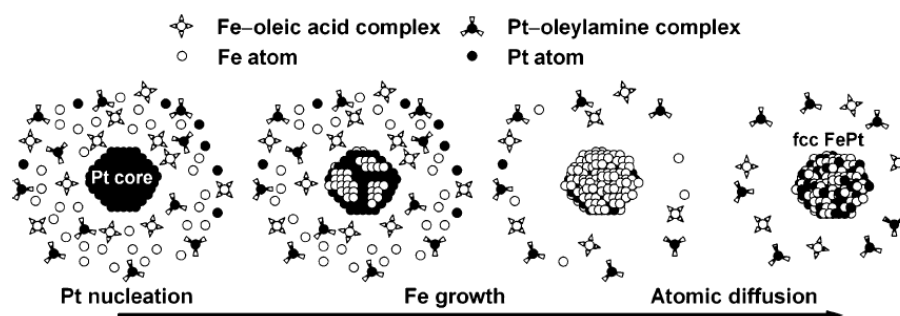


Figure 3.5 Schematic drawing of the nucleation and growth of FePt NPs. (Reproduced with permission from (20), copyright 2005, American Chemical Society.)

The $\text{Fe}(\text{OEt})_3/\text{Pt}(\text{acac})_2$ system received an in-depth consideration and was used to carry out detailed investigations of FePt NPs formation mechanism.^{20, 40, 71} It is to be noted that no 1,2-hexadecanediol was used in this system, and FePt NPs were obtained by heating the mixture of metal precursors, oleic acid, oleylamine and octyl ether to 297 °C for 30 min. Results showed that > 70% NPs are in the range of $40 < x < 60$ ($\text{Fe}_x\text{Pt}_{100-x}$). The narrower composition distribution compared to $\text{Fe}(\text{CO})_5$ is believed to result from a better synchronization between thermal decomposition of $\text{Fe}(\text{OEt})_3$ and the reduction of $\text{Pt}(\text{acac})_2$.²⁰ A detailed mechanism is presented in Figure 3.5:

- i) At an early stage of the heating, part of ethoxide ligands detaches from $\text{Fe}(\text{OEt})_3$ through β -hydride elimination at ~60 - 100 °C. Fe atoms or more

likely Fe-ligands complexes are then generated with the surrounding oleic acid molecules.

- ii) Fe atoms or complexes are believed not to form nuclei, i.e. the core of the NPs but instead to catalyze the reduction of $\text{Pt}(\text{acac})_2$, this come in contrast with Pt nuclei catalyzing the highly stable $\text{Fe}(\text{CO})_5$ precursor used the more standard system. The reduction of $\text{Pt}(\text{acac})_2$ takes place at $\sim 180^\circ\text{C}$. Formed Pt-oleylamine complexes (or Pt atoms) conversely would act as catalyst for the further decomposition of $\text{Fe}(\text{OEt})_3$.
- iii) The allelocatalytic thermal decomposition of $\text{Fe}(\text{OEt})_3$ and reduction of $\text{Pt}(\text{acac})_2$ accelerate at $\sim 250^\circ\text{C}$. When the metal atoms reach a nucleation supersaturation concentration, FePt NPs start to form dominated by Pt nucleation and followed by a slow addition of Fe and Pt atoms to the Pt rich core.
- iv) It is then suggested that heating at 297°C favors the formation of *fcc* FePt NPs through atomic diffusion.

It is noticeable that despite the earlier release of the Fe atoms, the FePt NPs formation mechanism in this system is still dominated by Pt nucleation and growth by a slow addition of Fe and Pt atoms to the Pt rich core. The stabilization of Fe and Pt atoms by the oleic acid and oleylamine, respectively, was confirmed by XPS.²⁰ This would contribute to explain that even though Fe atoms are released earlier than their Pt counterpart, the core of the NPs is still Pt rich. The NPs size could be tuned by adjusting ligand to precursor ratio (Figure 3.5).²⁰ For instance, the increase of $[\text{oleylamine}]/[\text{Pt}(\text{acac})_2]$ decreases the Pt atoms concentration available for nucleation.²⁰ Therefore, this simple parameter induces a decrease in the number density of Pt nuclei therefore leads to larger Pt rich core. In addition, reducing the number density of Pt nuclei also results in a slower catalytic activity on Fe precursor which could also explain the presence of larger Pt core. In contrast increasing $[\text{oleic acid}]/[\text{Fe}(\text{OEt})_3]$ ratio which decreases the concentration of Fe atoms available for the NPs growth results in a smaller NPs size and Pt richer NPs composition. As a final comparison between the $\text{Fe}(\text{CO})_5$ and $\text{Fe}(\text{OEt})_3$ systems, it is noticeable that the NPs nucleation and growth kinetics

differs not only due to 1,2-hexadecanediol acting as reducing agent, but also due to the difference in physical chemistry property (e.g. valence and decomposition temperature) of the Fe precursors. In contrast to the potential for tuning the NPs growth, the ligands oleic acid and oleyamine seem to drive most of the NP growth mechanism as illustrated in Figure 3.4 and Figure 3.5.

The composition is referred as a key-concern for FePt nanoparticles and to gain better control over the individual NP composition, one of the most noticeable step has relied on $\text{Na}_2\text{Fe}(\text{CO})_4$, so called Collman's reagent, to replace more conventional iron precursors.^{19, 72-73} The use of $\text{Na}_2\text{Fe}(\text{CO})_4$ started about 4 years ago and in contrast with most Fe precursors, Collman's reagent provides the Fe^{2-} anion which can act as a reducing agent for $\text{Pt}(\text{acac})_2$, through the simple chemical reaction $\text{Fe}^{2-} + \text{Pt}^{2+} \rightarrow \text{FePt}$. This direct reduction of Pt^{2+} by Fe^{2-} seems to favor the simultaneous presence of Fe and Pt in an equal molar ratio, which is essential to get stoichiometric FePt NPs. It was indeed demonstrated that the composition of 83% of the individual NPs prepared by this route lies in the range of $40 < x < 60$ ($\text{Fe}_x\text{Pt}_{100-x}$).¹⁹ The experimental results showed partially *fcc* FePt can be obtained by using tetracosane as a solvent when synthesis was carried out at 389 °C, as illustrated in Figure 3.6.

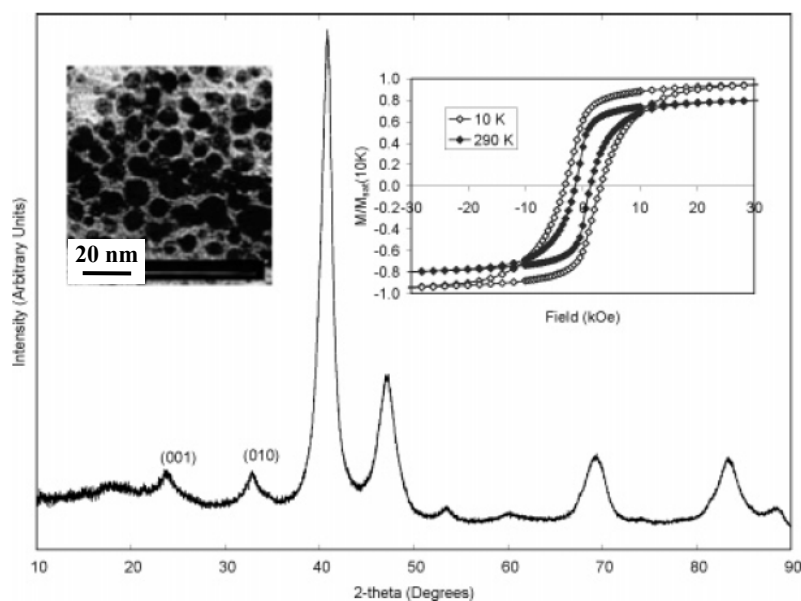


Figure 3.6 XRD pattern and TEM image of as-synthesized *fcc*-FePt nanoparticles in tetracosane at 389 °C, using oleylamine as ligands. Hysteresis loops of directly synthesized *fcc*-FePt NPs at 10 and 290 K. (Reproduced with permission from ⁽⁷²⁾. Copyright 2005 American Chemical Society.)

The NPs are aggregated and not uniform as indicated by TEM, but the *fcc* formation is indicated by the (001) and (010) XRD peaks and the ferromagnetism observed at 290 K by measuring the sample magnetization when sweeping the magnetic field.⁷² Aiming at the direct synthesis of *fcc*-FePt nanoparticles, further investigations were completed by the same research group. By focusing on the use of high boiling point solvents, it was argued that the *fcc* phase could be formed at temperatures as low as 350 °C, even though the authors only provide XRD data and that both magnetic and TEM characterisation critical to assess the overall quality of the material were not provided for these samples.¹⁹ It is also noticeable that *fcc* formation only occurred when oleic acid had been removed from the synthetic media. Using oleic acid was said to lead to only small size NP, i.e. less than 3 nm, which is the size limit for the *fcc* ordering formation.

3.2.1.2. Co-reduction of Fe and Pt Precursors

FePt alloy NPs can also be prepared with the co-reduction of both Fe and Pt precursors by a strong and soluble reducing agent like metal borohydrides in a reaction system similar to the reduction/thermal decomposition route at high temperature described previously.⁷⁴⁻⁷⁶ For example, the co-reduction of preheated FeCl₂ and Pt(acac)₂ mixture in diphenyl ether containing oleic acid, oleylamine together with 1,2-hexadecandiol was completed by the addition of LiBEt₃H at 200 °C, and a refluxing at ~260 °C for 30 min. The advantages are numerous i) the particle growth is self-limited with the size being independent of the amount of ligands, ii) the formation by-products such as Li salts with Cl⁻ and acac⁻ can be removed by using alcohol while BEt₃ can be removed under nitrogen flow. Refluxing at 263 °C from 30 min to 2 h would only improve the morphology of the NPs and resulted in 4 nm FePt NPs (Figure 3.7B) which can self organise on a TEM grid.⁷⁵

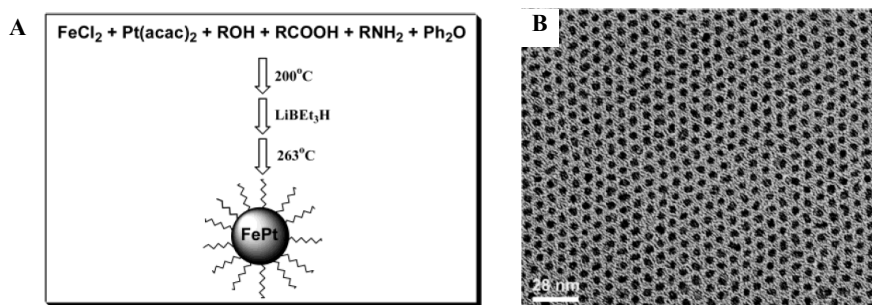


Figure 3.7 Schematic illustration of FePt nanoparticle synthesis by co-reduction of FeCl_2 and $\text{Pt}(\text{acac})_2$ by LiBEt_3H at $\sim 260^\circ\text{C}$, in the presence of oleic acid, oleylamine, and 1,2-hexadecanediol (A). TEM image of a 2-D array of synthesized 4 nm FePt nanoparticles (B). (Reprinted with permission from ⁽⁷⁵⁾. Copyright 2003 American Chemical Society.)

As will be seen later in this thesis, in contrast to either elemental analysis or inductively coupled plasma-optic emission spectrometry, the most convincing argument regarding the NP composition was the use of Rutherford backscattering spectrometry leading to compositions ranging between 59:41 to 61:39 Fe:Pt.⁷⁵

A further study showed that NPs synthesized with this superhydride method could have a narrower composition distribution than observed as a result of standard $\text{Fe}(\text{CO})_5$ thermal-reduction.⁷⁶ The suggested mechanism of FePt NPs formation in this process is again based on Pt rich nuclei formed around 160°C ,⁵⁰ and FePt NPs grow by the incorporation of subsequently reduced Fe atoms into Pt rich nuclei. After the addition of superhydride at 200°C the reduction of the FeCl_2 would be more instantaneous than $\text{Fe}(\text{CO})_5$,⁷⁶ and the formation of Pt nuclei would be more homogenous due to the separate Pt and Fe reduction. Alternatively, LiBEt_3H is a fairly strong reducing agent could level off kinetic differences between the metal precursors and thus allow better synchronization of generation and incorporation of Fe and Pt atoms, an interpretation based on our study on co-reduction of Fe and Pt in aqueous media as presented in Chapter 4.

Not only powerful reducing agent like metal borohydrides, but diol or polyol which are milder organic reducing agent have also been used as both reducing agents and high boiling point solvents to produce FePt NPs.^{9, 32, 77-83} In that context, the thermal decomposition assisted by the 1,2-hexadecanediol reducing

agent discussed above does not qualify for a polyol process as the 1,2-hexadecanediol is not used as a solvent. Nonetheless, diol and polyol, which typical chemical structures are given in Figure 3.8A, are mild reducing agents as illustrated by the fact that the reduction of Fe alone in a polyol process is rather difficult. However, reduced Pt atoms can act as catalysts which in turn accelerates the reduction of Fe ions and leads to the formation of FePt alloy NPs.^{14, 78-79, 68}

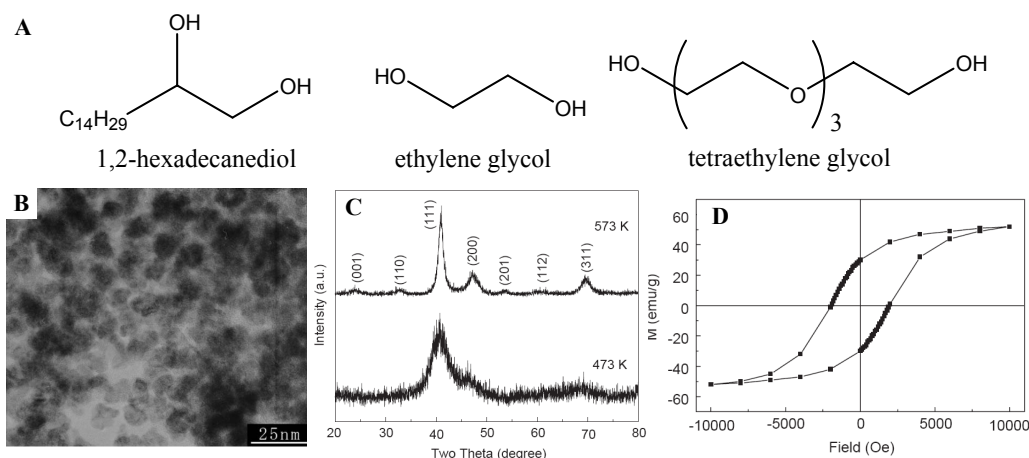


Figure 3.8 Chemical structure of typical reducing solvents used in “polyol” process (A). TEM image of partially ordered *fct* FePt nanoparticles (B). X-ray diffraction patterns of the synthesized at ~ 200 (*fcc*) and 300 °C (*fct*) in tetraethylene glycol (C). Room temperature hysteresis loop for FePt nanoparticles synthesized at 300 °C (D). (Adopted from ⁽⁸⁴⁾). Copyright 2005, with permission from Elsevier.)

It is noticeable that without oleic acid and oleylamine, formation of partial *fct*-FePt NPs with a *fct* ordering parameter (S) of 0.76 was observed by direct heating a solution containing $Fe(acac)_3$ and $Pt(acac)_2$ dispersed in ethylene glycol or tetraethylene glycol (Figure 3.8A) at 300 °C. The partial *fct* order is indicated by the emergence of (001) and (110) peaks on the XRD spectra (Figure 3.8C), and a coercivity of 2.1 kOe at room temperature (Figure 3.8D).⁸⁴ Not surprisingly, the NPs tended to aggregate as a result of not using stabilizers (Figure 3.8B). In addition, the NPs display a multi-domain and polycrystalline morphology which is made of agglomerates consisting 3-5 FePt subgrains of 2-3 nm, a structure which likely results from the absence of stabilizers.¹⁴ The reason behind the *fct* FePt NPs formation was suggested to be the slow reaction kinetics of Fe and Pt salts in the polyol system,¹⁴ even though the mechanism associated with *fct* phase formation

well below usual annealing temperature is not fully explained and understood.^{14, 84} Similar uncertainties and lack of quantifiabes are noticeable regarding how/if the solvent viscosity, radical formation and chemical structure can impact on the nanoparticle growth. It will be clear to the readers that the availability of such information could potentially allow the synthesis of fully *fcc* ordered NPs.

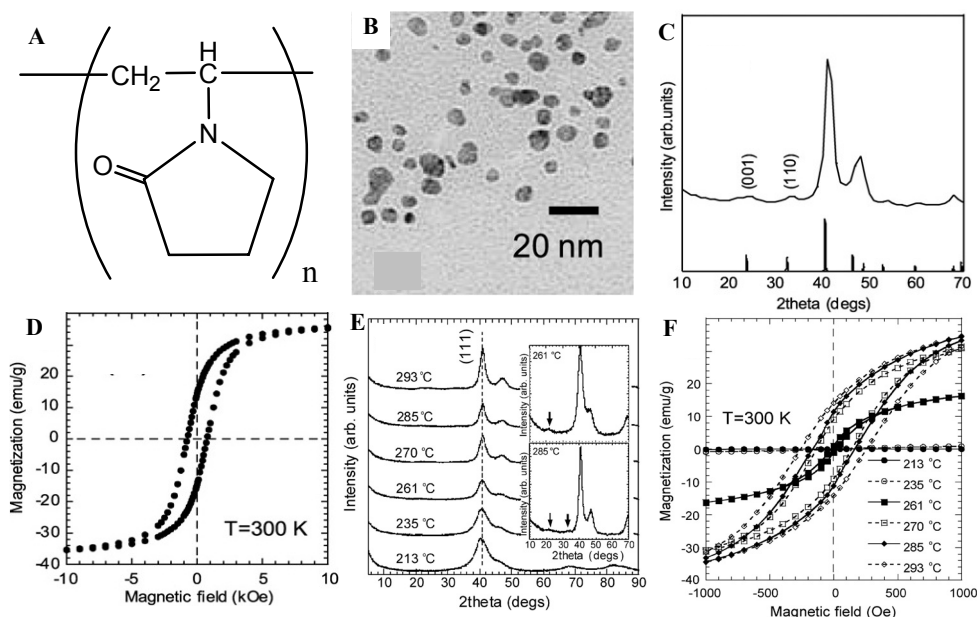


Figure 3.9 Chemical structure of PVP (poly(*N*-vinyl-2-pyrrolidone) (A). TEM image (B), XRD pattern (C) and magnetic hysteresis loop at 300 K (D) of PVP protected FePt NPs synthesized by refluxing at 300 °C for 3 h. XRD patterns of FePt NPs prepared at reaction temperature from 213 to 293 °C (E) and corresponding hysteresis loop at 300 K (F). (Adopted from ⁽⁸⁵⁾. Copyright 2007, with permission from Elsevier.)

Due to the aggregation of NPs synthesized by polyol protocol, PVP (poly(*N*-vinyl-2-pyrrolidone) (Figure 3.9A) was used as a protective agent to improve the dispersibility of nanomaterial.⁸⁵⁻⁸⁸ PVP is widely used for other metals such as silver,⁸⁹⁻⁹⁰ it has a boiling point of ~250 °C, it is thermally stable up to 400 °C as suggested by thermogravimetric analysis.⁸⁵ It is also a weakly coordinating polymer. Taking advantage of this latter property, the synthesis protocol is almost identical to the standard polyol synthesis method mentioned above, except PVP is used as a protective polymer and mixed at ambient temperature with the metal precursors from the beginning of the synthesis. The NPs obtained after 3 hours at 300 °C are ~5 nm in diameter, and seem to be better dispersed on a TEM grid than those obtained with the conventional polyol process

even though the NPs remain polydispersed in size and shape (Figure 3.9B).

As for the conventional polyol process, formation of partially *fcc* FePt with a *fcc* ordering parameter (S) of ~ 0.5 is also observed as indicated by the two weak superlattice peaks of (001) and (110) planes at 24° and 33° respectively (Cu source) (Figure 3.9C). S is smaller and the coercivity is of ~ 750 Oe at 300 K which is about two thirds smaller than what has been reported for the polyol products (Figure 3.9D). The size of NPs could be tuned by adjusting the PVP to precursors molar ratio, the refluxing time and the reaction temperature. A later study showed that partially *fcc* FePt can be obtained at $\sim 260^\circ\text{C}$ (Figure 3.9E) and small coercivity of ~ 20 Oe at room temperature (Figure 3.9F).⁸⁶

In that report the coordination of PVP to precursors ions was suggested to be responsible for the *fcc* direct synthesis. Implicitly this would then coincidentally add up to the previously mentioned hypothesis of slow reaction kinetics of Fe and Pt salts in the polyol system which did not contain any PVP. In contrast with the standard thermal decomposition approach and its thorough step by step aliquots size and composition characterization, very little information is actually available in polyol system to quantify and fully understand the effect of temperature on the nanoparticles growth. A similar statement could be made regarding the kinetics (Fe, Pt, Fe-Pt) in polyol system, how these kinetics would impact on the NPs crystal structure and much they differ from a “standard” thermal decomposition approach. It is also difficult to comment on the specific effect of PVP on *fcc* FePt formation, as very few thorough data have been reported so far and as a consequence, it is difficult to make a comparison between the polyol systems, including PVP and excluding PVP, to assess whether PVP could contribute to trigger the *fcc* FePt formation at temperatures lower than 300°C .

To the best of our knowledge the hypotheses put forwards have not been fully tested but certainly call for more attention in the future. The TEM pictures of polyol FePt NPs certainly do not look as nice as self-assembled *fcc* NPs, however the direct formation of *fcc* phase in the solution phase is exceptional in itself, at

relatively low temperature is a 2nd exception. These evidences certainly set aside the polyol protocols when dealing with FePt solution syntheses and once the direct *fct* growth mechanism(s) will be better understood, there will be plenty of opportunity to address the cosmetic appearance of the NPs.

3.2.2. Low temperature: Co-reduction in Amphiphilic System

Temperature is certainly an essential parameter to produce nanocolloids. As illustrated above, it can be used as a trigger to provide plenty of exciting results. If there is a chance to obtain similar or the same outcomes at room temperature, this is certainly worth the effort which has been developed in water based media.

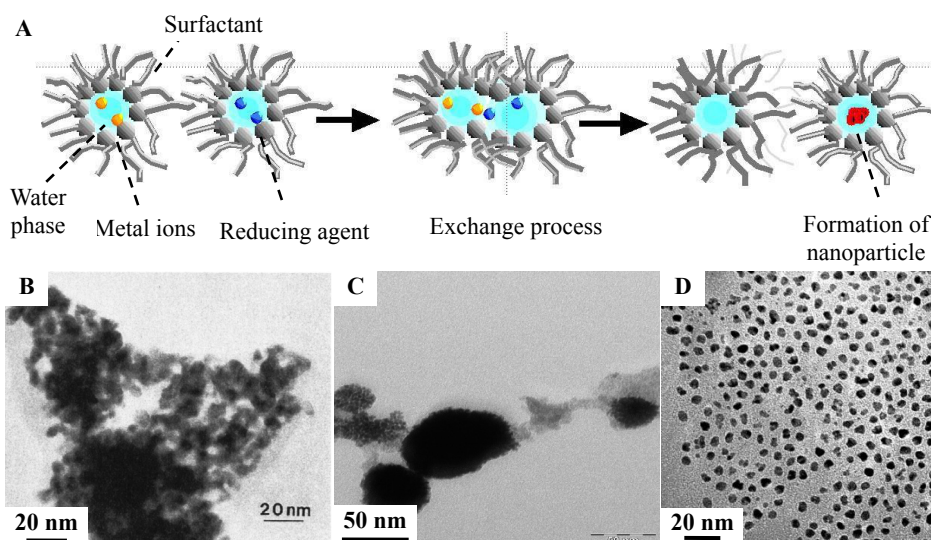


Figure 3.10 Schematic drawing of a metal reduction reaction in an amphiphilic system through water content exchange between water droplets stabilized by surfactants (A). Representative TEM image of $\text{Fe}_x\text{Pt}_{1-x}$ NPs as synthesized by a water/CTAB/butanol/octane system (B),⁹¹ (Reprinted with permission from (91). Copyright2000, American Institute of Physics) a water/triton/cyclohexane system (C),⁹² (Adopted from (92). Copyright 2007, with permission from Elsevier.) and water/Brij52(or Brij56)/butanol/isooctane (D),⁹³ (Copyright 2006, Wiley-VCH Verlag GmbH & Co. KGaA. Reproduced with permission.) respectively.

Briefly, an amphiphilic molecule (surfactant) is composed of two antagonist parts having opposite solvent affinities. For instance a polar part (ion, sugar, methyl oxide, etc) associated with another apolar part (alkyl chain either hydrogenated or fluorinated) force the surfactants to sit at the interface of two antagonist liquids.

Amphiphilic system is often composed of two immiscible phases, i.e. water and oil, stabilized by interfacial film of surfactant molecules.³ These compartments can be taken advantage of to control chemical reactions through the exchange of water content when water droplets collide, coalesce and separate again when subject to Brownian motion (Figure 3.10).⁹⁴

For instance, when a water-in-oil amphiphilic solution containing a dissolved metal salt is mixed with a second solution containing a reducing agent, the metal ions can be reduced to the metallic state and form nanoparticles. Amphiphilic systems have been widely and successfully applied to nanoparticles ranging from metals, such as silver and copper, to semiconductor and magnetic materials, such as cadmium sulfide and Cobalt,⁹⁵⁻¹⁰² providing control over both size and shape of the NPs. In the regards to FePt NP, it is noticeable that there have been only very few reports published so far on the use of amphiphilic system for FePt NP synthesis,^{30, 91-92, 96, 103-107} and very few of these provided insight into compositional variations between individual NPs which has been demonstrated to be a challenging element for FePt NPs synthesis through thermal decomposition methods.

Among these reports, the co-reduction of FeCl_2 and H_2PtCl_6 (the specific salts are not stated in the publication but obtained by contacting the corresponding author) were carried out in a water/CTAB/butanol/octane system leading to FePt NPs of 10 nm in diameter and with a apparent composition determined by EDX following the initial molar ratio of precursors in the system.⁹¹ In addition, $\text{FeCl}_2/\text{H}_2\text{PtCl}_6$ /hydrazine in a water/triton/cyclohexane system led to 3.7 nm (FePt) and 8.4 nm (FePt_3) NPs obtained depending on the initial molar ratio of precursors. TEM associated with both studies show polydispersed and aggregated NPs, while no detailed composition data was presented in the paper.⁹² A potentially more successful study relied on $\text{FeCl}_3/\text{K}_2\text{PtCl}_4$ /anhydrous hydrazine mixed in water/Brij52(or Brij56)/butanol/isooctane solution leading to well dispersed NPs which size between 8 and 20 nm was apparently controlled by adjusting the hydration of the surfactant. While the composition appeared by EDX analysis to follow the initial precursors molar ratio,⁹³ no detailed nanometer scale EDX data

was presented.

In view of its potentials for room temperature FePt NPs synthesis and its flexibility, the water/Brij52/butanol/isooctane system was investigated as part of my PhD study. A detailed investigation on individual NP composition and NP formation mechanism in aqueous media are presented in Chapter 4.¹⁰⁸

3.3. FePt NPs Surface Functionalisation for Biomedical Purposes

Due to their high surface energy, uncoated nanoparticles tend to aggregate in solution.³ It is then necessary to introduce a chemical coating around the NP surface to stabilize the colloid. For medical purpose, an ideal surface coating should satisfy the following basic requirements:

- i) Providing water solubility;
- ii) Preventing NPs from aggregation;
- iii) Maintaining the chemical stability of the NPs, e.g. preventing oxidation, metal etching in physiological environment;
- iv) Providing the biocompatibility of NPs,
- v) Allowing further bio-Functionalisation like drug or targeting ligand attachment.^{3, 109-112}

3.3.1. Molecular Coating

Steric repulsion, electrostatic repulsion or a combination of both can be used to stabilize NPs,^{109, 113} or even extract the NPs from a liquid media.¹¹⁴ After synthesis, FePt NPs are often coated with oleic acid and oleylamine which are not soluble in aqueous solution. (Figure 3.11A) Using hydrophobic interaction is a common strategy to transfer hydrophobic NPs into water soluble colloids (Figure 3.11E).

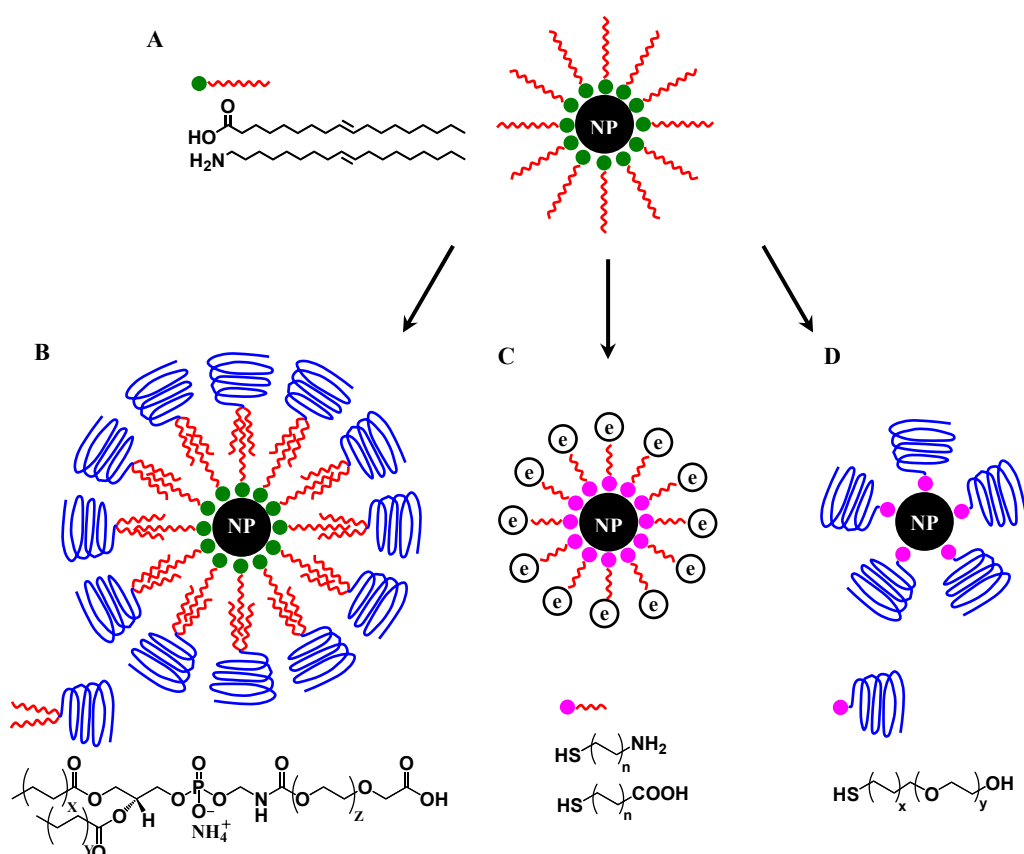


Figure 3.11 Schematic drawing of typical surface Functionalisation strategies on as-synthesized hydrophobic magnetic nanoparticles (A) towards biomedical applications by hydrophobic interactions (A) and ligand exchange protocol (C-D).

Water soluble FePt NPs can be prepared by adding amphiphilic phospholipids (DSPE-PEG(2000)carboxylic acid lipid, 1,2-distearoyl-sn-glycero-3-Phosphor ethanolamine-N-[carboxy(poly-ethylene glycol)-2000].¹¹⁵ The phospholipid forms a bilayer structure with the long hydrocarbon chains of both oleic acid and oleylamine. The poly-ethylene glycol group provides excellent water solubility and stability and $-\text{COOH}$ group at the end of phospholipid allows further chemical conjugation. However, the potential drawback of this approach is that the coating can be sensitive to environmental conditions.¹¹⁶ The collapse of the bilayer might exposure potentially toxic ligands like oleic acid and oleylamine and the metallic core to the biological environment, which in an interesting twist can be used to develop targeted therapy for tumour inhibition.^{115, 117}

Ligand exchange protocol is another popular protocol, which often takes

advantages of the affinity of the ligand binding to the surface of the NPs. For instance, thiol provides stronger bonding to iron and platinum than carboxylic acid and amine.¹¹⁸⁻¹¹⁹ Therefore, original oleic acid and oleylamine coatings can be replaced with ligands or polymers which contain thiol in the chemical structure. In this context, it has been demonstrated that FePt NPs can be coated with carboxylic acid group terminated mercapto ligand like 11-mercaptoundecanoic acid (Figure 3.11B),¹¹⁹ N-[N α ,N α -Bis(carboxymethyl)-L-Lysine]12-Mercaptodecanamide,¹²⁰ or amine terminated mercapto ligand like cysteamine (Figure 3.11C).^{117, 121-122} These ligands not only make the FePt NPs soluble and stable in water solution through electrostatic repulsion but also allow further surface Functionalisation with either covalent or non-covalent conjugation of biological molecules or proteins.^{116, 123-124} Alternatively, FePt NPs can also be coated with polyethylene glycol(PEG)-terminated thiol (Figure 3.11D)¹²⁵ the resulting NPs are appealing for use as long circulating drug carriers or imaging probes which would be able to avoid fast clearance by the Reticuloendothelial System (RES) due to the stealth effect provided by PEG coating, as described in Chapter 2.

3.3.2. Thin Film Coating

Stability is a crucial requirement for magnetic nanoparticles, especially as pure metals, including Fe, Co, and Ni are sensitive to oxidation. Although metal alloy NPs show higher stability against air exposure than pure metal NPs, surface oxidation of the NPs can still happen and can result in loss of magnetic moment.¹²⁶⁻¹²⁷ Therefore, it is of high interest to develop efficient strategies to improve the chemical stability of magnetic NP interfaces. The introduction of a protection layer which is chemically inert and impenetrable thus averting the contact of NPs surface with oxygen seems to be the most straightforward method. Various inorganic materials such as noble metals, graphite, silica, metal oxide have been exploited to serve this purpose, and some of them could also introduce special features like optical properties to create multifunctional NPs.^{3, 110, 116, 128}

3.3.2.1. Carbon Coating

The interest of using carbon material to protect magnetic NPs is justified by its higher chemical and thermal stability as compared to organic ligand coatings.^{3, 129} The thermal stability of the carbon shell is then of special benefit to prepare *fcc*-FePt NPs, which often requires high temperature annealing normally above 550 °C. *alit* was reported the preparation of FePt-carbon coated NPs obtained through the annealing of polymer encapsulated FePt NPs.¹³⁰ The polymer poly(vinyl butral-covinyl alcohol-co-acetate) PVB as the carbon source supply was injected into the iron-platinum/ligands reaction system at about 220 °C, then heated up to ~300 °C for 3 h to obtain polymer encapsulated FePt NPs (Figure 3.12A1).

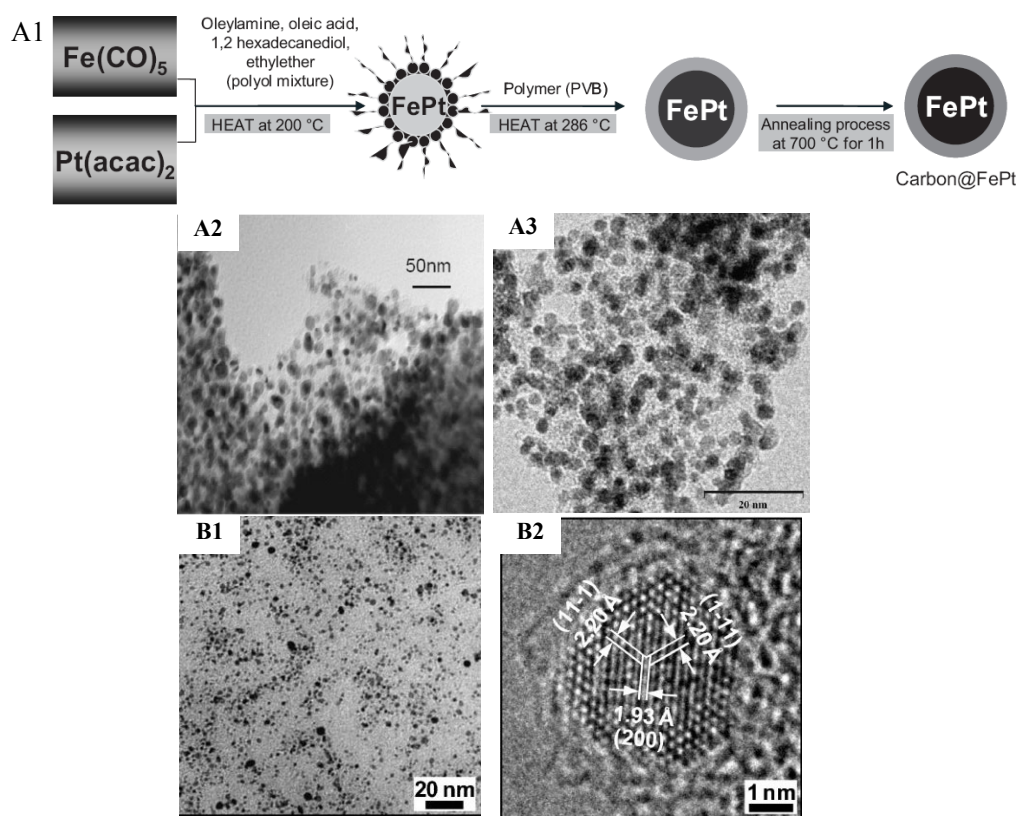


Figure 3.12 Synthetic procedure for the preparation of FePt-carbon NPs from polymer PVB (poly(vinyl butral-co-vinyl alcohol-co-acetate) encapsulated FePt NPs (A1), and corresponding TEM image (A2) FePt-carbon NPs prepared with different synthesis method involving glucose at 900 °C (A3).¹³⁰ (Copyright 2007, Wiley-VCH Verlag GmbH & Co. KGaA. Reproduced with permission.) Low resolution TEM image of FePt-carbon NPs prepared through methane chemical-vapor deposition method (B1), and high resolution TEM image show FePt core surrounded by an amorphous carbon shell (B2).¹³¹ (Copyright 2008, Wiley-VCH Verlag GmbH & Co. KGaA. Reproduced with permission.)

These NPs were further annealed at 700 °C for another 2 h leading to both carbon shell formation by the decomposition of polymer and an *fcc* to *fcc* phase conversion. However, a severe NPs sintering occurred during the preparation procedure as indicated in Figure 3.12A2. Another synthetic method involves hydrothermal treatment of Fe and Pt precursors in glucose followed by calcination at 900 °C which could lead to better dispersed FePt NPs (Figure 3.12A3).¹³⁰ Alternatively, rather than a solution based synthesis pathway, carbon coated FePt can be obtained by heating a silica powder loaded with iron and platinum salts to 800 °C under H₂, and then subject to methane chemical-vapor deposition for carbon film formation. 2-3 nm *fcc*-FePt NPs were obtained as presented in Figure 3.12B1 and B2.¹³¹

In summary, even though very promising at first sight, one of the main obstacles for FePt-carbon NPs preparation is the often observed aggregation of the NPs. A low degree of understanding and control of the carbon shell formation mechanism might be to blame and consequently the preparation of individual and dispersible NPs with a controllable carbon-coated shell thickness remain a challenge.³ Noticeably, a simple carbon shell also provides only two elements (iii and iv) of the checklist we established at the beginning of the section, which reduces its attractiveness.

3.3.2.2. Noble Metal Coating

Over the past 10 years, noble metals like platinum,¹³² silver,¹³³ and gold,¹³³⁻¹³⁹ have also been investigated to form a protective layer around magnetic NPs. Owing to their low chemical reactivity but facile surface Functionalisation, and together with their special physical-chemistry properties, such coatings indeed appear as versatile protective shells to build more complex structure onto. For example, a layer of Au coating can provide efficient protection for a magnetic NP core against oxidation; in addition, gold shell can provide magnetic NPs with appealing optical properties due to the surface plasmon resonance (SPR) effect. The popular approaches for gold coating on magnetic NPs include reactions in

microemulsion,¹⁴⁰⁻¹⁴¹ redox transmetalation,¹⁴²⁻¹⁴³ iterative hydroxylamine seeding pathways.¹⁴⁴ While a lot of efforts has been dedicated to iron oxide NPs,^{133-134, 145-147} there are only a few reports on gold coating of FePt NPs.^{136-138, 148} The preparation of FePt-Au NPs is normally carried out by mixing pre-synthesized FePt NPs with a gold precursor like gold acetate at temperature as high as 265 °C through thermal decomposition,¹³⁸ or by reduction at a relatively low temperature of about 150 °C (Figure 3.13A), when the FePt NPs are solubilised in a diol solvent such as hexadecanediol.¹³⁸

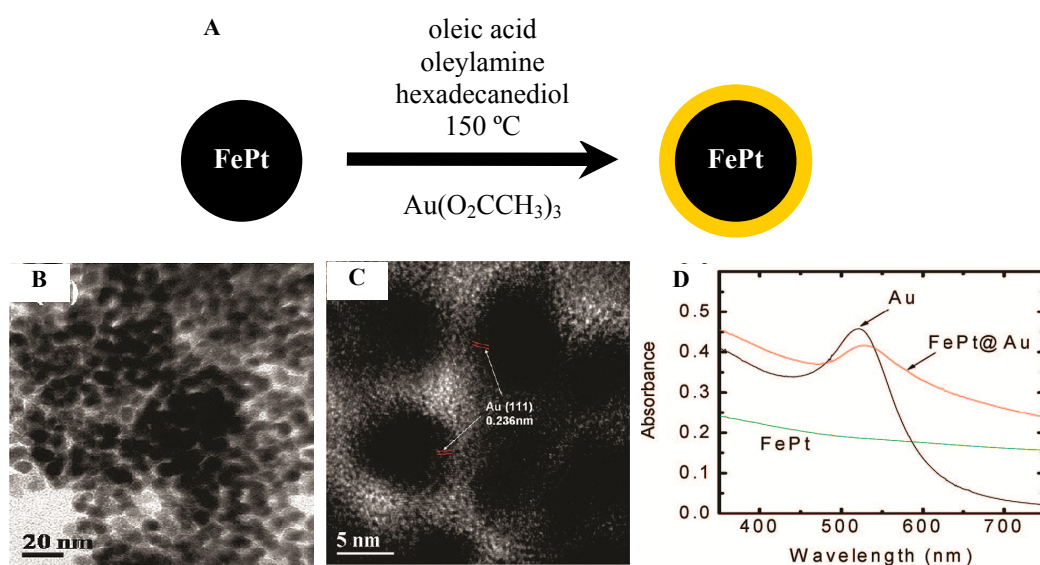


Figure 3.13 Schematic drawing of the preparation of FePt-Au core-shell NPs (A), corresponding low (B) and high (C) magnification TEM images of FePt-Au NPs, and UV-vis absorption spectra of FePt, Au and FePt-Au NPs (D). (Adopted with permission from (¹³⁸). Copyright 2009 American Chemical Society.)

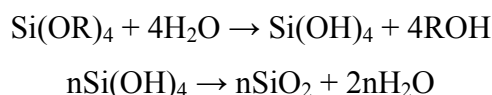
The Au coating was confirmed by TEM images (Figure 3.13B-C), and FePt-Au NPs indeed shows a red-shift of UV-vis absorption as compared to pure FePt and Au NPs (Figure 3.13D).

3.3.2.3. Silica Coating

Silica coating is perhaps one of the most promising and important approaches to form a protective but biocompatible layer around magnetic NPs. While its high

thermal stability can also prevent NPs aggregation during any annealing post treatment, this attractiveness is certainly due to the high chemical inertness of silica as well as the negatively charged surface of the silica, which already have ticked 4 elements of our check-list (i, iii, iv and v). Furthermore, the existence of silanol group on the silica surface also allows further versatile surface Functionalisation with a variety of functional groups through the rich chemistry of siloxane-based monolayers.^{2, 149} Of further interest to guaranty the integrity of the NPs properties, a silica shell can also prevent the direct contact of the magnetic core with additional agents linked to the silica surface thus avoiding unwanted interactions.

Sol–gel and reverse microemulsion are the two most commonly used approaches to complete silica coating around a very wide range of NPs.¹⁵⁰⁻¹⁵⁴ In the sol-gel pathway, the silica coating process is carried out in alcohol based solvents, like ethanol or 2-propanol mixed with water solution. A base, like ammonia solution, is often added to catalyze the hydrolysis reaction of the silane precursor.¹⁴⁹ The silica is then formed in situ through the hydrolysis and condensation of a sol-gel precursor, like triethoxysilane (TEOS). The reaction equations are briefly presented below:¹⁵⁵



Under basic conditions, water dissociates to produce nucleophilic hydroxyl anions (-OH) which attacks the silicon atom and replace the alkoxide groups (OR) resulting in the formation of Si(OH)₄. The released alkoxide groups (OR) undergo hydrolysis reaction with H⁺ to form ROH and the condensation of Si(OH)₄ leads to the formation of silica shells which appear to be monodisperse after fine tuning of the experimental conditions.¹⁵⁵

For this process, making FePt NPs water soluble and enhancing the affinity of FePt NPs surface towards silica are two crucial elements to obtained well isolated single FePt core silica shell NPs. Typical strategies include Functionalisation of the FePt NPs with a primer which has a silane group like aminopropoxysilane,¹⁵⁶ or by

adding another layer of amphiphilic molecules such as $\text{CH}_3(\text{CH}_2)_{15}\text{SO}_3\text{H}$, $\text{CH}_3(\text{CH}_2)_{15}(\text{CH}_2\text{CH}_2)_8\text{OH}$ or $\text{CH}_3(\text{CH}_2)_{15}\text{N}^+(\text{CH}_3)_3\text{Br}$ through hydrophobic interactions, see Section 3.3.1.¹⁵⁷⁻¹⁵⁹

Reverse micelles (see Section 3.2.2) have also been used to confine and control the coating of silica on magnetic NPs.^{38, 160} One of the advantages of the microemulsion protocol over the sol-gel approach is that hydrophobic FePt NPs can be directly coated without requiring the preparation of water soluble NPs as an intermediate step. Indeed, as-synthesized hydrophobic FePt NPs with oleic acid and oleylamine coating can be dispersed directly into a water-in-oil microemulsion together with a silane precursor, and the silica shell formation can start after adding a base to trigger the hydrolysis reaction of the silane precursor.³⁸ A mechanism to form a silica coating on hydrophobic NPs in reverse microemulsion using QDs as model was developed.¹⁶⁰ In that study, evidence indicated replacement of hydrophobic amine ligand coating on QDs by hydrolyzed TEOS molecules and surfactant, therefore transfer of the QDs into the hydrophilic interior of the micelles, and also enhance the affinity of NPs surface to silica. This mechanism could be applied to other hydrophobic nanoparticles such as iron oxide, gold, or FePt nanocrystals and is investigated in Chapter 6.

3.4. Conclusion

This chapter has presented an overview of the magnetic properties of FePt NPs and their syntheses and Functionalisation. The high Curie temperature, saturation magnetic moment and magneto-crystalline anisotropy make FePt attractive magnetic materials compared to conventional iron, cobalt, nickel, their oxides and some of their alloys. Various chemical pathways have been developed for FePt NPs synthesis, which can be divided into two main classes. the first one normally requires the reaction to be completed at high temperature of the order of $\sim 300^\circ\text{C}$ if not above (the thermal decomposition pathway) while the 2nd is carried out at temperature close to room temperature (the amphiphilic pathway).

The NP composition is always a key element to be careful about when considering alloy NPs synthesis including FePt. The desired composition for FePt should contain 35 – 60% Fe to allow a crystalline structure optimization. So far there is no detailed individual composition analysis reported for FePt NPs obtained by co-reduction at low temperature. Therefore a systematic NPs composition investigation and NPs formation mechanism study is presented in Chapter 4.

For FePt NPs synthesized at high temperature, it has been demonstrated that the NPs often have a broad individual NP composition distribution. This is mainly attributed to the low boiling point of the commonly used $\text{Fe}(\text{CO})_5$ iron precursor and to the temperature difference between reduction of $\text{Pt}(\text{acac})_2$ and the decomposition of $\text{Fe}(\text{CO})_5$. Thus a lot of effort has been dedicated to explore alternative iron precursors including $\text{Fe}(\text{acac})_3$, $\text{Fe}(\text{OEt})_3$ and $\text{Na}_2\text{Fe}(\text{CO})_4$. Stoichiometry close to a 1:1 ratio of FePt NPs was obtained by using this Fe^{2-} precursor ($\text{Na}_2\text{Fe}(\text{CO})_4$) and this method was further developed as part of this PhD study, and the results are presented in Chapter 5.

Direct synthesis of *fct* FePt NPs has also attracted some attention. It is noticeable that traditional chemistry methods often produce *fcc* FePt NPs. To obtain *fct* FePt, a post-treatment, such as annealing at $> 550\text{ }^\circ\text{C}$, is normally required. However, this process often leads to significant NPs sintering. It has been reported that partially *fct* FePt could be obtained by using $\text{Na}_2\text{Fe}(\text{CO})_4$ when the reaction was carried out at $389\text{ }^\circ\text{C}$; alternatively, the polyol process can also lead to partially ordered *fct* FePt NPs at a relatively lower temperature $\sim 300\text{ }^\circ\text{C}$. However, in both case there is very little understanding of the associated mechanisms. Over the course of this PhD study, a lot of effort has been dedicated to the investigation of new opportunities based on the use of ionic liquids for the direct *fct* FePt synthesis as presented in Chapter 5.

As-synthesized FePt NPs are often coated with hydrophobic molecules, and to form water soluble FePt NPs suitable for biomedical applications, ligand exchange, and hydrophobic interaction are the most common approaches

providing the NPs with a protective shell against oxidation, and chemical degradation. These coatings are also ideal platforms for allowing further NPs Functionalisation and production of multifunctional NPs for biomedical applications. In this PhD study, cysteamine coated FePt NPs through ligand exchange, and silica shell coated NPs were both prepared and the results are presented in Chapter 6.

References

- (1) This search was carried out through ISI web of Science by searching a set of keywords as follows: iron platinum, “(TS=FePt or TS=(iron platinum) or TS=(iron-platinum)) and TS=nano* or TS=colloid*) and PY=1995-2005”; iron oxide, “(TS=(iron oxide) and TS=nano* or TS=colloid*) and PY=1995-2005”, search completed on Nov. 2010.
- (2) Jeong, U.; Teng, X. W.; Wang, Y.; Yang, H.; Xia, Y. N. *Adv. Mater.* **2007**, 19, 33-60.
- (3) Lu, A. H.; Salabas, E. L.; Schuth, F. *Angew. Chem. Int. Edit.* **2007**, 46, 1222-1244.
- (4) Kittel, C., *Introduction to solid state physics*. ed.; 2007.
- (5) Gutfleisch, O.; Lyubina, J.; Muller, K. H.; Schultz, L. *Adv. Eng. Mater.* **2005**, 7, 208-212.
- (6) Weller, D.; Moser, A. *Ieee. T. Magn.* **1999**, 35, 4423-4439.
- (7) Bedanta, S.; Kleemann, W. *J. Phys. D. Appl. Phys.* **2009**, 42, 013001.
- (8) Lyubina, J. V. Nanocrystalline Fe-Pt alloys: phase transformations, structure and magnetism. Dresden, Techn. Univ., 2006.
- (9) Sun, S. H. *Adv. Mater.* **2006**, 18, 393-403.
- (10) Wang, J. P. *P. Ieee.* **2008**, 96, 1847-1863.
- (11) Goya, G. F. *Solid. State. Commun.* **2004**, 130, 783-787.
- (12) Matsui, I. *J. Nanopart. Res.* **2006**, 8, 429-443.
- (13) Yu, A. C. C.; Mizuno, M.; Sasaki, Y.; Kondo, H. *Appl Phys Lett.* **2004**, 85, 6242-6244.
- (14) Takahashi, M.; Ogawa, T.; Hasegawa, D.; Jeyadevan, B. *J Appl Phys.* **2005**, 97, 10J307.
- (15) Kim, J. M.; Rong, C. B.; Liu, J. P.; Sun, S. H. *Adv. Mater.* **2009**, 21, 906-909.
- (16) Sun, S. H.; Murray, C. B.; Weller, D.; Folks, L.; Moser, A. *Science.* **2000**, 287, 1989-1992.
- (17) Rong, C. B.; Li, D. R.; Nandwana, V.; Poudyal, N.; Ding, Y.; Wang, Z. L.; Zeng, H.; Liu, J. P. *Adv. Mater.* **2006**, 18, 2984-2988.
- (18) Dai, Z. R.; Sun, S. H.; Wang, Z. L. *Nano. Lett.* **2001**, 1, 443-447.
- (19) Nguyen, H. L.; Howard, L. E. M.; Stinton, G. W.; Giblin, S. R.; Tanner, B. K.; Terry, I.; Hughes, A. K.; Ross, I. M.; Serres, A.; Evans, J. S. O. *Chem. Mater.* **2006**, 18, 6414-6424.
- (20) Saita, S.; Maenosono, S. *Chem Mater.* **2005**, 17, 6624-6634.
- (21) Li, D. R.; Poudyal, N.; Nandwana, V.; Jin, Z. Q.; Elkins, K.; Liu, J. P. *J. Appl. Phys.* **2006**, 99, 08E911.
- (22) Liu, J. P. *Jom-Us.* **2010**, 62, 56-61.
- (23) Jia, Z.; Seetala, N.; Misra, R. D. K. *Physica. B.* **2010**, 405, 2189-2193.
- (24) Rong, C. B.; Poudyal, N.; Chaubey, G. S.; Nandwana, V.; Skomski, R.; Wu, Y. Q.; Kramer, M. J.; Liu, J. P. *J. Appl. Phys.* **2007**, 102, 043913.
- (25) Kang, S.; Harrell, J. W.; Nikles, D. E. *Nano. Lett.* **2002**, 2, 1033-1036.
- (26) Harrell, J. W.; Nikles, D. E.; Kang, S. S.; Sun, X. C.; Jia, Z.; Shi, S.; Lawson, J.; Thompson, G. B.; Srivastava, C.; Seetala, N. V. *Scripta. Mater.* **2005**, 53, 411-416.
- (27) Kang, S. S.; Nikles, D. E.; Harrell, J. W. *J. Appl. Phys.* **2003**, 93,

- 7178-7180.
- (28) Jia, Z. Y.; Kang, S. S.; Nikles, D. E.; Harrell, J. W. *Ieee. T. Magn.* **2005**, 41, 3385-3387.
- (29) Huang, T. W.; Tu, T. H.; Huang, Y. H.; Lee, C. H.; Lin, C. M. *Ieee. T. Magn.* **2005**, 41, 941-943.
- (30) Nakanishi, M.; Furusawa, G. I.; Waki, K.; Hattori, Y.; Kamino, T.; Sasaki, K.; Kuroda, K.; Saka, H. *Mater. Trans.* **2007**, 48, 2572-2579.
- (31) Kim, J.; Rong, C. B.; Lee, Y.; Liu, J. P.; Sun, S. H. *Chem. Mater.* **2008**, 20, 7242-7245.
- (32) Kang, S.; Shi, S.; Nikles, E.; Harrell, J. W. *J. Appl. Phys.* **2008**, 103, 07D503.
- (33) Gupta, G.; Patel, M. N.; Ferrer, D.; Heitsch, A. T.; Korgel, B. A.; Jose-Yacamán, M.; Johnston, K. P. *Chem. Mater.* **2008**, 20, 5005-5015.
- (34) Wilhelm, F.; Rogalev, A.; Pouloupoulos, P.; Angelakerist, M.; Tsiaoussis, J.; Simeonidis, K.; Mourdikoudis, S.; Kalogirou, O. *Mod. Phys. Lett. B.* **2007**, 21, 1189-1196.
- (35) Kang, S. S.; Shi, S.; Miao, G. X.; Jia, Z. Y.; Nikles, D. E.; Harrell, J. W. *J. Nanosci. Nanotechno.* **2007**, 7, 350-355.
- (36) Wang, H. L.; Huang, Y.; Zhang, Y.; Hadjipanayis, G. C.; Weller, D.; Simopoulos, A. *J. Magn. Magn. Mater.* **2007**, 310, 22-27.
- (37) Varanda, L. C.; Jafelicci, M. *J. Am. Chem. Soc.* **2006**, 128, 11062-11066.
- (38) Lee, D. C.; Mikulec, F. V.; Pelaez, J. M.; Koo, B.; Korgel, B. A. *J. Phys. Chem. B.* **2006**, 110, 11160-11166.
- (39) Zafiropoulou, I.; Tzitzios, V.; Petridis, D.; Devlin, E.; Fidler, J.; Hoefinger, S.; Niarchos, D. *Nanotechnology.* **2005**, 16, 1603-1607.
- (40) Saita, S.; Maenosono, S. *Chem. Mater.* **2005**, 17, 3705-3710.
- (41) Nandwana, V.; Elkins, K. E.; Liu, J. P. *Nanotechnology.* **2005**, 16, 2823-2826.
- (42) Liu, C.; Wu, X. W.; Klemmer, T.; Shukla, N.; Weller, D. *Chem. Mater.* **2005**, 17, 620-625.
- (43) Nakaya, M.; Tsuchiya, Y.; Ito, K.; Oumi, Y.; Sano, T.; Teranishi, T. *Chem. Lett.* **2004**, 33, 130-131.
- (44) Vedantam, T. S.; Liu, J. P.; Zeng, H.; Sun, S. *J. Appl. Phys.* **2003**, 93, 7184-7186.
- (45) Jeyadevan, B.; Hobo, A.; Urakawa, K.; Chinnasamy, C. N.; Shinoda, K.; Tohji, K. *J. Appl. Phys.* **2003**, 93, 7574-7576.
- (46) Sun, S.; Murray, C. B.; Weller, D.; Folks, L.; Moser, A. *Science.* **2000**, 287, 1989-1992.
- (47) Vazquez, M.; Luna, C.; Morales, M. P.; Sanz, R.; Serna, C. J.; Mijangos, C. *Physica B.* **2004**, 354, 71-79.
- (48) Gu, H.; Ho, P. L.; Tsang, K. W. T.; Wang, L.; Xu, B. *J. Am. Chem. Soc.* **2003**, 125, 15702-15703.
- (49) Gao, J.; Liang, G.; Zhang, B.; Kuang, Y.; Zhang, X.; Xu, B. *J. Am. Chem. Soc.* **2007**, 129, 1428-1433.
- (50) Bagaria, H. G.; Johnson, D. T.; Srivastava, C.; Thompson, G. B.; Shamsuzzoha, M.; Nikles, D. E. *J. Appl. Phys.* **2007**, 101, 104313.
- (51) Hyeon, T.; Lee, S. S.; Park, J.; Chung, Y.; Na, H. B. *J. Am. Chem. Soc.* **2001**, 123, 12798-12801.

- (52) Srivastava, C.; Nikles, D. E.; Thompson, G. B. *J. Appl. Phys.* **2008**, 104, 064315.
- (53) Bagaria, H. G.; Johnson, D. T.; Srivastava, C.; Thompson, G. B.; Shamsuzzoha, M.; Nikles, D. E. *J Appl Phys.* **2007**, 101, 104310.
- (54) Puzder, A.; Williamson, A. J.; Zaitseva, N.; Galli, G.; Manna, L.; Alivisatos, A. P. *Nano Lett.* **2004**, 4, 2361-2365.
- (55) Manna, L.; Wang, L. W.; Cingolani, R.; Alivisatos, A. P. *J. Phys. Chem. B.* **2005**, 109, 6183-6192.
- (56) Yu, M.; Fernando, G. W.; Li, R.; Papadimitrakopoulos, F.; Shi, N.; Ramprasad, R. *Appl. Phys. Lett.* **2006**, 88, 231910.
- (57) Srivastava, C.; Nikles, D. E.; Thompson, G. B. *J. Appl. Phys.* **2008**, 104, 104314.
- (58) Chen, M.; Liu, J. P.; Sun, S. *J. Am. Chem. Soc.* **2004**, 126, 8394-8395.
- (59) Nandwana, V.; Elkins, K. E.; Poudyal, N.; Chaubey, G. S.; Yano, K.; Liu, J. P. *J Phys Chem C.* **2007**, 111, 4185-4189.
- (60) Shevchenko, E. V.; Talapin, D. V.; Schnablegger, H.; Kornowski, A.; Festin, O.; Svedlindh, P.; Haase, M.; Weller, H. *J. Am. Chem. Soc.* **2003**, 125, 9090-9101.
- (61) Chen, M.; Kim, J.; Liu, J. P.; Fan, H. Y.; Sun, S. H. *J. Am. Chem. Soc.* **2006**, 128, 7132-7133.
- (62) Shukla, N.; Liu, C.; Roy, A. G. *Mater. Lett.* **2006**, 60, 995-998.
- (63) Shukla, N.; Nigra, M. M. *Surf Sci.* **2007**, 601, 2615-2617.
- (64) Chou, S. W.; Zhu, C. L.; Neeleshwar, S.; Chen, C. L.; Chen, Y. Y.; Chen, C. C. *Chem. Mater.* **2009**, 21, 4955-4961.
- (65) Poudyal, N.; Chaubey, G. S.; Rong, C. B.; Liu, J. P. *J. Appl. Phys.* **2009**, 105, 07A749.
- (66) Shukla, N.; Nigra, M. M.; Nuhfer, T.; Bartel, M. A.; Gellman, A. J. *Nanotechnology.* **2009**, 20, 065602.
- (67) Wang, C.; Hou, Y. L.; Kim, J. M.; Sun, S. H. *Angew. Chem. Int. Edit.* **2007**, 46, 6333-6335.
- (68) Nakaya, M.; Kanehara, M.; Teranishi, T. *Langmuir.* **2006**, 22, 3485-3487.
- (69) Elkins, K. E.; Vedantam, T. S.; Liu, J. P.; Zeng, H.; Sun, S. H.; Ding, Y.; Wang, Z. L. *Nano. Lett.* **2003**, 3, 1647-1649.
- (70) Elkins, K. E.; Chaubey, G. S.; Nandwana, V.; Liu, J. P. *J. Nano. Res.* **2008**, 1, 23-29.
- (71) Saita, S.; Maenosono, S. *Phys. Status. Solidi. A.* **2006**, 203, 1206-1210.
- (72) Howard, L. E. M.; Nguyen, H. L.; Giblin, S. R.; Tanner, B. K.; Terry, I.; Hughes, A. K.; Evans, J. S. O. *J. Am. Chem. Soc.* **2005**, 127, 10140-10141.
- (73) Delalande, M.; Marcoux, P. R.; Reiss, P.; Samson, Y. *J Mater Chem.* **2007**, 17, 1579-1588.
- (74) Gao, X.; Tam, K.; Yu, K. M.; Tsang, S. C. *Small.* **2005**, 1, 949-952.
- (75) Sun, S. H.; Anders, S.; Thomson, T.; Baglin, J. E. E.; Toney, M. F.; Hamann, H. F.; Murray, C. B.; Terris, B. D. *J. Phys. Chem. B.* **2003**, 107, 5419-5425.
- (76) Srivastava, C.; Balasubramanian, J.; Turner, C. H.; Wiest, J. M.; Bagaria, H. G.; Thompson, G. B. *J. Appl. Phys.* **2007**, 102, 104310.
- (77) Hinotsu, T.; Jeyadevan, B.; Chinnasamy, C. N.; Shinoda, K.; Tohji, K. *J.*

- Appl. Phys.* **2004**, 95, 7477-7479.
- (78) Harpeness, R.; Gedanken, A. *J. Mater. Chem.* **2005**, 15, 698-702.
- (79) Jeyadevan, B.; Shinoda, K.; Justin, R. J.; Matsumoto, T.; Sato, K.; Takahashi, H.; Sato, Y.; Tohji, K. *Ieee. T. Magn.* **2006**, 42, 3030-3035.
- (80) Shinoda, K.; Sato, K.; Jeyadevan, B.; Tohji, K.; Suzuki, S. *J. Magn. Mater.* **2007**, 310, 2387-2389.
- (81) Joseyphus, R. J.; Shinoda, K.; Sato, Y.; Tohji, K.; Jeyadevan, B. *J. Mater. Sci.* **2008**, 43, 2402-2406.
- (82) Wen, M.; Qi, H. Q.; Zhao, W. G.; Chen, J.; Li, L. J.; Wu, Q. S. *Colloid. Surface. A.* **2008**, 312, 73-78.
- (83) Minami, R.; Kitamoto, Y.; Chikata, T.; Kato, S. *Electrochim. Acta.* **2005**, 51, 864-866.
- (84) Sato, K.; Jeyadevan, B.; Tohji, K. *J. Magn. Mater.* **2005**, 289, 1-4.
- (85) Iwamoto, T.; Matsumoto, K.; Kitamoto, Y.; Toshima, N. *J. Colloid. Interf. Sci.* **2007**, 308, 564-567.
- (86) Iwamoto, T.; Matsumoto, K.; Matsushita, T.; Inokuchi, M.; Toshima, N. *J. Colloid. Interface. Sci.* **2009**, 336, 879-888.
- (87) Kitamoto, Y.; He, J. S. *Electrochim. Acta.* **2009**, 54, 5969-5972.
- (88) Iwamoto, T.; Kitamoto, Y.; Toshima, N. *Physica. B.* **2009**, 404, 2080-2085.
- (89) Sun, Y.; Xia, Y. *Adv. Mat.* **2002**, 14, 833.
- (90) Skrabalak, S. E.; Au, L.; Li, X. D.; Xia, Y. *Nat. Protoc.* **2007**, 2, 2182-2190.
- (91) Carpenter, E. E.; Sims, J. A.; Wienmann, J. A.; Zhou, W. L.; O'Connor, C. J. *J. Appl. Phys.* **2000**, 87, 5615-5617.
- (92) Hyie, K. M.; Yaacob, I. D. *J. Mater. Process. Tech.* **2007**, 191, 48-50.
- (93) Yan, Q. Y.; Purkayastha, A.; Kim, T.; Kroger, R.; Bose, A.; Ramanath, G. *Adv. Mater.* **2006**, 18, 2569-2573.
- (94) Cushing, B. L.; Kolesnichenko, V. L.; O'Connor, C. J. *Chem. Rev.* **2004**, 104, 3893-3946.
- (95) Eastoe, J.; Cox, A. R. *Colloid. Surface. A.* **1995**, 101, 63-76.
- (96) Filankembo, A.; Giorgio, S.; Lisiecki, I.; Pileni, M. P. *J. Phys. Chem. B.* **2003**, 107, 7492-7500.
- (97) Filankembo, A.; Pileni, M. P. *Appl. Surf. Sci.* **2000**, 164, 260-267.
- (98) Maillard, M.; Giorgio, S.; Pileni, M. P. *J. Phys. Chem. B.* **2003**, 107, 2466-2470.
- (99) Pinna, N.; Weiss, K.; Sack-Kongehl, H.; Vogel, W.; Urban, J.; Pileni, M. P. *Langmuir.* **2001**, 17, 7982-7987.
- (100) Tanori, J.; Pileni, M. P. *Langmuir.* **1997**, 13, 639-646.
- (101) Park, J.; Joo, J.; Kwon, S. G.; Jang, Y.; Hyeon, T. *Angew. Chem. Int. Edit.* **2007**, 46, 4630-4660.
- (102) André, P.; Charra, F.; Chollet, P. A.; Pileni, M. P. *Adv. Mater.* **2002**, 14, 601-603.
- (103) Bai, L. T.; Wan, H. Y.; Street, S. C. *Colloid. Surface. A.* **2009**, 349, 23-28.
- (104) Gao, Y.; Zhang, X. W.; Yin, Z. G.; Qu, S.; You, J. B.; Chen, N. F. *Nanoscale. Res. Lett.* **2010**, 5, 1-6.
- (105) Reiss, B. D.; Mao, C. B.; Solis, D. J.; Ryan, K. S.; Thomson, T.; Belcher, A. M. *Nano. Lett.* **2004**, 4, 1127-1132.

- (106) Qu, S.; Zhang, X. W.; Gao, Y.; You, J. B.; Fan, Y. M.; Yin, Z. G.; Chen, N. F. *Nanotechnology*. **2008**, 19, 135704.
- (107) Chen, S.; Maclaren, D.; Baker, R.; Chapman, J.; Cole-Hamilton, D. J.; Lee, S.; André, P. *J. Mat. Chem.* **2011**, 21, 3646-3654.
- (108) Chen, S.; Maclaren, D.; Baker, R.; Chapman, J.; Cole-Hamilton, D. J.; Lee, S.; André, P. *J. Mat. Chem.* **2010**, 21, 3646-3654.
- (109) Petros, R. A.; DeSimone, J. M. *Nat. Rev. Drug. Discov.* **2010**, 9, 615-627.
- (110) Latham, A. H.; Williams, M. E. *Accounts Chem Res.* **2008**, 41, 411-420.
- (111) Berry, C. C.; Curtis, A. S. G. *J. Phys. D-Appl. Phys.* **2003**, 36, R198-R206.
- (112) Berry, C. C. *J. Phys. D. Appl. Phys.* **2009**, 42, 224003.
- (113) Hao, R.; Xing, R. J.; Xu, Z. C.; Hou, Y. L.; Gao, S.; Sun, S. H. *Adv. Mater.* **2010**, 22, 2729-2742.
- (114) Wang, C. L.; Fang, M.; Han, J. S.; Zhang, H.; Cui, Y. P.; Yang, B. *J. Phys. Chem. C*. **2009**, 113, 19445-19451.
- (115) Xu, C. J.; Yuan, Z. L.; Kohler, N.; Kim, J. M.; Chung, M. A.; Sun, S. H. *J. Am. Chem. Soc.* **2009**, 131, 15346-15351.
- (116) Veisheh, O.; Gunn, J. W.; Zhang, M. Q. *Adv. Drug. Deliver. Rev.* **2010**, 62, 284-304.
- (117) Chen, S.; Wang, L.; Duce, S. L.; Brown, S.; Lee, S.; Melzer, A.; Cuschieri, S. A.; Andre, P. *J. Am. Chem. Soc.* **2010**, 132, 15022-15029.
- (118) Gehl, B.; Aleksandrovic, V.; Erbacher, M.; Juergens, B.; Schurenberg, M.; Kornowski, A.; Weller, H.; Baumer, M. *Chemphyschem.* **2008**, 9, 821-825.
- (119) Bagaria, H. G.; Ada, E. T.; Shamsuzzoha, M.; Nikles, D. E.; Johnson, D. T. *Langmuir*. **2006**, 22, 7732-7737.
- (120) Xu, C.; Xu, K.; Gu, H.; Zhong, X.; Guo, Z.; Zheng, R.; Zhang, X.; Xu, B. *J. Am. Chem. Soc.* **2004**, 126, 3392-3393.
- (121) Tanaka, Y.; Maenosono, S. *J. Magn. Magn. Mater.* **2008**, 320, L121-L124.
- (122) Chou, S. W.; Shau, Y. H.; Wu, P. C.; Yang, Y. S.; Shieh, D. B.; Chen, C. C. *J. Am. Chem. Soc.* **2010**, 132, 13270-13278.
- (123) Josephson, L.; Tung, C. H.; Moore, A.; Weissleder, R. *Bioconjugate Chem.* **1999**, 10, 186-191.
- (124) Thanh, N. T. K.; Green, L. A. W. *Nano. Today*. **2010**, 5, 213-230.
- (125) Hong, R.; Fischer, N. O.; Emrick, T.; Rotello, V. M. *Chem Mater.* **2005**, 17, 4617-4621.
- (126) de la Presa, P.; Rueda, T.; Hernando, A.; Ramallo-Lopez, J. M.; Giovanetti, L. J.; Requejo, F. G. *J. Appl. Phys.* **2008**, 103, 103909.
- (127) Liu, C.; Klemmer, T. J.; Shukla, N.; Wu, X. W.; Weller, D.; Tanase, M.; Laughlin, D. J. *J. Magn. Magn. Mater.* **2003**, 266, 96-101.
- (128) Gao, J. H.; Gu, H. W.; Xu, B. *Accounts. Chem. Res.* **2009**, 42, 1097-1107.
- (129) Seo, W. S.; Lee, J. H.; Sun, X. M.; Suzuki, Y.; Mann, D.; Liu, Z.; Terashima, M.; Yang, P. C.; McConnell, M. V.; Nishimura, D. G.; Dai, H. J. *Nat. Mater.* **2006**, 5, 971-976.
- (130) Caiulo, N.; Yu, C. H.; Yu, K. M. K.; Lo, C. C. H.; Oduro, W.; Thiebaud, B.; Bishop, P.; Tsang, S. C. *Adv. Funct. Mater.* **2007**, 17, 1392-1396.
- (131) Seo, W. S.; Kim, S. M.; Kim, Y. M.; Sun, X.; Dai, H. J. *Small*. **2008**, 4,

- 1968-1971.
- (132) Park, J. I.; Cheon, J. *J. Am. Chem. Soc.* **2001**, 123, 5743-5746.
- (133) Xu, Z.; Hou, Y.; Sun, S. *J. Am. Chem. Soc.* **2007**, 129, 8698-8699.
- (134) Wang, L. Y.; Luo, J.; Fan, Q.; Suzuki, M.; Suzuki, I. S.; Engelhard, M. H.; Lin, Y. H.; Kim, N.; Wang, J. Q.; Zhong, C. J. *J. Phys. Chem. B.* **2005**, 109, 21593-21601.
- (135) Jin, Y.; Jia, C.; Huang, S.; O'Donnell, M.; Gao, X. *Nat. Comm.* **2010**, DOI: 10.1038, Published online 27 Jul 2010.
- (136) de la Presa, P.; Multigner, M.; Morales, M. P.; Rueda, T.; Fernandez-Pinel, E.; Hernando, A. *J. Magn. Magn. Mater.* **2007**, 316, E753-E755.
- (137) de la Presa, P.; Rueda, T.; Morales, M. P.; Hernando, A. *Ieee. Trans. Magn.* **2008**, 44, 2816-2819.
- (138) Yano, K.; Nandwana, V.; Chaubey, G. S.; Poudyal, N.; Kang, S.; Arami, H.; Griffis, J.; Liu, J. P. *J. Phys. Chem. C.* **2009**, 113, 13088-13091.
- (139) Goon, I. Y.; Lai, L. M. H.; Lim, M.; Munroe, P.; Gooding, J. J.; Amal, R. *Chem. Mater.* **2009**, 21, 673-681.
- (140) Rivas, J.; Sanchez, R. D.; Fondado, A.; Izco, C.; Garcabastida, A. J.; Garciaotero, J.; Mira, J.; Baldomir, D.; Gonzalez, A.; Lado, I.; Quintela, M. A. L.; Oseroff, S. B. *J. Appl. Phys.* **1994**, 76, 6564-6566.
- (141) Carpenter, E. E.; Sangregorio, C.; O'Connor, C. J. *Ieee. T. Magn.* **1999**, 35, 3496-3498.
- (142) Park, J. I.; Cheon, J. *J. Am. Chem. Soc.* **2001**, 123, 5743-5746.
- (143) Ban, Z.; Barnakov, Y. A.; Li, F.; Golub, V. O.; O'Connor, C. J. *J. Mater. Chem.* **2005**, 15, 4660-4662.
- (144) Lyon, J. L.; Fleming, D. A.; Stone, M. B.; Schiffer, P.; Williams, M. E. *Nano. Lett.* **2004**, 4, 719-723.
- (145) Weinstein, J. S.; Varallyay, C. G.; Dosa, E.; Gahramanov, S.; Hamilton, B.; Rooney, W. D.; Muldoon, L. L.; Neuwelt, E. A. *J. Cerebr. Blood. F. Met.* **2010**, 30, 15-35.
- (146) Liang, C. H.; Wang, C. C.; Lin, Y. C.; Chen, C. H.; Wong, C. H.; Wu, C. Y. *Anal. Chem.* **2009**, 81, 7750-7756.
- (147) Lim, J. K.; Majetich, S. A.; Tilton, R. D. *Langmuir.* **2009**, 25, 13384-13393.
- (148) Pazos-Perez, N.; Rodriguez-Gonzalez, B.; Hilgendorff, M.; Giersig, M.; Liz-Marzan, L. M. *J. Mater. Chem.* **2010**, 20, 61-64.
- (149) Lu, Y.; Yin, Y. D.; Mayers, B. T.; Xia, Y. N. *Nano. Lett.* **2002**, 2, 183-186.
- (150) Hunyadi, S. E.; Murphy, C. J. *J. Phys. Chem. B.* **2006**, 110, 7226-7231.
- (151) Salgueirino-Maceira, V.; Correa-Duarte, M. A.; Hucht, A.; Farle, M. *J. Magn. Magn. Mater.* **2006**, 303, 163-166.
- (152) Santra, S.; Tapecc, R.; Theodoropoulou, N.; Dobson, J.; Hebard, A.; Tan, W. H. *Langmuir.* **2001**, 17, 2900-2906.
- (153) Nann, T.; Mulvaney, P. *Angew. Chem. Int. Edit.* **2004**, 43, 5393-5396.
- (154) Yi, D. K.; Selvan, S. T.; Lee, S. S.; Papaefthymiou, G. C.; Kundaliya, D.; Ying, J. Y. *J. Am. Chem. Soc.* **2005**, 127, 4990-4991.
- (155) Darbandi, M.; Lu, W. G.; Fang, J. Y.; Nann, T. *Langmuir.* **2006**, 22, 4371-4375.
- (156) Aslam, M.; Fu, L.; Li, S.; Dravid, V. P. *J. Colloid. Interf. Sci.* **2005**, 290, 444-449.

- (157) Fan, H.; Yang, K.; Boye, D. M.; Sigmon, T.; Malloy, K. J.; Xu, H.; Lopez, G. P.; Brinker, C. J. *Science*. **2004**, 304, 567-571.
- (158) Tamada, Y.; Yamamoto, S.; Takano, M.; Nasu, S.; Ono, T. *Appl. Phys. Lett.* **2007**, 90, 162509.
- (159) Zhelev, Z.; Ohba, H.; Bakalova, R. *J. Am. Chem. Soc.* **2006**, 128, 6324-6325.
- (160) Koole, R.; van Schooneveld, M. M.; Hilhorst, J.; Donega, C. D.; 't Hart, D. C.; van Blaaderen, A.; Vanmaekelbergh, D.; Meijerink, A. *Chem. Mater.* 2008, 20, 2503-2512.

Chapter 4

FePt Magnetic Nanoparticles Synthesized at Low Temperature in Aqueous Media

4.1. Introduction

The possibility of synthesising nanoparticles (NPs) in aqueous media is attractive because of the low synthesis temperature. It often relies on surfactant molecules to control the NPs growth and to stabilize a water phase used to dissolve both the precursor salts and a reducing agent. NPs can then form through the exchange between water phases, with a rate that is controlled by Brownian motion and the lability of the surfactant interface.¹⁻² Even though aqueous media pathway has been successfully used to synthesize numerous types of NPs with metal to semiconductor NPs,³⁻¹⁴ for iron platinum (FePt) NPs, low-temperature syntheses have attracted less interest. Indeed, as presented in Chapter 3, only a few publications have reported on FePt NPs formation in amphiphilic systems,¹⁵⁻²² and very few have focused specifically on the chemical composition of the NPs at a nanometer scale.

In this chapter, a detailed investigation of low temperature solution syntheses focusing on the stoichiometry and the composition of FePt NPs is presented. A quaternary system based on water, isooctane, and Brij52 as *non-ionic* surfactant and butanol as a co-surfactant was used to synthesis FePt NPs.²³ By combining Inductively Coupled Plasma Optical Emission Spectrometry (ICP-OES), Wide-angle powder X-ray diffraction (XRD), Transmission Electron Microscopy (TEM), Scanning Transmission Electron Microscope, Energy Dispersive X-ray analysis (STEM-EDX) and magnetometer (SQUID), a precise composition analysis of individual NPs was carried out and revealed an inhomogeneous distribution of Fe and Pt between particles. This work was aimed to understand the limiting parameters on NP composition and identify suitable strategies to increase the iron content of NPs. A number of systems including reaction time, precursor ions and reducing agents were investigated to gain insight into the mechanisms associated with the insertion of iron atoms in the $\text{Fe}_x\text{Pt}_{1-x}$ NPs. It was concluded that a degree of control is possible but that there remain substantial limitations. Limiting parameters including iron salts hydrolysis and a mismatch in the co-reduction kinetic of the two salts. These results indicate that to overcome these problems and obtain higher stoichiometry in FePt NPs by co-reduction at low temperature, future investigations should focus on preventing the formation of hydrolytically unstable iron complexes, preferably by working in the absence of water.²³

4.2. Experimental Results

4.2.1. Amphiphilic System Characterization

A non-ionic surfactant, Brij52, was chosen to reduce the influence of the variation of the precursor ion content over the course of the synthesis of interest. Its

hydrophobic block is a 16 carbon long alkyl chain and its hydrophilic head includes 2 ethylene oxide and is terminated by a hydroxyl group (Figure 4.1A).

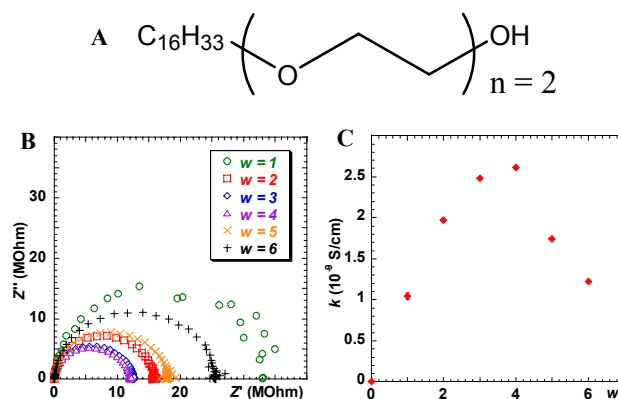


Figure 4.1 Chemical structure of Brij52 non-ionic surfactant (A). Real impedance Z' (V) vs. imaginary impedance Z'' (V) curve of water / isooctane / Brij52 / butanol amphiphilic system measured at 30°C, [Brij52] = 0.3 mol/L, [Brij52] / [butanol] = 5, hydration $w = 1$ (○), 2 (□), 3 (◇), 4 (△), 5 (×) and 6 (+) (B). Conductivity variation as a function of water content, w (C).

The phase behavior of the precursor free water / isooctane / Brij52 / butanol amphiphilic system was characterized by impedance spectroscopy. As shown in Figure 4.1B, the impedance spectra, $Z'' = f(Z')$, are dominated by semi-circular features for all the hydration values, $w = [\text{H}_2\text{O}] / [\text{surfactant}] = 1$ to 6, defined at the ratio of water molecule per surfactant. The diameter of the semi-circles is related to the conductivity of the system and the spectra were fitted to extract the resistance values associated with these semi-circular features. Conductivity values were calculated and follow a non-monotonic behavior with the hydration, w , of the system (Figure 4.1C). The conductivity indeed first increases with w , reaches a maximum at $w = 4$, and then decreases at higher hydration. Up to $w = 4$, conductivity value reflects an increased salt content associated with the hydration, the variation of the rigidity of surfactant interface, and consequently the variation of the exchange rate of the water phases in the amphiphilic system. Above $w = 4$, the system becomes unstable and progressively phase separates into an upper phase rich in oil and a lower phase rich in water. The solution was kept under stirring over the 3 h duration of the syntheses which were then completed at $w =$

4, corresponding to the maximum of the conductivity values to optimize the exchange rate (Figure 4.1C).

4.2.2. $\text{N}_2\text{H}_4\cdot\text{H}_2\text{O}$ as Reducing Agent

In a typical synthesis, a surfactant solution was prepared by mixing isooctane, Brij52 and butanol in a surfactant to alcohol ratio of 5:1. Dissolution was obtained after 15 min sonication. Platinum and iron respective aqueous stock solutions were added to the amphiphilic system to obtain the desired $[\text{Pt}^{2+}]$ and $[\text{Fe}^{3+}]$ concentrations. 30 min sonication was then applied, followed by injection of the reducing agent to reach the targeted molar ratio of [reducing agent] to $[\text{Fe}+\text{Pt}]$.

The final water to surfactant molar ratio, w , was reached after addition of the hydrated reducing agent solution. The system was stirred at 30 °C for 3 h. Dodecane thiol was then injected and the solution aged for a further 15 min. The NPs were then precipitated by adding alcohol and next collected by centrifugation. This extraction step was repeated several times. A similar protocol was followed when the syntheses were completed with different iron and platinum precursors, and different reducing agents. A detailed example of NPs preparation protocol is given in the appendix.

To tune the composition of the NPs, syntheses were completed with variation of the initial precursor molar ratio incrementing the concentration of FeCl_3 whilst keeping the concentration of K_2PtCl_4 constant. The particles were then synthesized with precursor salt ratios, $[\text{Fe}]:[\text{Pt}]$, ranging from 0.2 to 1.8. To quantify the average composition of the NPs, the product of each synthesis was dissolved in aqua regia solution and the ratio of Fe to Pt elements in the final solution was determined by Inductively Coupled Plasma Optical Emission Spectrometry (ICP-OES, Figure 4.2A). All the results are reproducible and very consistent from one sample to another.

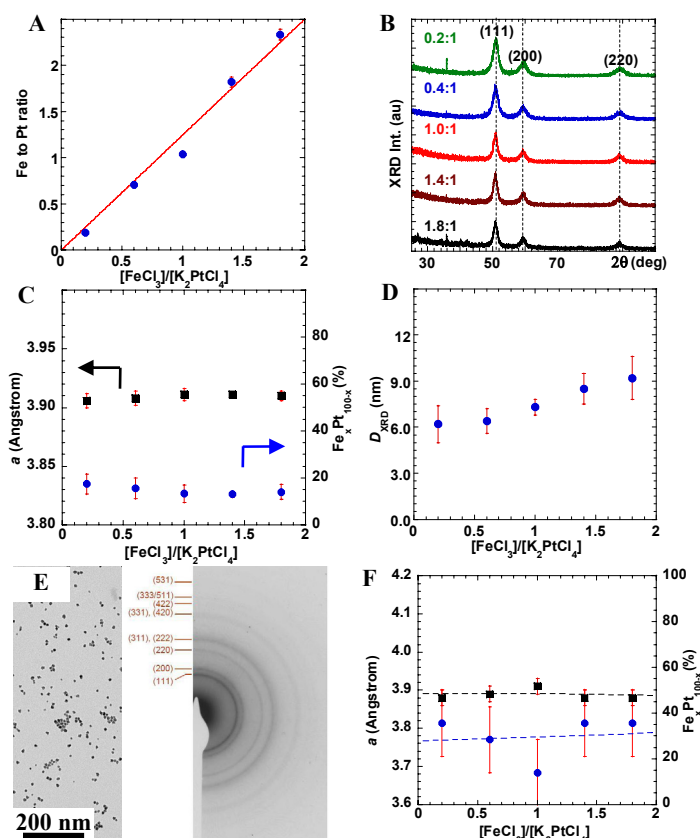


Figure 4.2 FePt NPs synthesized with varied FeCl_3 concentration, $[\text{N}_2\text{H}_4\cdot\text{H}_2\text{O}] / [\text{Fe}^{3+} + \text{Pt}^{2+}] = 40$. Composition analysis by ICP-OES (A) XRD patterns (B), Lattice constant (■), chemical composition (●) (C) and crystalline grain size in diameter (D_{XRD}) as a function of Fe to Pt precursor molar ratio (D) deduced from XRD. A typical selected area electron diffraction pattern of FePt NPs (E), and the lattice constant (■) and chemical composition (●) as a function of Fe to Pt precursors molar ratio deduced from electron diffraction analysis (F).

The final NP stoichiometry appears to correlate with the initial ratio of precursor salts, as illustrated by the linear variation of the ICP-OES composition as a function of the initial precursor molar ratio in the synthetic media which reveals an apparent ability to control the global composition of FePt NPs (Figure 4.2A). Wide-angle powder X-ray diffraction (XRD) spectra are characteristic of FePt NPs with a face centre cubic (*fcc*) crystalline structure (Figure 4.2B). The strong peaks lying around 51° , 60° and 89° arise from the (111), (200) and (220) diffraction. It is, however, noticeable from Figure 4.2B that the position of the XRD peaks and the implied lattice constant remains independent of the relative

iron and platinum precursor concentrations. This is in contradiction to the ICP-OES results (Figure 4.2A) since the composition change suggested by ICP-OES should manifest as a shift of peaks towards higher 2θ values and a simultaneous reduction of the lattice constant with increased Fe content (Figure 4.2C).²⁴ In contrast to the known lattice-constant of $\text{Fe}_{50}\text{Pt}_{50}$ (~ 3.834 Å), the values for all the samples appear to be close to 3.910 Å. When compared with the lattice constant of Pt metal (~ 3.930 Å); this suggests a fixed Fe composition of about 15% across the entire set of samples (Figure 4.2C). Electron diffraction data yielded similar information. The electron diffraction pattern (Figure 4.2E) indicates *fcc*-FePt phase. In addition, regardless of the initial Fe to Pt precursor ratio, all the FePt NPs samples have a lattice constant varying between 3.88 and 3.92 Å, as deduced from electron diffraction patterns (Figure 4.2F). The corresponding chemical compositions would vary from 15 to 35% with a large error bar of about 15%. In the present experiments, the uncertainty associated with the determination of the lattice constant obtained from TEM-ED (Figure 4.2F) is much larger than XRD (Figure 4.2C). In the context of NPs size, Figure 4.2D illustrates the increase of the crystalline size with the Fe to Pt precursor ratio. Table 4.1 summarizes all these results.

Table 4.1 X-ray diffraction data of FePt NPs synthesized with $[\text{N}_2\text{H}_4\cdot\text{H}_2\text{O}] / [\text{Fe}^{3+} + \text{Pt}^{2+}] = 40$. a is the lattice constant deduced from the (111), (200) and (220) peak positions, x is the iron content in $\text{Fe}_x\text{Pt}_{1-x}$, the diameter D_{XRD} is the crystalline grain size calculated based on FWHM of 3 different XRD peaks.²⁵

Fe/Pt salt ratio	a (Å)	x (%)	D_{XRD} (nm)
0.2	3.906 ± 0.006	17.4 ± 4.3	6.2 ± 1.2
0.6	3.908 ± 0.006	15.6 ± 4.4	6.4 ± 0.8
1.0	3.911 ± 0.005	13.2 ± 3.6	7.3 ± 0.5
1.4	3.911 ± 0.002	13.0 ± 1.2	8.5 ± 1.0
1.8	3.910 ± 0.004	14.0 ± 3.1	9.2 ± 1.4

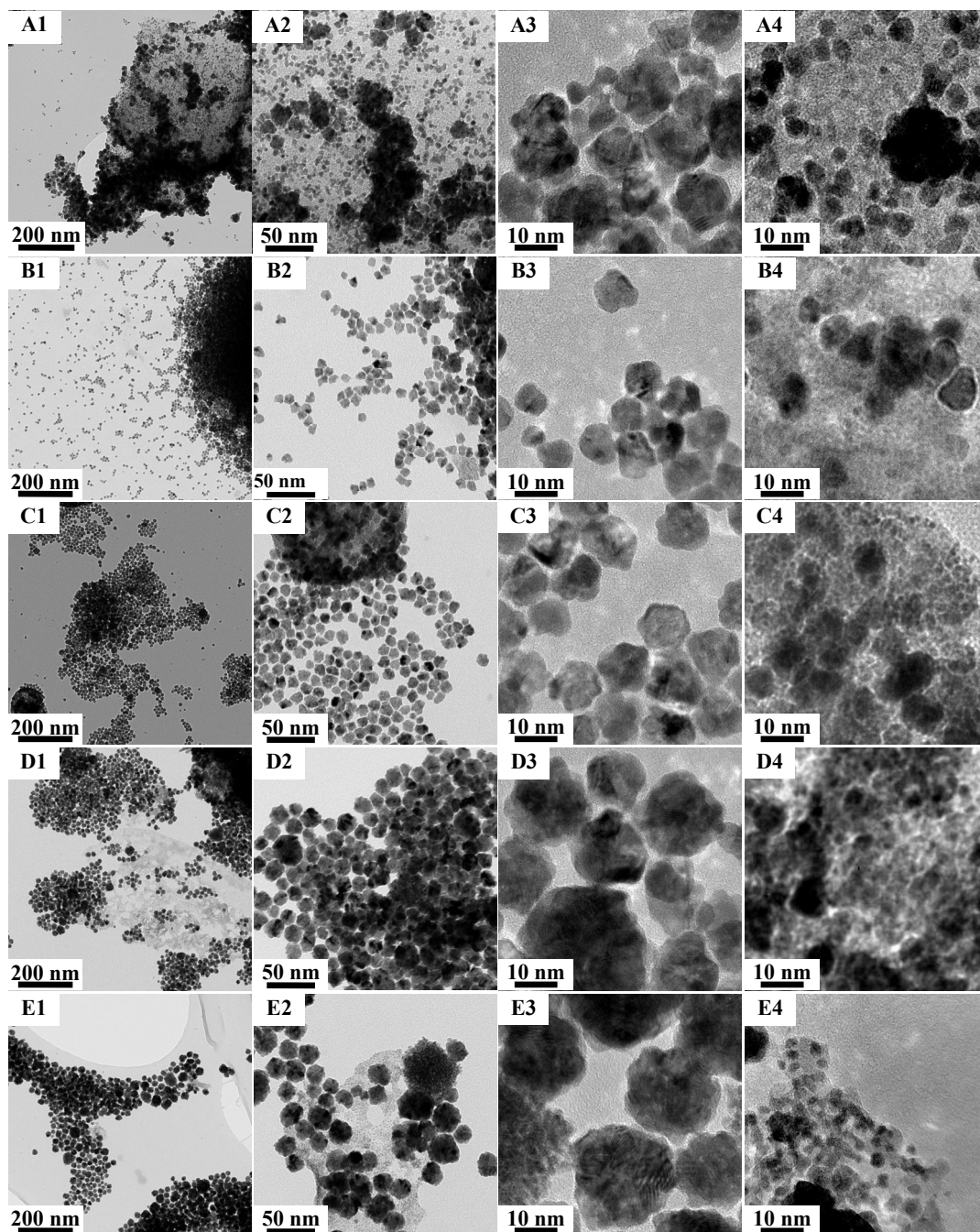


Figure 4.3 TEM images of FePt NPs synthesized with $[\text{N}_2\text{H}_4 \cdot \text{H}_2\text{O}] / [\text{Fe}^{3+} + \text{Pt}^{2+}] = 40$, $[\text{K}_2\text{PtCl}_4]$ is controlled as a constant equal to 2.5 mmol/L, and $[\text{FeCl}_3]$ to $[\text{K}_2\text{PtCl}_4]$ molar ratio is varied from 0.2 (A), 0.6 (B), 1.0 (C), 1.4 (D) to 1.8 (E).

The apparent contradiction between ICP-OES and XRD data sets can be resolved by TEM analysis (Figure 4.3) which reveals that the reaction products are inhomogeneous and comprise well defined, Pt-rich NPs together with larger fragments of Fe-rich materials. In Figure 4.3, the first two columns on the left-hand side show large length scale NPs landscape, while the two columns on the right-hand side display higher magnification TEM images. The FeCl_3 to K_2PtCl_4 molar ratio is tuned from 0.2 (Figure 4.3A), 0.6 (Figure 4.3B), 1.0 (Figure 4.3C) and 1.4 (Figure 4.3D) to 1.8 (Figure 4.3E).

Figure 4.3A presents TEM characterization of FePt synthesized with an initial $[\text{FeCl}_3]$ to $[\text{K}_2\text{PtCl}_4]$ ratio of 0.2. Individual NPs are associated with a film-like material (Figure 4.3A1), while two distinct populations of NPs appears in Figure 4.3B. Small size NPs are smaller than 10 nm in diameter which is close to the XRD size of 6.2 nm in diameter. NPs larger than 10 nm appear to be NPs aggregated and fused together (Figure 4.3A2). Figure 4.3A3 and A4 show higher magnification TEM of the NPs and the film material, respectively. All the samples presented in Figure 4.3 agree well with such description and the common features in all samples can be summarized as follow:

- i) The NPs of darker contrast are fairly well dispersed and are mixed with a film-like material of weaker contrast, which could also be amorphous. The darker regions in bright field TEM arise from the average atomic number (Z) dependent scattering and the darker the material, typically the denser or heavier it is. The NPs are polydisperse in size and shape, with a similar structure and morphology regardless of the Fe to Pt precursor ratio (1st and 2nd columns).

- ii) The NPs have knobby like morphology and appear to be polydomain, probably resulting from the coalescence of smaller NPs during synthesis (3rd column).
- iii) The particles increase in TEM size with increasing initial $[\text{FeCl}_3]$ concentration while the size distributions broaden (Figure 4.4). This trend is consistent with the XRD data presented in Table 4.1 (3rd column).
- iv) High magnification TEM images illustrate the formation of the film-like material of lower electronic contrast (4th column).

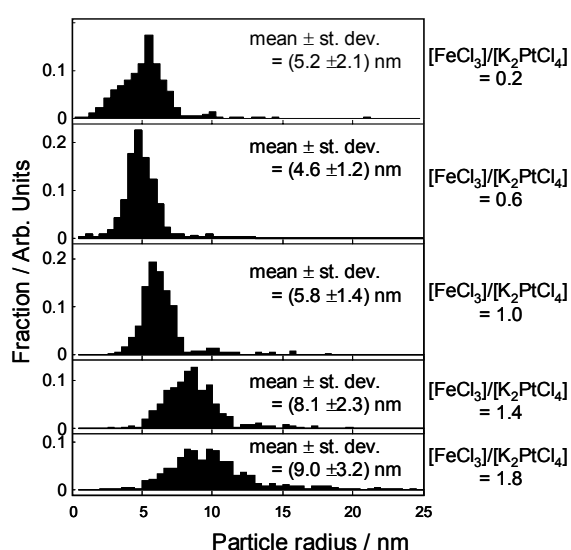


Figure 4.4 TEM size distribution in radius of FePt NPs synthesized with $[\text{N}_2\text{H}_4\cdot\text{H}_2\text{O}] / [\text{Fe}^{3+} + \text{Pt}^{2+}] = 40$, $[\text{K}_2\text{PtCl}_4] = 2.5$ mmol/L and $[\text{FeCl}_3]$ to $[\text{K}_2\text{PtCl}_4]$ molar ratio is varied from 0.2 to 1.8.

Elemental analysis by False-coloured Energy Filtered TEM (EF-TEM) image and nanometer scale Scanning Transmission Electron Microscopy and Energy Dispersive X-ray analysis (nanoSTEM-EDX) were completed to complement both ICP-OES and XRD data, by providing the composition of the $\text{Fe}_x\text{Pt}_{1-x}$ NPs at a nanometer scale, as presented in Figure 4.5.

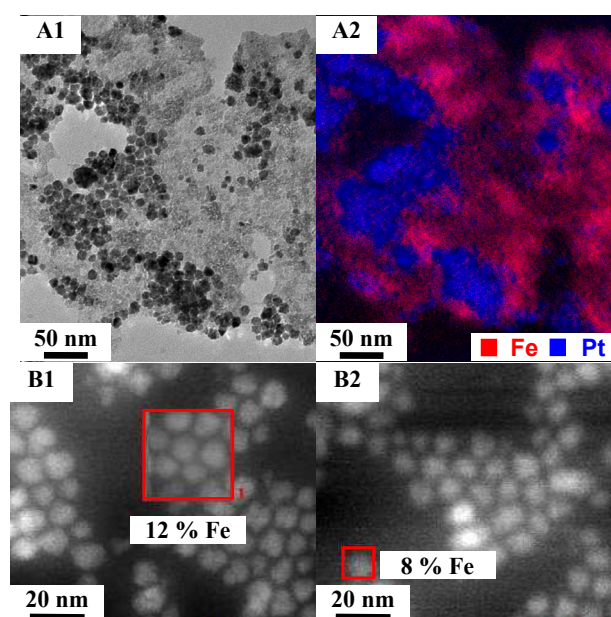


Figure 4.5 Bright field TEM picture (A1), corresponding EFTEM image showing Pt in blue and Fe in red (A2) and dark field nanoSTEM-EDX data (B1-B2) of FePt NPs synthesized with $[\text{N}_2\text{H}_4 \cdot \text{H}_2\text{O}] / [\text{Fe}^{3+} + \text{Pt}^{2+}] = 40$. $[\text{FeCl}_3] / [\text{K}_2\text{PtCl}_4] = 1.0$.

Figure 4.5A1 corresponds to a regular bright field TEM image and displays the same duality as reported in Figure 4.3 with a coexistence of higher contrast NPs and a lower contrast film-like material, while Figure 4.5A2 is the EF-TEM image of the same area, showing Pt in blue and Fe in red. The dark discrete particles of Figure 4.5A1 are Pt-rich whilst the lighter material is Fe-rich. Figure 4.5B1 and B2 are nanoSTEM-EDX analysis from a large set of NPs and single NPs, respectively. The red squares in Figure 4.5B indicate the areas where nanoSTEM-EDX was completed to extract the composition at a nanometer scale. The general trend of the nanoSTEM-EDX spectra is similar for all samples, displaying a large composition inhomogeneity, and more nanoSTEM-EDX data are presented as below.

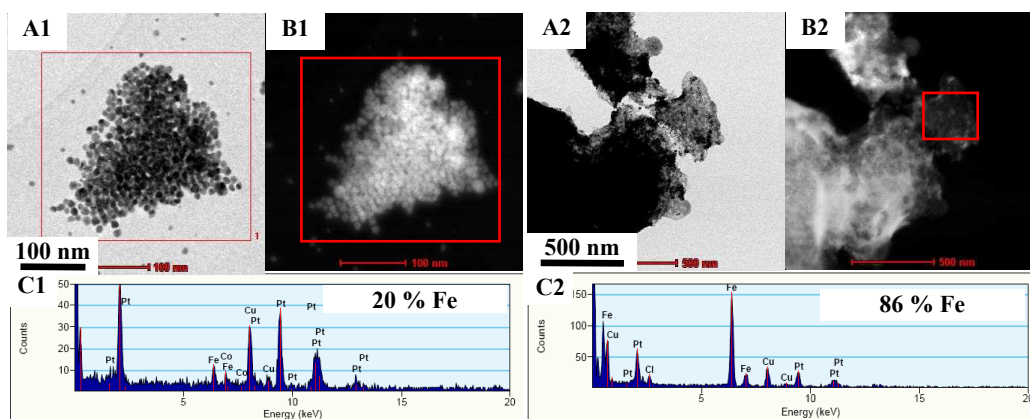


Figure 4.6 Bright field STEM picture (A), corresponding high angle annular dark field (HAADF) STEM image with red squares indicating areas analyzed by nanoSTEM-EDX (B) and EDX spectra (C) of FePt NPs synthesized with $[\text{N}_2\text{H}_4\cdot\text{H}_2\text{O}] / [\text{Fe}^{3+} + \text{Pt}^{2+}] = 40$ and $[\text{FeCl}_3] / [\text{K}_2\text{PtCl}_4] = 0.2$.

Figure 4.6 shows nanoSTEM-EDX data of FePt NPs synthesized with initial 0.2:1 molar ratio of Fe to Pt precursor. Figure 4.6A1 and A2 are bright field STEM images showing separated and dispersed NPs and film-like matrix, respectively. Corresponding high angle annular dark field (HAADF) STEM image are presented in Figure 4.6B1 and B2. HAADF-STEM is an incoherent imaging technique that collects electrons scattered through a relatively wide angle in the electron microscope, beyond the usual Bragg scattering angles. Thus, HAADF images show little or no diffraction effects and the scattering process is found to be approximately proportional to the square of atomic number, i.e. proportional to Z^2 . The technique is therefore ideal for elemental-specific imaging and for revealing thickness variations that may be obscured in conventional TEM imaging. HAADF can reveal the features which sometimes are difficult to be viewed in bright field imaging. For instance, Figure 4.6B2 shows the area labelled with red square comprised of both NPs and film materials. With regard to the composition, the NPs appear to be Pt rich in composition (Figure 4.6C1) and the Fe is found in the film-like material (Figure 4.6C2).

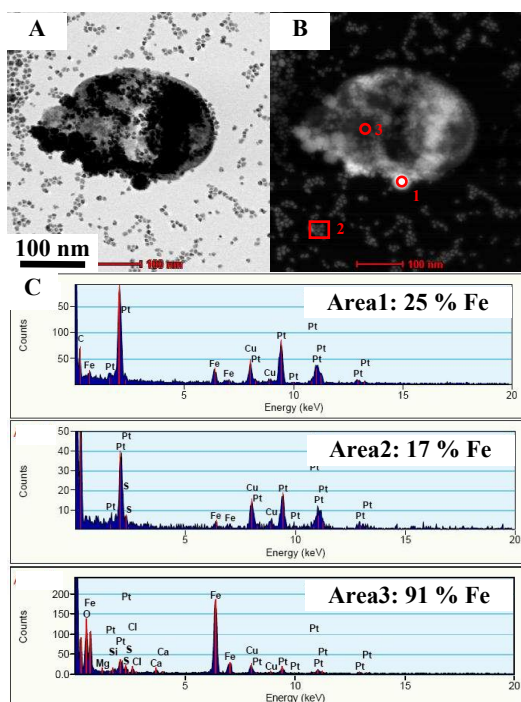


Figure 4.7 Bright field STEM picture (A), corresponding high angle annular dark filed (HAADF) STEM image with red squares indicating areas analyzed by nanoSTEM-EDX (B) and EDX spectra (C) of FePt NPs synthesized with $[\text{N}_2\text{H}_4\cdot\text{H}_2\text{O}] / [\text{Fe}^{3+} + \text{Pt}^{2+}] = 40$ and $[\text{FeCl}_3] / [\text{K}_2\text{PtCl}_4] = 0.6$.

Figure 4.7 displays nanoSTEM-EDX data of FePt NPs synthesized with initial 0.6:1 molar ratio of Fe to Pt precursor. Well dispersed NPs as well as film-like materials are also shown in Figure 4.7A-B. The NPs are relatively polydisperse in size (Figure 4.7A-B), Pt rich (Figure 4.7C) and apparently inhomogeneous in composition (Figure 4.7C). Film-like material is Fe rich and traces of oxygen and chlorine may suggest the incomplete reduction of Fe precursor, or the hydrolysis product of Fe salt $\beta\text{-FeOOH}$ (Figure 4.7C).

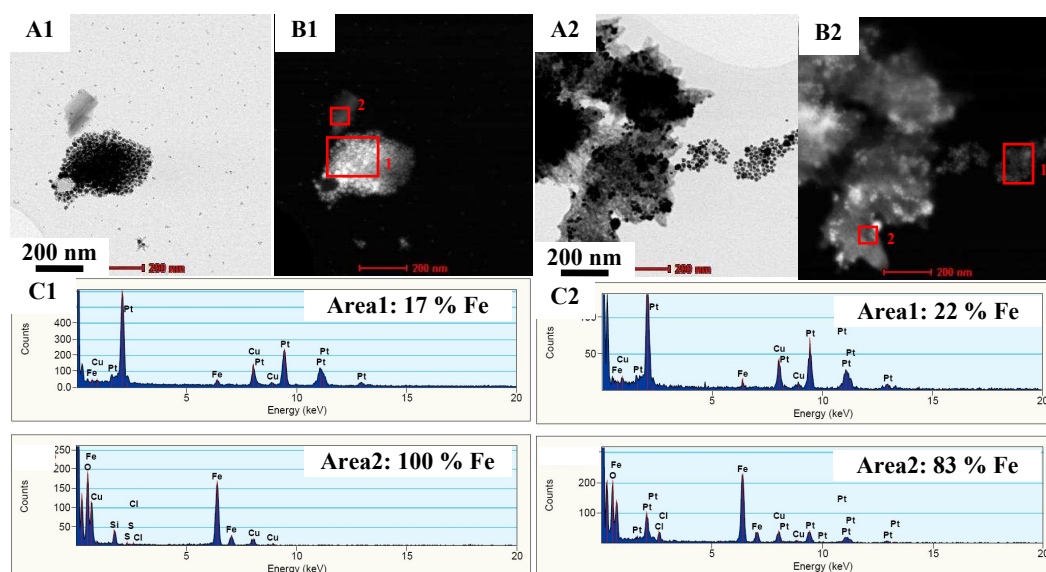


Figure 4.8 Bright field STEM picture (A), corresponding high angle annular dark filed (HAADF) STEM image with red squares indicating areas analyzed by nanoSTEM-EDX (B) and EDX spectra (C) of FePt NPs synthesized with $[\text{N}_2\text{H}_4\cdot\text{H}_2\text{O}] / [\text{Fe}^{3+} + \text{Pt}^{2+}] = 40$. $[\text{FeCl}_3]$ to $[\text{K}_2\text{PtCl}_4]$ molar ratios are equal to 1.0 (A1 to C1), and 1.4 (A2 to C2) respectively.

Figure 4.8 presents nanoSTEM-EDX data of FePt NPs synthesized with initial 1:1 and 1.4:1 molar ratio of Fe to Pt precursor. NP contain 17 to 22% of Fe (Figure 4.8A1-C1 and A2-C2, Area 1). Again the samples appear inhomogeneous in composition. Fe was found in film material, as shown in Figure 4.8A1-C1 and A2-C2, Area 2.

Figure 4.9 shows similar results even though the synthesis was carried out with a much larger initial Fe to Pt precursor ratio, i.e. 1.8. Again Fe can be found in the film-like material which also contains trace of oxygen and chlorine (Figure 4.9C2), this is consistent with the other samples.

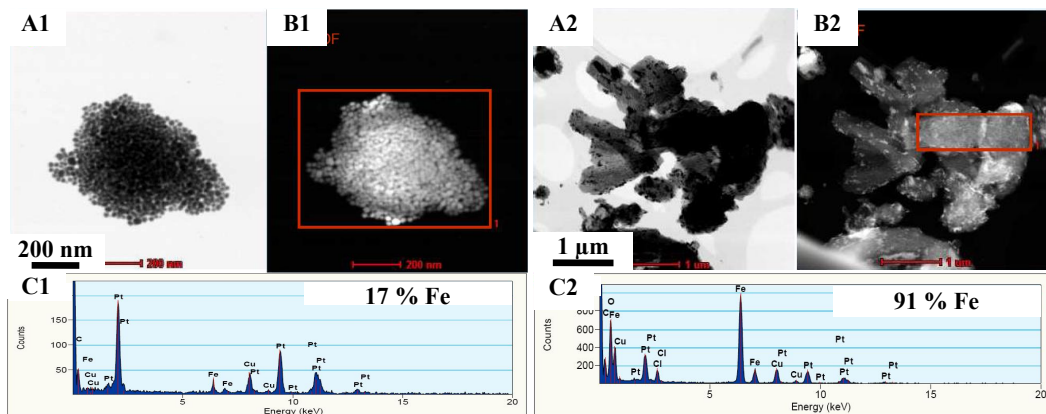


Figure 4.9 Bright field STEM picture (1), corresponding high angle annular dark field (HAADF) STEM image with red squares indicating areas analyzed by nanoSTEM-EDX (2) and EDX spectra (3) of FePt NPs synthesized with $[\text{N}_2\text{H}_4\cdot\text{H}_2\text{O}] / [\text{Fe}^{3+} + \text{Pt}^{2+}] = 40$, and $[\text{FeCl}_3] / [\text{K}_2\text{PtCl}_4] = 1.8$.

In summary, while NPs appear systematically to be Pt rich, the film like material is consistently characterized as Fe rich regardless of the initial iron to platinum salt ratio used for the syntheses.

4.3. Discussion

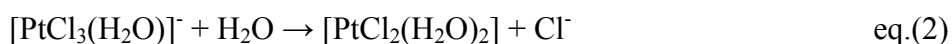
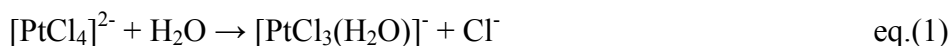
Homogeneous chemical composition is a key requirement for both basic and technological investigations to be completed with alloyed NPs. For low temperature syntheses of FePt NPs to be used, this major challenge needs to be addressed. To summarize the data presented so far, FePt NPs syntheses were carried out with $\text{FeCl}_3 / \text{K}_2\text{PtCl}_4 / \text{hydrazine monohydrate}$ in water / isooctane / Brij52 / butanol amphiphilic system. The hydration of 4 molecules of water per molecule of surfactant was chosen to have maximum conductivity, i.e. higher exchange rate, throughout the system. The knobby appearance of the NPs suggests that their formation follows a two-stage growth mechanism in which nanocrystals first nucleate in a supersaturated solution and next grow by both aggregating and fusing to form larger particles. The size of NPs increases with the Fe to Pt precursor ratio in the synthesis media.

While ICP-OES shows the linear trend of composition with initial iron to platinum precursors ratio (Figure 4.2A), XRD indicates a constant composition, i.e. ~15% Fe, independent of the variation of precursors ratio (Figure 4.2B and C). This indicates the limitation of ICP-OES, which provides only global composition information of final reaction product. Compared to ICP-OES, XRD can provide nanocrystal information including composition based on lattice constant. However, it may not pick the core-shell structure when it is in the nanoscale or other amorphous inhomogeneties.²⁶ Therefore, other techniques including TEM (Figure 4.3), EF-TEM (Figure 4.5A) and nanoSTEM-EDX (Figure 4.5 to Figure 4.9) which can provide nanoscale composition information were employed in this study. The nanoscale composition data confirms XRD results that NPs are Pt rich, and further reveals that the NPs composition is inhomogeneous, and could not be tuned by changing the initial Fe to Pt precursor ratio.

Chlorine and oxygen found in the iron rich materials (Figure 4.6 to Figure 4.9) suggest incomplete FeCl_3 reduction or formation of akaganeite ($\beta\text{-FeOOH}$). The formation of $\beta\text{-FeOOH}$ from the hydrolysis of Fe^{3+} in aqueous solution favored by the presence of chloride ion.²⁷⁻²⁸ It is known that FeCl_3 hydrolyses to $[\text{Fe}(\text{OH}_2)_6]^{3+}$ in the presence of water, but that the high charge to radius ratio in Fe^{3+} induces deprotonation leading via ololation and oxolation to oxobridged iron species which precipitate as 2-4 nm spheres containing $\sim 10^2$ Fe^{III} ions, most likely in octahedral $\text{Fe}(\text{O},\text{OH},\text{H}_2\text{O})_6$ coordination.²⁷ It would be tempting to associate such material with the small (ca. 2 nm) NPs of light contrast, observed in larger amounts in the HR-TEM image of the molar ratio 1.8 sample (Figure 4.3E4). This would have provided further evidence to indicate that it is the hydrolysis of FeCl_3 which leads to the film-like material. However, the small size of these 2 nm light contrast NPs would only provide broad XRD peaks, which would be undiscernable from the background in the present situation. In addition, the reduction strength of hydrazine is weakened by the decreasing pH afforded by the deprotonation of the

$[\text{Fe}(\text{OH}_2)_6]^{3+}$.²⁹ Indeed, such a pH decrease down to 1.2 was observed when the FeCl_3 concentration was increased. Thus the hydrolysis of FeCl_3 in the presence of base (hydrazine) leads to insoluble iron salts which prevents the Fe ions from reacting with the platinum salts or the initially formed Pt clusters, and may also at a later stage prevent the formation of an Fe rich shell surrounding Pt rich NPs. The validity of this hypothesis is explored in the following section.

In contrast, two $[\text{PtCl}_2(\text{H}_2\text{O})_2]$ complexes can be formed through hydrolysis of $[\text{PtCl}_4]^{2-}$ but precipitation of platinum does not occur. The hydrolysis reaction of $[\text{PtCl}_4]^{2-}$ is shown in Equation (1) and (2).³⁰



The formed complexes can be reduced to a $\text{Pt}^{\text{II}}\text{--Pt}^{\text{I}}$ dimer stabilized with Cl^- .³⁰⁻³² A $\text{Pt}^{\text{I}}\text{--Pt}^{\text{I}}$ dimer can be formed through the addition of another electron to $\text{Pt}^{\text{I}}\text{--Pt}^{\text{II}}$ dimer. Both the $\text{Pt}^{\text{II}}\text{--Pt}^{\text{I}}$ and $\text{Pt}^{\text{I}}\text{--Pt}^{\text{I}}$ dimers can react with a third $[\text{PtCl}_2(\text{H}_2\text{O})_2]$ complex to form a trimer. These partially reduced dimers and trimers probably represent early intermediates toward the formation of larger clusters or nuclei from which the NPs grow. Dimers and trimers have higher electron affinities than the original Pt precursor due to orbital delocalization. Reduction is then expected to occur preferentially via electron transfer from the reductant to these dimeric and trimeric units.³¹⁻³²

4.3.1. Hypotheses and Strategy Development

Assuming that FeCl_3 and K_2PtCl_4 could be reduced at very different rates or that FeCl_3 could hydrolyze to insoluble and unreactive oxohydroxo species and that

consequently the iron cannot be incorporated into the NPs, a number of strategies was explored with the aim of increasing the iron content:

- i) Reaction time: the potential formation of an iron ‘richer’ shell is investigated in Section 4.3.2 by considering the effect of the reaction time on the NPs.
- ii) Fe and Pt salts: more hydrolytically stable iron precursors should give higher incorporation of iron into the NPs. The effect of this parameter on the NPs composition is investigated in Section 4.3.3.
- iii) Reducing agent strength: hydrazine monohydrate is known as having moderate efficiency in reducing FeCl_3 .^{29, 33} A faster reducing agent might compete with hydrolysis of the iron precursor and allow greater Fe incorporation into the NPs. The use of sodium borohydride is discussed in Section 4.3.4.^{29, 33}

4.3.2. Reaction Time

Reaction time was varied from 0.25 h to 16 h to assess the effect of time on the Fe incorporation in the NPs. The XRD patterns are presented in Figure 4.10, and the results are summarized in Table 4.2. There is no significant variation of the XRD peaks positions (Figure 4.10) hence the lattice constant and implied composition, regardless of the time scale of the synthesis (Table 4.2).

Table 4.2 XRD data of FePt NPs synthesized with varied reaction time, $[\text{N}_2\text{H}_4\cdot\text{H}_2\text{O}] / [\text{Fe}^{3+} + \text{Pt}^{2+}] = 40$. t_r is the reaction time, a is the lattice constant calculated based on (111), (200) and (220) peaks, x is the iron content in $\text{Fe}_x\text{Pt}_{1-x}$, D_{XRD} is the crystalline grain size in diameter calculated based on FWHM of 3 different XRD peaks.

t_r (h)	a (Å)	x (%)	D_{XRD} (nm)
0.25	3.909 ± 0.004	14.6 ± 3.5	7.4 ± 1.4
3.00	3.910 ± 0.004	13.2 ± 3.6	7.3 ± 0.5
16.00	3.906 ± 0.001	15.3 ± 3.1	9.2 ± 1.0

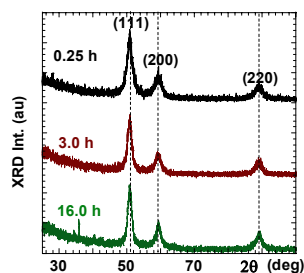


Figure 4.10 XRD patterns of FePt NPs synthesized with varied reaction time, $[\text{N}_2\text{H}_4\cdot\text{H}_2\text{O}] / [\text{Fe}^{3+}+\text{Pt}^{2+}] = 40$.

The only effect is that the NPs become slightly larger at longer times as indicated by TEM (Figure 4.11A1 vs. B1). After 0.25 h reaction, NPs of ~5 - 10 nm have already formed (Figure 4.11A1). By increasing the reaction time to 16 h, the population of NPs larger than 10 nm with knobby appearance is increased (Figure 4.11B1), but without a significant crystalline grain size variation within experimental uncertainties (Table 4.2). This suggests that Pt rich NPs grow mainly through an aggregation manner.

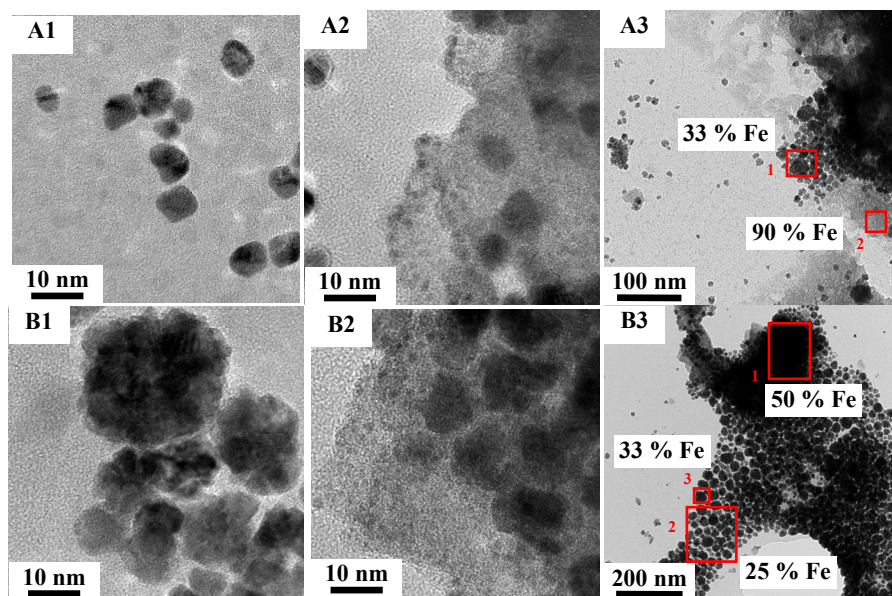


Figure 4.11 TEM images (1-2) and bright field STEM pictures (3) with red squares indicating the areas analyzed by nanoSTEM-EDX. FePt NPs were synthesized with varied reaction time, 0.25 h (A) and 16 h (B), $[\text{N}_2\text{H}_4\cdot\text{H}_2\text{O}] / [\text{Fe}^{3+}+\text{Pt}^{2+}] = 40$.

There is no TEM evidence of formation of core shell type structure supporting the hypothesis that Fe is reduced gradually and forms a Fe rich shell on Pt rich core NPs with longer reaction times. Fe was still found in separate film material coexisting with NPs regardless of reaction time, as shown in Figure 4.11A2 and B2. The compositions of these two types of materials were characterized by nanoSTEM-EDX (Figure 4.11A3 and B3). The NPs formed within 15 mins are indeed Pt rich (Figure 4.11A3, Area 1). It is noticeable that the Fe content is slightly high, this is attributed to small amounts of film material included in the analyzed area. More Fe was found in the film material, as shown in Figure 4.11A3, Area 2. NPs synthesized with a 16 h reaction show similar composition results as a 0.25 h sample. Film materials are rich in Fe (Figure 4.11B3, Area 1), and NPs show no obvious increase in the Fe content (Figure 4.11B3, Area 1 and 3). nanoSTEM-EDX data demonstrated that there was very little change in the composition of the NPs and the only slight effect is for the Pt rich NPs to become slightly larger at longer reaction times, growing by aggregation type processes. In summary, these results revealed that Pt rich NPs have formed within 15 min and grow through an aggregation manner with no significant change of composition, whereas FeCl_3 is unreduced or hydrolyzed and appears as a film like material regardless of longer reaction time.

4.3.3. Impact of Pt and Fe precursors

While synthesizing alloyed nanoparticles, the effects of mixing the salt precursors also need to be considered. Indeed, K_2PtCl_6 can form when mixing FeCl_3 and K_2PtCl_4 salts in aqueous solution, leading to insoluble yellow crystals as characterized by XRD (Figure 4.12A). Whereas K_2PtCl_6 precipitates are dissolved when hydrazine is added to the aqueous solution, their formation could contribute

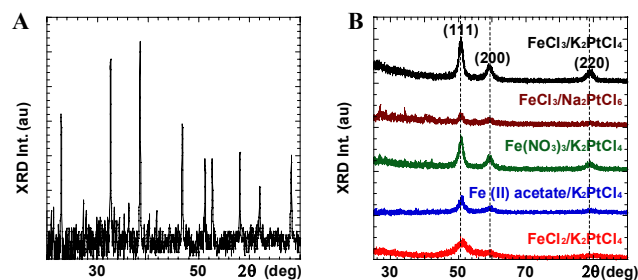


Figure 4.12 XRD patterns of yellow precipitates formed by mixing of FeCl_3 and K_2PtCl_4 aqueous solution directly at 30 °C, $[\text{Fe}^{3+}] = [\text{Pt}^{2+}] = 0.14 \text{ M}$ (A); FePt NPs synthesized with different precursors, $[\text{N}_2\text{H}_4 \cdot \text{H}_2\text{O}]/[\text{Fe}^{3+} + \text{Pt}^{2+}] = 40$ (B).

to the observed inhomogeneous nucleation of Pt and Fe materials. This was investigated by using Na_2PtCl_6 as a Pt source. In addition and as indicated above, a major problem with the use of aqueous systems is that FeCl_3 hydrolyses rapidly to insoluble oxyhydroxide species, but it is well known that Fe^{II} is less hydrolytically unstable because of the lower charge to radius ratio. In addition Fe^{II} salts will not react with K_2PtCl_4 to give K_2PtCl_6 . Therefore, the effect of Fe^{II} precursors, $\text{Fe}(\text{acetate})_2$ and FeCl_2 as well as Fe^{III} salts free of chlorine atoms like $\text{Fe}(\text{NO}_3)_3$ were investigated. The XRD characterization of the products is presented in Figure 4.12B, and summarized in Table 4.3.

Table 4.3 X-ray diffraction data of FePt NPs synthesized with different Fe and Pt precursors, $[\text{N}_2\text{H}_4 \cdot \text{H}_2\text{O}] / [\text{Fe}^{2+/3+} + \text{Pt}^{2+}] = 40$. a is the lattice constant, x is the iron content in $\text{Fe}_x\text{Pt}_{1-x}$, the diameter D_{XRD} is the crystalline grain size.

Precursors	a (Å)	x (%)	D_{XRD} (nm)
$\text{FeCl}_3 / \text{K}_2\text{PtCl}_4$	3.911 ± 0.005	13.2 ± 3.6	7.3 ± 0.5
$\text{FeCl}_3 / \text{Na}_2\text{PtCl}_6$	3.910 ± 0.006	15.0 ± 1.3	8.8 ± 1.4
$\text{Fe}(\text{NO}_3)_3 / \text{K}_2\text{PtCl}_4$	3.911 ± 0.005	13.3 ± 3.6	7.4 ± 1.8
$\text{Fe}(\text{acetate})_2 / \text{K}_2\text{PtCl}_4$	3.899 ± 0.003	21.5 ± 2.2	5.8 ± 1.1
$\text{FeCl}_2 / \text{K}_2\text{PtCl}_4$	3.882 ± 0.005	33.9 ± 3.4	2.6 ± 0.5

The data shows that the platinum precursor does not have much impact on the composition of NPs (Figure 4.12B and Table 4.3). Similarly, all Fe^{3+} precursor based samples regardless of the Pt precursors, have a similar lattice constant, corresponding to ~15% Fe composition. Strikingly though, Fe^{2+} precursors are associated with an increase of the Fe insertion in the NPs by more than 60% and

150% for Fe(acetate)₂ and FeCl₂, respectively. The difference between Fe(acetate)₂ and FeCl₂ between could result from the different dissociation constant associated with the acetate and the chlorine salts. The general trend of increased iron insertion in the NPs can be explained by greater hydrolytic stability of Fe²⁺ precursors, but may also be influenced by the lower reduction potential of Fe^{II/0} compared with Fe^{III/0} (Table 4.4).

Table 4.4 Decreasing Standard redox potentials.³⁴

Chemical Reaction	E° (V)
[PtCl ₄] ²⁻ + 2e ⁻ ↔ Pt ⁰ + 4Cl ⁻	0.755
[PtCl ₆] ²⁻ + 2e ⁻ ↔ Pt ⁰ + 6Cl ⁻	0.68
Fe ³⁺ + 3e ⁻ ↔ Fe ⁰	-0.037
N ₂ H ₄ .H ₂ O ↔ N ₂ + 5H ⁺ + 4e ⁻ + OH ⁻	-0.23
Fe ²⁺ + 2e ⁻ ↔ Fe ⁰	-0.447
Fe ³⁺ + e ⁻ ↔ Fe ²⁺	-0.771
BH ⁴⁻ + 3H ₂ O ↔ B(OH) ₃ + 7H ⁺ + 8e ⁻	-1.73

For all precursors, TEM reveals similar typical features as previously highlighted including the presence of both NPs which show a multidomain structure and film like materials (Figure 4.13), while slight variations of the NPs size can be observed (Table 4.3). The multidomain feature is stronger for the synthesis completed with FeCl₂ and K₂PtCl₄ (Figure 4.13D1), which is also associated with the smallest crystalline grain size of about 2.5 nm in diameter. Larger length scale TEM images and nanoSTEM-EDX results are presented in the 2nd row of Figure 4.13, with the main features being the large inhomogeneous distribution of Fe and Pt materials together with the coexistence of Pt rich NPs with Fe rich film-like material. This can be observed regardless of the precursor set.

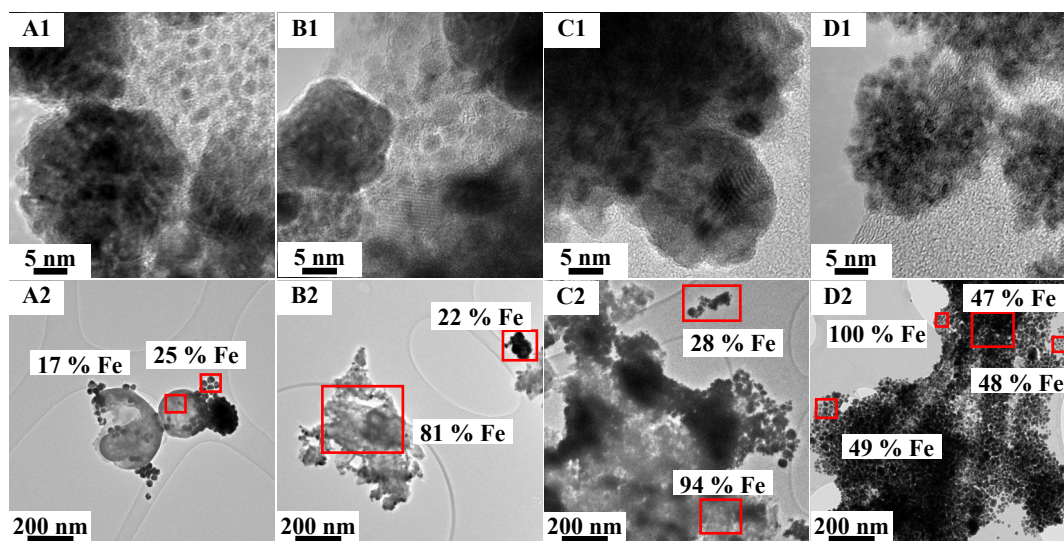


Figure 4.13 TEM images of FePt NPs with different precursors FeCl_3 and Na_2PtCl_6 (A), $\text{Fe}(\text{NO}_3)_3$ and K_2PtCl_4 (B), $\text{Fe}(\text{acetate})_2$ and K_2PtCl_4 (C), FeCl_2 and K_2PtCl_4 (D), $[\text{N}_2\text{H}_4 \cdot \text{H}_2\text{O}] / [\text{Fe}^{3+/2+} + \text{Pt}^{2+}] = 40$.

While the formation of K_2PtCl_6 could be avoided by changing Pt and Fe precursors, the most important parameter for increasing the iron content in the alloyed FePt NPs appears to be the oxidation state of the Fe ions. Fe^{2+} ions are more stable to hydrolysis and hence remain available for reduction to Fe^0 and incorporation into the NPs increasing the iron content up to ~34% (Table 4.3).

4.3.4. NaBH_4 as reducing agent

NaBH_4 which is commonly used for the synthesis of nanomaterials, is a much stronger reducing agent than hydrazine monohydrate (Table 4.4).^{25, 35} Marcus theory and experimental results for a large range of nanoparticles³⁶⁻⁴¹ suggest that it is also a faster reducing agent implying that the reduction to Fe^0 may then become competitive with the hydrolysis reaction.

Compared to when using hydrazine, the XRD peak positions are shifted towards higher 2θ values (Figure 4.14), corresponding to a decrease of the lattice spacing and a concomitant higher Fe content, up to 35% (Table 4.5). This value is similar

to the 34% value obtained with $\text{FeCl}_2 / \text{K}_2\text{PtCl}_4 / \text{N}_2\text{H}_4\cdot\text{H}_2\text{O}$, supporting a kinetic related strategy is appropriate to co-reduce Fe and Pt precursors simultaneously, but also implying that a limit to Fe insertion may have been reached.

Table 4.5 XRD data of FePt NPs synthesized with $[\text{NaBH}_4] / [\text{Fe}^{3+/2+} + \text{Pt}^{2+}] = 2.5, 5$ and 10 . a is the lattice constant, x is the iron content in $\text{Fe}_x\text{Pt}_{1-x}$, the diameter D_{XRD} is the crystalline grain size.

	Ratio	a (Å)	x (%)	D_{XRD} (nm)
(a)	2.5	3.887 ± 0.005	30.2 ± 3.3	4.0 ± 0.7
	5.0	3.881 ± 0.002	34.6 ± 1.3	3.5 ± 0.5
	10.0	3.880 ± 0.005	35.6 ± 3.4	3.2 ± 0.7
(b)	5.0	3.882 ± 0.003	34.4 ± 2.1	3.8 ± 0.8

(a) $\text{FeCl}_3/\text{K}_2\text{PtCl}_4 / \text{NaBH}_4$, (b) $\text{FeCl}_2/\text{K}_2\text{PtCl}_4 / \text{NaBH}_4$

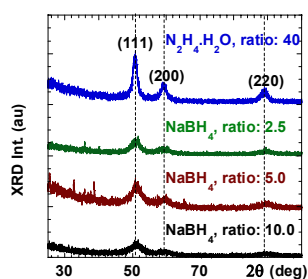


Figure 4.14 XRD patterns of FePt NPs synthesized with NaBH_4 as a reducing agent with varied reducing reagent to precursors ratio compared to $\text{N}_2\text{H}_4\cdot\text{H}_2\text{O}$.

Figure 4.15A1 and B1 are typical TEM images and fully consistent with the data previously presented showing both knobbly NPs and thin-film like material. nanoTEM-EDX demonstrates once again inhomogeneous distribution of Fe and Pt regardless of the iron precursor being used (Figure 4.15A2-B2).

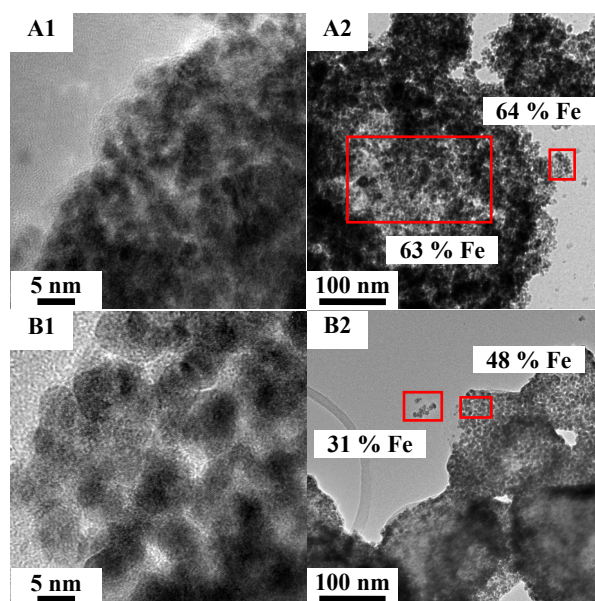


Figure 4.15 TEM images of FePt NPs synthesized with NaBH₄ as reducing agent with [NaBH₄] / [Fe^{3+/2+}+Pt²⁺] = 5: FeCl₃ and K₂PtCl₄ (A), FeCl₂ and K₂PtCl₄ (B).

The increase of Fe content in NPs was further confirmed by magnetic characterization by SQUID magnetometer (Figure 4.16). Despite the smaller size compared to NPs synthesized with hydrazine, NPs with higher Fe content reduced with NaBH₄ show stronger magnetic properties. The *ZFC-FC* curves indicate a low blocking temperature of 30 K and 25 K for both NPs obtained with hydrazine and sodium borohydrate respectively (Figure 4.16A1 and B1). However, it is noticeable that in contrast to the NPs obtained with NaBH₄ (Figure 4.16B1), the *FC* magnetization curve of the NPs synthesized with N₂H₄.H₂O does not reach saturation at temperatures below T_b (Figure 4.16A1). In addition, the hysteresis loop of NPs of ~15% Fe synthesized by hydrazine showed similar to paramagnetic material behaviour, without reaching saturation even at 5.0 T (Figure 4.16A2). Whereas NPs of ~35% Fe synthesized by NaBH₄, showed superparamagnetic properties (Figure 4.16B2), the magnetic moment of NPs were saturated at a much smaller external magnetic field. This is attributed the higher Fe content in NPs synthesized with NaBH₄.

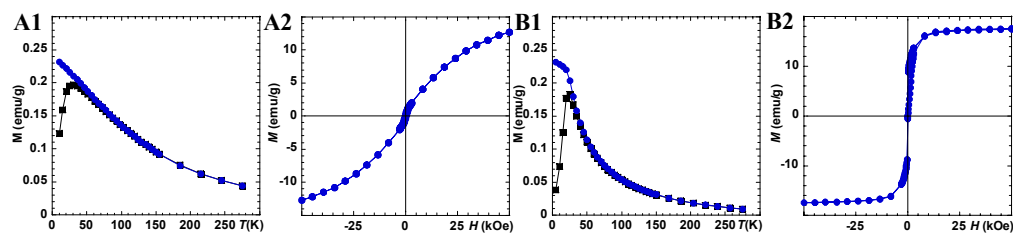


Figure 4.16 Magnetic characterization of FePt NPs synthesized with hydrazine as reducing agent at $[\text{N}_2\text{H}_4 \cdot \text{H}_2\text{O}] / [\text{Fe}^{3+} + \text{Pt}^{2+}] = 40$ (A1-2) and sodium borohydride at $[\text{NaBH}_4] / [\text{Fe}^{3+} + \text{Pt}^{2+}] = 5$ (B1-2). ZFC-FC magnetization curves were obtained in a field of 100 Oe (1) and hysteresis loops were measured at 5 K (2).

Consequently, we have demonstrated not only that it is possible to increase the iron content in the NPs, but also that aqueous media induced a limit to the Fe content which could insert into the alloyed iron-platinum magnetic nanoparticles synthesized. This was demonstrated by focusing on both increasing the reduction rate of the iron ions and decreasing the hydrolysis of the Fe precursor. This investigation was deliberately undertaken using a non-ionic surfactant in order to limit its interactions with the ionic precursors and reduce its potential impact on the alloy. Rather than a limitation of amphiphilic systems, our results highlight what appears to be a limitation of the co-reduction method to form alloyed NPs when water is present. These results then imply that future attempts to synthesize should focus on overcoming the formation of hydrolytically unstable iron complexes to develop room temperature co-reduction syntheses of FePt NPs with homogenous chemical composition. This would best be achieved by eliminating water entirely from the system. Tuning the size of the product obtained in non-aqueous media and more specifically increasing the size of the NPs might then later be achieved by decreasing the reduction rate difference between the two precursors.

4.4. Conclusion

$\text{Fe}_x\text{Pt}_{1-x}$ alloy NPs were synthesized at low temperature in non-ionic amphiphilic systems made of water, isooctane, Brij52, butanol, for which the conductivity was measured to identify the hydration providing the highest conductivity. By combining characterization techniques including ICP-OES, XRD, EFTEM and nanoSTEM-EDX, this investigation highlights a two-stage growth mechanism of the NPs. Primary Pt rich nanocrystals first nucleate in a supersaturated solution and then keep on growing and coalescing into larger knobbly particles. Polydomain Pt rich NPs are already formed after 15 min of synthesis. While excess of Fe is found in film-like material, extending reaction time up to 16 h leads to larger NPs but does not alter the NPs Fe to Pt ratio because the competitive hydrolysis of the iron precursors is completed within 15 min. This was confirmed by using the faster reducing agent, NaBH_4 and the less hydrolytically unstable Fe^{II} precursors which both increased the iron content of the nanoparticles from 15% to ~34%.

To obtain stoichiometric FePt NPs by co-reduction at room temperature, future investigations should first focus on overcoming the formation of hydrolytically unstable iron complexes, preferably by working in the absence of water. Due to limitations of co-reduction synthesis in aqueous media, future synthesis was focused on a modified thermal decomposition method, and the results are presented in the following Chapter 5.

References

- (1) Cason, J. P.; Miller, M. E.; Thompson, J. B.; Roberts, C. B. *J. Phys. Chem. B.* **2001**, 105, 2297-2302.
- (2) Cushing, B. L.; Kolesnichenko, V. L.; O'Connor, C. J. *Chem. Rev.* **2004**, 104, 3893-3946.
- (3) Eastoe, J.; Cox, A. R. *Colloid. Surface. A.* **1995**, 101, 63-76.
- (4) Filankembo, A.; Pileni, M. P. *Appl. Surf. Sci.* **2000**, 164, 260-267.
- (5) Pinna, N.; Weiss, K.; Sack-Kongehl, H.; Vogel, W.; Urban, J.; Pileni, M. P. *Langmuir.* **2001**, 17, 7982-7987.
- (6) Andre, P.; Charra, F.; Chollet, P. A.; Pileni, M. P. *Adv. Mater.* **2002**, 14, 601-603.
- (7) Filankembo, A.; Giorgio, S.; Lisiecki, I.; Pileni, M. P. *J. Phys. Chem. B.* **2003**, 107, 7492-7500.
- (8) Maillard, M.; Giorgio, S.; Pileni, M. P. *J. Phys. Chem. B.* **2003**, 107, 2466-2470.
- (9) Tilley, R. D.; Warner, J. H.; Yamamoto, K.; Matsui, I.; Fujimori, H. *Chem. Commun.* **2005**, 1833-1835.
- (10) Park, J.; Joo, J.; Kwon, S. G.; Jang, Y.; Hyeon, T. *Angew. Chem. Int. Edit.* **2007**, 46, 4630-4660.
- (11) Li, Z. Y.; Wilcoxon, J. P.; Yin, F.; Chen, Y.; Palmer, R. E.; Johnston, R. L. *Faraday. Discuss.* **2008**, 138, 363-373.
- (12) Abecassis, B.; Testard, F.; Zemb, T. *Soft. Matter.* **2009**, 5, 974-978.
- (13) Ganguli, A. K.; Ganguly, A.; Vaidya, S. *Chem Soc Rev.* **2010**, 39, 474-485.
- (14) Xuan, S. H.; Wang, F.; Wang, Y. X. J.; Yu, J. C.; Leung, K. C. F. *J. Mater. Chem.* **2010**, 20, 5086-5094.
- (15) Nakanishi, M.; Furusawa, G. I.; Waki, K.; Hattori, Y.; Kamino, T.; Sasaki, K.; Kuroda, K.; Saka, H. *Mater. Trans.* **2007**, 48, 2572-2579.
- (16) Bai, L. T.; Wan, H. Y.; Street, S. C. *Colloid. Surface. A.* **2009**, 349, 23-28.
- (17) Carpenter, E. E.; Sims, J. A.; Wienmann, J. A.; Zhou, W. L.; O'Connor, C. J. *J. Appl. Phys.* **2000**, 87, 5615-5617.
- (18) Hyie, K. M.; Yaacob, I. D. *J. Mater. Process. Tech.* **2007**, 191, 48-50.
- (19) Yan, Q. Y.; Purkayastha, A.; Kim, T.; Kroger, R.; Bose, A.; Ramanath, G. *Adv. Mater.* **2006**, 18, 2569-2573.
- (20) Gao, Y.; Zhang, X. W.; Yin, Z. G.; Qu, S.; You, J. B.; Chen, N. F. *Nanoscale Res Lett.* **2010**, 5, 1-6.
- (21) Reiss, B. D.; Mao, C. B.; Solis, D. J.; Ryan, K. S.; Thomson, T.; Belcher, A. M. *Nano. Lett.* **2004**, 4, 1127-1132.

- (22) Qu, S.; Zhang, X. W.; Gao, Y.; You, J. B.; Fan, Y. M.; Yin, Z. G.; Chen, N. F. *Nanotechnology*. **2008**, 19, 135704.
- (23) Chen, S.; Maclaren, D.; Baker, R.; Chapman, J.; Cole-Hamilton, D. J.; Lee, S.; André, P. *J. Mat. Chem.* **2011**, 21, 3646-3654.
- (24) A. Bonakdarpour, J. W., D.A. Stevens, S. Sheng, T.L. Monchesky, R. Löffel, R.T. Atanasoski, A.K. Schmoeckel, G.D. Vernstrom, M.K. Debe, J.R. Dahna, *J. Electrochem. Soc.* **2005**, 152, A61-72.
- (25) Wu, J.; Walukiewicz, W.; Yu, K. M.; Ager, J. W.; Haller, E. E.; Lu, H.; Schaff, W. J.; Saito, Y.; Nanishi, Y. *Appl. Phys. Lett.* **2002**, 80, 3967-3969.
- (26) Michaël Delalande, P. R. M., Peter Reiss and Yves Samson. **2007**, 17, 1579.
- (27) Flynn, C. M. *Chem. Rev.* **1984**, 84, 31-41.
- (28) Refait, P.; Genin, J. M. R. *Corros. Sci.* **1997**, 39, 539-553.
- (29) Yang, C. L.; Xing, J. M.; Guan, Y. P.; Liu, J. G.; Liu, H. Z. *J. Alloy. Compd.* **2004**, 385, 283-287.
- (30) Sanders, C. I.; Martin, D. S. *J. Am. Chem. Soc.* **1961**, 83, 807-810.
- (31) Ciacchi, L. C.; Pompe, W.; De Vita, A. *J. Am. Chem. Soc.* **2001**, 123, 7371-7380.
- (32) Ciacchi, L. C.; Pompe, W.; De Vita, A. *J. Phys. Chem. B.* **2003**, 107, 1755-1764.
- (33) Iida, H.; Nakanishi, T.; Takada, H.; Osaka, T. *Electrochim. Acta.* **2006**, 52, 292-296.
- (34) Lide, D. R.; Weast, R. C.; Company, C. R., *CRC Handbook of Chemistry and Physics*. 83rd ed.; CRC Press: Boca Raton, Fla., 2002.
- (35) Foos, E. E.; Snow, A. W.; Twigg, M. E.; Ancona, M. G. *Chem. Mat.* **2002**, 14, 2401-2408.
- (36) Ban, I.; Drofenik, M.; Makovec, D. *J. Magn. Magn. Mater.* **2006**, 307, 250-256.
- (37) Couto, G. G.; Klein, J. J.; Schreiner, W. H.; Mosca, D. H.; de Oliveira, A. J. A.; Zarbin, A. J. G. *J. Colloid. Interf. Sci.* **2007**, 311, 461-468.
- (38) Jung, J. S.; Chae, W. S.; McIntyre, R. A.; Seip, C. T.; Wiley, J. B.; O'Connor, C. J. *Mater. Res. Bull.* **1999**, 34, 1353-1360.
- (39) Bagwe, R. P.; Khilar, K. C. *Langmuir*. **2000**, 16, 905-910.
- (40) Zhao, Y.; Cui, G.; Wang, J.; Fan, M. *Inorg. Chem.* **2009**, 48, 10435-10441.
- (41) Chen, M.; Tang, B.; Nikles, D. E. *Ieee. T. Magn.* **1998**, 34, 1141-1143.

Chapter 5

FePt Magnetic Nanoparticles Synthesized through Thermal Decomposition

5.1. Introduction

In Chapter 4, the synthesis of FePt NPs in aqueous media at low temperature was investigated. This work focused on the composition issue. The iron salts hydrolysis and the mismatch in the co-reduction kinetic of the iron and platinum salts were identified to be the limiting parameters preventing the formation of 1:1 stoichiometry FePt NPs. Those results indicate that to obtain higher stoichiometry in FePt NPs, investigation should focus on preventing the formation of hydrolytically unstable iron complexes, preferably by working in the absence of water.

This chapter focuses on FePt NPs synthesis completed in organic media, hence avoiding the hydrolysis reaction of iron salts in aqueous solution. The FePt synthesis in a conventional high-boiling solvent, i.e. benzyl ether is first investigated. Next the potentials of ionic liquids (ILs) are further explored to be used as novel solvents for NPs synthesis.

5.2. Reminder of the Mechanism of NPs Nucleation and Growth

In order to understand the work herein, a brief description of the NPs nucleation and growth mechanism based on the classic LaMer Mechanism is presented.¹ For the thermal decomposition route, the precursor compounds are either decomposed or reduced to generate zero-valent metal atoms, which are the building blocks of the nanocrystals. The nucleation and growth mechanism of the NPs is illustrated in Figure 5.1.

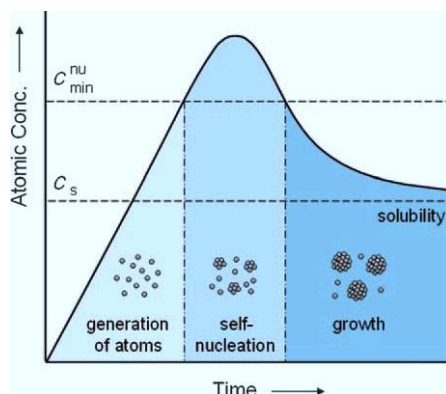


Figure 5.1 Plot of atomic concentration against time, illustrating the NPs nucleation and growth mechanism.² (Copyright 2008, Wiley-VCH Verlag GmbH & Co. KGaA. Reproduced in part with permission.)

As the precursors are reduced or decomposed, the concentration of metal atoms steadily increases with time and reaches the supersaturation point (C_s). Once the degree of supersaturation is high enough to overcome the energy barrier for self-nucleation, the atoms start to form small clusters, i.e. nuclei. The minimum supersaturation point required for nucleation is defined as C_{min}^{nu} which varies with every system. The nuclei then increase in an accelerated manner, therefore the concentration of metal atoms in solution drops. Once the concentration of atoms drops below the level of C_{min}^{nu} , no additional nuclei will be generated. With a

continuous supply of metal atoms via ongoing precursor decomposition or reduction, the nuclei will grow into larger nanocrystals until an equilibrium state between the atoms on the surface of the nanocrystals and the atoms in the solution is reached. Besides growth via atom addition, the nuclei and nanocrystals can also directly merge into larger objects via agglomeration. In addition, a process known as Ostwald ripening takes place if the supersaturation is too low for all the particles to keep growing. In this process, particle of a size smaller than the minimum radius of a nucleus that can grow spontaneously in the supersaturated solution dissolves and generates metal atoms. The reprecipitation of these atoms on larger NPs leads to a continuous growth of NPs but generally broadens the particles size distribution.²⁻³

5.3. Conventional High-boiling Chemical as a Solvent

Benzyl ether has been widely used as a solvent for inorganic NPs synthesis including FePt NPs,⁴⁻⁵ a choice justified by its relative chemical inertness and a high boiling point of ~298 °C.⁶ In this study, FePt NPs are synthesized through a modified thermal decomposition approach in benzyl ether, with Na₂Fe(CO)₄ and Pt(acac)₂ as precursors and oleyl amine and oleic acid as ligands.⁷⁻⁸

5.3.1. Experiment Protocol

In a standard synthesis protocol, a mixture of Pt(acac)₂ (1 mmol), oleyl amine (8 mmol) and oleic acid (4 mmol) in 10 mL of benzyl ether was placed in a 50 mL round bottom flask connected to a condenser. Under stirring, the mixture was heated up to 100 °C for 1 h to remove oxygen and moisture. Then Na₂Fe(CO)₄ (1 mmol) in 10 mL benzyl ether mixture was added and heated up to 150 °C for 1 h. The mixture was further heated up to reflux for 3 h. The dark solution was left to

cool down to room temperature and the NPs were collected by centrifugation after washing with hexane and ethanol.

5.3.2. Experiment Results

After synthesis, the dark colour product was characterized by powder X-ray diffraction (XRD). The XRD pattern shows peaks around 51° , 60° and 89° which are characteristic of *fcc*-FePt (111), (200) and (220) peaks, respectively (Figure 5.2A). It is noticeable that the (200) and (220) peaks are very weak. This is attributed to the small NP size. Therefore the composition and crystalline size of FePt NPs was calculated based on the (111) peak which gives the strongest signal to noise ratio. It suggests a composition of $43.8 \pm 1.3\%$ in Fe,⁹ and a crystalline size about 3.6 ± 0.1 nm in diameter.

Transmission electron microscopy (TEM) images (Figure 5.2B1-B2) display a single layer of well dispersed FePt NPs coating on the carbon film on the TEM grid. The TEM size of NPs is 4.8 ± 0.8 nm in diameter, which is close to the XRD crystalline size. To characterize individual NP composition, nanometer scale scanning transmission electron microscopy and energy dispersive X-ray (STEM-EDX) composition analysis was completed on different nanoscale areas including single or several NPs and the representative data are shown in Figure 5.2C-D. The peak ratio of Fe K_α at ~ 6.4 keV and Pt L_α at ~ 9.4 keV (Figure 5.2C3 and D3) implies a $\sim 1:1$ ratio of Fe to Pt in composition, which agrees with XRD composition value. It is noticeable that there are no significant composition variations between different regions of the TEM grid holding the NPs, which support a homogenous composition distribution of the FePt NPs.

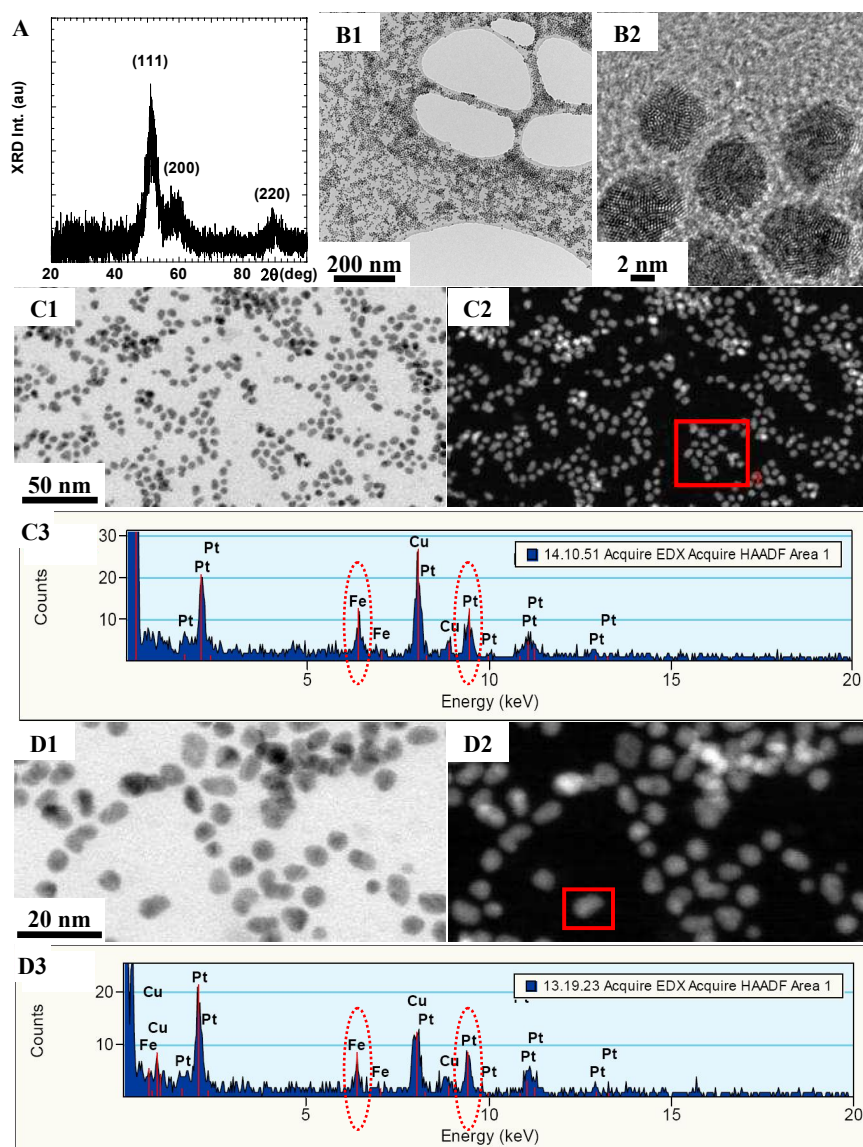


Figure 5.2 XRD pattern (A), TEM images (B1-2) and nanoSTEM-EDX data (C, D) of FePt NPs synthesized in benzyl ether at under reflux. $[\text{Na}_2\text{Fe}(\text{CO})_4] = [\text{Pt}(\text{acac})_2] = 0.05 \text{ M}$, $[\text{oyleylamine}]/[\text{Pt}(\text{acac})_2] = 8$, $[\text{oleic acid}]/[\text{Na}_2\text{Fe}(\text{CO})_4] = 4$, heat rate 15°C/min . The nanoSTEM-EDX data include bright field STEM pictures (C1 and D1), corresponding high angle annular dark filed (HAADF) STEM images (C2 and D2) with red squares indicating analyzed areas and EDX spectra (C3 and D3).

The magnetic properties of the NPs were characterized by a superconducting quantum interference device (SQUID) as shown in Figure 5.3. The zero field cooling/field cooling (ZFC/FC) measurement presents a peak on the ZFC curve known as the blocking temperature (T_b). At T_b the relaxation time of NPs becomes

comparable to SQUID measurement time (T_m) which is about 100 s.¹⁰ If the NPs have a broad size distribution, there will be a mismatch between T_b and the temperature T_{irr} at which the ZFC and FC curves coincide. At T_{irr} the remanence and the coercivity of the largest NPs vanish.¹¹

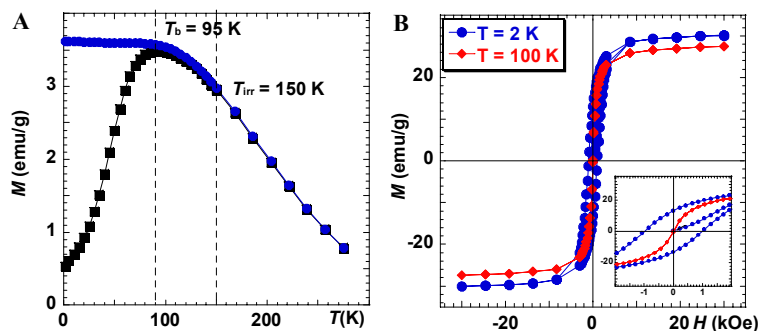


Figure 5.3 SQUID data of FePt NPs synthesized in benzyl ether at ~ 300 °C: ZFC-FC (A) under a magnetic field of 100 Oe and hysteresis loops (B) at 2 K and 100 K, the insert shows hysteresis ranging from -2 to 2 kOe.

As shown in Figure 5.3A, the as-synthesized FePt NPs have a T_b of ~ 95 K and a $T_{irr} \sim 150$ K. At 2 K, i.e. lower than T_b , FePt hysteresis loop displays a ferromagnetic behaviour with a coercivity value of 980 Oe and a saturation moment (M_s) of ~ 30 emu/g. At 100 K, FePt NPs do not display coercivity as expected for superparamagnetic NPs. They also have a smaller M_s of ~ 27 emu/g (Figure 5.3B).

5.3.3. Discussion and Comparison with Literature

As discussed in Chapter 3, using conventional iron precursors, such as $\text{Fe}(\text{CO})_5$, $\text{Fe}(\text{acac})_3$, $\text{Fe}(\text{OEt})_3$, FeCl_2 , often lead to a broad individual NP composition distribution, due to the kinetic difference between the decomposition and reduction of iron and platinum precursors. Therefore, $\text{Na}_2\text{Fe}(\text{CO})_4$ is selected in this study as a Fe precursor based on the literature.^{8, 12} $\text{Na}_2\text{Fe}(\text{CO})_4$ is a Fe^{2-}

precursor, which can act as a reducing agent itself to react with $\text{Pt}(\text{acac})_2$ through the reaction: $\text{Fe}^{2+} + \text{Pt}^{2+} \rightarrow \text{Fe} + \text{Pt}$.^{8, 12} Consequently Fe and Pt atoms are expected to be generated simultaneously, which leads to formation of FePt NPs of better stoichiometry.

In this work, the synthesis protocol was modified to target larger size NPs with a narrow composition distribution. The two main modifications are:

- i) In contrast to heating the mixture of iron and platinum precursors straight up to reflux ($\sim 300^\circ\text{C}$) as reported,^{8, 12} a step allowing the reaction mixture to be heated at 150°C for 1 h is inserted before heating the system to the refluxing point in our synthesis protocol. This is expected to favor the interaction of Fe^{2+} and Pt^{2+} by suppressing or avoiding the self reduction of $\text{Pt}(\text{acac})_2$ which occurs above 200°C .^{4, 13} In addition, Fe-oleic acid has a larger coordination strength than that of Pt-oleylamine, because oleic acid is a bidentate ligand while oleylamine is a monodentate ligand.¹³ In order to compensate the binding difference, the amine to Pt molar ratio used in this study was 2 times larger than the acid to Fe molar ratio. These changes are expected to be beneficial to obtain a narrow NP composition distribution.
- ii) When compared with the literature, the ligand to precursor ratios were increased by a factor of ~ 4 in this study. The higher ligand concentration stabilizing Fe and Pt atoms by forming metal-ligand complexes should lead to a slower nucleation rate and thus larger NPs. Indeed, FePt NP of TEM size ~ 5 nm were produced based on this modified protocol, which is two times larger than what was reported.^{8, 12} Besides the higher ligand concentration, the heating step at 150°C could also contribute to the formation of larger size NPs, as it allows a slower nucleation rate.

5.4. Ionic Liquids as Solvents

The results of the study of FePt NPs synthesis in benzyl ether opens up the possibility of using ionic liquids (ILs) as novel solvents for FePt NPs synthesis. ILs are low-melting organic salts many of which are liquid over a wide range of temperature.¹⁴⁻¹⁸ While ILs can be designed to be environmentally friendly and have negligible vapor pressure, a variety of physico-chemical properties such as melting point, solvation, polarity, viscosity, and hydrophobicity can all be achieved through appropriate choice of ions. Besides the potential of being made recyclable, ILs are also easier to handle than other high-boiling organic solvents like nonadecane (mp 32-34 °C, bp 330 °C). In addition, ILs are promising alternatives to replace the conventional organic solvents used for material fabrications including both organic and inorganic materials.¹⁴⁻¹⁸ ILs have been presented as attractive tools for creating new synthetic opportunities in material science including the fabrication of inorganic nanomaterials such as metals,¹⁹⁻²² metal oxide,²³⁻²⁵ and alloys.²⁶⁻²⁷ Studies have shown that nanostructures with new features, which are difficult to be fabricated via conventional approaches, can be accomplished by using ILs.^{15, 28} A typical example is the fabrication of ZnO, morphologies of which are strongly dependent on the nature of ILs.^{24, 29-30} However, very few investigations have been completed on alloy NPs, especially for magnetic NPs such as CoPt,²⁶ and FePt NPs.²⁷ This chapter will demonstrate that ILs can not only be used as a solvents for FePt NPs synthesis, but can also provide an exciting alternative pathway leading to direct synthesis of *fcc* FePt NPs.

In this study, FePt NPs syntheses in two ILs with a same anion were investigated (Figure 5.4A-B). The synthesis was first carried out in [P₆₆₆₁₄][NTf₂] as a solvent. This IL is comprised with a phosphonic cation bonding to long alkyl chains, associated with a fluoro-amide anion (Figure 5.4A). Due to the negative charge,

the anion is expected to link strongly to NPs surface and the bonding strength is much stronger than the dative bond formed between oleylamine and FePt.³¹ The synthesis protocol of FePt NPs in $[P_{66614}][NTf_2]$ is similar to the synthesis completed in benzyl ether, but with IL replacing benzyl ether as a solvent.⁹ The following sections focus on the synthesis results, first by considering the NPs evolutions as a function of the heating time and next by investigating the impact of ILs on FePt NPs synthesis.

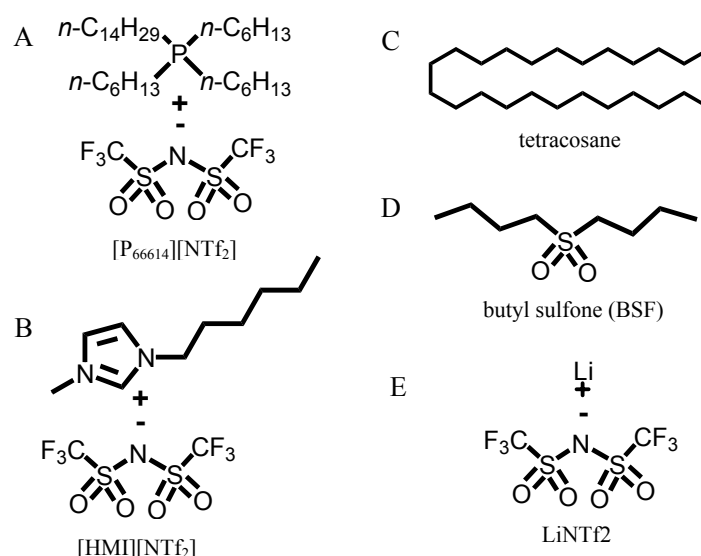


Figure 5.4 Chemical structure: $[P_{66614}][NTf_2]$, tri-n-hexyl-n-tetradecylphosphonium bis(trifluoromethylsulfonyl)imide (A), $[HMI][NTf_2]$, 1-hexyl-3-methylimidazolium bis(trifluoromethylsulfonyl)imide (B), tetracosane (C), butyl sulfone (D) and $LiNTf_2$, Lithium bis(trifluoromethylsulfonyl)imide (E).

5.4.1. Reaction Time Investigation

The formation mechanism of FePt NPs in $[P_{66614}][NTf_2]$ was investigated by extracting aliquots at different reaction temperatures and times following a pattern as illustrated in Figure 5.5A. XRD, TEM and SQUID were then systematically used to gain insight into the formation mechanism of FePt NPs in this IL.

Table 5.1 XRD data of FePt NPs synthesized in $[P_{66614}][NTf_2]$ as a solvent. $[Na_2Fe(CO)_4] = [Pt(acac)_2] = 0.05$ M, $[oleylamine]/[Pt(acac)_2] = 8$, $[oleic\ acid]/[Na_2Fe(CO)_4] = 4$. Heat rate $15^\circ C/min$. Aliquots were collected at $300^\circ C$ 0.5 h, 1.0 h, 2.0 h and 3.0 h. 2θ is the position of the (111) peak, a is the lattice constant, D_{XRD} is the crystalline grain size, D_{TEM} is the TEM size in diameter and x is the iron content in Fe_xPt_{1-x} .

Reaction time h	(111) 2θ (degree)	a (Å)	x in Fe_xPt_{1-x} (%)	D_{XRD} (nm)	D_{TEM}^* (nm)
0.5	51.40 ± 0.04	3.866 ± 0.003	42.1 ± 2.1	2.3 ± 0.1	2.6 ± 2.2
1.0	51.34 ± 0.04	3.871 ± 0.003	41.2 ± 2.0	2.2 ± 0.1	2.8 ± 2.4
2.0	51.45 ± 0.04	3.863 ± 0.003	42.9 ± 2.3	2.7 ± 0.1	4.1 ± 4.6
3.0	51.37 ± 0.03	3.868 ± 0.002	41.7 ± 1.5	2.8 ± 0.1	3.9 ± 4.7

*TEM size distribution was quantified with Image J software by counting over 100 NPs as shown in corresponding TEM images (Figure 5.6C-F).

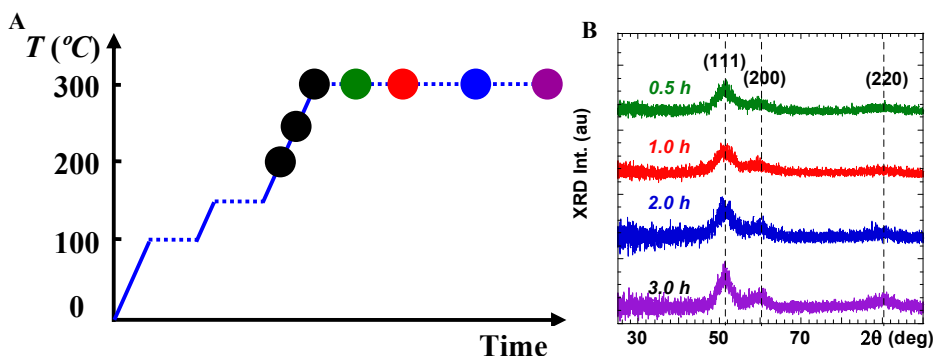


Figure 5.5 A schematic drawing (A) displays the reaction time investigation. The temperatures and reaction times at which aliquots are extracted for investigation are labeled with “●”, their corresponding TEM images are presented in Figure 5.6. XRD patterns (B) of FePt NPs synthesized at $\sim 300^\circ C$ in $[P_{66614}][NTf_2]$ with varied reaction times.

Simultaneous monitoring of the NPs crystallinity above $300^\circ C$ was characterized by XRD (Figure 5.5 and Table 5.1). The formation *fcc*-FePt is confirmed by the peaks lying around $\sim 51^\circ$, 60° and 89° corresponding to *fcc*-FePt (111), (200) and (220) diffractions, respectively (Figure 5.5B). The (200), (220) peaks of 0.5 and 1.0 h samples are too weak to be identified, due to the small NPs size. The data indicate that within experimental uncertainties the NPs composition remains constant at $\sim 40\%$ Fe through out the whole synthesis. D_{XRD} shows size increases after 1 h reaction time at $300^\circ C$ (Table 5.1).

To gain more insight into the FePt NPs formation in ILs, the evolution of NPs at temperatures starting from 200 °C was analyzed by TEM as presented in Figure 5.6.

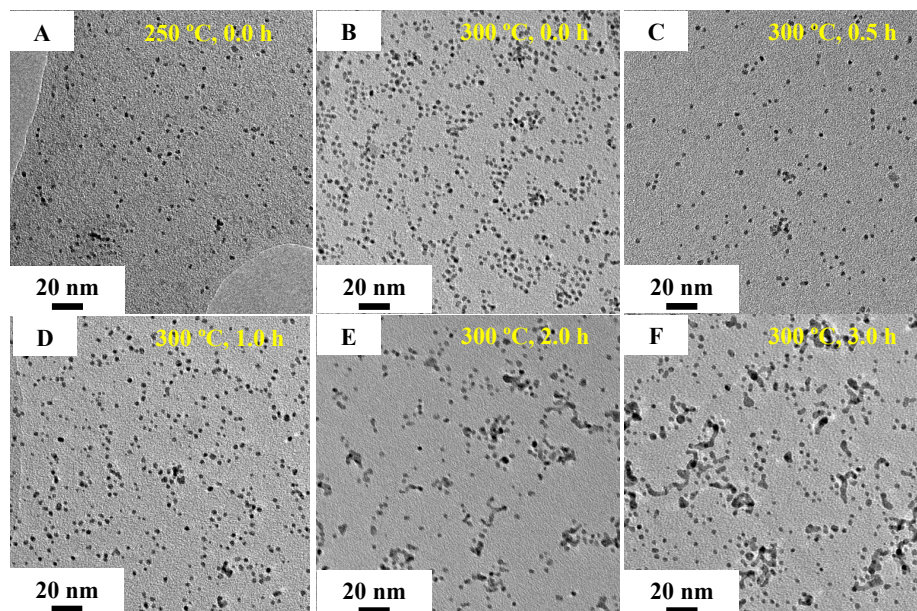


Figure 5.6 TEM images of samples were collected during FePt NPs synthesis in $[P_{66614}][NTf_2]$ as a solvent at 250 °C, 0.0 h (A), 300 °C, 0.0 h (B), 300 °C, 0.5 h (C), 300 °C, 1h (D), 300 °C, 2 h (E), and 300 °C, 3 h (F), as illustrated in Figure 5.5A. $[Na_2Fe(CO)_4] = [Pt(acac)_2] = 0.05$ M, $[oleylamine]/[Pt(acac)_2] = 8$, $[oleic\ acid]/[Na_2Fe(CO)_4] = 4$, heat rate 15 °C/min.

At the 200 °C step, TEM shows mainly the formation of nuclei (data is not shown). The presence of well dispersed NPs begun to be observed at 250 °C (Figure 5.6A). Once the temperature reaches 300 °C, NPs apparently fuse with one another and longer reaction time leads to increased population of fused NPs. At 300 °C, 0.0 h (Figure 5.6B), 0.5 h (Figure 5.6C) and 1.0 h (Figure 5.6D), the majority of NPs are well dispersed, accompanied with a small population of fused NPs. However, significant amounts of sintered NPs started to be observed when the reaction time is longer than 1.0 h (Figure 5.6E and F), as illustrated by the significantly increased TEM size of NPs (D_{TEM}) and polydispersity index (i.e. deviation from the average diameter value) as shown in Table 5.1. D_{TEM} was determined with the assistance of Image J software. This size analysis method is

mostly suitable for spherical shaped NPs, while the NPs fusion and aggregation can still be observed in the change of polydispersity index, which was increased from 2.2 to 4.7 nm when the reaction was extended from 30 min to 3 h (Table 5.1).

The evolution of the magnetic properties above 300 °C are presented in Figure 5.7 with the top row displaying ZFC-FC curves while the bottom row shows hysteresis curves obtained at 2 K. The magnetic characterization is summarized in Table 5.2.

Table 5.2 Magnetic properties of the FePt NPs synthesized in $[P_{66614}][NTf_2]$ as a solvent. T_b is the blocking temperature, T_{irr} is the temperature when the remanence and the coercivity of the largest NPs vanish, H_c is the coercivity, M_s the magnetization at saturation and M_r the remanent magnetization.

Reaction time h	T_b (T_{irr}) K	H_c kOe	M_s emu/g	M_r emu/g
0.5	20 (185)	3.2	12.2 ± 1.2	5.5 ± 0.6
1.0	20 (185)	3.3	13.2 ± 1.3	5.9 ± 0.6
2.0	20 (256)	2.4	14.2 ± 1.4	6.0 ± 0.6
3.0	120 (275)	1.4	11.6 ± 1.2	5.2 ± 0.5

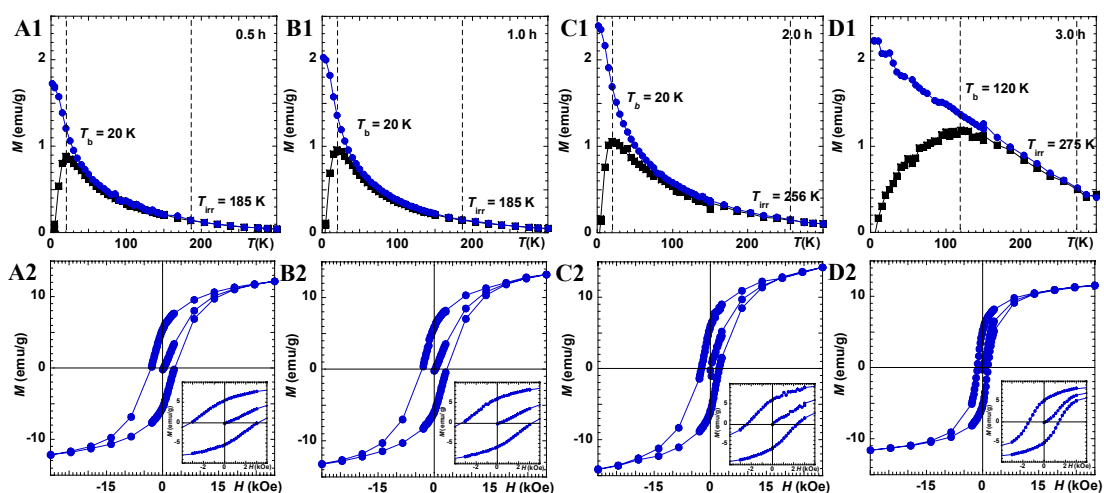


Figure 5.7 SQUID characterization of FePt NPs synthesized in $[P_{66614}][NTf_2]$ as a solvent, at 300 °C 0.5 h (A1-2), 1.0 h (B1-2), 2 h (C1-2) and 3 h (D1-2). ZFC-FC magnetization curves obtained in a magnetic field of 100 Oe (top row), and hysteresis loops at 2 K (bottom row). The inserts zoom in the hysteresis loops between -4 to 4 kOe.

There is no variation of T_b values from the 0.5 h sample to the 2.0 h sample (Figure 5.7A1-C1). The T_b is small, ~ 20 K, which is consistent with the small size of NPs ~ 2 nm. In contrast, the 3.0 h sample has a higher T_b of 120 K (Figure 5.7D1), which could be attributed to better NPs crystallinity because of the longer heating time or an increased population of the large size NPs. All the samples have a much larger T_{irr} than T_b which suggests a broad size distribution. Moreover, T_{irr} increases with increasing heating time which also suggests larger size NPs.

The 0.5 and the 1.0 h samples have H_c of ~ 3.3 kOe, which are close to the literature values.⁸ Compared to NPs synthesized within 1.0 h, the H_c of the 2.0 h and 3.0 h samples tend to decrease. This behavior of the coercivity may be caused by a multidomain structure of those fused NPs which was also observed on the 2.0 h sample (Figure 5.7C2), as intergranular exchange couple leads to a reduction of magnetocrystalline anisotropy.³² This would be consistent with D_{XRD} which shows no variation with synthetic time. The reduced coercivity may also be attributed to the magnetic dipole coupling between nanocrystals.³³⁻³⁵ When preparing NPs samples for the SQUID measurements, the NPs were dispersed in Poly(methyl methacrylate) (PMMA) matrix to reduce to the magnetic dipole coupling as much as possible. However, the fused NPs obtained after 3 h synthesis may still induce some the magnetic dipole coupling, which could reduce the coercivity and also lead to the constricted hysteresis loops, see inserts in Figure 5.7A2 vs. Figure 5.7D2.

In summary, the reaction time investigation experiment suggests a FePt NPs growth mechanism in ILs, which can be summarized as follows:

- i) The nucleation starts at ~ 200 °C.
- ii) NPs form rapidly at $\sim 200 - 250$ °C. Approximately 2 nm crystallite size NPs without significant fusion were obtained at 300 °C within 1.0 h.

- iii) NPs grow in a diffusion manner at 300 °C. Significant aggregation can be observed after 1 h reaction time at 300 °C.

The nucleation temperature in $\text{Na}_2\text{Fe}(\text{CO})_4$ / $\text{Pt}(\text{acac})_2$ / $[\text{P}_{66614}][\text{NTf}_2]$ system is lower than $\text{Fe}(\text{OEt})_3$ / $\text{Pt}(\text{acac})_2$ / octyl ether system,¹³ in which the nucleation takes place at 250 to 297 °C. The fast nucleation contributes to relative small NPs size obtained in $[\text{P}_{66614}][\text{NTf}_2]$. The fast nucleation rate maybe attributed to three factors:

- i) The relatively low solubility of Fe, Pt/ligands complexes in ILs may lead to a faster nucleation rate. Though the four long alkyl chains on $[\text{P}_{66614}]$ ion would be expected to provide enough hydrophobicity, after all $[\text{P}_{66614}][\text{NTf}_2]$ is a salt, its polarity may cause lower solvation of Fe, Pt/ligands complexes than in other organic solvents like benzyl ether. As a consequence, it would lead to a higher degree of supersaturation of complexes in ILs, therefore faster nucleation of FePt NPs, thus smaller NPs size.
- ii) In contrast to $\text{Fe}(\text{OEt})_3$ / $\text{Pt}(\text{acac})_2$ system,¹³ the reaction of $\text{Na}_2\text{Fe}(\text{CO})_4$ with $\text{Pt}(\text{acac})_2$ may accelerate the generation of zero-valent metal atoms which consequently leads to faster nucleation rate.
- iii) It was also claimed that low surface tension of ILs could lead to high nucleation rate, therefore very small NPs are generated.³⁶ However, it is noticeable that the authors did not provide information such as in which system small NPs generation was observed. There is also very limited ILs surface tension information has been reported in the literature, making it difficult to draw a solid conclusion when commenting on the surface tension of ILs.

After nucleation, the NPs appear to grow in a diffusion manner above 300 °C with increasing reaction time. In order to obtain well dispersed NPs, it is crucial to

confine the heat time within 1 h above 300 °C.

5.4.2. NPs Size Tuning

Based on the NPs nucleation and growth mechanism as presented in Section 5.2, two strategies are often applied to obtain larger size NPs:

- i) Reduce the number of nuclei at the nucleation stage. When the total amount of precursors is certain, fewer nuclei will lead to larger size NPs. By applying a slower heating rate or increasing the ligand to precursor ratio, a slower nucleation rate can be expected.⁵ In addition, using a smaller precursor concentration can also lead to a slower nucleation rate.^{5, 13, 37} However, when adjusting the concentration of precursors, it should be noted that if the precursors concentration is too low, there will be not enough precursors to allow NPs to grow to large.
- ii) Feed the NPs with more building monomers while they are at the growth stage. This can be achieved by an injection of additional precursors into NPs seeds.

In this study, reaction parameters such as heating rate, ligands to precursors ratio and additional precursors injection were investigated to further explore this IL based system and identify differences with more traditional solvents. In addition, all the syntheses were carried out at 300 °C for a 1 h time period to reduce the risk of NPs aggregation.

In contrast to benzyl ether as a solvent,⁵ XRD and TEM results that the heating rate only has a small impact on NPs size in $[P_{66614}][NTf_2]$ system. By decreasing the heating rate from 15 to 5 °C/min, the XRD size was increased by ~20% (Figure 5.8 and Table 5.3). This is shown in the increase of average TEM size from 2.8 nm to 3.2 nm (Figure 5.8A2-3 and Table 5.3).

Table 5.3 FePt NPs synthesized in $[P_{66614}][NTf_2]$ as a solvent with a heat rate of 5 °C/min. $Na_2Fe(CO)_4/Pt(acac)_2$ oleylamine (OAM)/oleic acid (OA) were used as precursors and ligands respectively. 2θ , a , D_{XRD} , D_{TEM} and x are defined in Table 5.1.

Sample	[Fe]=[Pt]	[OAM]/[Pt]	[OA]/[Fe]	2θ of (111)	a	x in Fe_xPt_{1-x}	D_{XRD}	D_{TEM}
	M			(degree)	(Å)	(%)	(nm)	(nm)
A	0.05	8	4	51.30±0.04	3.873±0.003	40.5±2.0	2.5±0.1	3.2±3.8
B	0.05	24	12	51.55±0.01	3.856±0.001	44.7±0.6	4.0±0.1	--
C	0.025	16	8	51.36±0.04	3.870±0.003	41.2±2.2	2.7±0.1	3.3±2.9
D*	injection	8	4	51.26±0.03	3.876±0.002	39.7±1.6	3.2±0.1	4.4±4.8

*Sample D: Injection of Fe and Pt precursor at 300 °C.

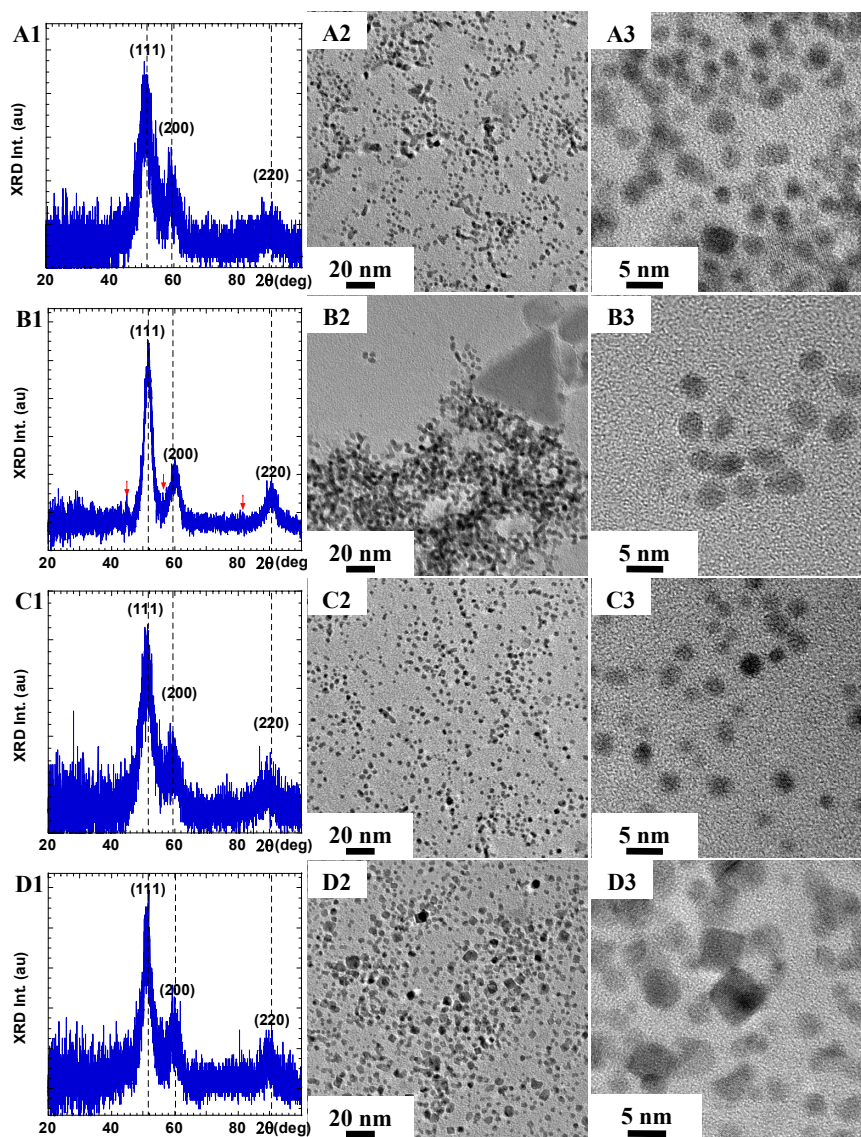


Figure 5.8 XRD patterns (1) and TEM images (2-3) of FePt NPs obtained with the experimental parameters presented in Table 5.3.

Slower than 5 °C/min heating rate was not applied, because competition between the nucleation and the growth may take place which would lead to smaller NPs. For instance, it is reported that the size of NPs was decreased from 8 to 5 nm when the heating rate decreased from 5 to 1 °C/min in a system composed of $\text{Fe}(\text{CO})_5/\text{Pt}(\text{acac})_2/\text{benzyl ether}$.⁵ In addition, while the size of NPs is increased, the slower heating rate induces aggregation and fusion of the NPs (Figure 5.8A2-A3), because of the relative extended heating time.

While the heating rate is shown to have only a small impact on NPs size, adjusting the ligand to precursor molar ratio was demonstrated to be a more efficient way to tune the NPs size in the present reaction system. Indeed, the XRD crystal size was increased by 85% to 4.0 nm, when the ligand to precursor molar ratio was increased by a factor of 4. However, the trace of Fe_3O_4 was also detected by XRD. This is suggested by the 3 peaks lying at $\sim 45^\circ$, $\sim 55^\circ$ and $\sim 82^\circ$ corresponding to Fe_3O_4 (311), (400) and (440) diffraction, as indicated by arrows in Figure 5.8A2. Fe_3O_4 species are present as triangular, lozenge shapes as indicated by TEM (Figure 5.8B2). Because of the aggregation of NPs, a TEM size distribution could not be calculated (Figure 5.8B2 and B3).

Decreasing the precursor concentration did not lead to larger size NPs. To have a constant ligand concentration to compare with the initial experiments, the molar ratio of oleyl amine to $\text{Pt}(\text{acac})_2$ and of oleic acid to $\text{Na}_2\text{Fe}(\text{CO})_4$ were multiplied by two, led to 16 and 8 respectively. XRD (Table 5.3) and TEM (Figure 5.8C) data suggest NPs size constant within the experimental uncertainty.

Injection of additional precursors was also applied while monitoring the size of the NPs. This was carried out after the synthetic solution remained at 300 °C for 0.5 h and by using the NPs as nuclei while feeding their growth with additional

drop-wise injection of precursors. XRD showed an average crystal size about 3.2 nm, increased by ~45% (Table 5.3). The average TEM size is also increased by ~42% up to 4.4 nm (Table 5.3 and Figure 5.8D2-D3). This is demonstrated to be the most efficient way to increase NPs size in present reaction system, even though there is also presence of small size NPs which could be attributed to the competition between the nucleation and growth.

Comparing to the literature, tuning the NPs size through heating rate and ligand to precursor ratio in $\text{Fe}(\text{CO})_5/\text{Pt}(\text{acac})_2/\text{benzyl ether}$ system seems to be more efficient than with ILs. It was reported that the NPs size was increased from 6 to 8 nm, as heating rate was decreased from 15 to 5 °C/min. The size of NPs was also increased from 5 to 9 nm, when the ligand to precursor ratio increased from 5 to 10.⁵ In this study, it seems more difficult to achieve efficient size control over $\text{Na}_2\text{Fe}(\text{CO})_4/\text{Pt}(\text{acac})_2 / [\text{P}_{66614}][\text{NTf}_2]$ system, as compared to the $\text{Fe}(\text{CO})_5/\text{Pt}(\text{acac})_2/\text{benzyl ether}$ system. It could probably be due to a fast nucleation rate attributed to the reactivity of Fe^{2-} with Pt^{2+} precursors and a relatively low solubility of metal-ligand complexes in ILs. In addition, the ILs anions $[\text{NTf}_2]^-$ which bond to NPs surface strongly could also prevent further growth of FePt NPs.

5.4.3. Direct *fct*-FePt Synthesis

After the study of *fcc*-FePt synthesis in ILs at 300 °C, the possibility of direct *fct*-FePt synthesis by using ILs at 340 °C is further demonstrated. The formation of *fcc*-FePt in $[\text{P}_{66614}][\text{NTf}_2]$ is indicated by the presence of two peaks in XRD, at around 29° and 41° corresponding to *fct*-FePt (001) and (110) diffractions, respectively (Table 5.4 and Figure 5.9A1).

Table 5.4 XRD data of FePt NPs at 340 °C for 1 h, with [OAM]/[Pt] = 8 and [OA]/[Fe] = 4, heating rate 15 °C/min. D_{XRD} is the crystalline grain size, x is the iron content in $\text{Fe}_x\text{Pt}_{1-x}$ and S is the *fct* crystalline order parameter.

Sample	Fe precursor/Solvent	(001)	(110)	(111)	D_{XRD} (nm)	S (-)
		2θ (deg.)	2θ (deg.)	2θ (deg.)		
A	$\text{Na}_2\text{Fe}(\text{CO})_4$ / $[\text{P}_{66614}][\text{NTf}_2]$	29.2 ± 0.8	42.2 ± 0.8	51.48 ± 0.02	7.0 ± 0.2	0.59
B	$\text{Fe}(\text{CO})_5$ / $[\text{P}_{66614}][\text{NTf}_2]$	29.0 ± 0.5	41.7 ± 0.5	51.41 ± 0.01	10.3 ± 0.2	0.50
C	$\text{Na}_2\text{Fe}(\text{CO})_4$ / $[\text{HMI}][\text{NTf}_2]$	29.5 ± 0.5	41.5 ± 0.5	51.44 ± 0.01	11.9 ± 0.6	0.63

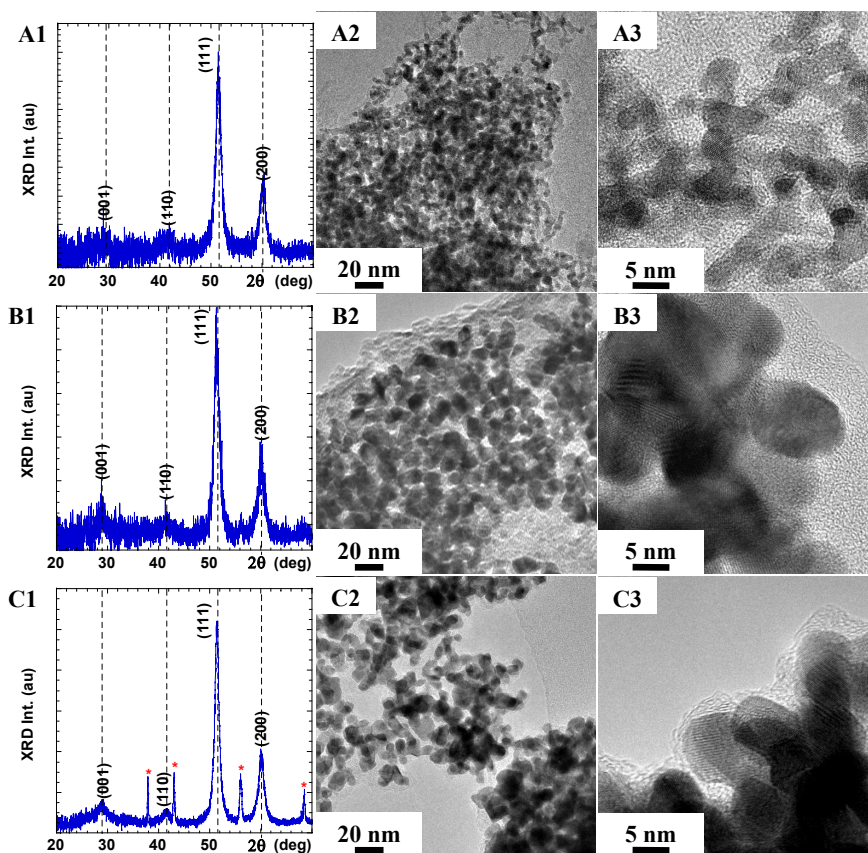


Figure 5.9 XRD patterns (1) and TEM images (2-3) of FePt NPs synthesized with the experimental parameters described in Table 5.4.

The *fct* order parameter (S) was found to be ~ 0.59 (Table 5.4).⁹ It is noticeable that similar results were obtained with different iron precursors and ILs. For instance, *fct*-FePt is also formed when using the conventional iron precursor $\text{Fe}(\text{CO})_5$ (Figure 5.9B1 and Table 5.4), and a different IL i.e. $[\text{HMI}][\text{NTf}_2]$ comprised by a same anion as $[\text{P}_{66614}][\text{NTf}_2]$ (Table 5.4 and Figure 5.9B2). It is noticeable NPs are

agglomerated when syntheses were carried out at 340 °C as indicated by TEM (Figure 5.9 Column 2 and 3). In addition, XRD indicated there is formation of Fe_7S_8 in the $[\text{HMI}][\text{NTf}_2]$ sample (Figure 5.9C1), the diffraction peaks are labelled with stars.

Table 5.5 Magnetic characterization of FePt NPs with the experimental parameters described in Figure 5.10: T_b is the blocking temperature, T_{irr} is the temperature when the remanence and the coercivity of the largest NPs vanish, H_c is the coercivity, M_s is the magnetization at saturation and M_r is the remanent magnetization.

Sample	Fe precursor/Solvent	T_b (T_{irr})	H_c		M_s		M_r	
			2K	300K	2K	300K	2K	300K
		(K)	(kOe)		(emu/g)		(emu/g)	
A	$\text{Na}_2\text{Fe}(\text{CO})_4 / [\text{P}_{66614}][\text{NTf}_2]$	165 (270)	2.1	0	16.9	5.9	6.2	0
B	$\text{Fe}(\text{CO})_5 / [\text{P}_{66614}][\text{NTf}_2]$	162 (202)	1.9	0	14.7	7.6	7.4	0
C	$\text{Na}_2\text{Fe}(\text{CO})_4 / [\text{HMI}][\text{NTf}_2]$	260 (320)	1.8	0.06	21.5	12.3	11.6	0.71

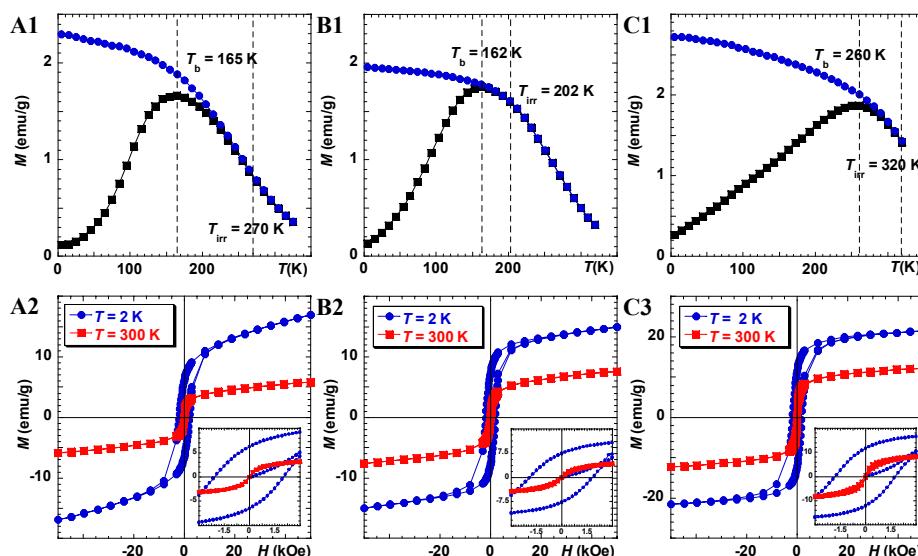


Figure 5.10 SQUID characterization of FePt NPs synthesized with $\text{Na}_2\text{Fe}(\text{CO})_4/\text{Pt}(\text{acac})_2/[\text{P}_{66614}][\text{NTf}_2]$ (A), $\text{Fe}(\text{CO})_5/\text{Pt}(\text{acac})_2/[\text{P}_{66614}][\text{NTf}_2]$ (B) and $\text{Na}_2\text{Fe}(\text{CO})_4/\text{Pt}(\text{acac})_2/[\text{HMI}][\text{NTf}_2]$ (C). ZFC-FC curves obtained in a field 100 Oe (1), and hysteresis loop at 2 K (2).

The formation of *fcc*-FePt was associated with a significant T_b enhancement, which is about 8-13 times larger (Figure 5.10) as compared to 300 °C 1.0 h sample

(Figure 5.7). Especially for the [HMI][NTf₂] sample, T_b is ~260 K which is close to room temperature (Figure 5.10C3). Additionally, a H_c of ~60 Oe was observed at 300 K (Figure 5.10C4). T_b was found to be lower than room temperature and could be attributed to four factors:

- i) Surface effects induced by the IL and the ligands lead to the formation of a non-magnetic shell by electron transfer.³⁸⁻⁴¹
- ii) The *fct* phase of the nanocolloids may be too small to provide large enough magneto anisotropy to compensate the thermal agitation at ambient conditions.
- iii) It may be attributed to the NP multidomain structure, as intergranular exchange couple leads to a reduction of magnetocrystalline anisotropy.³²
- iv) The reduced coercivity may also be attributed to the magnetic dipole coupling between nanocrystals.³³⁻³⁵

As discussed in Chapter 3, there are very few examples in the literature of direct *fct* FePt synthesis in solution. It is reported the direct synthesis of FePt NPs that contain a fraction of *fct* phase by preparing the particles in the high-boiling chemical hexadecylamine at ~360 °C with Fe(CO)₅ and Pt(acac)₂.⁴² The formation of *fct*-FePt NPs was also observed by the direct heating of a solution containing Fe(acac)₃ and Pt(acac)₂ dispersed in ethyl glycol or tetraethylene glycol with or without PVP at ~260-300 °C.⁴³⁻⁴⁵ In addition, Howard et al. also reported the possibility of the direct synthesis of partially *fct*-FePt NPs using Na₂Fe(CO)₄ at ~350-389 °C.^{8, 12} Even though the direct synthesis of *fct*-FePt have been reported, it is noticeable that the origin of *fct*-FePt formation is still poorly understood in all these systems.

In this study, we propose that the formation of *fct*-FePt phase may be attributed to special chemical structure of the anion, i.e. [NTf₂]⁻ which exists both in

[P₆₆₆₁₄][NTf₂] and [HMI][NTf₂] ILs (Figure 5.7A and B). The current hypothesis is that the nitrogen and four oxygens in sulfite could bind to Fe and Pt atoms and hold them together like a claw, thus favoring the formation of *fcc*-FePt phase, where the alternating Fe and Pt atom planes stacked along the (001) direction.

To investigate the role of the anion [NTf₂]⁻ for the formation of *fcc*-FePt, a reference synthesis was first completed under the same experimental conditions, but replacing the IL with a conventional high-boiling chemical tetracosane (Figure 5.4C). Figure 5.11A2 and A3 show that the NPs are fused to form worm like nanomaterials as indicated by TEM. With regard to the crystal structure, XRD data indicate that within the experimental uncertainty there is no *fcc* FePt presence. The (110) peak which is supposed to lay at ~42° is not visible, while the very weak (001) peak could be guessed at ~29° but with a signal to noise ratio of ~1 making it impossible quantify a potential ordering parameter.

As a next step, a synthesis was carried out in tetracosane at 340 °C with the presence of butyl sulfone (Figure 5.4D). Its chemical structure has two oxygens connected by a sulfite, chosen to mimic half NTf₂ molecule. A molar ratio of butyl sulfone to precursors of 13.5 was used, based on the NTf₂ to precursors molar ratio in the standard synthesis in ILs. TEM shows that the NPs are aggregated and about ~10 nm in diameter (Figure 5.11B1 to B2). XRD indicates only formation of *fcc* FePt together with other impurities which could not be matched with any material in the PDF library. This however may underline the crucial role of the nitrogen in the NTf₂ structure, which acts as a bridge connecting two sulfone groups. To further explore this system, LiNTf₂ (Figure 5.4E), which has the same anion as [P₆₆₆₁₄][NTf₂] and [HMI][NTf₂], was selected to be added into the reaction system. Again, the data indicates no *fcc*-FePt formation, as implied by the absence of two superlattice peaks at ~29° and ~42° (Figure 5.11C1). This could be

attributed to the relatively poor thermal stability of LiNTf_2 , due to the formation of LiF as detected by XRD (Figure 5.11C1).

Table 5.6 XRD data of FePt NPs synthesized using tetracosane at 340 °C for 1 h with $[\text{OAM}]/[\text{Pt}] = 8$ and $[\text{OA}]/[\text{Fe}] = 4$, heating rate 15 °C/min. For Sample A, no other additives were added, Sample B: butyl sulfone was introduced at $[\text{butyl sulfone}]/[\text{Fe+Pt}]=13.5$ and Sample C: LiNTf_2 was added at $[\text{NTf}_2]/[\text{Fe+Pt}]=13.5$. D_{XRD} is the crystalline grain size.

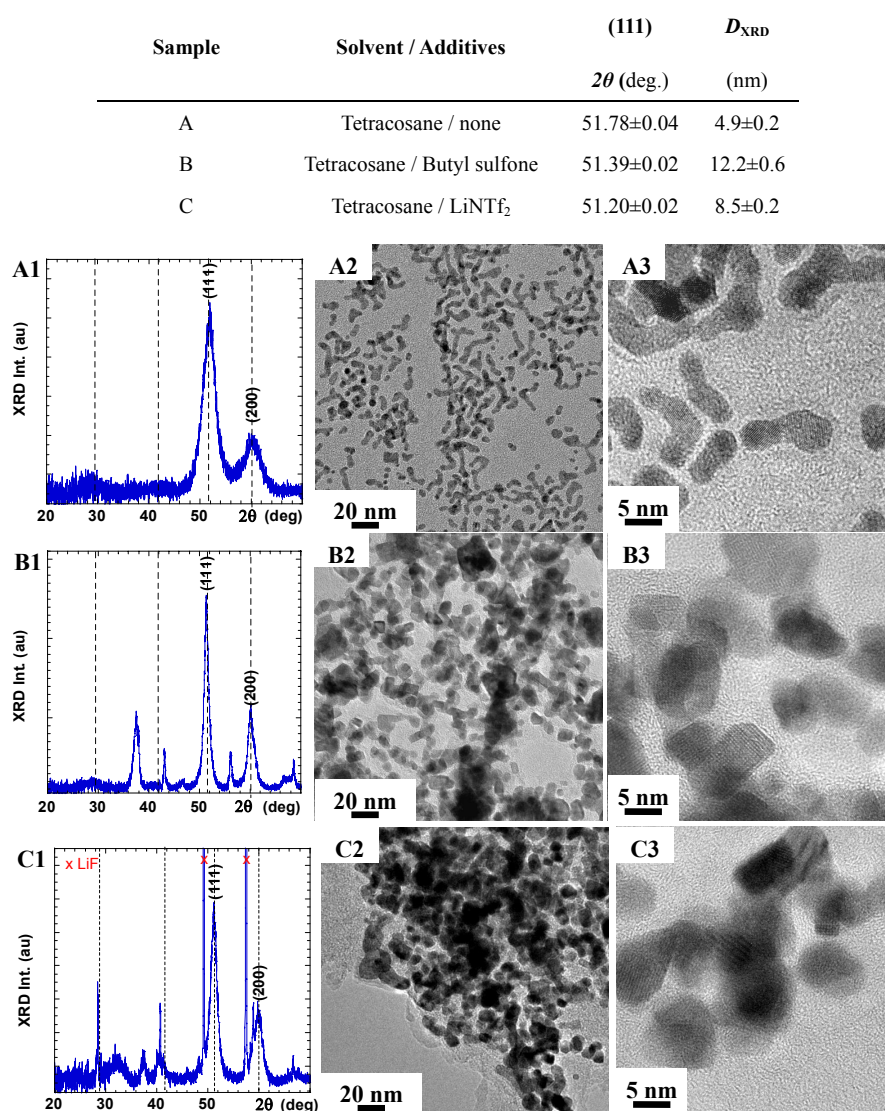


Figure 5.11 XRD patterns (1) and TEM images (2-3) of FePt NPs at 340 °C for 1 h with $[\text{OAM}]/[\text{Pt}] = 8$ and $[\text{OA}]/[\text{Fe}] = 4$, heating rate 15 °C/min. Experiment parameters are described in Table 5.6.

In addition, the limited solubility of LiNTf_2 in the hydrophobic solvent, which likely hinders the interaction between $[\text{NTf}_2]^-$ with metal atoms, could also

contribute to the absence of *fct* FePt. These results could be used to emphasize that each part of the ILs is important. For instance, the presence of an organic counter ion in ILs will provide a better solubility and thermal stability to the NTf₂ anion as compared to a more conventional Li based salt. As a consequence, it will be easier for the [NTf₂]⁻ to coordinate with Fe and Pt atoms in ILs and lead to formation of *fct*-FePt.

5.5. Conclusion

This chapter presents the development of a modified thermal decomposition method for FePt NPs synthesis. In contrast to the synthesis carried out in aqueous media as presented in the Chapter 4, the synthesis was carried out in an organic solvent, benzyl ether, therefore the hydrolysis reaction of iron salt was avoided. In addition, Na₂Fe(CO)₄/Pt(acac)₂ were used as precursors, through the reaction $\text{Fe}^{2+} + \text{Pt}^{2+} \rightarrow \text{Fe} + \text{Pt}$, close to 1:1 ratio stoichiometry *fcc*-FePt NPs can be obtained.

Based on the study of FePt NPs synthesis in benzyl ether, the potential of [P₆₆₆₁₄][NTf₂] as a solvent for FePt NPs synthesis was investigated. Experimental results indicate a faster NPs nucleation in [P₆₆₆₁₄][NTf₂] as compared to conventional organic solvents. Small crystallite size NPs of ~2 nm were obtained at 300 °C, which is smaller than ~5 nm NPs synthesized in benzyl ether. This could be attributed to the lower solubility of metal-ligand complexes in ILs due to the polarity of ILs, which induces a higher supersaturation of metal complexes. Another possibility is that ILs anions which bond strongly on NPs surface could prevent the growth of NPs. In addition, NPs grow in a diffusion manner above 300 °C with increasing reaction time. In order to obtain well dispersed NPs, results suggested it is crucial to confine the heat time to be within 1 h above 300 °C.

To explore further the IL based synthesis and using the size of the NPs as a reference, reaction parameters such as tuning heating rate, ligand to precursor ratio, precursor concentration, additional precursors injection were investigated. It was demonstrated that ~4.0 nm NPs could be obtained by using higher ligand to precursors ratio and additional precursor injection. However, further size increasing was found rather difficult due to the high reactivity of iron precursor, the fast NP nucleation rate in ILs. To obtain larger size NPs, future synthesis should overcome the fast NPs nucleation issue in ILs. Potentially, designing ILs comprised with functional groups capable to bind to metal atoms.

More importantly, this study demonstrates the formation of *fcc*-FePt NPs in [P₆₆₆₁₄][NTf₂] at 340 °C, highlighting the essential role played by the combination of temperature and IL structure. Further study shows that the formation of *fcc*-FePt can also be obtained by using a different precursor Fe(CO)₅, or ILs with same anion like [HMI][NTf₂]. These results lead to the hypothesis that the [NTf₂]⁻ anion triggers the formation of *fcc*-FePt, because of its chemical structure comprised by one nitrogen and four oxygens in a sulfite each of them could bind to Fe and Pt atoms thus holding them together like a claw. Further work is currently carried out in collaboration with computational chemists at the School of Chemistry at St Andrews to gain further insight into *fcc*-FePt formation mechanism in ILs.

These results are very exciting when only very few systems have shown the ability of allowing direct *fcc* formation in solution. However, further work is obviously needed both to obtain well dispersed nanocolloids with controlled morphology and trigger *fcc*-FePt formation in solution synthesis at even lower temperature. This could be achieved by identifying appropriate stabilizers, but primarily the *fcc*-phase formation would need to be fully understood and controlled, a challenge which will require significant experimental work to be combined with

extensive numerical simulations to gain further insight into the interplay between the Fe/Pt precursors, the components of the ILs and the ligands aimed preventing the NPs aggregation. To the best of our knowledge, this ability of ILs to alter NPs crystallinity has not been demonstrated before this work and opens up exciting perspectives as the direct synthesis of *fct*-FePt nanocolloids will find a broad range of applications including data storage, sensors and biomedicine.

References

- (1) LaMer, V. K.; Dinegar, R. H. *J. Am. Chem. Soc.* **1950**, 11, 4847-4854.
- (2) Xia, Y.; Xiong, Y. J.; Lim, B.; Skrabalak, S. E. *Angew. Chem. Int. Edit.* **2009**, 48, 60-103.
- (3) Park, J.; Joo, J.; Kwon, S. G.; Jang, Y.; Hyeon, T. *Angew. Chem. Int. Edit.* **2007**, 46, 4630-4660.
- (4) Chen, M.; Liu, J. P.; Sun, S. *J. Am. Chem. Soc.* **2004**, 126, 8394-8395.
- (5) Nandwana, V.; Elkins, K. E.; Poudyal, N.; Chaubey, G. S.; Yano, K.; Liu, J. P. *J. Phys. Chem. C* **2007**, 111, 4185-4189.
- (6) Lide, D. R.; Weast, R. C.; Company, C. R., *CRC Handbook of Chemistry and Physics*. 83rd ed.; CRC Press: Boca Raton, Fla., 2002.
- (7) Sun, S. H.; Murray, C. B.; Weller, D.; Folks, L.; Moser, A. *Science*. **2000**, 287, 1989-1992.
- (8) Nguyen, H. L.; Howard, L. E. M.; Stinton, G. W.; Giblin, S. R.; Tanner, B. K.; Terry, I.; Hughes, A. K.; Ross, I. M.; Serres, A.; Evans, J. S. O. *Chem Mater*. **2006**, 18, 6414-6424.
- (9) See Appendix for details.
- (10) Lu, A. H.; Salabas, E. L.; Schuth, F. *Angew. Chem. Int. Edit.* **2007**, 46, 1222-1244.
- (11) Skumryev, V.; Stoyanov, S.; Zhang, Y.; Hadjipanayis, G.; Givord, D.; Nogues, J. *Nature*. **2003**, 423, 850-853.
- (12) Howard, L. E. M.; Nguyen, H. L.; Giblin, S. R.; Tanner, B. K.; Terry, I.; Hughes, A. K.; Evans, J. S. O. *J Am Chem Soc.* **2005**, 127, 10140-10141.
- (13) Saita, S.; Maenosono, S. *Chem. Mater*. **2005**, 17, 6624-6634.
- (14) Wang, Y.; Maksimuk, S.; Shen, R.; Yang, H. *Green. Chem.* **2007**, 9, 1051-1056.
- (15) Li, Z. G.; Jia, Z.; Luan, Y. X.; Mu, T. C. *Curr. Opin. Solid. St. M.* **2009**, 12, 1-8.
- (16) Buhler, G.; Zharkouskaya, A.; Feldmann, C. *Solid. State. Sci.* **2008**, 10, 461-465.
- (17) Earle, M. J.; Esperanca, J. M. S. S.; Gilea, M. A.; Lopes, J. N. C.; Rebelo, L. P. N.; Magee, J. W.; Seddon, K. R.; Widegren, J. A. *Nature*. **2006**, 439, 831-834.
- (18) Torimoto, T.; Tsuda, T.; Okazaki, K.; Kuwabata, S. *Adv. Mater*. **2010**, 22, 1196-1221.
- (19) Redel, E.; Walter, M.; Thomann, R.; Vollmer, C.; Hussein, L.; Scherer, H.; Kruger, M.; Janiak, C. *Chem-Eur. J.* **2009**, 15, 10047-10059.
- (20) Zhao, Y.; Cui, G.; Wang, J.; Fan, M. *Inorg.Chem.* **2009**, 48, 10435-10441.
- (21) Redel, E.; Thomann, R.; Janiak, C. *Chem. Commun.* **2008**, 1789-1791.
- (22) Redel, E.; Kramer, J.; Thomann, R.; Janiak, C. *J. Organomet. Chem.*

- 2009**, 694, 1069-1075.
- (23) Wang, Y.; Yang, H. *Chem. Eng. J.* **2009**, 147, 71-78.
- (24) Zhu, H. G.; Huang, J. F.; Pan, Z. W.; Dai, S. *Chem. Mat.* **2006**, 18, 4473-4477.
- (25) Nakashima, T.; Kimizuka, N. *J. Am. Chem. Soc.* **2003**, 125, 6386-6387.
- (26) Wang, Y.; Yang, H. *J. Am. Chem. Soc.* **2005**, 127, 5316-5317.
- (27) Osaka, T.; Hachisu, T.; Sugiyama, A.; Kawakita, I.; Nakanishi, T.; Iida, H. *Chem. Lett.* **2008**, 37, 1034-1035.
- (28) Ma, Z.; Yu, J. H.; Dai, S. *Adv. Mater.* **2010**, 22, 261-285.
- (29) Wang, W. W.; Zhu, Y. J. *Inorg. Chem. Commun.* **2004**, 7, 1003-1005.
- (30) Zhou, X.; Xie, Z. X.; Jiang, Z. Y.; Kuang, Q.; Zhang, S. H.; Xu, T.; Huang, R. B.; Zheng, L. S. *Chem. Commun.* **2005**, 5572-5574.
- (31) Green, M. J. *Mater. Chem.* **2010**, 20, 5797-5809.
- (32) Rong, C. B.; Li, D. R.; Nandwana, V.; Poudyal, N.; Ding, Y.; Wang, Z. L.; Zeng, H.; Liu, J. P. *Adv. Mater.* **2006**, 18, 2984-2988.
- (33) Held, G. A.; Grinstein, G.; Doyle, H.; Sun, S. H.; Murray, C. B. *Phys. Rev. B.* **2001**, 6401, 012408.
- (34) Lee, D. C.; Mikulec, F. V.; Pelaez, J. M.; Koo, B.; Korgel, B. A. *J. Phys. Chem. B.* **2006**, 110, 11160-11166.
- (35) Jeyadevan, B.; Urakawa, K.; Hobo, A.; Chinnasamy, N.; Shinoda, K.; Tohji, K.; Djayaprawira, D. D. J.; Tsunoda, M.; Takahashi, M. *Jpn. J. Appl. Phys. 2.* **2003**, 42, L350-L352.
- (36) Antonietti, M.; Kuang, D. B.; Smarsly, B.; Yong, Z. *Angew. Chem. Int. Edit.* **2004**, 43, 4988-4992.
- (37) Shevchenko, E. V.; Talapin, D. V.; Schnablegger, H.; Kornowski, A.; Festin, O.; Svedlindh, P.; Haase, M.; Weller, H. *J. Am. Chem. Soc.* **2003**, 125, 9090-9101.
- (38) Wu, X. W.; Liu, C.; Li, L.; Jones, P.; Chantrell, R. W.; Weller, D. *J. Appl. Phys.* **2004**, 95, 6810-6812.
- (39) Angappane, S.; Park, J.; Jang, Y. J.; Hyeon, T.; Park, J. G. *J. Phys-Condens. Mat.* **2008**, 20, 295209.
- (40) Tanaka, Y.; Saita, S.; Maenosono, S. *Appl. Phys. Lett.* **2008**, 92, 093117.
- (41) Kittilstved, K. R.; Gamelin, D. R. *J. Am. Chem. Soc.* **2005**, 127, 5292-5293.
- (42) Kang, S. S.; Jia, Z. Y.; Shi, S. F.; Nikles, D. E.; Harrell, J. W. *J. Appl. Phys.* **2005**, 97, 10J318.
- (43) Takahashi, M.; Ogawa, T.; Hasegawa, D.; Jeyadevan, B. *J. Appl. Phys.* **2005**, 97, 10J307.
- (44) Sato, K.; Jeyadevan, B.; Tohji, K. *J. Magn. Magn. Mater.* **2005**, 289, 1-4.
- (45) Iwamoto, T.; Matsumoto, K.; Matsushita, T.; Inokuchi, M.; Toshima, N. *J. Colloid. Interface. Sci.* **2009**, 336, 879-888.

Chapter 6

Biomedical Applications of FePt Nanoparticles

6.1. Introduction

Magnetic resonance imaging (MRI) is widely regarded as a powerful and non-invasive medical imaging tool capable of identifying disease pathways and physiology at the organ, cellular and sub-cellular levels. It relies upon the interaction of the nuclear spin of the hydrogen nucleus in water with an external magnetic field. Spatial information can be obtained by applying additional magnetic field gradients. The signal in an image originates predominately from water, lipids and a number of parameters contribute to image contrast. In medical diagnosis, differentiation between normal and pathological tissue is often desirable, but with the introduction of exogenous contrast agents, this can successfully be achieved. According to their effects on the relaxation rate of water protons in tissue, MRI contrast agents are typically categorized as either longitudinal relaxation time (T_1) agents or transverse relaxation time (T_2) agents. The T_1 -agents (e.g. gadolinium (III) complexes, manganese (II) complexes) accelerate the longitudinal relaxation rates ($1/T_1$) of water protons more than the transverse relaxation rates ($1/T_2$), resulting in an increase of signal intensity

(hyperintensity) on T_1 weighted images thereby exhibiting bright contrast. The T_2 -agents (e.g. superparamagnetic NPs such as Fe_3O_4 , $\gamma\text{-Fe}_2\text{O}_3$, MnFe_2O_4 , FeCo NPs) increase the transverse relaxation rates ($1/T_2$) of water in surrounding tissue resulting in dark contrast (hypointensity) in T_2 weighted images.¹⁻³ A more detailed introduction of the basic principle of MRI and contrast agents is presented in Chapter 2.

Superparamagnetic iron oxide (SPIO) nanoparticles have become an important class of contrast agent since their development and application to the liver almost twenty years ago.^{2, 4} However, they have some limitations which originate from their synthetic processes. They are generally synthesized by a coprecipitation reaction in water at a relatively low temperature, resulting in the formation of polydispersed and poorly crystalline nanoparticles with inferior magnetic properties.^{2, 5-6} Additional disadvantages of SPIO NPs include fast clearance rate by phagocytic cells and hence limited transendothelial passage and tissue penetration.⁷ There is therefore a continuing need to develop clinically viable and targeted MRI contrast agents with improved retention properties. The design and syntheses objectives of new generation of MRI contrast agents will likely focus on strengthening the MRI contrast effect, prolonging intravascular retention, improving tissue delineation.

FePt metallic alloy nanoparticles have emerged as promising candidates for a new generation of magnetic nano-material, thanks to their high Curie temperature and magneto-crystalline anisotropy.⁸ Studies have demonstrated the biomedical potential of FePt NPs, such as magnetic separation,⁹⁻¹⁰ hyperthermic ablation¹¹⁻¹² and as T_2 MRI contrast agents.^{11, 13-15} However, toxicity remains a major concern preventing their use as a bioplatfrom for diagnosis and therapy.¹⁵⁻¹⁷

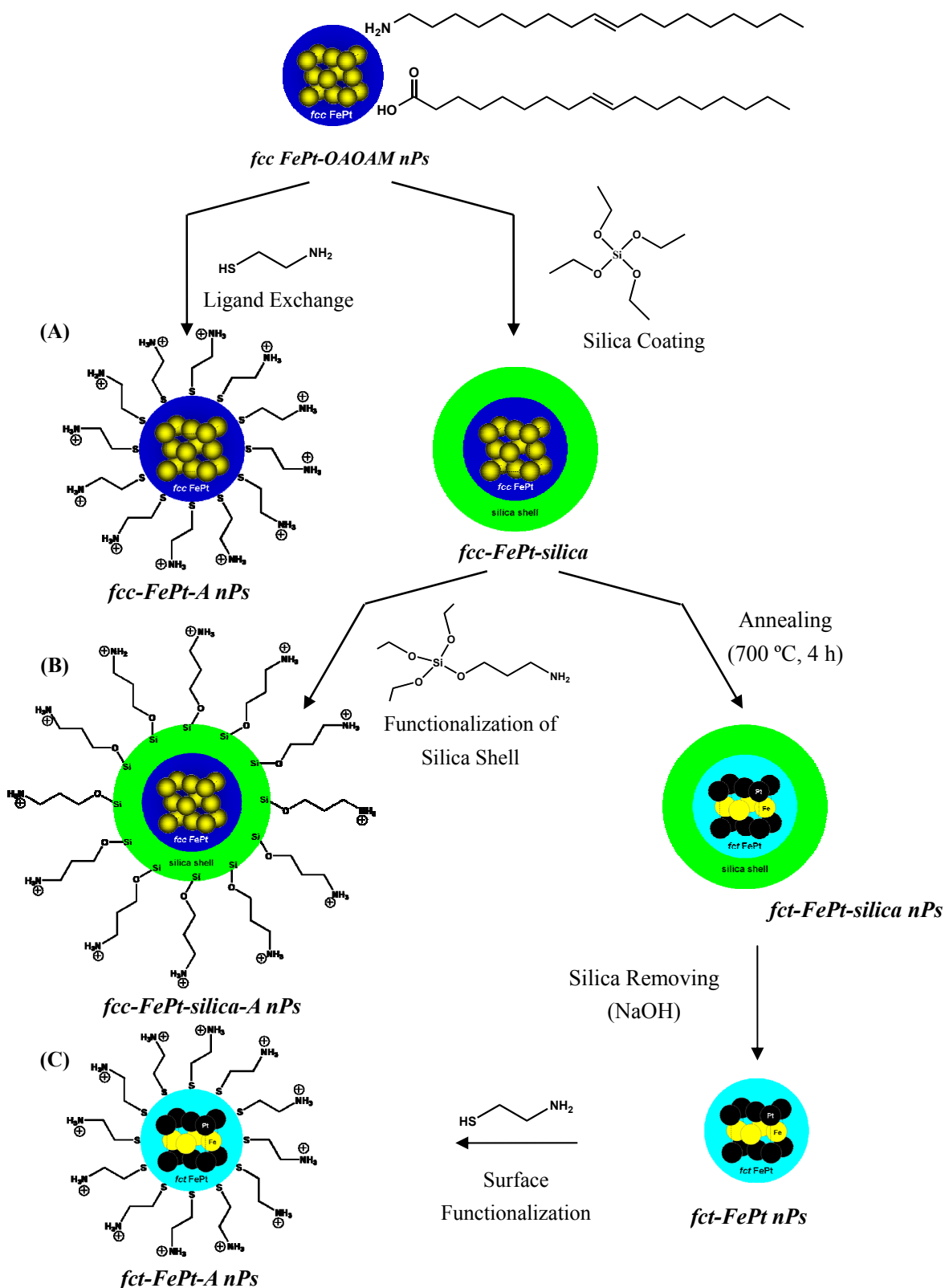


Figure 6.1 Schematic drawing of preparation of *fcc*-FePt-A NPs (A), *fcc*-FePt-silica-A NPs (B), and *fct*-FePt-A NPs (C).

In this study, three biocompatible FePt NPs are designed and fabricated for biomedical applications. Figure 6.1 displays the schematic drawing and preparation of face centered cubic (*fcc*) FePt NPs with cysteamine coating, *fcc*-FePt-A NPs (Figure 6.1A), silica coated *fcc* FePt NPs with further surface functionalization with (3-aminopropyl) triethoxysilane, *fcc*-FePt-silica-A NPs (Figure 6.1B) and face centered tetragonal (*fct*) FePt NPs functionalized with cysteamine, *fct*-FePt-A NPs (Figure 6.1C).

After synthesis, FePt NPs are coated with oleylamine and oleic acid, thus are soluble in organic solvents like hexane and chloroform. Through ligand exchange process, the original oleylamine and oleic acid coating is replaced with cysteamine, due to two aspects: 1) thiol-Pt bond is much stronger than amine-Pt bond;¹⁸ 2) the bonding between ligand and NP is a dynamic process.¹⁹ When a large excess of cysteamine is available, oleic acid can be replaced, even though thiol is known to form weaker bonds with iron than carboxylic acid.¹⁸ Silica coated FePt NPs were produced in a reverse microemulsion through the hydrolysis reaction of saline precursor in a base environment. FePt-silica NPs were further functionalized with (3-aminopropyl) triethoxysilane to obtain *fcc*-FePt-silica-A NPs. *fct* phase FePt NPs were prepared through annealing of silica coated *fcc*-FePt NPs. The *fct*-FePt NP silica coating was removed and cysteamine was utilized to functionalize the NPs to obtain *fct*-FePt-A NPs. The detailed preparation methods are presented in appendix.

Each type of FePt NPs has their own advantages for biomedical applications:

- i) *fcc*-FePt-A NPs: the diameter of the NPs is ~5 nm, which gives them a longer blood half-life since fast uptake by the liver and spleen is avoided, consequently their chances of reaching other targets can be improved.^{2,6} The positive charges on the NPs surface provided by amine groups is used to

develop sufficient electrostatic repulsion to increase water solubility.¹⁸ In addition, the positively charged surface allows increased cell internalization efficiency, and will bind biomedical materials such as DNA and proteins through electrostatic attraction. In addition, amine terminated surface is an ideal platform for conjugation with a large range of biomolecules, including antibodies, proteins, peptides, polysaccharides, and aptamers.^{2, 20-21}

- ii) *fcc*-FePt-silica-A NPs: in addition to organic coating, utilizing biocompatible and inert silica shell is commonly considered as the most attractive approach for engineered NPs. Not only does silica shell serve as protective layer against chemical degradation of the metal core but it also allows easy surface functionalization through the use of alkoxysilanes such as those containing amine or acid groups.
- iii) *fcc*-FePt-A NPs: *fcc* FePt NPs have stronger magnetic properties and higher chemical stability than *fcc* phase FePt making them attractive for medical applications.²²

While it was reported that FePt NPs were able to induce severe cell damage using MTT (3-(4,5-Dimethylthiazol-2-yl)-2,5-diphenyltetrazolium bromide) assay,^{15-16,}²² e.g. phospholipids coated *fcc*-FePt NPs showed 50% cell death at ~7,8 µg/mL,²² no significant *fcc*-FePt-A NPs cytotoxicity was detected at concentrations lower than 30 µg/mL by using MTS ((3-(4,5-dimethylthiazol-2-yl)-5-(3-carboxymethoxyphenyl)-2-(4-sulfophenyl)-2H-tetrazolium)) assay in the work presented in this chapter. MTS assay is an updated version of MTT assay and has the advantage of being soluble hence no solubilisation step is required. Furthermore, the first data on cysteamine functionalized FePt NPs cellular uptake mechanisms and a 6-fold increase in the FePt-based T_2 contrast properties compared to those of clinical iron oxide NPs were reported in this study. The relationship between the MRI contrast properties and the NPs' architecture was explored and rationalized

as the basis for the design of NPs as enhanced MRI contrast agents. Finally, the first observations of cellular and *in vivo* MR imaging with FePt NPs was presented.²³ These results open the way for several applications of FePt NPs, such as regenerative medicine and stem cell therapy, in addition to enhanced MR diagnostic imaging, thus providing a platform to develop novel diagnostic and therapeutic agents.

6.2. Experimental Results and Discussion

6.2.1. FePt NPs Characterization

6.2.1.1. FTIR

After synthesis, FePt NPs are capped with oleic acid and oleylamine ligands and are only soluble in organic solvents like hexane. Through ligand exchange process,²⁴ oleic acid and oleylamine are replaced by cysteamine and FePt NPs bound with cysteamine become water soluble. Figure 6.2 provides a straightforward illustration of the effectiveness of the ligand exchange protocol.

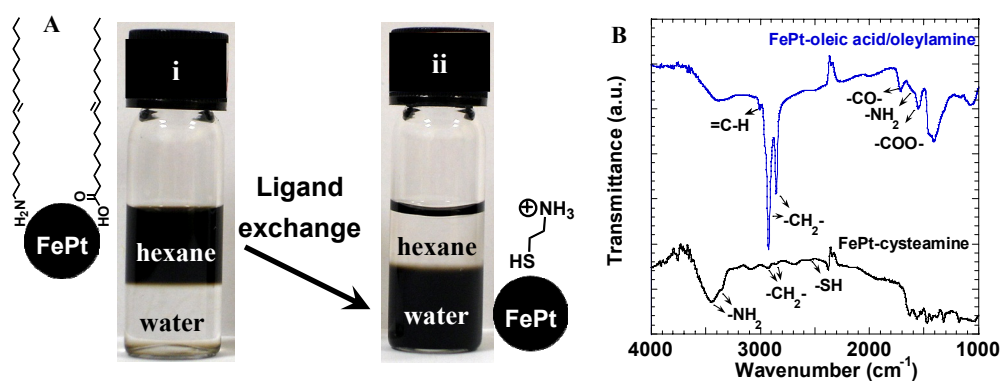


Figure 6.2 Chemical structure of the ligands and photographs (A) of FePt NPs dispersions in hexane or water phase: oleic acid and oleylamine capped FePt NPs (i), and cysteamine capped FePt (ii). FTIR spectra (B) of as-synthesized NPs coated with oleic acid and oleylamine (top) and cysteamine (bottom) after ligand exchange. (Reprinted with permission from ⁽²³⁾. Copyright 2010 American Chemical Society.)

Hexane and water are not miscible, and water which is denser (1.0 g/mL vs 0.7 g/mL) lies beneath the hexane phase. FePt NPs with oleic acid and oleylamine coating are soluble in hexane therefore manifest a black colour to the upper phase while the deionized water remains colourless (Figure 6.2A-i). Figure 6.2A-ii presents the cysteamine capped FePt NPs which are soluble in deionized water leading the lower phase to be black whilst the upper hexane phase remains transparent. After having replaced oleic acid and oleylamine with cysteamine, the NPs are soluble in water solution and stable for more than 8 months.

The efficiency of ligand exchange was further confirmed by Fourier transform infrared spectroscopy (FTIR). The FTIR spectra of NPs before and after ligand exchange are shown in Figure 6.2B, with all characteristic transmission peaks labelled and matching the literature values.²⁵ The upper spectra in Figure 6.2B is characteristic of the NPs coated with oleic acid and oleylamine. The peaks at 1552 and 1713 cm^{-1} can be assigned to the bidentate ($-\text{COO}-$) and monodentate ($-\text{CO}-$) modes of oleic acid binding. The shoulder at 1595 cm^{-1} is due to the scissoring mode of the molecularly bonded oleylamine. The two peaks at 2854 and 2924 cm^{-1} correspond to the symmetric and asymmetric C-H stretching modes of the oleyl group. The peak at 3005 cm^{-1} is characteristic of the stretching of $=\text{C}-\text{H}$.²⁵

The original oleic acid and oleylamine coating of the FePt NPs surface was replaced by cysteamine through the ligand exchange protocol and demonstrated by the bottom FTIR spectra in Figure 6.2B characterised by

- i) the absence of $-\text{COO}-$ and $-\text{CO}-$, $=\text{C}-\text{H}$ peaks, and
- ii) the dramatic decrease of the C-H stretching transmission mode. The shoulder at 2560 cm^{-1} is associated with $-\text{SH}$,²⁶ while the peaks at 3350 and 3448 cm^{-1} are consistent with the $-\text{NH}_2$ end group of the cysteamine.²⁷

6.2.1.2. TEM

Figure 6.3 shows schematic structure and TEM, XRD and SQUID characterization of Feridex NPs (Column A), face centered cubic (*fcc*) FePt NPs coated with cysteamine (*fcc*-FePt-A) (Column B), silica coated *fcc*-FePt NPs further surface functionalized with (3-aminopropyl) triethoxysilane (*fcc*-FePt-silica-A) (Column C) and face centered tetragonal FePt NPs functionalized with cysteamine (*fcc*-FePt-A) (Column D).

Feridex is a clinical iron oxide NP coated with dextran (Figure 6.3A1). In agreement with published literature,⁵ TEM revealed that the commercial iron oxide NP samples (Figure 6.3A2) are composed of aggregated crystals of approximately 5 nm in diameter, embedded in an organic coating. These aggregates have a size distribution ranging from 20 nm to over 50 nm. In contrast, the *fcc*-FePt-A NPs (Figure 6.3B1) are well dispersed with diameters of ~5 nm (Figure 6.3B2). The *fcc*-FePt-silica-A (Figure 6.3C1) NPs are coated with a silica shell of ~17 nm in thickness (Figure 6.3C2). It should be noted that, careful control of the experimental parameters such as NP and TEOS concentrations prevented the formation of blank silica NPs without any FePt. Such silica shell prevented sintering of the NPs during the annealing process allowing *fcc* to *fcc* phase transition. The size of *fcc*-FePt-A (Figure 6.3D1) is ~10 nm, slightly larger than *fcc*-FePt-A NPs (Figure 6.3D2).

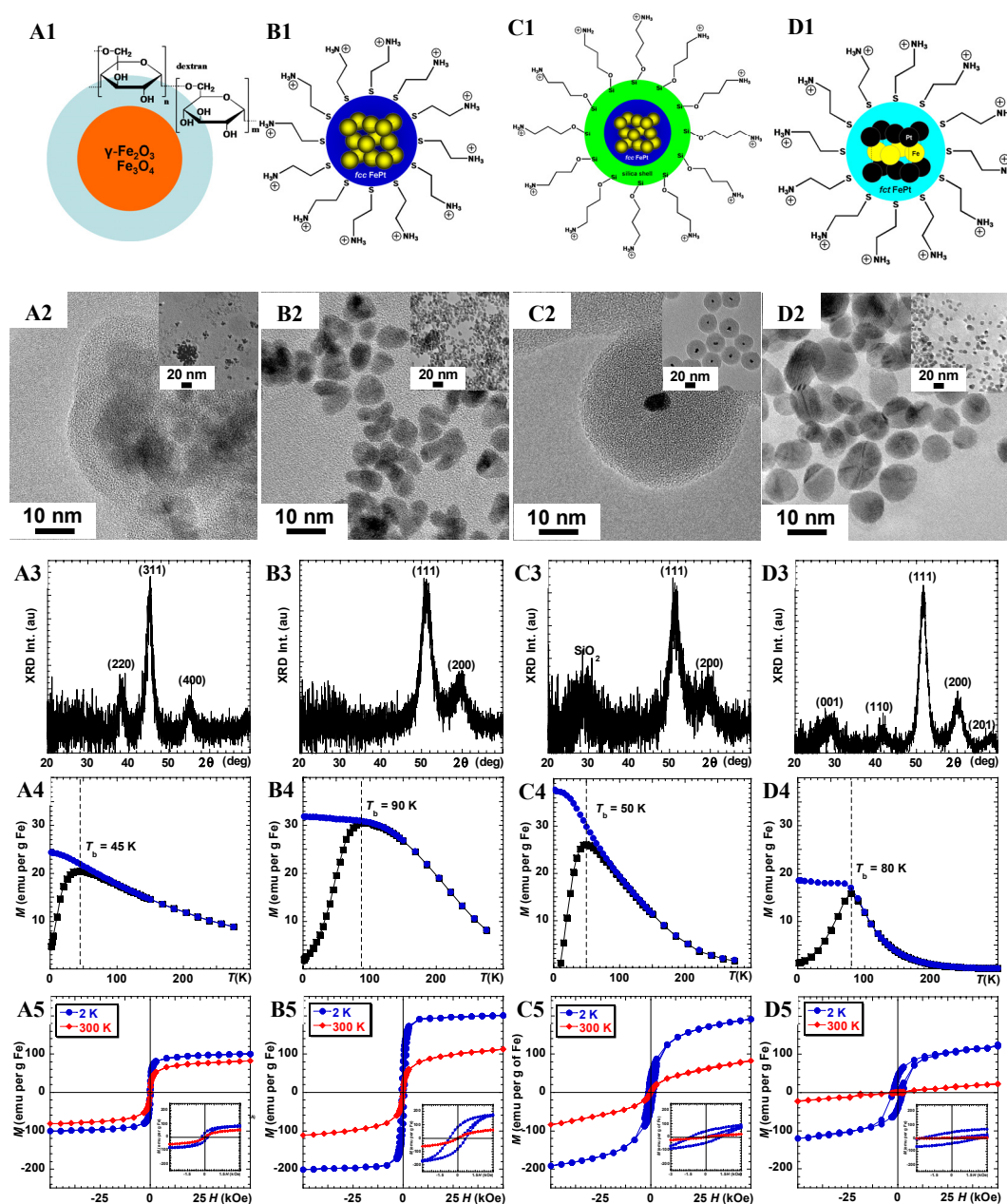


Figure 6.3 Schematic representation, TEM images, XRD pattern, ZFC-FC and hysteresis curves of Feridex (A1-5), *fcc*-FePt-A NPs (B1-5), *fcc*-FePt-silica-A NPs (C1-5), *fcc*-FePt-A NPs (D1-5). (Reprinted in part with permission from ⁽²³⁾. Copyright 2010 American Chemical Society.)

6.2.1.3. XRD

XRD pattern of the Feridex iron oxide confirms the presence of magnetite (Fe_3O_4),

the broad peaks at 38° , 45° , 55° corresponding to (220), (311), (400) peaks, respectively (Figure 6.3A3). Figure 6.3B3-C3 show peaks around 51° and 60° characteristic of *fcc*-FePt (111) and (200) peaks, respectively. The (111) peak position suggests a NP composition of 40 - 45% of Fe (Table 6.1).²⁴ For the silica coated NPs, SiO_2 is observed at $\sim 28^\circ$ (Figure 6.3C3). The crystal size is ~ 3.6 nm in diameter for *fcc*-FePt-A and *fcc*-FePt-silica-A NPs (Table 6.1). After annealing, *fcc* crystal phase is observed around 29° , 41° and 68° corresponding to (001), (110) and (201) *fcc*-FePt peaks, respectively (Figure 6.3D3). The resulting size and *fcc* order parameter are 6 nm in diameter and ~ 0.7 respectively (Table 6.1).²⁴

6.2.1.4. SQUID

Zero field cooling and field cooling (ZFC-FC) of Feridex samples highlight a 45 K blocking temperature (T_b , Figure 6.3A4). At 2 K, i.e. lower than T_b , Feridex hysteresis loop measurements display ferrimagnetic behaviour with a small coercivity value of 300 Oe and a saturation moment (M_s) of 101 emu/g of Fe. At 300 K, Feridex is superparamagnetic with no coercivity (Figure 6.3A5). The M_s is 82 emu/g of Fe, in agreement with literature values.⁵⁻⁶ The *fcc*-FePt-A NPs have a higher $T_b \sim 90$ K (Figure 6.3B4). More importantly, when compared to Feridex, the M_s of *fcc*-FePt-A NPs is ~ 2 times larger at 2 K and 35% stronger at 300 K (Figure 6.3B5 vs. Figure 6.3A5 and Table 6.1). After silica coating, the blocking temperature is reduced to 50 K, and the ZFC slope below T_b is steeper (Figure 6.3C4). At 2 K and 5 T, the magnetization of *fcc*-FePt-silica-A NPs is $\sim 5\%$ lower than *fcc*-FePt-A and 2 times larger than Feridex. At 300 K and 5 T, the magnetization of *fcc*-FePt-silica-A NPs is $\sim 36\%$ lower than *fcc*-FePt-A NPs and similar to Feridex (Figure 6.3C5, Table 6.1). The alteration of the magnetic properties of the NPs after the silica coating is attributed to partial oxidization the FePt surface resulting in a thin layer of softer magnetic material like iron oxide in

the strong base environment associated with the silica coating, the thickness of which is not visible by XRD or TEM.²⁸⁻²⁹

Table 6.1 XRD and SQUID data of various FePt NPs compared to Feridex. Grain size D_{XRD} of FePt NPs or Feridex is calculated according to Scherrer's formula,³⁰ $D_{\text{XRD}} = 0.9\lambda/(B \cos \theta)$ where D_{XRD} is the “average” dimension of the crystallites, λ is the wavelength of the X-ray source (for Fe source is equal to 0.1936 nm), B is the full width at half maximum of the peak intensity of FePt (111) or Feridex (311) peak, and θ is the corresponding glancing angle. $\text{Fe}_x\text{Pt}_{1-x}$ is obtained based on FePt lattice constant vs. composition curve reported by Bonakdarkpour et al.^{24, 31} T_b is blocking temperature obtained from $FC-ZFC$ curves, M_s is the saturation moment. H_c is coercivity obtained from hysteresis loop.

Sample	D_{XRD} (nm)	$\text{Fe}_x\text{Pt}_{1-x}$ %	T_b (K)	M_s at 2 K emu per g Fe	M_s at 300 K emu per g Fe	H_c at 2K kOe
<i>fcc</i> FePt-A	3.6±0.1	42.7±0.7	90	201	112	0.7
<i>fcc</i> FePt-silica-A	3.6±0.1	43.8±1.4	50	191	83	1.3
<i>fct</i> FePt-A	6.1±0.1	~ 43	80	125	22	2.5
Feridex I.V.® (Endorem™)	5.3±0.1	-	45	101	82	0.3

fct-FePt-A NPs displayed a T_b of 80 K (Figure 6.3D4). At 2 K, the NPs magnetization was reduced by 38% but the coercivity was increased by a factor 3.5 up to 2.5 kOe when compared with *fcc*-FePt-A NPs (Figure 6.3D5). This confirms the *fcc* to *fct* crystal phase conversion. However, annealing also induced a dramatic drop in both magnetization and coercivity attributed to silicide formation.²⁹ It was reported by Thomson *et al.*²⁹ that annealing FePt NPs on a Si substrate induced formation of silicides leading to a strong reduction of the NPs magnetic moment, a schematic drawing of which is shown in Figure 6.4. A Long annealing of FePt at 725 °C resulted in increasing the *fct* ordered fraction compared to the *fcc* crystalline structure (Figure 6.4B). This is associated with a larger coercivity (Figure 6.4C) which could be observed below T_b (20 K). However, annealing longer than 20 min induced a drop of the coercivity leading to a non-monotonous behaviour of the coercivity variation with the annealing time (Figure 6.4C). Furthermore, a continuous drop in magnetization (Figure 6.4D) was observed at 9 T. This can be

attributed to the formation of Fe_xSi_y . The crystalline fraction of FePt was calculated to include both *fcc* and *fct* structures with $\Phi_{\text{FePt}} + \Phi_{\text{Fe silicide}} = 1$ and only 40% of FePt remained fraction after annealing at 725 °C for 2 h (Figure 6.4E) which reduced the magnetization by about 35% (Figure 6.4D).²⁹

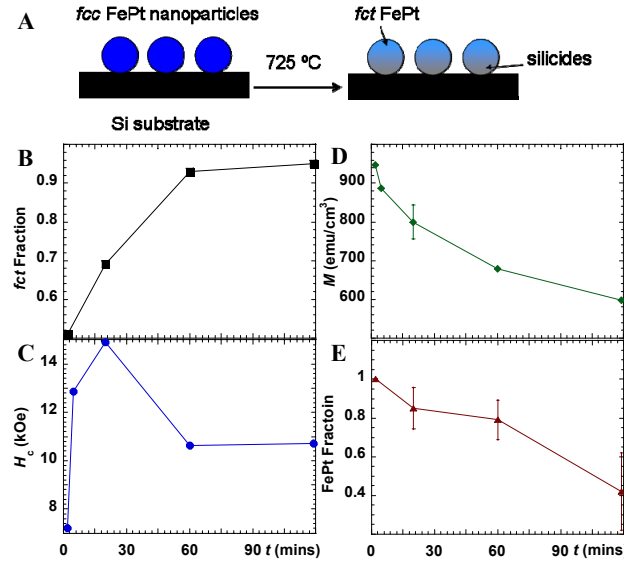


Figure 6.4 Schematic drawing of silicides formation (A) as annealing of FePt NPs on Si substrate. Curves of *fct*-FePt fraction (B), coercivity at 20 K (C), magnetization at 9 T (D) and fraction of FePt relative to Fe silicide (E) as a function of annealing time at 725 °C. The lines are included as a guide to the eye. Data extracted from Thomson *et al.*²⁹

In Thomson *et al.*'s work,²⁹ NPs were annealed on a silicon substrate, such that atoms could only diffuse from the contact point between NPs and substrate. In contrast, our FePt NPs were coated with a silica shell so that annealing could be expected to form silicides all around the NPs. A 40 min annealing time was chosen to balance

- i) an increase of the *fct* ordered fraction, and
- ii) a potential reduction of the magnetic properties.

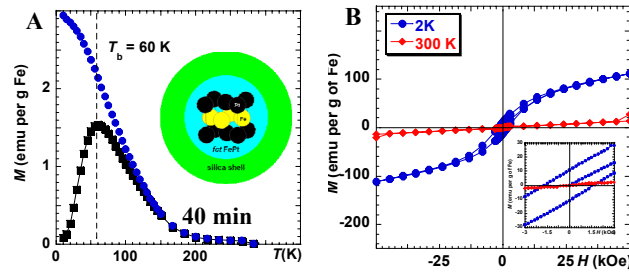


Figure 6.5 SQUID data of *fct*-FePt-silica NPs annealed at 700 °C for 40 min. ZFC-FC under a 100 Oe magnetic field (A) and hysteresis curves at 2 K and 300 K (B).

Figure 6.5 presents the characterisation of the magnetic properties of *fct*-FePt-silica NPs which were annealed for 40 min. The *fct* phase formation was confirmed by the increased blocking temperature (Figure 6.5B and Table 6.2) by 20% and coercivity by 31% respectively, as compared to prior annealing *fcc*-FePt-silica-A NPs (Figure 6.5 A-B and Table 6.2)

Table 6.2 SQUID data of the FePt NPs. T_b is the blocking temperature, M_s is the saturation moment and H_c is the magnetic coercivity of the NPs.

Sample	T_b (K)	M_s (2 K) <i>emu per g of Fe</i>	M_s (300 K) <i>emu per g of Fe</i>	H_c kOe
<i>fcc</i> -FePt-A	90	201	112	0.7
<i>fcc</i> -FePt-silica-A	50	191	83	1.3
<i>fct</i> -FePt-silica (40 min, 700°C)	60	111	13	1.7

The formation of silicides induced by the annealing process, however reduced the magnetization measured at 5 T by 42% and 84% at 2 K and 300 K respectively (Figure 6.5 B and Table 6.2). In our study, the 40 min annealing time scale confirmed the formation of silicide at the periphery of the NPs, similar to the observations at 4 h annealing.

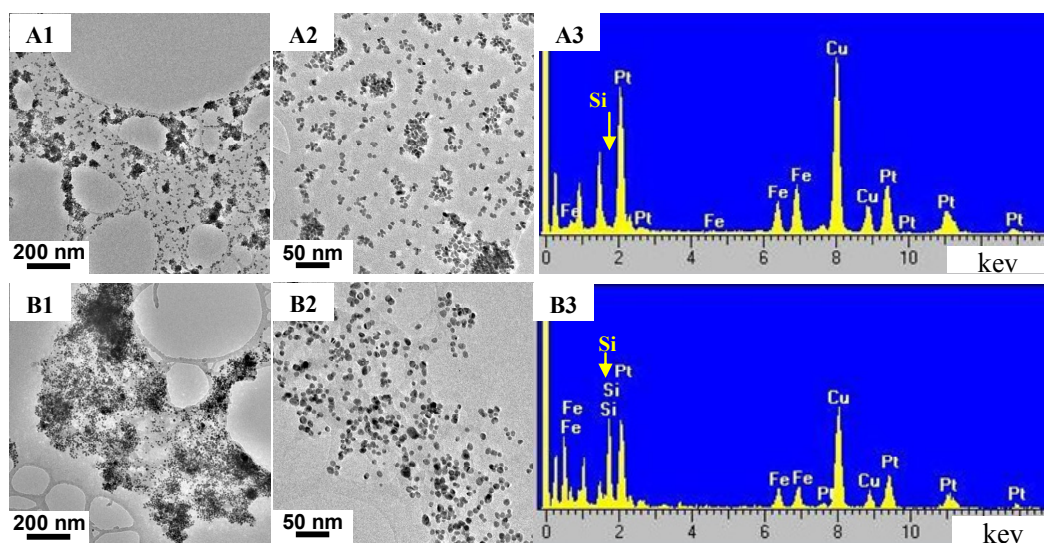


Figure 6.6 TEM and EDX data: as synthesized *fcc*-FePt-A NPs (A1-3), *fct*-FePt-A NPs annealed at 700 °C for 4 h (B1-3).

It was difficult to detect the presence of thin layer of metal silicide formation on NPs surface by XRD (Figure 6.3D3), however, the presence of Si in *fct* FePt NPs was confirmed by TEM-EDX analysis. Figure 6.6 presents a typical TEM-EDX characterization of two sets of FePt NPs. *fcc*-FePt-A NPs do not present any trace of silicon atoms (Figure 6.6A), but *fct*-FePt-A NPs annealed at 700 °C for 4 h do present a strong EDX peak at 1.7474 keV (Si $K\alpha_1$) which is a characteristic of silicon. The composition characterization of each sample was carried out by TEM-EDX analysis on three different areas, the composition results of which are presented in Table 6.3.

Table 6.3 TEM-EDX data of the FePt NPs.

Sample	Fe (%)	Pt (%)	Si (%)
<i>fcc</i> -FePt-A (as prepared)	43.1 ± 0.7	51.5 ± 1.0	5.4 ± 1.5
<i>fct</i> -FePt-A (4h, 700°C)	20.6 ± 0.7	25.4 ± 3.6	54.0 ± 3.0

In contrast with the Fe/Pt ratio which remained constant at Fe_{0.43}Pt_{0.57}, the silicon

ratio increased from a nominal background signal of 5.4% up to 54.0% corresponding to a signal to noise ratio of about 10. Due to the weakened magnetic moment of the *fcc*-FePt-A NPs, the remainder of this study focuses on *fcc*-FePt-A and *fcc*-FePt-silica-A NPs.

6.2.2. Biomedical Applications

6.2.2.1. Cell Toxicity

A major hurdle preventing wide use of FePt NPs in biomedicine is their potential toxicity. Toxicity studies of FePt NPs are currently being performed *in vitro*, and no *in vivo* studies have been reported to date. Since the first reliable cytotoxicity study on FePt NPs reported in 2007,¹⁶ very few publications have thereafter developed the cytotoxicity of FePt NPs.^{15, 17, 22} A summary of the cytotoxicity data of FePt NPs is presented in Table 6.4. It is noticeable that there is little consistent literature on FePt NPs cytotoxicity, leaving the subject rather unclear. It was reported that whilst FePt-cysteine NPs had no significant toxicity at concentrations below 5 µg/mL, 50% cell damage was observed at 15.5 µg/mL after incubation.¹⁶ Additionally, FePt-Fe₃O₄ NPs showed no significant cell viability damage up to 3 days at 10 µg/mL,¹⁵ but FePt-Fe₂O₃ and FePt-CoS₂ were reported to induce significant, ~50% cell viability damage even at concentrations as low as 1.5 µg/mL and 8.5 µg/mL of NPs, respectively.¹⁵⁻¹⁶ A hypothesis of mechanism of cytotoxicity of FePt NPs was proposed by Gao. *et al* where FePt cores are oxidized and destroyed to release platinum ions (Pt²⁺) under the acidic cellular environment like lysosomes. Pt²⁺ can enter into the nucleus and mitochondria, and has the ability to damage the DNA double-helix chains leading to cell apoptosis.²⁸

Table 6.4 Summary of FePt NP cytotoxicity studies reported in the literature: Cells stands for the cell line, [NPs] is the nanoparticle concentration, $t_{inc.}$ is the incubation time. (Reprinted with permission from ⁽²³⁾. Copyright 2010 American Chemical Society.)

Material	Fe Precursors [§]	Coating	Cells	Cytotoxicity			Cell Damage (%)	Ref.
				[NPs] (µg/mL)	[Fe] (µg/mL)	$t_{inc.}$ (h)		
FePt-CoS ₂	Fe(CO) ₅	CoS ₂ shell	Hela	1.5	~0.007	24	50	¹⁶
FePt-Cys	Fe(CO) ₅	Cysteine	Hela	5	~0.7	24	~10	¹⁶
				15.5	~2.5	24	50	
FePt-Fe ₂ O ₃	Fe(CO) ₅	Fe ₂ O ₃ shell, L-dopa coating	Hela	~8.3	~0.045 [†] ~3.8 [‡]	24	50	¹⁵
				40	#	24	~10	
FePt-Fe ₃ O ₄	Fe(CO) ₅	Fe ₃ O ₄ shell	Hela	10	#	72	~10	¹⁵
				20	#	72	~30	
FePt-COOH	Fe(CO) ₅	Bilayer of phospholipid (DSPE-PEG-2000 carboxylic acid lipid) and oleic acid / oleylamine	Hela	~10.7	1.72	24	~40	²²
			A431	~10.7	1.72	24	~40	
			SK-BR3	~10.7	1.72	24	~20	
			HEK-293	~10.7	1.72	24	~30	
			A2780	~7.8	1.25	24	50	
FePt-SiO ₂ -A	Na ₂ Fe(CO) ₄	SiO ₂ shell	A375M, MCF, U2OS	200	~2	168	0	*
FePt-A	Na ₂ Fe(CO) ₄	Cysteamine	A375M, MCF, U2OS	30	~5.3	168	0	*
				60	~10.5	72	~10	

[§] Pt precursor always Pt(acac)₂, [†] Fe contribution from Fe₂O₃ shell not included, [‡] Fe from Fe₂O₃ shell included, # [Fe] can not be calculated * Data presented in this work.

A later toxicity study with phospholipids coated *fcc*-FePt NPs showed 50% cell viability damage at only 1.25 µg/mL Fe concentration (~7.8 µg/mL Fe₄₀Pt₆₀ NPs).²²

In this study, high toxicity was attributed to the fast Fe release rather than Pt release from phospholipids coated *fcc*-FePt NPs. It was reported that whereas no Pt ion releasing was detectable, ~6% Fe was already released after 6 h incubation, and the percentage of Fe was further increased to ~20% after 24 h incubation in pH 4.8 PBS.²² Whilst iron is essential for almost all living organism, it is still toxic and can

for instance act as a catalyst in the Fenton reaction which generates a wide range of free radical species including hydroxyl radicals, i.e. $\cdot\text{OH}$.³²



These are among the most reactive free radical species known and have the ability both to react with a wide range of cellular constituents including pyrimidine bases of DNA and trigger lipid peroxidation in cellular membranes leading to cell death.³²

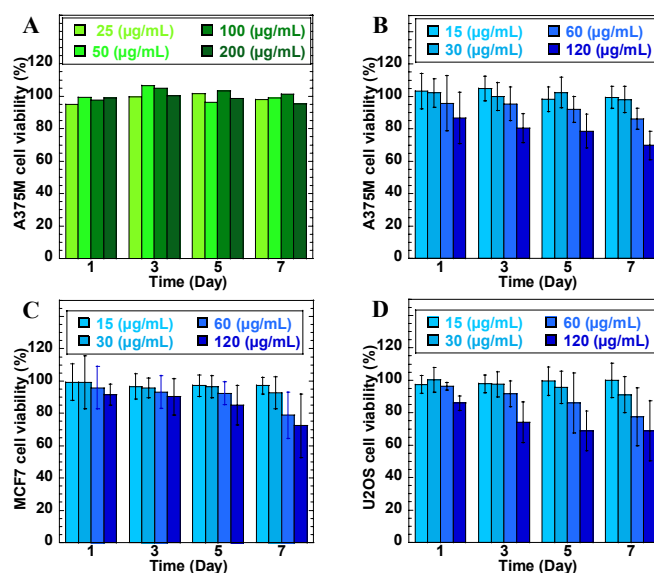


Figure 6.7 Viability of A375M cells incubated with *fcc*-FePt-silica-A NPs (A) at different FePt-silica-A concentrations (25, 50, 100, 200 $\mu\text{g/mL}$) up to 7 days, and A375M cells (B) MCF7 cells (C) and U2OS cells (D) incubated with *fcc* FePt-A NPs at different FePt metal core concentrations (15, 30, 60, 120 $\mu\text{g/mL}$). (Reprinted with permission from ⁽²³⁾. Copyright 2010 American Chemical Society.)

In this study, cytotoxicity of the NPs was evaluated by MTS assay on an A375M cell line treated with *fcc*-FePt-silica-A and *fcc*-FePt-A NPs with various concentrations and incubation times.³³ *fcc*-FePt-silica-A NPs have good biocompatibility as expected (Figure 6.7A). There is no cell viability damage at incubation concentrations of *fcc*-FePt-silica-A up to 200 $\mu\text{g/mL}$ even after 7 days

of incubation. One likely explanation is due to the protection of the inert silica shell.

Both dose responses and time course studies on *fcc*-FePt-A NPs were also performed (Figure 6.7B). At 120 $\mu\text{g/mL}$, *fcc*-FePt-A NPs exhibited cytotoxicity which increases with incubation time. At concentration of 60 $\mu\text{g/mL}$, *fcc*-FePt-A NPs incubated with cells for 7 days showed a $\sim 15\%$ loss of cell viability. Significantly, there is no loss of cell viability at concentrations of 30 $\mu\text{g/mL}$ and below, even after prolonged incubation periods of up to 7 days. Similar results were obtained with *fcc*-FePt-A NPs and both MCF7 and U2OS tumour cell lines (Figure 6.7C and D).

To confirm these results, the chemical stability of *fcc*-FePt-A NPs in acidic environment of similar pH to lysosomal environment was investigated by incubation of *fcc*-FePt-A in pH 4.8 buffer solutions.¹⁷ The concentration of FePt NPs incubated in buffer solution is $\sim 120 \mu\text{g/mL}$ to match the highest NP concentration used in the cytotoxicity study (Figure 6.7B-C). In a pH 4.8 phosphate buffered saline (PBS), cysteamine coated FePt NPs show excellent chemical stability with only $\sim 0.7\%$ Fe, i.e. less than $0.1 \mu\text{g/mL}$ of iron was released after 7 days of incubation (Figure 6.8A1). As suggested by the recent literature,³⁴⁻³⁵ an *in vitro* lysosomal model, i.e. RPMI-1640 cell media containing 20 mM sodium citrate (pH 4.8) was also used to better match the metabolic conditions in lysosome. In these more extreme conditions, more Fe was released, $0.3 \mu\text{g/mL}$ (2.2%) after 6 h and up to $\sim 2.4 \mu\text{g/mL}$ (19.4%) after 7 days, but importantly it remained at a level comparable to the release observed with Feridex (Figure 6.8A2).

The Pt release is insignificant in both buffer solutions, and the level of released Pt is between $\sim 0.04\%$ - 0.45% corresponding to ~ 0.04 - 0.45 $\mu\text{g/mL}$ from 6 h to 7 days at 120 $\mu\text{g/mL}$ incubation concentration (Figure 6.8A1 and 2). The small amount of Pt release might be partially responsible for cell damage observed at very high dosage treatment, e.g. above 60 $\mu\text{g/mL}$ (Figure 6.7B-C).

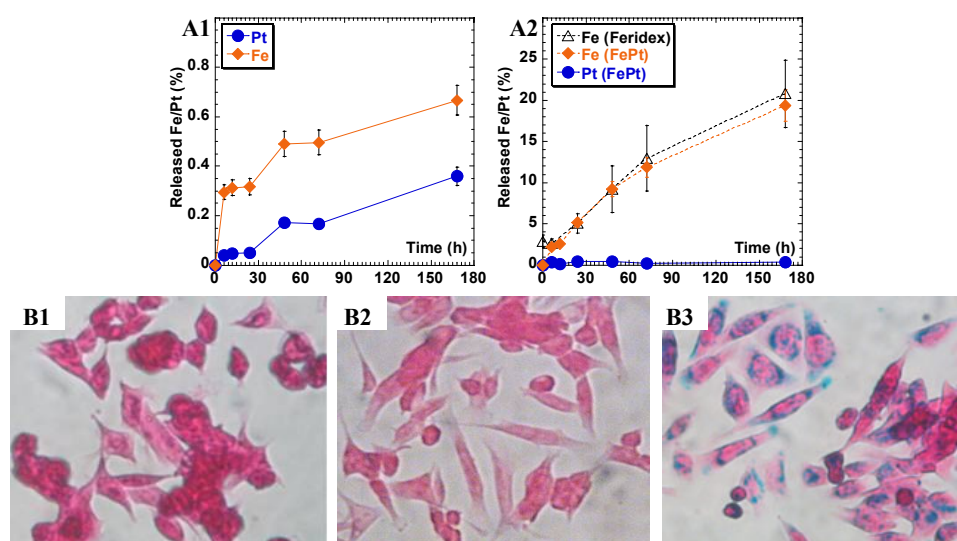


Figure 6.8 Fe released from *fcc*-FePt-A NPs (\blacklozenge) in pH 4.8 PBS (A1). Fe Released from *fcc*-FePt-A NPs (\blacklozenge) and from Feridex (Δ)³⁵ in solutions at pH ~ 4.8 of RPMI-1640 cell media containing 20 mM sodium citrate. The incubation concentrations for FePt and Feridex³⁵ are 120 $\mu\text{g/mL}$ and 25 $\mu\text{g/mL}$ respectively (A2). Photomicrographs (magnification $\times 40$) of Prussian blue-stained A375M cells cultured on cover slips in cell media (B1), media containing 30 $\mu\text{g/mL}$ of *fcc*-FePt-A NPs (B2) and media containing 30 $\mu\text{g/mL}$ of Feridex (B3) after overnight incubation. (Reprinted in part with permission from (23). Copyright 2010 American Chemical Society.)

In contrast to the above mentioned results found in the literature, our study reveals that cysteamine coated *fcc*-FePt NPs have a very high chemical stability in pH 4.8 PBS. Fe released after 24 h incubation is $\sim 0.3\%$, with only a slight increase to $\sim 0.7\%$ after 7 days of incubation (Figure 6.8A1). In an *in vitro* model, i.e. cell media containing sodium citrate,³⁴⁻³⁵ *fcc*-FePt-A NPs were found to release as little Fe as Feridex (Figure 6.8A2), with $\sim 5.2\%$ Fe found to be released after 24 h and $\sim 19.4\%$ after 7 days. On the one hand, this confirms that the low pH in

endosome/lysosome environment is not enough to dissolve the NPs, and that the presence of endogenous citrate or similar metallic chelates which can promote the dissolution of the iron by binding to solubilised Fe atoms is also necessary.³⁴⁻³⁵ On the other hand, such outcome is very important, because it suggests when considering the Fe release the safety of *fcc*-FePt-A NPs can be comparable to Feridex under similar experimental condition. While emphasising further the importance of the NPs environment, the chemical stability of the *fcc*-FePt-A NPs is further supported by the Prussian blue-stained experiments (Figure 6.8B). Indeed, photomicrographs obtained after overnight incubation show no stain for both blank control sample (Figure 6.8B1) and *fcc*-FePt-A NPs labeled cells (Figure 6.8B2). In contrast, Feridex labeled cells show significant stainings (Figure 6.8B3) characteristic of the release of Fe^{3+} in the cells. These results confirm that the cysteamine coating provides *fcc*-FePt-A NPs with high chemical stability.

The high chemical stability of cysteamine coated FePt NPs certainly contributes to the NPs' low cytotoxicity, and metal release is only one parameter that contributes to this. It is quite possible that differences in the NPs preparation, surface coating, ligand exchange, and extraction protocols could account for the spread of the cytotoxicity data reported in the literature. The toxicity may not necessarily be due to material itself through the release of its constituent. In the present study, we used the Collman's reagent, $\text{Na}_2\text{Fe}(\text{CO})_4$, to control the FePt NP stoichiometry and to ensure the simultaneous presence of Fe and Pt species during the formation of FePt alloy NPs, while the use of $\text{Fe}(\text{CO})_5$ has been shown to form NP with a core and a shell rich in platinum and iron, respectively.³⁶ Furthermore, after ligand exchange, the extraction process was repeated up to 6 times to ensure removal of hazardous chemicals such as chloroform, oleic acid and oleylamine, while the thiol group provides a strong bonding between the cysteamine and the NP surface

preventing the ligands becoming lethal. While this publication was submitted, cysteamine coated FePt NPs were reported to induce very low cell damage on Veron cells after 24 h.¹⁴ However it is noticeable that a strong bonding to the surface of the nanoparticles protecting them from the cell's environment comes in contrast with, for instance, a coating made with a bilayer structure of phospholipids, carboxylic acid and oleic acid/oleylamine.²² Indeed, even though this phospholipid approach provides aqueous solubility, it is also characterised by a weaker bonding strength and a more dynamic behaviour allowing the coating to slowly disperse in the cell. By doing so, the “free” ligands can alter the cell viability as well as the release of the NP constituents, since the surface of the particle is exposed to the cell. The NP chemical integrity can thus be further compromised. Such outcomes have been reported by Xu *et al.* although the authors focused on the opportunity this provided to use the NPs as a metal reservoir to kill cancerous cells.²²

While the very high chemical stability of *fcc*-FePt-A NPs was demonstrated in this report, cytotoxicity was observed at high concentrations above 30 µg/mL FePt and with long incubation times. This could be explained by contributions from *i*) the very small release of Fe and Pt, and *ii*) the high concentration of positive surface charges which could also interact with the more negatively charged cell membranes and induce membrane disruption.³⁷ In addition, ligands with strong anchoring groups can reduce the toxicity, as illustrated in this publication, and it is noticeable that the present results were obtained with commercially available ligands (i.e. cysteamine); such that one should expect enhanced viability from, for instance, custom made bidentate thiol as developed recently for quantum dots.³⁸⁻³⁹ These could provide cell viability at higher NP concentrations than 30 µg/mL.

In this context, the little consistency observed when considering FePt NPs

cytotoxicity data available in the literature, stresses that the measured toxicity should always be associated to the nanocolloids, i.e. inorganic NPs plus organic stabilisers. The interplay between each component will indeed contribute to the cytotoxicity results with for instance a weak bonding to the NP surface increasing the probability of the nanocolloid to be toxic. It then appears that to be able to compare cytotoxicity data in a meaningful way, one needs to develop and use standardised approaches including the correlation between *i*) the evolution of the nanocolloids integrity, relying on both the inorganic NPs and the organic stabilisers, and *ii*) the cell viability. It should be noticed that in the context of apparently toxic NPs, the nanocolloid solution stability could easily be measured by time resolved transmission monitored sedimentation experiments. As the ligands come off the NPs surface the NPs tend to aggregate and fall out of solution.

6.2.2.2. Cellular Uptake

The cell plasma membrane is a dynamic structure that functions to segregate the chemically distinct intracellular milieu from the extracellular environment by regulating and coordinating the entry and exit of small and large molecules. Small molecules, such as amino acids, sugars and ions, can traverse the plasma membrane through the action of integral membrane protein pumps or channels. The cellular entry of macromolecules and particles involves various mechanisms that are used by cells to internalize macromolecules and particles within membrane bound vesicles derived by the invagination and pinching-off of pieces of the plasma membrane in a process termed endocytosis. Endocytosis is a global term and is divided into two broad categories, phagocytosis or cell eating (the uptake of large particles) and pinocytosis or cell drinking (the uptake of fluid and solutes). The phagocytosis process starts by the formation of membrane protrusion

triggered by the binding of phagocyte surface receptors to the ligands on the surface of a particle like a bacterium. The protrusion will engulf the ligand coated particles and will form an internal vesicle called phagosome (Figure 6.9A). Whereas the phagocytosis is typically only conducted by specialized mammalian cells, such as monocytes, macrophages, neutrophils, and microglia; the pinocytosis occurs in all cells by mainly four basic mechanisms: macropinocytosis, clathrin-mediated endocytosis, caveolae-mediated endocytosis, and clathrin- and caveolae- independent endocytosis (Figure 6.9B to F).

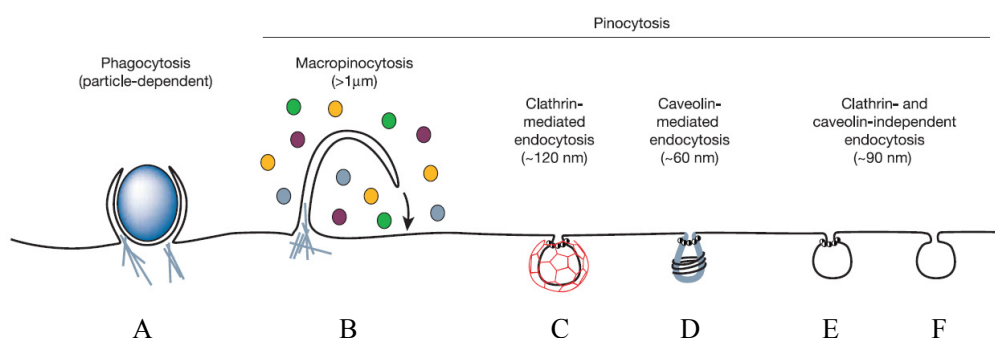


Figure 6.9 Multiple portals of entry into the mammalian cell. The endocytic pathways differ with regard to the size of the endocytic vesicle, the nature of the cargo (ligands, receptors and lipids) and the mechanism of vesicle formation. (Reprinted by permission from Macmillan Publishers Ltd: [Nature] ⁽⁴⁰⁾, copyright 2003.)

The pinocytosis pathways differ with regard to endocytic vesicles and mechanisms of vesicles formation which can be viewed directly under TEM. One of the pinocytosis mechanisms is called macropinocytosis which accompanies the actin-driven formation of membrane protrusions upon stimulation by growth factors or other signals. These protrusions then collapse into the plasma membrane and fuse back with the plasma membrane, forming normally larger than 1 μm irregular-sized vesicles called macropinosomes (Figure 6.9B). Another pinocytic pathway is clathrin mediated (Figure 6.9C). Clathrin is a three legged structured protein, which has the ability to self-assemble into cages and curve

lattices under the director of the assembly proteins. The clathrin cages are typically about 120 nm in diameter and are responsible for driving membrane invagination and vesicle formation. Another class of coated vesicles are called caveolae which are flask-shaped invaginations of the lipid rafts which are cholesterol and sphingolipid-enriched microdomains found in cell plasma membranes. The caveolae are coated with caveolin, which is a dimeric protein and has ability to self-associate to form a striated caveolin coat on the surface of the membrane invaginations (Figure 6.9D). Caveolae are relatively smaller in diameter (50 to 60 nm) as compared to clathrin-coated pits. The last class of endocytic pathway is called clathrin- and caveolin- independent endocytosis, which are lipid rafts mediated invagination of cell membranes which are about 90 nm in diameter and able to diffuse freely on the cell surface (Figure 6.9E and F). In addition, dynamine which is a multidomain GTPase that can assemble into a spiral or ‘collar’ recruited to the necks of vesicles, is required for clathrin-, caveolae- mediated and some clathrin- and caveolae- independent endocytosis pathways (Figure 6.9C, D and E).^{6, 40-44}

A TEM study was carried out in order to investigate the internalization of cysteamine coated FePt NPs into non-phagocytic tumour cells. Figure 6.10A illustrates that cysteamine modified *fcc*-FePt NPs can efficiently enter A375M non-phagocytic human cells without any external allied force such as transfection agents or electroporation. This can be attributed to the electrostatic attraction of cationic NPs to the negatively charged cell membrane. TEM analysis also demonstrated efficient cell internalization of *fcc*-FePt-A NPs into MCF7 and U2OS cells, as shown in Figure 6.10B-C. In contrast, the internalization of Feridex into non-phagocytic cell is poor. This is due to the lack of efficient binding of non-charged hydrophilic dextran coating to the plasma membrane, which limits the capability of cell internalization to the fluid phase endocytosis

pathway.⁴⁵⁻⁴⁶ To enhance the cellular uptake of dextran coated NPs, transfection agents or further surface functionalization are necessary.⁴⁷

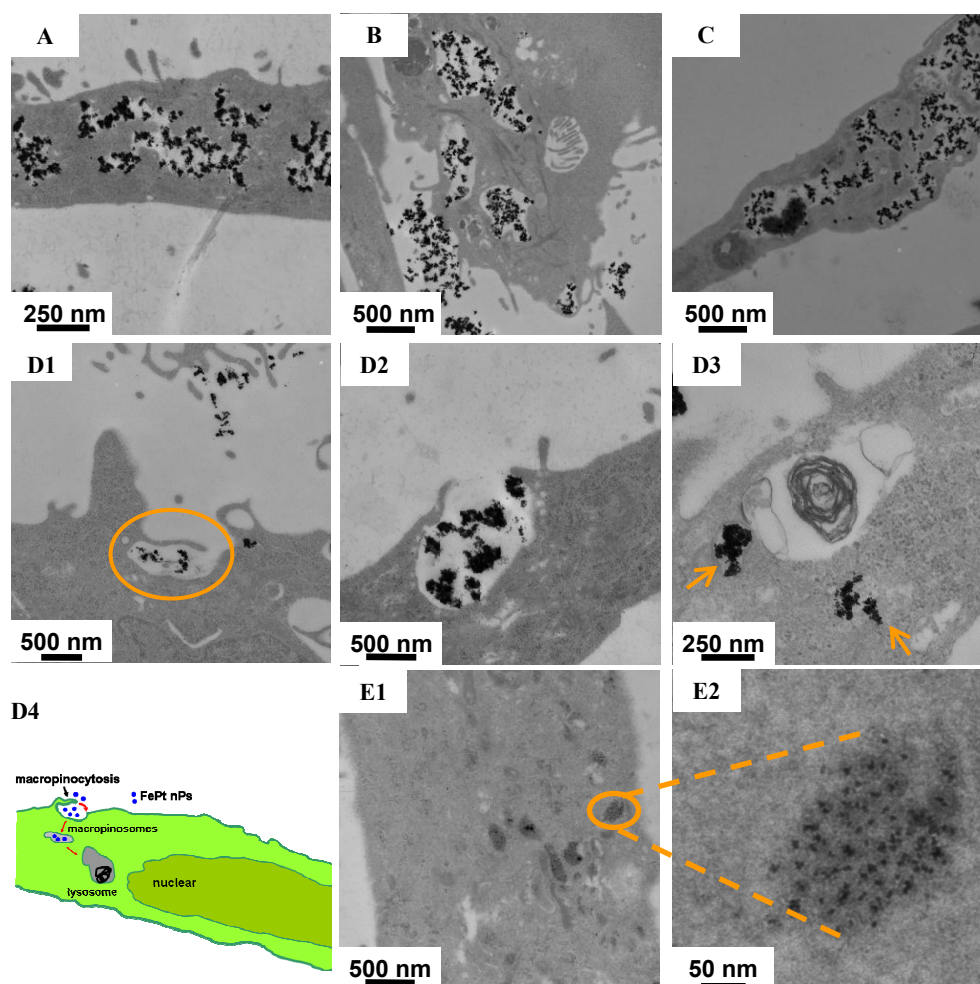


Figure 6.10 TEM images of A375M (A) MCF7 (B) and U2SO (C) cells after 16 h incubation in media containing 30 $\mu\text{g}/\text{mL}$ of *fcc*-FePt-A NPs. The cell uptake mechanism of *fcc*-FePt-A NPs through macropinocytosis in A375M cells as revealed by TEM images (D1-3) and a schematic drawing (D4). Cell internalization of *fcc*-FePt-silica-A NPs by A375M cells (E1), incubated at a NP concentration of 50 $\mu\text{g}/\text{mL}$ after 16 h, and the zoomed in area (E2) of the cellular internalized *fcc*-FePt-silica-A NPs as labeled by the orange circle in (E1). (Reprinted in part with permission from ⁽²³⁾. Copyright 2010 American Chemical Society.)

With regard to the cellular uptake mechanism of *fcc*-FePt-A NPs, we often observed protrusions of the plasma membrane surrounding a cluster of NPs providing strong evidence for macropinocytosis, a non-specific endocytic process

that involves the internalization of large areas of plasma membrane together with significant amounts of fluid. A series of typical TEM images of this phenomenon are presented in Figure 6.10D1-3. An early stage of macropinocytosis phenomenon, cell membrane protrusion formed and surrounded FePt NPs including large amount of fluid is indicated by Figure 6.10D1. The protrusion collapsed together with the NPs and tended to fuse back with the cell membrane to form large irregular vesicles called macropinosomes with sizes larger than 1 μm (Figure 6.10D2). Macropinosomes moved towards the centre of the cell shrank by losing water, changed from early-endosome-like organelle to a late-endosome-like organelle then merge completely into the lysosomal compartment (Figure 6.10D3).⁴³ A schematic drawing of this type of cellular uptake is shown in Figure 6.10D4. The intercellular presence of *fcc*-FePt-silica-A NPs is shown in Figure 6.10E1 and E2. *fcc*-FePt-silica-A NPs also demonstrated efficient non-phagocytic human cell internalization by straightforward incubation, without any external allied force such as transfection agents or electroporation.

There was no evidence in our study to support the involvement of the other pathways of endocytosis, the clathrin- and caveolae- dependent and independent pathways.^{42, 44} Further study will be needed to clarify the mechanism associated with cellular internalization and subsequent intracellular trafficking of cysteamine functionalized and silica coated FePt NPs.

6.2.2.3. *In vitro* MRI

The effectiveness of *fcc*-FePt-A and *fcc*-FePt-silica-A as MRI contrast agents was investigated by measuring the dependence of the longitudinal T_1 and transverse T_2 relaxation rates of water in 1% agarose gel on the Fe concentration of the NPs. The results are presented in Figure 6.11A-B respectively. Relaxivity r_1 is the

effectiveness of a contrast agent to enhance the relaxation of the water protons and is used to measure the efficiency of the NPs as MRI contrast agents. r_1 is defined as longitudinal relaxivity ($i = 1$) or transverse relaxivity ($i = 2$).^{6, 24}

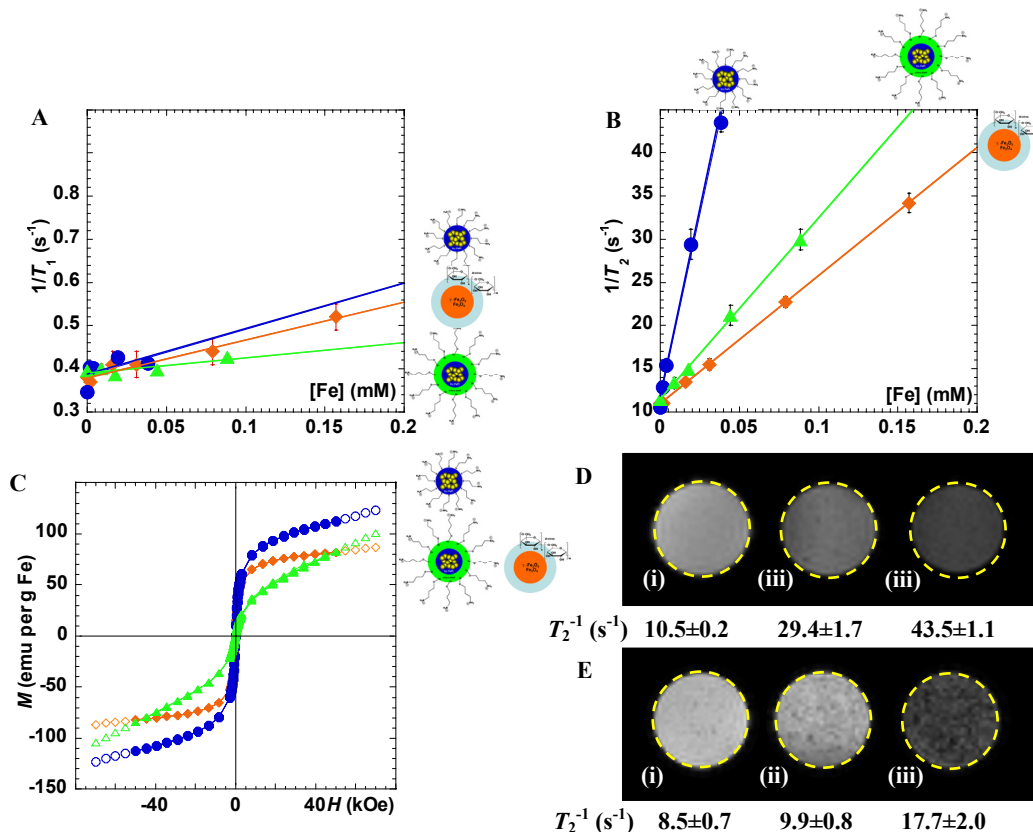


Figure 6.11 T_1^{-1} (s⁻¹) (A) and T_2^{-1} (s⁻¹) (B) vs. [Fe] (mM) of the water in 1 % w/v agarose gel containing (●) *fcc* FePt-A, (▲) *fcc* FePt-silica-A and (◆) Feridex. Hysteresis curves (C) of *fcc*-FePt-A NPs (●), *fcc*-FePt-silica-A NPs (▲), and Feridex (◆) measured by SQUID from -5.0 T to 5.0 T at 300 K. Data points are extrapolated to ± 7.1 T and labeled as hollow markers. ¹H longitudinal relaxation rate of T_2 -weighted MRI images (D) of 1 % agarose gel water solution containing FePt-A NPs with (i) [Fe] = 0 mM, (ii) 0.02 mM ($C_{\text{FePt}} = 6 \mu\text{g/mL}$), (iii) 0.04 mM ($C_{\text{FePt}} = 12 \mu\text{g/mL}$). T_2 -weighted cellular imaging (E) of A375M cells loaded with FePt-A NPs with a cell density of (i) 10×10^3 cells/mL, (ii) 100×10^3 cells/mL, (iii) 1000×10^3 cells/mL. All measurements were completed by MRI (3D Spin Echo, $T_E = 30$ ms, $T_R = 1$ s) at 7.1 T. (Reprinted in part with permission from (23). Copyright 2010 American Chemical Society.)

The r_1 and r_2 values of two FePt NPs and Feridex, a commercial MRI contrast agent are shown in Table 6.5. At 7.1 T, the FePt NPs and Feridex only have a weak influence on the T_1 relaxation rate of water protons.⁶ In contrast, the

presence of FePt NPs has significant effect upon water T_2 relaxation rate of the gels (Figure 6.11B). At 7.1 T, the r_2 relaxivity of the Feridex is about $148 \text{ s}^{-1}\text{mM}^{-1}$ which agrees with the literature value (Table 6.5). The *fcc*-FePt-silica-A NPs have a 40% larger r_2 than Feridex. This is attributed to higher magnetization of *fcc*-FePt-silica-A NPs than Feridex at 7 T. By design, the commercial SQUID magnetometer's highest external magnetic field is 5 T, whilst MRI experiments were performed at 7.1 T. However, a higher magnetization of *fcc*-FePt-silica-A NPs compared to Feridex can be expected by extrapolating the magnetization curves from 5 T to 7.1 T (Figure 6.11C). It is indeed noticeable that Feridex has already saturated at 5 T, while the silica coated FePt NPs had yet to reach saturation magnetization. The extrapolation to 7.1 T implies that under MRI magnetic field, the magnetic response of *fcc*-FePt-silica-A NPs is larger than that of Feridex.

Table 6.5 ^1H relaxivity values (r_1 and r_2) for agarose gel solution containing Feridex I.V.[®], *fcc*-FePt-A and *fcc*-FePt-silica-A NPs,²³ (Reprinted with permission from (²³). Copyright 2010 American Chemical Society.) compared to values of some commercial contrast agents base on the current literature (7.1 T, 300 MHz MRI).⁶

Sample	$r_1 (\text{s}^{-1}\text{mM}^{-1})$	$r_2 (\text{s}^{-1}\text{mM}^{-1})$
<i>fcc</i> FePt-A	2.5 ± 1.0	887 ± 32
<i>fcc</i> FePt-silica-A	0.3 ± 0.1	210 ± 3
Feridex I.V.[®] (Ferumoxides)	0.9 ± 0.1	148 ± 1
Feridex I.V. [®] as reported	1.8^*	132^*
Ferucarbotran. A [®]	1.6^*	205^*
Ferumoxtran-10 [®]	1.4^*	71^*
Ferumoxytol [®]	2^*	95^*

*Experimental uncertainties are not reported.

The main result is that the r_2 relaxivity of the *fcc*-FePt-A NPs is 6 times larger than that of Feridex (Figure 6.11C and Table 6.5). For example, the ^1H T_2 relaxation rate of water in gels with no contrast agent was $\sim 10 \text{ s}^{-1}$, but when the *fcc*-FePt-A NPs at $[\text{Fe}] = 0.04 \text{ mM}$ was present, the T_2 relaxation rate increased approximately four times (43.5 s^{-1}). The presence of Feridex at twice the iron

concentration ($[\text{Fe}] = 0.16 \text{ mM}$) only increased the relaxation rate of water by about two times (34.1 s^{-1}). Typical T_2 weighted MRI images of *fcc*-FePt-A NPs in gel as shown in Figure 6.11D; the signal intensity decreases in the T_2 -weighted MR thus appearing darker as the concentration of NPs increases. The FePt NPs produce distinct image contrast within gels at concentrations as low as $6 \mu\text{g/mL}$. This is well within the safety range as supported by our cytotoxicity data (Figure 6.7A). The high MRI relaxivity r_2 of *fcc*-FePt-A NPs is attributed to a combination of i) high FePt magnetization (Figure 6.11C), ii) a thin organic coating, and iii) their small size resulting in effective dispersion across a sample. This combination creates a very effective T_2 MRI contrast agents even at $\mu\text{g/mL}$ concentrations. Our results underline the importance of engineering the interface of NPs and demonstrate that a strong magnetic moment such as FePt's combined with a thin coating layer which has an open molecular structure allowing very close aqueous proximity, are essential parameters for the design of new generations of diagnostic and therapeutic MRI contrast agents.

Cellular imaging is a technique that is able to visualize specific cells in an intact animal. MR cellular imaging is a powerful non-invasive technique therefore is able to detect specific cells of interest in living organisms over time, which distinguishes conventional cellular imaging from histology and molecular biology protocols which typically require a disintegration of the organisms.⁶ For MR cellular imaging, a MRI contrast agent is normally required in order to gain enough sensitivity and selectivity to distinguish cells of interest from other biological subjects. A good contrast agent should be able to selectively and efficiently enter cells of interest. Magnetic NPs are T_2 contrast agents and have been applied to monitor the migration, biodistribution, and behaviour of cells *in vivo* by MRI with a typical spatial resolution of the order of tens of microns.

fcc-FePt-A NPs have shown great potential to be used as a new highly sensitive

MRI probe for cellular imaging, as it has demonstrated a much stronger T_2 effect than iron oxide NPs. Furthermore, efficient cellular uptake of *fcc*-FePt-A NPs by non-phagocytic tumour cells during incubation without transfection agent assistance or electroporation treatment has been revealed by TEM (Figure 6.10A-C). In this study, we further demonstrate the capability of *fcc*-FePt-A NPs to be used as MRI probes for cellular imaging by analyzing labelled cells *in vitro* in agarose gels.

Typically the limit of spatial resolution of μ -MRI scanners is of the order of tens of microns. However cells can be studied by MRI by labelling the cells with MRI contrast agents and their presence detected by observing their effect upon image contrast. Indeed, MR imaging on FePt labelled A375M cell shows significant signal intensity loss induced by the effect of FePt NPs and this signal loss is proportional to cell density in agarose gel (Figure 6.11E). The signal intensity loss could be observed with cell densities as low as 10-100 cells/ μ L. In addition to the stronger T_2 effect of FePt NPs, it should be noticed that they also provided higher chemical stability than iron oxide NPs, as observed in the Prussian blue-stained experiments (Figure 6.8B). This is a very promising indication that *fcc*-FePt-A NPs will demonstrate enhanced stability in biological environments including for example lysosomes where the pH is below 5.5. This makes *fcc*-FePt-A NPs an appealing platform for cell tracking investigations.

6.2.2.4. *In vivo* MRI

To investigate the *in vivo* potential of the FePt NPs as MRI contrast agents, cell media containing varying concentrations of *fcc*-FePt-A NPs were injected into the eyes of *in ovo* Day 4 quail embryos. The purpose of this experiment is to investigate the concentration of FePt NPs required to produce hypointensities in

an *in vivo* environment. 3D MRI images were acquired of the embryos *in-ovo* after injection. The eye injected with FePt NPs in cell media was compared to the other eye without injection. Moreover, injection of blank cell media solution was used as a control.

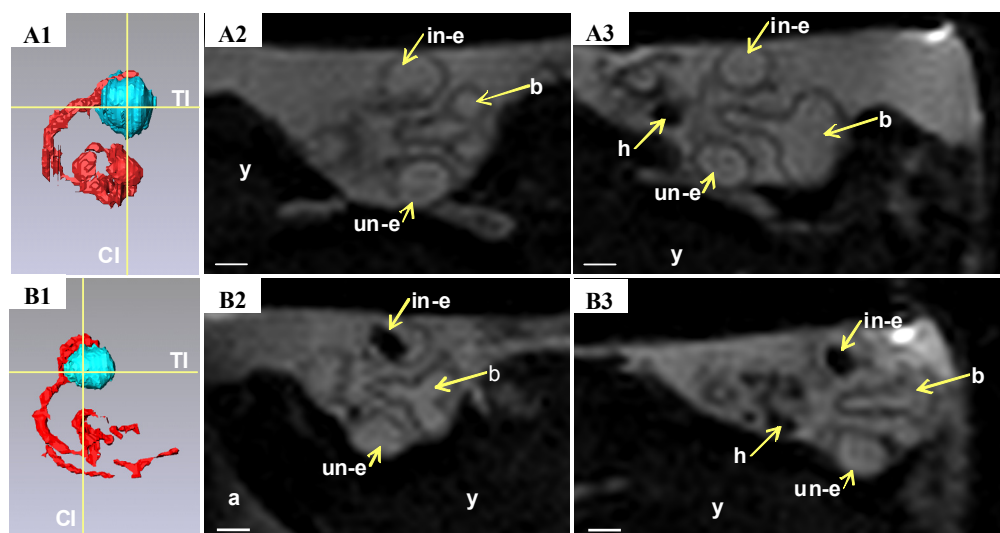


Figure 6.12 Embryo injected *in ovo* with cell culture media (1 μL) containing no NPs (A) and 20 $\mu\text{g/mL}$ *fcc*-FePt-A (B). 3D surface reconstruction of embryo eyes (blue) and blood vessels (red) showing the position (yellow) of the transverse and coronal images (A1-B1); Dorsal view of transverse image of the embryo's head aligned through the eyes (A2-B2); Anterior view of coronal image of the embryo's head aligned through the eyes (A3-B3). 2D slices from 128x128x128 3D Rare-8 MRI data set of Day 4 quail embryo egg ($T_R/T_E = 250/25$ ms), field of view of 30 mm and pixel dimensions of 0.234mm/pixel. Label: y= yolk, a= albumen, b= brain, in-e= injected eye, un-e= un-injected eye, h= heart; scale bar indicates 1mm. All the MRI measurements were completed at 7.1 T. (Reprinted with permission from ⁽²³⁾. Copyright 2010 American Chemical Society.)

Figure 6.12A and B display 3D MRI image data sets after injection which have been processed to highlight embryo eyes in blue, the blood vessels in red, and the NPs in green. The transverse and coronal images through the embryo's head are presented. The un-injected eye (un-e) acts as an internal control. There is no difference in the contrast between the un-injected and the uppermost eye which had been injected with a 1 μL of culture media only (Figure 6.12A2-A3). However, when the injection media contained 20 $\mu\text{g/mL}$ of *fcc*-FePt-A NPs, a very

distinct hypointensity appears in the injected eye (Figure 6.12B2-B3). This was consistently observed when varying the NP concentration.

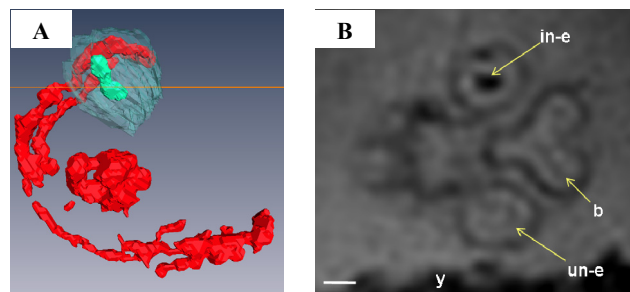


Figure 6.13 Embryo injected *in-ovo* with cell culture media (1 μ L) containing *fcc*-FePt-silica-A NPs at FePt core concentration 27 μ g/mL. 3D surface reconstruction of embryo eyes (blue), blood vessels (red) and NPs (green) of the transverse image (A). Dorsal view of transverse image of the embryo's head aligned through the eyes (B). 2D slices from 128x128x128 3D Rare-8 MRI data set of Day 4 quail embryo egg ($T_R/T_E = 250/25$ ms), field of view of 30 mm and pixel dimensions of 0.234mm/pixel. Label: y = yolk, b = brain, in-e = injected eye, un-e = un-injected eye; scale bar indicates 1mm. (Reprinted with permission from ⁽²³⁾. Copyright 2010 American Chemical Society.)

Figure 6.13 also illustrates the effect of injecting embryo with *fcc*-FePt-silica-A NPs (27 μ g/mL FePt core concentration). Figure 6.13A is the 3D surface reconstruction of the transverse image shown in Figure 6.13 B, with the green colour indicating the position of the injected contrast agents. Figure 6.13B illustrate the presence of the NPs solution produced a strong hypointensity in the images clearly visible because of the darker contrast when comparing with the eye which has not been injected.

In summary, we have demonstrated that FePt NPs can be successfully used as cellular and *in vivo* MRI probes. This is illustrated both by cell MRI (Figure 6.11E) and distinct hypointensity of ~ 1 mm in size observed in *in vivo* environment the FePt NPs were injected into (Figure 6.12 and Figure 6.13). Their high transverse relaxivity r_2 allows using less NPs than with iron oxide contrast

agents such as Feridex which makes FePt NPs very promising contrast agent to identify small lesions such as lymphnode metastases. In addition, FePt NPs can be used as potent MRI probes for cellular imaging, even at very low NP concentrations. This will allow, for instance, cell biodistribution, migration and behaviour to be monitored *in vivo*.

6.3. Conclusion

In conclusion, this chapter has presented the synthesis and characterization of a family of FePt NPs: *fcc*-, *fcc*-FePt-A NPs, and *fcc*-FePt-silica-A NPs. The reduction of magnetic properties observed with both SQUID and MRI relaxivity of *fcc*-FePt-A NPs prepared via annealing of silica coated NPs, is attributed to the formation of silicides. Although widely used, we have shown that this approach can be extremely detrimental to the targeted biomedical applications. Thus, research should focus on both direct *fcc*-FePt synthesis and buffer layers engineering to prevent atomic diffusion.

In sharp contrast with some previous reports, our biocompatibility studies clearly demonstrate the absence of cytotoxicity at concentrations below 30 $\mu\text{g/mL}$, even after 7 days incubation. The biocompatibility is mainly attributed to the strong surface coating and the extraction protocols. Another striking feature for cellular imaging is the ability we have shown for FePt NPs to efficiently enter tumour cells without requiring any external mediation; the cellular uptake by non-phagocytic tumour cells occurs via an apparent macropinocytosis mechanism. The 7.1 T MRI studies, *in vitro* and *in vivo*, have confirmed that both *fcc*-FePt-A and *fcc*-FePt-silica-A NPs are stronger T_2 contrast agents than commercial Feridex, with *fcc*-FePt-A T_2 relaxivity (r_2) being more than six times larger. The superior capability of MRI contrast enhancement of FePt NPs makes them an ideal platform

for the design of diagnostic and therapeutic agents for image-guided magnetic drug delivery and hyperthermic tumour ablation. The findings of this study underline the importance of engineering magnetic NP interfaces combining intrinsically strong magnetizations with coating layers. Finally, our studies have also demonstrated that FePt NPs can be used successfully for cellular and *in vivo* imaging, thus confirming the potential of FePt NPs in regenerative medicine and stem cell therapy.

References

- (1) Yan, G.; Robinson, L.; Hogg, P. *Radiography*. **2007**, 13, e5-e19.
- (2) Na, H. B.; Song, I. C.; Hyeon, T. *Adv. Mater.* **2009**, 21, 2133-2148.
- (3) Kim, J.; Piao, Y.; Hyeon, T. *Chem. Soc. Rev.* **2009**, 38, 372-390.
- (4) Dias, M. H. M.; Lauterbur, P. C. *Magnet. Reson. Med.* **1986**, 3, 328-330.
- (5) Jung, C. W.; Jacobs, P. *Magn. Reson. Imaging*. **1995**, 13, 661-674.
- (6) Modo, M. M. J.; Bulte, J. W. M., *Molecular and Cellular MR Imaging*. 1st ed.; CRC Press: London, 2007.
- (7) Bulte, J. W. M.; Kraitichman, D. L. *Nmr Biomed.* **2004**, 17, 484-499.
- (8) Sun, S. H. *Adv. Mater.* **2006**, 18, 393-403.
- (9) Gu, H. W.; Ho, P. L.; Tsang, K. W. T.; Yu, C. W.; Xu, B. *Chem. Commun.* **2003**, 1966-1967.
- (10) Gu, H.; Ho, P. L.; Tsang, K. W. T.; Wang, L.; Xu, B. *J. Am. Chem. Soc.* **2003**, 125, 15702-15703.
- (11) Maenosono, S.; Saita, S. *Ieee. T. Magn.* **2006**, 42, 1638-1642.
- (12) Seehra, M. S.; Singh, V.; Dutta, P.; Neeleshwar, S.; Chen, Y. Y.; Chen, C. L.; Chou, S. W.; Chen, C. C. *J. Phys. D. Appl. Phys.* **2010**, 43, 145002.
- (13) Maenosono, S.; Suzuki, T.; Saita, S. *J. Magn. Magn. Mater.* **2008**, 320, L79-L83.
- (14) Chou, S. W.; Shau, Y. H.; Wu, P. C.; Yang, Y. S.; Shieh, D. B.; Chen, C. C. *J. Am. Chem. Soc.* **2010**, 132, 13270-13278.
- (15) Gao, J. H.; Liang, G. L.; Cheung, J. S.; Pan, Y.; Kuang, Y.; Zhao, F.; Zhang, B.; Zhang, X. X.; Wu, E. X.; Xu, B. *J. Am. Chem. Soc.* **2008**, 130, 11828-11833.
- (16) Gao, J.; Liang, G.; Zhang, B.; Kuang, Y.; Zhang, X.; Xu, B. *J. Am. Chem. Soc.* **2007**, 129, 1428-1433.
- (17) Xu, C. J.; Yuan, Z. L.; Kohler, N.; Kim, J. M.; Chung, M. A.; Sun, S. H. *J. Am. Chem. Soc.* **2009**, 131, 15346-15351.
- (18) Tanaka, Y.; Maenosono, S. *J. Magn. Magn. Mater.* **2008**, 320, L121-L124.
- (19) Green, M. *J. Mater. Chem.* **2010**, 20, 5797-5809.
- (20) Josephson, L.; Tung, C. H.; Moore, A.; Weissleder, R. *Bioconjugate Chem.* **1999**, 10, 186-191.
- (21) Kang, H. W.; Josephson, L.; Petrovsky, A.; Weissleder, R.; Bogdanov, A. *Bioconjugate Chem.* **2002**, 13, 122-127.
- (22) Xu, C.; Yuan, Z.; Kohler, N.; Kim, J.; Chung, M. A.; Sun, S. *J. Am. Chem. Soc.* **2009**, 131, 15346-15351.
- (23) Chen, S.; Wang, L.; Duce, S. L.; Brown, S.; Lee, S.; Melzer, A.; Cuschieri, S. A.; Andre, P. *J. Am. Chem. Soc.* **2010**, 132, 15022-15029.
- (24) See Appendix for details.

- (25) Bagaria, H. G.; Ada, E. T.; Shamsuzzoha, M.; Nikles, D. E.; Johnson, D. T. *Langmuir*. **2006**, 22, 7732-7737.
- (26) Torimoto, T.; Tsumura, N.; Nakamura, H.; Kuwabata, S.; Sakata, T.; Mori, H.; Yoneyama, H. *Electrochim. Acta*. **2000**, 45, 3269-3276.
- (27) Koji, N., *Infrared Absorption Spectroscopy*. 1 st ed.; Holden-Day, Inc., San Francisco and Nankodo Company Limited, Tokyo: 1962.
- (28) Lee, D. C.; Mikulec, F. V.; Pelaez, J. M.; Koo, B.; Korgel, B. A. *J. Phys. Chem. B*. **2006**, 110, 11160-11166.
- (29) Thomson, T.; Terris, B. D.; Toney, M. F.; Raoux, S.; Baglin, J. E. E.; Lee, S. L.; Sun, S. J. *Appl. Phys.* **2004**, 95, 6738-6740.
- (30) Azaroff, L. V., *Elements of X-ray Crystallography*. 1st ed.; McGraw-Hill, Inc.: New York, 1968.
- (31) A. Bonakdarpour, J. W., D.A. Stevens, S. Sheng, T.L. Monchesky, R. Loebel, R.T. Atanasoski, A.K. Schmoedel, G.D. Vernstrom, M.K. Debe, J.R. Dahna, *J. Electrochem. Soc.* **2005**, 152, A61-72.
- (32) Crichton, R. R.; Wilmet, S.; Legssyer, R.; Ward, R. J. *J Inorg Biochem.* **2002**, 91, 9-18.
- (33) Wu, J.; Walukiewicz, W.; Yu, K. M.; Ager, J. W.; Haller, E. E.; Lu, H.; Schaff, W. J.; Saito, Y.; Nanishi, Y. *Appl. Phys. Lett.* **2002**, 80, 3967-3969.
- (34) Skotland, T.; Sontum, P. C.; Oulie, I. *J. Pharmaceut. Biomed.* **2002**, 28, 323-329.
- (35) Arbab, A. S.; Wilson, L. B.; Ashari, P.; Jordan, E. K.; Lewis, B. K.; Frank, J. A. *Nmr. Biomed.* **2005**, 18, 383-389.
- (36) Delalande, M.; Marcoux, P. R.; Reiss, P.; Samson, Y. *J. Mater. Chem.* **2007**, 17, 1579-1588.
- (37) Bilensoy, E. *Expert. Opin. Drug. Deliv.* **2010**, 7, 795-809.
- (38) Han, G.; Mokari, T.; Ajo-Franklin, C.; Cohen, B. E. *J. Am. Chem. Soc.* **2008**, 130, 15811-15813.
- (39) Mei, B. C.; Susumu, K.; Medintz, I. L.; Mattoussi, H. *Nat. Protoc.* **2009**, 4, 412-423.
- (40) Conner, S. D.; Schmid, S. L. *Nature*. **2003**, 422, 37-44.
- (41) Mailander, V.; Landfester, K. *Biomacromolecules*. **2009**, 10, 2379-2400.
- (42) Dausend, J.; Musyanovych, A.; Dass, M.; Walther, P.; Schrezenmeier, H.; Landfester, K.; Mailander, V. *Macromol. Biosci.* **2008**, 8, 1135-1143.
- (43) Swanson, J. A.; Watts, C. *Trends. Cell. Biol.* **1995**, 5, 424-428.
- (44) Kirkham, M.; Parton, R. G. *Biochim. Biophys. Acta*. **2005**, 1745, 273-286.
- (45) Arbab, A. S.; Bashaw, L. A.; Miller, B. R.; Jordan, E. K.; Lewis, B. K.; Kalish, H.; Frank, J. A. *Radiology*. **2003**, 229, 838-846.
- (46) Arbab, A. S.; Yocum, G. T.; Wilson, L. B.; Parwana, A.; Jordan, E. K.; Kalish, H.; Frank, J. A. *Mol. Imaging*. **2004**, 3, 24-32.

- (47) Wang, L. J.; Wang, Z. G.; Frank, T. G.; Brown, S. I.; Chudek, S. A.; Cuschieri, A. *Nanomedicine-Uk*. **2009**, 4, 305-315.

Chapter 7

Conclusion

Due to their unique magnetic and thermal properties, magnetic NPs offer unique opportunities for magnetic separation, targeted drug delivery, and hyperthermic ablation of cancer and as contrast agents in magnetic resonance imaging (MRI). While iron oxide NPs have been explored as important nano-magnetic materials for a wide range of biomedical applications over the past two decades, iron platinum (FePt) metallic alloy NPs have recently emerged as promising candidates for a new generation of magnetic nano-medicine. Control of composition and crystalline structure are among the main challenges faced by scientists working at synthesizing FePt NPs. In the context of this PhD study, three main approaches have been applied to synthesize FePt NPs before focusing on their toxicity and properties as MRI contrast agent.

In Chapter 4, a systematic investigation of low temperature aqueous solution syntheses focusing on the stoichiometry and the composition of FePt NPs was presented. A quaternary system based on water, isooctane, and Brij52 as non-ionic surfactant and butanol as a co-surfactant was used. A precise composition analysis

of individual NPs was carried out and revealed an inhomogeneous distribution of Fe and Pt between particles. By combining characterization techniques including ICP-OES, XRD, EFTEM and nanoSTEM-EDX, this investigation revealed a two-stage growth mechanism of the NPs. Primary Pt rich nanocrystals first nucleate in a supersaturated solution and then keep on growing and coalescing into larger knobbly particles. Polydomain Pt rich NPs are already formed after 15 min of synthesis. While excess of Fe is found in film-like material. Extending reaction time up to 16 h lead to larger NPs but did not alter the Fe to Pt ratio because the competitive hydrolysis of the iron precursors is completed within 15 min. The major limiting parameters are iron salts hydrolysis and a mismatch in the co-reduction kinetic of the two salts used to form the alloy. This was confirmed by using the less hydrolytically unstable Fe^{II} precursors and the faster reducing agent, NaBH_4 which could level off part of the reaction kinetic difference between Pt and Fe precursors. Both approaches increased the iron content of the nanoparticles from 15% to ~34%. It was concluded that while a degree of control is possible, to obtain better stoichiometry in FePt NPs synthesized at room temperature, future investigations should first focus on overcoming the formation of hydrolytically unstable iron complexes, preferably by working in the absence of water.

Based on the knowledge and experience learned from the FePt NPs synthesis in aqueous solution, a modified thermal decomposition method was developed for FePt NPs synthesis in Chapter 5. By using benzyl ether as a high-boiling organic solvent with $\text{Na}_2\text{Fe}(\text{CO})_4/\text{Pt}(\text{acac})_2$ in the presence of oleic acid and oleylamine, uniform, well dispersed and close 1 to 1 iron to platinum ratio *fcc*-FePt NPs were obtained. The Fe^{2-} precursor can act as a reducing agent for $\text{Pt}(\text{acac})_2$, through the reaction $\text{Fe}^{2-} + \text{Pt}^{2+} \rightarrow \text{Fe} + \text{Pt}$, thus simultaneous generation of iron and platinum can be expected. In addition, the potential of ionic liquids (ILs), as novel solvents for FePt NPs synthesis was explored. ILs are low-melting organic salts, many of which

are liquid over a wide range of temperature, and can be used as solvents for numerous inorganic and organic materials.⁷⁻¹¹ The results indicate that ILs can not only be used as a solvent for high temperature synthesis of FePt NPs, but also can provide an exciting alternative pathway to direct synthesis *fcc*-FePt NPs. Extension of this work will need to focus on gaining further insight into *fcc*-FePt formation mechanism in ILs, reduce NPs aggregation and control the polydispersity of *fcc*-FePt NPs.

In Chapter 6, the bioapplication of FePt NPs as MRI contrast agents was investigated. A family of FePt NPs including cysteamine coated *fcc*, *fcc* FePt NPs and silica coated *fcc* FePt were specifically designed as model NPs to determine their toxicity parameters and assess the criteria needed to optimise the nano MRI contrast agent architecture. The reduction of magnetic properties observed with *fcc*-FePt-A NPs prepared via annealing of silica coated NPs was attributed to the formation of silicides. Although widely used, this approach can be extremely detrimental to the targeted biomedical applications as shown in this work. Thus, research should focus on both direct *fcc*-FePt synthesis and buffer layers engineering to prevent atomic diffusion. In contrast with previous reports, this work demonstrated that FePt NPs could be made non-toxic at the NP concentration as high as 30 $\mu\text{g/mL}$. TEM revealed that positively charged FePt NPs can efficiently enter tumour cells without requiring any external mediation. The cellular uptake by non-phagocytic tumour cells occurs via an apparent macropinocytosis mechanism. The 7.1 T MRI studies, *in-vitro* and *in-vivo*, confirmed that both *fcc*-FePt-A and *fcc*-FePt-silica-A NPs are stronger T_2 contrast agents than commercial Feridex, with *fcc*-FePt-A T_2 relaxivity (r_2) being more than six times larger. The superior chemical stability and capability of MRI contrast enhancement of FePt NPs makes them an ideal platform for the design of diagnostic and therapeutic agents for image-guided magnetic drug delivery and hyperthermic tumour ablation.

In summary, different synthetic approaches for FePt NPs synthesis have been investigated. Whereas the aqueous media pathway is compromised by the hydrolysis of the iron precursor, the thermal decomposition method appears to be more promising to synthesize FePt NPs with controlled stoichiometry. In parallel, ILs have been demonstrated can not only be used as solvents for FePt NPs synthesis, but also can provide an exciting alternative pathway to synthesize *fct*-FePt NPs directly. As often when identifying new potentials for a chemical pathway, more work is needed to better understand the *fct*-FePt formation mechanism in ILs. For bioapplications of FePt NPs, it was demonstrated that FePt NPs could be made non-toxic at concentration used in the clinical environment. FePt NPs showed 6 times stronger MRI T_2 contrast effect than Feridex, which makes them an ideal platform for the development of multifunctional diagnostic and therapeutic nano-tools in biomedicine.

Appendix

Appx. I. Experimental Methods for Chapter 4

Appx. I.1. Materials

All chemical reagents, unless otherwise stated, were purchased from Sigma (Poole, UK). All chemicals were degassed before use. Iron (III) chloride (FeCl_3 , reagent grade, 97%), iron (II) chloride (FeCl_2 , anhydrous, beads, 99.9% trace metals basis), iron (II) acetate ($\text{Fe}(\text{CO}_2\text{CH}_3)_2$, 99.995% trace metals basis), Iron(III) nitrate nonahydrate ($\text{Fe}(\text{NO}_3)_3 \cdot 9\text{H}_2\text{O}$, ACS reagent, $\geq 98\%$), potassium tetrachloroplatinate (II) (K_2PtCl_4 , 98%), sodium hexachloroplatinate (IV) hexahydrate ($\text{Na}_2\text{PtCl}_6 \cdot 6\text{H}_2\text{O}$, 98%), hydrazine monohydrate ($\text{N}_2\text{H}_4 \cdot \text{H}_2\text{O}$, reagent grade, 98%), sodium borohydride (NaBH_4 , ReagentPlus[®], 99%), polyethylene glycol hexadecyl ether, Brij52 ($\text{C}_{16}\text{H}_{33}(\text{OCH}_2\text{CH}_2)_2\text{OH}$, average $M_n \sim 330$ kD), 1-dodecane thiol ($\text{CH}_3(\text{CH}_2)_{11}\text{SH}$, $\geq 98\%$), isooctane (ACS reagent, $\geq 99.0\%$), hexane (ACS reagent, 99.0%), ethanol (ACS reagent, $\geq 99.5\%$), methanol (ACS reagent, $\geq 99.8\%$), HCl (Trace SELECT[®], $\geq 37\%$) and HNO_3 (Trace SELECT[®], $\geq 69.0\%$).

Appx. I.2. FePt Nanoparticles Synthesis

In a typical synthesis, a surfactant (Brij52) solution (0.3 mol/L) was prepared by mixing isooctane (20 mL), Brij52 (1.98 g) and butanol (110 μ L) in a surfactant to alcohol molar ratio of 5:1. Dissolution was obtained after 15 min sonication. K_2PtCl_4 (277 mmol/L) and $FeCl_3$ (277 mmol/L) aqueous stock solutions were added to the amphiphilic system to obtain equal $[Pt^{2+}]$ and $[Fe^{3+}]$ concentration (2.5 mmol/L). 30 min sonication was then applied, followed by injection of $N_2H_4.H_2O$ to reach a molar ratio of $[N_2H_4.H_2O] / [Fe+Pt] = 40$.

The hydration, w , is the molar ratio of water to surfactant molecules,

$$w = [H_2O] / [Brij52] \quad \text{eq.(1)}$$

and the final w is reached 4 after addition of hydrazine monohydrate. The system was stirred at 30 $^{\circ}C$ for 3 h. Dodecane thiol was then injected and the solution aged for further 15 min. The NPs were then precipitated by adding alcohol, and collected by centrifugation. This extraction step was repeated several times.

A similar protocol was followed when the syntheses were completed with different iron and platinum precursors and a different reducing agent.

Appx. I.3. Characterization Techniques

Impedance spectroscopy was used to quantify the electrical conductivity of the amphiphilic solutions. All samples had a surfactant concentration of $[Brij52] = 0.3$ mol/L, and a surfactant to co-surfactant ratio of $[Brij52] / [butanol] = 5$. Water content, w , was varied from 1 to 6. The investigation of electrochemical properties of non-ionic amphiphilic systems is notoriously difficult due to the lack of charge

carriers. Therefore a dilute salt solution (10^{-3} mol/L NaCl in this work) is typically used instead of water to provide sufficient charge carriers to allow a detectable signal to be obtained while making sure the chemical phase behavior is not affected.¹ The electrochemical test cell consisted of two disk-shaped electrodes within a thermally regulated cylindrical container. The test sample was placed between these electrodes and the height of the upper electrode was adjusted to bring it into contact with the upper surface of the solution to be tested. The temperature was controlled at 30 ± 1 °C using a closed loop circulating water heating system.

Impedance can be expressed as the sum of a real (Z') and an imaginary (Z'') component.

$$Z = Z' + jZ'' \quad \text{eq.(2)}$$

Z' relates to the resistive properties of a sample while z'' is related to the reactive elements, that is capacitances and inductances. Impedance spectra are obtained by sweeping the frequency over a wide range, so causing variations in the values of Z' , Z'' and Z .² Such spectra are conveniently presented as so-called Nquist plots in which Z'' is plotted against Z' . Such impedance spectra were obtained using a Solartron 1260 Frequency Response Analyser operating in two-electrode mode and run using ZPlot software. An a.c. potential of amplitude 400 mV was applied over a frequency range of 0.5 Hz to 1 MHz. The resulting Nyquist spectra contained approximately semicircular features which can be fitted to an equivalent electronic circuit model consisting of a resistance, R , and a capacitance, C , connected in parallel. The distance between the two intercepts of the semicircular arc with the Z' axis gives the value of R . C is related to the value of signal frequency, f (Hz), at the maximum height of the arc

where:²⁻³

$$C = \frac{I}{2\pi fR} \quad \text{eq.(3)}$$

Values of R and C were extracted from the impedance data using this fitting procedure in the ZView software package. The conductivity k (S/cm) of the solutions were calculated according to the following equation:³

$$k = \frac{d}{AR} \quad \text{eq.(4)}$$

where d (cm) is the distance between the electrodes and A (cm²) the effective area of the electrodes. In this experiment, the electrode radii were 1 cm and the distance between the electrodes was set to 0.3 cm. Standard deviation values of the conductivity were obtained by repeating each impedance measurement 3 times and fitting each resulting spectrum separately.

Inductively Coupled Plasma Optical Emission Spectroscopy (ICP-OES) measurements were completed with a Perkin Elmer Optima 5300 DV spectrometer. FePt NPs were dissolved overnight at room temperature by addition of hydrochloric acid (Trace SELECT®, ≥37%) and nitric acid (Trace SELECT®, ≥ 69.0%) mixed in 3:1 volume ratio (aqua regia). After full dissolution of the NPs, the solutions were further diluted with deionised water.

Wide-angle powder X-ray diffraction (XRD) spectra were collected on a Stoe STADI/P powder diffractometer operating in transmission mode and with a small angle position sensitive detector. The peaks were fitted by Lorentzians with STOEwinXpow and Kaleida-Graph software to determine the peak positions and

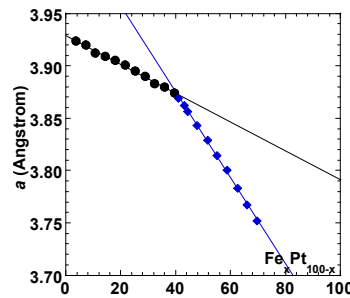
width. The crystalline grain size equivalent to the “average” dimension of the crystallites, D_{XRD} , of the FePt NPs was calculated according to Scherrer’s formula:

4

$$D_{\text{XRD}} = 0.9\lambda / (B \cos\theta) \quad \text{eq.(5)}$$

where $\lambda = 1.936 \text{ \AA}$ corresponding to the wavelength of the incident X-ray radiation generated using a $\text{Fe}_{\text{K}\alpha 1}$ source, B is the full width at half maximum of the peak intensity (FWHM), θ is the glancing angle.⁴ D_{XRD} is determined based on (111), (200) and (220) peaks.

The composition of $\text{Fe}_x\text{Pt}_{1-x}$ NPs was deduced from the published variation of the *fcc*-FePt lattice constant with the alloy composition (Appx.Fig. 1).⁵



Appx.Fig. 1 FePt lattice constant (*a*) analyzed by XRD vs. composition curve. Data were extracted from ref.⁵ (Reprinted with permission from ⁽⁶⁾). Copyright 2010 American Chemical Society.)

Appx.Fig. 1 leads to the following equations:

$$x\%_{\text{Fe}} < 40\% \quad a = -0.0014 x\%_{\text{Fe}} + 3.929 \quad \text{eq.(6)}$$

$$x\%_{\text{Fe}} > 40\% \quad a = -0.0041 x\%_{\text{Fe}} + 4.039 \quad \text{eq.(7)}$$

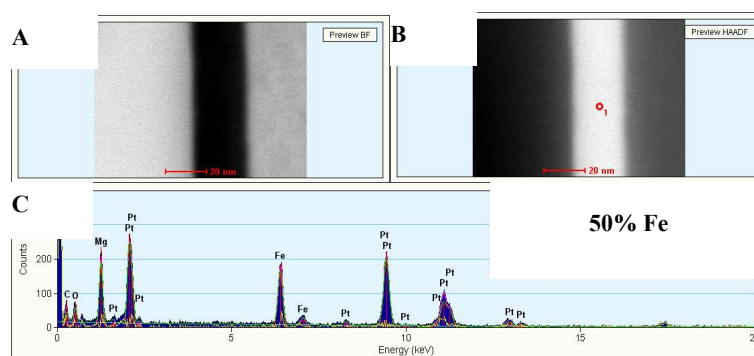
It is noticeable that the alloys used by Bonakdarkpour *et al* were prepared by sputtering of Fe and Pt sources. Ideally nanoparticles and not films would have been used for us to compare with. However, at the moment, there is not a

consistent set of data available in the literature covering size, composition and surface chemistry of colloidal FePt NPs. At the current stage of development of FePt alloy NPs controlling the size and composition is already a challenge, as illustrated by our report, and using vacuum depositing films of $\text{Fe}_x\text{Pt}_{100-x}$ provides the most reliable reference to compare our material with.

In our study, a was determined based on (111), (200) and (220) peaks to reduce potential risks of systematic error compared to a single peak analysis. A Rietveld approach could have been used as an alternative, however it would have been more time consuming without necessarily increasing the data precision.⁷

Transmission electron microscopy (TEM) was conducted on an FEI Tecnai F20 transmission electron microscope equipped with a field emission gun and operating at 200 kV.

Nanometer scale scanning transmission electron microscopy and energy dispersive X-ray Energy dispersive X-Ray analysis was performed in both TEM and STEM modes using an EDAX spectrometer. Fe and Pt composition ratios were determined by comparing the intensity of K_α and L_α EDX peaks from a thin film FePt sample of known stoichiometry. Appx.Fig. 2A and B shows respectively the bright/dark field image of a well-characterised *fcc*-FePt - 1:1 Fe:Pt ratio - grown by molecular beam epitaxy (MBE) on MgO substrate.⁸ The red box in Appx.Fig. 2B indicates the area from where the nanoSTEM-EDX spectrum was obtained. The reference spectrum was shown in Appx.Fig. 2C, the ratio of Fe K_α at 6.398 keV and Pt L_α at 9.441 keV is about 0.8 ± 0.1 and was used as a reference to determine the composition of FePt NPs samples at a nanometer scale.



Appx.Fig. 2 Bright field STEM picture (A), corresponding high angle annular dark field (HAADF) STEM image with red squares indicating areas analyzed by nanoSTEM-EDX (B) and EDX spectra (C) of a 1:1 Fe:Pt ratio MBE-grown FePt(L1₀)/MgO sample.

False-coloured energy filtered TEM (EF-TEM) images were obtained by using the Pt-M_{4,5} and Fe-L_{2,3} EELS edges, respectively, to map and overlap Pt and Fe rich areas.

A **superconducting quantum interference device (SQUID)** magnetometer (MPMS XLTM from Quantum Design) was used to characterize the NPs magnetic properties. Zero-Field Cooled and Field Cooled (*ZFC/FC*) measurements were completed as follows: the sample was first cooled from room temperature to 5 K without applying any external field, then a small field of 100 Oe was applied and the magnetization of NPs was recorded as the temperature was slowly increased to 275 K. The *FC* curve was obtained by cooling the sample back to 5 K while the same external field of 100 Oe was applied. The magnetization was then measured as the temperature was slowly increased to 275 K. Hysteresis measurements were completed at temperatures of 5 K and 300 K with an external field sweep from -5 to 5 Tesla.

Appx. II. Experimental Methods for Chapter 5

Appx. II.1. Materials

All chemical reagents, unless otherwise stated, were purchased from Sigma, used without further purification but degassed before use: disodium tetracarbonylferrate-dioxane complex ($\text{Na}_2\text{Fe}(\text{CO})_4 \cdot 1.5 \text{ C}_4\text{H}_8\text{O}_2$), platinum(II) acetylacetonate ($\text{Pt}(\text{acac})_2$, 97%), oleylamine (70%), oleic acid (90%). When it is available, ACS grade was chosen to select the solvents: dibenzyl ether ($\geq 98.0\%$), hexane (99.0%), ethanol ($\geq 99.5\%$) and chloroform ($\geq 99\%$, anhydrous).

Appx. II.2. Synthesis

Ionic liquids (ILs were provided by Dr. Mark Muldoon and Dr Kris Anderson from University of Belfast): Trihexyl(tetradecyl)phosphonium bis{(trifluoromethyl)sulfonyl}. amide ($[\text{P}_{66614}][\text{NTf}_2]$) was prepared by mixing trihexyl(tetradecyl)phosphonium chloride ($[\text{P}_{66614}]\text{Cl}$) (supplied by Cytec) with a slight excess (5 mol%) of $\text{Li}[\text{NTf}_2]$ which had been dissolved in de-ionized water. After stirring for 3 hours the hydrophobic $[\text{P}_{66614}][\text{NTf}_2]$ was washed with portions of de-ionized water to remove LiCl and excess $\text{Li}[\text{NTf}_2]$. After the aqueous washings were found to be chloride free by testing with silver nitrate (AgNO_3), the IL was washed a further twice. The resulting IL was then dried, first using a rotary evaporator, followed by further drying under high vacuum while heating at 70°C . The water content of the dried IL was found to be less than 400 ppm, and its structure was confirmed by ^1H NMR and ^{13}C NMR.

FePt NPs: All the syntheses were completed under inert atmosphere. In a typical reaction, $\text{Na}_2\text{Fe}(\text{CO})_4$ (0.2 mmol) and a mixture of $\text{Pt}(\text{acac})_2$ (0.2 mmol), oleyl

amine (1.6 mmol) and oleic acid (0.8 mmol) were dissolved in separate jars containing 2 mL of $[P_{66614}][NTf_2]$ used as a solvent. After stirring at 100 °C for 1 h, the two solutions were mixed together and the temperature rose up to 150 °C for 1 h. To initiate the reaction, the temperature of the solution was further increased up to 300-340 °C with a heating rate of 15 °C/min. After reaction, the solution was cooled down to room temperature. NPs were then precipitated by ethanol addition and centrifugation. The supernatant was discarded, while the sediment was dispersed in hexane, and precipitated two more times with ethanol and centrifugation.

For reaction time investigation experiments: aliquot NPs solutions were extracted to monitor the NPs growth mechanism at different reaction temperature and time. The reaction was quenched by mixing sample solution with ethanol immediately once taken from the reaction system.

Additional precursor injection protocol: synthesis was started with 4 mL of 0.025 M $Na_2Fe(CO)_4$ and $Pt(acac)_2$, $[oleylamine]/[Pt(acac)_2] = 16$, $[oleic\ acid]/[Na_2Fe(CO)_4] = 8$, heating rate = 5 °C/min. After heating the main solution to 300 °C for 0.5 h, additional Fe and Pt precursor solution was injected drop wise for a period of 0.5 h. The additional Fe and Pt precursors solution were injected according to following sequence: $Na_2Fe(CO)_4$ was added into 1 mL ionic liquid, $[Na_2Fe(CO)_4] = 1$ M. In another separate jar, Pt precursor and surfactants were added into 1 mL ionic liquid as well, $[Pt(acac)_2] = 1$ M, $[oleylamine] / [Pt(acac)_2] = 8$, $[oleic\ acid] / [Na_2Fe(CO)_4] = 4$. Both mixtures were kept at 100 °C for 0.5 h for dissolving purposes, mixed and stirred for 3 min before injection. After the slow injection of additional precursors, the final $[Na_2Fe(CO)_4] = [Pt(acac)_2] = 0.05$ M. The reaction solution was kept at 300 °C for another 0.5 h.

Appx. III. Experimental Methods for Chapter 6

Appx. III.1. FePt Nanoparticles Preparation

Materials: All chemical reagents, unless otherwise stated, were purchased from Sigma, used without further purification but degassed before use: disodium tetracarbonylferrate-dioxane complex ($\text{Na}_2\text{Fe}(\text{CO})_4 \cdot 1.5 \text{ C}_4\text{H}_8\text{O}_2$), platinum(II) acetylacetonate ($\text{Pt}(\text{acac})_2$, 97%), oleylamine (70%), oleic acid (90%), cysteamine (CA, $\text{HSCH}_2\text{CH}_2\text{NH}_2$, BioChemika, $\geq 98.0\%$), tetraethylorthosilicate (TEOS, $\text{Si}(\text{OC}_2\text{H}_5)_4$, GC, $\geq 99.0\%$), (3-Aminopropyl)triethoxysilane (APTES, $\text{H}_2\text{N}(\text{CH}_2)_3\text{Si}(\text{OC}_2\text{H}_5)_3$, $\geq 98\%$), IGEPAL® CO-520 (NP-5, $(\text{C}_2\text{H}_4\text{O})_n \cdot \text{C}_{15}\text{H}_{24}\text{O}$, $n \sim 5$). When it is available, ACS grade was chosen to select the solvents: dibenzyl ether ($\geq 98.0\%$), hexane (99.0%), ethanol ($\geq 99.5\%$), chloroform ($\geq 99\%$, anhydrous), methanol ($\geq 99.8\%$), cyclo-hexane (GC, $\geq 98.0\%$), ammonium hydroxide aqueous solution (NH_4OH , 28.0 - 30.0%).

***fcc*-FePt NPs synthesis:** All the syntheses were carried out inside a glove box. A mixture of $\text{Pt}(\text{acac})_2$ (1 mmol), oleyl amine (8 mmol) and oleic acid (4 mmol) in 10 mL of dibenzyl ether was placed in a 50 mL round bottom flask connected to a condenser. Under stirring, the mixture was heated up to 100 °C for 1 h to remove oxygen and moisture, then $\text{Na}_2\text{Fe}(\text{CO})_4$ (1 mmol) in 10 mL dibenzyl ether mixture was added and heated up to 150 °C for 1h. The mixture was further heated up to reflux ~ 300 °C to for 3 h. The dark solution was cooled down to room temperature and after washing with hexane and ethanol, the NPs were collected by centrifugation.⁹

***fcc*-FePt-A preparation:** Ligand exchange experiments were carried out in a glove box according to a modified protocol based on the literature.¹⁰ For a typical experiment, 30 mL hexane was added into 3 mL (13.5 mg/mL) of as-synthesized oleic acid/ oleylamine coated *fcc*-FePt hexane solution. To remove the excess of

ligands, the NPs were precipitated by addition of 60 mL ethanol and collected by centrifugation. The NPs were redispersed in 15 mL of chloroform assisted with sonication. 15 mL of cysteamine in methanol solution (0.5 M) was added dropwise to the FePt NPs/ CHCl_3 mixture under vigorous stirring. The final solution was left under stirring for 48 h to complete the ligand exchange. To extract the NPs, they were redispersed in 10 mL ethanol and sonicated, 20 mL hexane was added and the solution was centrifuged. This process was repeated twice to remove CHCl_3 , methanol and the excess of ligands. The NPs were then redispersed in 10 mL ethanol and 20 mL deionized water mixture, sonicated and collected by centrifugation. This step was repeated 6 times to obtain positively charged NPs stable in deionized water for more than 8 months.

***fcc*-FePt-silica-A NPs preparation:** The *fcc*-FePt-silica-A NPs were prepared by hydrolysis of tetraethylorthosilicate (TEOS) and the silica shell surface was further functionalized with (3-aminopropyl) triethoxysilane.¹¹ Reverse microemulsions were prepared by mixing under vigorous stirring 10 mL cyclohexane, 1.3 mL NP-5 and 50 μL DI H_2O . 2 mg ($\sim 3\text{--}4$ nmol) of FePt NPs were then dispersed in 1 mL cyclohexane and added dropwise into the reverse microemulsion. After 15 min, 80 μL TEOS was added dropwise. After another 15 min, 150 μL $\text{NH}_4\text{H}_2\text{O}$ (28-30%) was added dropwise. The solution was kept under constant stirring at 250 rpm for 72 h. To form amine functionalized FePt-silica NPs, 100 μL of APTES was added after 48 h and kept stirring for another 24 h. The NPs were precipitated by centrifugation after addition of 3 mL of ethanol and 2 mL of methanol. The NPs were redispersed in 5 mL of ethanol and precipitated by centrifugation after addition of 10 mL of hexane. This step was repeated up to 6 times to completely remove the surfactant. FePt-silica NPs were stable both in ethanol and DI water, while FePt-silica-A NPs were stable in deionized water.

***fct*-FePt-A NPs preparation:** 16 mL 4 M NaOH water solution contains 1.2 g of cysteamine was added into fine milled 170 mg *fct* FePt-silica NPs. The mixture was kept under vigorous stirring for 48 h to dissolve the silica shell as well as to functionalize the NP surface with cysteamine. After addition of 10 mL ethanol, the NPs were collected by centrifugation. NPs were extracted by centrifugation after further washing with 10 mL DI H₂O, 20 mL of ethanol.

Appx. III.2. FePt Nanoparticles Characterization

TEM: TEM images were recorded using a Gatan CCD camera on a JEOL JEM-2011 electron microscope operating at 200 kV. The chemical composition of FePt NPs was examined with energy-dispersive X-ray spectroscopy (EDX) using an Oxford Link system installed in the JEM-2011 microscope.

XRD: *fct* ordering parameter after annealing can be calculated with intensity ratio of (110) and (111) peaks, based on the eq. (8),¹²

$$S^2 = \frac{\{I_{(110)}/I_{(111)}\}_{obs}}{\{I_{(110)}/I_{(111)}\}_{bulk}} \quad \text{eq. (8)}$$

where S is chemical ordering parameter widely used to characterized the *fcc* to *fct* phase transition, varies from *fcc* ($S = 0.0$) to *fct* ($S = 1.0$). I is intensity of XRD diffraction peaks, $\{I_{(110)}/I_{(111)}\}_{obs}$ is the ratio of observed intensity ratio of (110) and (111) peaks, which is about 0.12. And $\{I_{(110)}/I_{(111)}\}_{bulk}$ is about 0.27 obtained based on PDF library card 03-065-9121.

SQUID: The NPs were dispersed in polyvinylpyrrolidone (PVP) matrix ($V_{Polymer}/V_{NPs} = 20$) to prevent interaction between the NPs while the resulting

sample was loaded into a low background gelatin capsule. Zero-Field Cooled and Field Cooled (ZFC/FC) measurements were completed as follow: the sample was first cooled from room temperature to 2 K without any external field, next a small field 100 Oe was applied and the NPs magnetization was recorded as the temperature was increased up 275 K. The FC curve was obtained by cooling the sample back to 2 K under a 100 Oe magnetic field. The magnetization was then measured while the temperature was increased up to 275 K. Hysteresis measurements were completed at temperatures of 2 K and 300 K. The magnetization of the gelatine capsules and the PVP matrix was subsequently subtracted.

ICP-OES (Perkin Elmer Optima 5300 DV): FePt NPs were dissolved by addition of hydrochloric acid (Trace SELECT®, $\geq 37\%$) and nitric acid (Trace SELECT®, $\geq 69.0\%$) mixed in 3:1 as volume ratio and left overnight at room temperature. After full dissolution of the NPs, the solution was further diluted with DI water for ICP-OES measurements.

The conversion of the weight concentration of FePt metal core into Fe molar concentration was completed according to the following equation:

$$[Fe] = \frac{C_{FePt} R_{Fe}}{M_{w-Fe}} \quad \text{eq. (9)}$$

where $[Fe]$ (mM) is the molar concentration of iron, C_{FePt} ($\mu\text{g/mL}$) is the FePt core concentration, M_{w-Fe} the molecular weight of the iron atom and R_{Fe} is the mass ratio of Fe in FePt metal core. The x in $\text{Fe}_x\text{Pt}_{1-x}$ NPs was found to be ~ 0.43 by XRD/ICP-OES, which implies that the mass ratio of Fe in the NP core is ~ 0.18 as obtained from the equation below:

$$R_{Fe} = \frac{xM_{w-Fe}}{xM_{w-Fe} + (1-x)M_{w-Pt}} \quad \text{eq. (10)}$$

A similar approach was used for *fcc*-FePt-silica-A NPs as described by eq. (11):

$$[Fe] = \frac{C_{FePt-silica-A} R'_{Fe}}{M_{w-Fe}} \quad \text{eq. (11)}$$

where $[Fe]$ (mM) is the molar concentration of iron, $C_{FePt-silica-A}$ is the concentration of FePt-silica-A in $\mu\text{g/mL}$, R'_{Fe} is the mass ratio of Fe in FePt-silica-A NPs which is ~ 0.01 according to eq. (12),

$$R'_{Fe} = yR_{Fe} \quad \text{eq. (12)}$$

where y is the mass ratio of FePt in FePt-silica-A NPs, i.e. $[\text{Fe}_x\text{Pt}_{1-x}]_y[\text{silica-A}]_{1-y}$, which was found to be ~ 0.052 by ICP-OES. According to eq.(11) and (12), the weight concentration of FePt-silica-A NPs at $100 \mu\text{g/mL}$ corresponds then to $\sim 0.02 \text{ mM}$ of Fe in molar concentration.

Appx. III.3. Cell culture

Materials: Human breast adenocarcinoma cell line MCF7 (ATCC; Cat# HTB-22), human osteosarcoma cell line U2OS (ATCC; Cat# HTB-96) were grown in Dulbecco's Modified Eagle Medium (DMEM; GIBCO, Invitrogen, Paisley, UK). Human malignant melanoma cell line A-375M was kindly provided by Dr Daniele Bergamaschi (Institute of Cell and Molecular Science, Barts and The London,

Queen Mary's School of Medicine and Dentistry) and was grown in RPMI-1640 medium (GIBCO, Invitrogen). All media were supplemented with 10% fetal calf serum, 2 mM glutamine, 100 IU/mL penicillin, and 100 µg/mL streptomycin. Cells were grown under standard cell culture conditions in 5% CO₂ at 37 °C to reach confluence of 60-70% before subjected to any further treatments.

Cellular labeling/uptake of FePt NPs and TEM: Cell culture media were removed and replaced with the media containing FePt-A (30 µg/mL). For control experiments, media without FePt NPs was used. After 12-16 h of culture, cells were washed and fixed with 4% (w/v) paraformaldehyde/2.5% (v/v) glutaraldehyde buffered in 0.2 mol/L PIPES as a standard buffer solution. After 30 min in fixative the cells were scraped off the flasks in 1 mL of fixative, transferred to Eppendorf tubes and centrifuged at 14000 g for 20 min. Pellets were washed in 0.2M PIPES and post fixed in 1% aqueous osmium tetroxide for 1 h, washed in water, and dehydrated in graded ethanol and propylene oxide before embedding in Durcupan resin (Sigma) and polymerisation at 60 °C for 24 h. 70 nm sections were cut on a Leica UCT ultramicrotome, mounted on Pioloform coated 100 mesh copper grids, stained with uranyl acetate and lead citrate before being examined in a Tecnai 12 electron microscope. Images were recorded in Digital Imaging Plates and scanned in a Ditabis Micron scanner (Pforzheim, Germany).

Cell viability study by MTS assay: The MTS CellTitre 96 AQueous One Solution Cell Proliferation Assay (Promega, *Southampton, UK*) was used to determine cell viability in control and FePt NPs treated cells. This colorimetric assay is based on the conversion of the 3-(4,5-dimethylthiazol-2-yl)-5-(3-carboxy methoxy-phenyl)-2-(4-sulfophenyl)-2H tetrazolium (MTS) compound to a colored, soluble formazan product in metabolically active cells. Cells were seeded at densities 1,250-10,000 cells/well in 96-well plates depending on the duration of

incubation time and cultured overnight. Cell culture media were then removed and replaced with the media containing the FePt NPs at various concentrations with the iron content being determined by XRD and ICP-OES. For control experiments, media without FePt NPs was used. MTS assay was performed at specific time intervals by addition of CellTiter 96[®] AQueous One Solution reagent to each well, in triplicate, and further incubation of cells with the reagent for 3 h at 37 °C in 5% CO₂. The colour development, i.e. absorbance, was read at 490 nm using a plate-reader (E-Max; Molecular Devices, CA, USA) and absorbance values of both labelled and control cells were subtracted by that of blank wells. Cell viability in labelled cells was expressed as percentage of that from the corresponding control cells.

Fe release experiment: 3.6 mg (~ 0.6 mg Fe) of FePt *fcc*-FePt-A NPs in aqueous solution was dispersed in a dialysis tubing (MWCO 1000, Spectrum Laboratories, Inc.) which was further immersed into a 30 mL PBS (pH 4.8) or RPMI-1640 (20 mM sodium citrate, pH 4.8) bath held at a constant temperature of 37 °C. 7-8 Aliquot buffer solution was then sampled at 6, 12, 24, 48, 72, 148 h, and its composition was subsequently analyzed with ICP-OES.

Prussian blue staining and light microscopy analysis: To gain insight in intracellular iron ions distribution, cells grown on glass coverslips or cytopun on glass slides were washed with PBS to remove the excess of ferumoxides and then fixed with 4% para-formaldehyde for 30 min. They were then washed with double distilled water (ddH₂O) and incubated for 30 min with 2.5% potassium ferrocyanide in 2.5% HCl to produce Fe(III) ferrocyanide (Prussian blue). Samples were then counterstained with nuclear fast red for cell nuclei. Cells were examined using a Zeiss microscope Axiovert 200 (Zeiss, Oberkochen, Germany) at x20, x40 and x63 magnification and Axiovision 4.6 software (Zeiss). Cells were

considered Prussian blue positive if intracytoplasmic blue granules could be identified.

Preparation of Agarose Gel Phantoms for MRI of FePt NPs and FePt

NP-labeled Cells: In the gel MRI study, 1% (w/v) low melting point agarose was dissolved in deionized water at 60-70 °C. The desired amount of NPs, i.e. Fe concentration as determined by XRD and ICP-OES was then added to the solution to obtain the targeted concentrations (up to 0.25 mM) and mixed gently. For cellular MRI, FePt labelled melanoma A375M cells were washed three times with PBS and harvested, suspended in low melting point agarose gel (1% in PBS at densities of 10^4 , 10^5 , 10^6 cell/mL, respectively. Samples were then transferred into 200 μ L thin wall tubes. In both cases, samples were rapidly cooled on ice to form homogenous gel suspensions and kept at 4 °C until further experiments.

Quail Eggs Preparation: Fertilized Japanese quail (*Coturnix japonica*) eggs were obtained from Rosedean, Huntingdon, Cambs. The eggs were then placed vertically with air sac uppermost in a humidified incubator with a temperature of 38 °C, this was referred to as Day 0. On Day 4, the shell above the air sac was pierced and cut away to remove the inner shell membrane and expose the embryo. The Day 4 embryos typically lay on their sides, the upper eye is visible allowing the solution containing the NPs to be injected into it using syringe with thin glass capillary needle. The top of the eggs were re-sealed with adhesive tape and then imaged. *fcc*-FePt NPs coated with either cysteamine or silica were added to cell culture media at concentrations ranging from 1-100 μ g/mL. A control medium without NPs was also used.

Appx. III.4. Micro-MRI

Micro-MRI data were acquired on a Bruker Avance FT NMR spectrometer with a wide bore 7.1 Tesla magnet resonating at 300.15 MHz for ^1H , fitted with Bruker micro-imaging magnetic field gradients. A birdcage radio frequency resonator with an internal diameter of 30 mm was used. MRI pulse sequences were taken from the Bruker Paravision® library. All acquisitions were made at 19 °C. Two acquisition sequences were collected and averaged to improve the signal-to-noise ratio and reduce artefacts.

Relaxation measurements were determined from 128 x 128 axial planes across the samples with field of view of 30 mm, in-plane resolution of 0.234 mm/pixel and image slice thickness of 1 mm. In a typical experiment, 9 tubes were studied simultaneously, gels with no contrast agent acted as a standard. A recycle time (T_R) of 12 s was used to avoid saturation. T_1 relaxation times were measured using an inversion recovery (180° - T_1 - 90°) imaging pulse sequence; 8 different inversion times (T_i) that ranged from 100 to 15000 ms were applied and the echo time (T_E) was 4 ms.

T_2 relaxation times were measured using a CPMG (Carr Purcell Meiboom Gill) spin echo imaging pulse sequence; a train of 16 echoes was acquired and the delay (τ) between 180° pulses ranged from 8 to 15 ms depending on the samples. Single exponential relaxation times were calculated from experimental data. Each sample was studied three times and average Longitudinal and transverse relaxation rate calculated.

r_i is defined as longitudinal relaxivity ($i=1$) or transverse relaxivity ($i=2$), and calculated with the following equation: eq.(13) ¹³

$$r_i[\text{CA}] = \frac{1}{T_i} - \frac{1}{T_{i0}} \quad \text{eq. (13)}$$

where $[\text{CA}]$ is the concentration of contrast agent, $1/T_i$ ($i=1$ or 2) is the longitudinal or transverse relaxation rate with the presence of contrast agent, $1/T_{i0}$ is the relaxation rate of the medium in the absence of contrast agent.

The $128 \times 128 \times 128$ three-dimensional RARE-8 (rapid acquisition with relaxation enhancement) experiments were acquired with T_R of 250 ms and TE between 180° pulses of 25 ms. The field of view was 30 mm and in-plane resolution was 0.234 mm/pixel. The scanning time was 34 minutes.

3D representation of the embryo eye and major blood vessels were produced using Amira® software (Visage Imaging, Inc. San Diego, CA USA).

Reference

- (1) Schrodle, S.; Buchner, R.; Kunz, W. *Chemphyschem.* **2005**, 6, 1051-1055.
- (2) Ed.s E. Barsoukov; J. R. MacDonald; Sons, J. W., *Impedance Spectroscopy: Theory, Experiment and Applications*. ed.; New Jersey: 2005.
- (3) Atkins, P., Julio de Paula, *Physical Chemistry*. 8th ed.; Oxford: 2006.
- (4) Azaroff, L. V., *Elements of X-ray Crystallography*. 1st ed.; McGraw-Hill, Inc.: New York, 1968.
- (5) A. Bonakdarpour, J. W., D.A. Stevens, S. Sheng, T.L. Monchesky, R. Loebel, R.T. Atanasoski, A.K. Schmoekkel, G.D. Vernstrom, M.K. Debe, J.R. Dahna, *J. Electrochem. Soc.* **2005**, 152, A61-72.
- (6) Chen, S.; Wang, L.; Duce, S. L.; Brown, S.; Lee, S.; Melzer, A.; Cuschieri, S. A.; Andre, P. *J. Am. Chem. Soc.* **2010**, 132, 15022–15029.
- (7) Pecharsky, V. K.; Zavalij, P. Y., *Fundamentals of powder diffraction and structural characterization of materials*. 2nd ed.; Springer: New York, 2009.
- (8) Seemann, K. M.; Baltz, V.; MacKenzie, M.; Chapman, J. N.; Hickey, B. J.; Marrows, C. H. *Phys. Rev. B.* **2007**, 76, 174435.
- (9) Yan, Q. Y.; Purkayastha, A.; Kim, T.; Kroger, R.; Bose, A.; Ramanath, G. *Adv. Mater.* **2006**, 18, 2569-2573.
- (10) Tanaka, Y.; Maenosono, S. *J. Magn. Magn. Mater.* **2008**, 320, L121-L124.
- (11) Koole, R.; van Schooneveld, M. M.; Hilhorst, J.; Donega, C. D.; 't Hart, D. C.; van Blaaderen, A.; Vanmaekelbergh, D.; Meijerink, A. *Chem. Mater.* **2008**, 20, 2503-2512.
- (12) Ding, Y.; Majetich, S. A.; Kim, J.; Barmak, K.; Rollins, H.; Sides, P. *J. Magn. Magn. Mater.* **2004**, 284, 336-341.
- (13) Modo, M. M. J.; Bulte, J. W. M., *Molecular and Cellular MR Imaging*. 1st ed.; CRC Press: London, 2007.

Publications

Patent

1. “Preparation of CoPt & FePt Nanoparticles”

P. André, **S. Chen**, M.J. Muldoon, K. Anderson (Filed: August 17th 2009,
Ref.P16260GB)

Publications

1. Engineered Biocompatible Nanoparticles for *in-vivo* Imaging Applications, *J. Am. Chem. Soc.*, 2010, 132 (42), 15022–15029.

S. Chen, L. Wang, S. Duce, S. Brown, S. Lee, A. Melzer, A. Cuschieri, P. André

2. Inhomogeneous Composition of Alloyed Iron-Platinum Magnetic Nanoparticles Synthesized at Low Temperature, *J. Mater. Chem.*, 2011, 21, 3646-3654.

S. Chen, D. MacLaren, R.T. Baker, J. Chapman, D.J. Cole-Hamilton, S. Lee, P. André

3. Colloidal Syntheses of FePt Nanoparticles (invited review), *J. Inter. J. Nanotech.*, in press.

S. Chen, P. André

4. Influence of Ionic Liquid on the Crystalline Structure of Nanocolloids, *CrystEngComm*, 2011, under revision.

S. Chen, M. Muldoon, K. Anderson, P. André

5. Direct *fct*-FePt Synthesis in Ionic Liquid Solutions (to be submitted)

S. Chen, M. Muldoon, K. Anderson, P. André

6. Impact of Non-Ionic Surfactants Oxyethylene Polar Group on the Synthesis of Iron-Platinum Nanoparticles (in preparation)

S. Chen, D. MacLaren, R.T. Baker, J. Chapman, D. J. Cole-Hamilton, S. Lee, P. André

7. Cellular Uptake Study on Cysteamine Functionalized FePt Nanoparticles (in preparation)

L. Wang, **S. Chen**, A. Melzer, A. Cuschieri, P. André

Oral Presentations

1. FePt Magnetic Nanoparticles Syntheses, Cell Toxicity Studies and as MRI Contrast Agent (# 1303456)

S. Chen, L. Wang, S. Brown, D. Cole-Hamilton, S. Lee, A. Melzer, Sir A. Cuschieri, P. André ; ACS 238th, Division of Colloid & Surface Chemistry (Nanoparticle-Biological Cell Interactions) ; Washington DC, USA, August 16-20, 2009

2. Synthesis of Iron Platinum Magnetic Nanoparticles in Amphiphilic Systems: Strategies to Overcome Coreduction Limits and Inhomogeneous Chemical Composition (# 1303444)

S. Chen, D. MacLaren, R. Baker, J. Chapman, D. Cole-Hamilton, S. Lee, P. André ; ACS 238th, Division of Colloid & Surface Chemistry (Patchy Particles and Surfaces of Engineered Heterogeneity: From Synthesis to Dynamic Function); Washington DC, USA, August 16-20, 2009

3. Nanoparticles Engineering for Medical Technologies

P. André, **S. Chen** ; JRI in Medical Technologies-Northern Research Partnership workshop on Nanotechnology in Medicine ; Aberdeen (Scotland) Nov. 20, 2008

Poster Presentations

1. Light Induced Hetero Nano-structures Fabrication

J.I. Baxter, P. Dayal, C. Brown, C.J. Booth, **S. Chen**, M. Ross, P. André; School of Physics and Astronomy, Presentation of research activities carried out by summer project students, St Andrews (UK), September 23, 2009

2. New Solvent: Advantages for FePt NPs Syntheses

S. Chen, M.J. Muldoon, K. Anderson, P. André; SCI Nanoparticles 2009: Synthesis, Properties and Applications of Nanoparticles, Liverpool (UK), September 02-04, 2009

3. FePt Magnetic NPs: Syntheses, Functionalization, Cell Toxicity & Application as MRI Contrast Agent

S. Chen, L. Wang, S. Duce, S. Brown, D. Cole-Hamilton, S. Lee, A. Melzer, Sir A. Cuschieri, P. André ; SCI Nanoparticles 2009: Synthesis, Properties and Applications of Nanoparticles, Liverpool (UK), September 02-04, 2009

4. Increasing Iron Ratio in Iron-Platinum Magnetic Nanoparticles Prepared in Amphiphilic Systems

S. Chen, D. MacLaren, R. Baker, J. Chapman, D. Cole-Hamilton, S. Lee, P. André ; SCI Nanoparticles 2009: Synthesis, Properties and Applications of Nanoparticles, Liverpool (UK), September 02-04, 2009

5. Designing Alternative Paths towards *fct*-FePt Magnetic Nanoparticles: Doped Syntheses and Ion-beam Bombardment Post-treatments

S. Chen, D. MacLaren, A. di Falco, J. Chapman, D. Cole-Hamilton, S. Lee, P. André ; SCI Nanoparticles 2009: Synthesis, Properties and Applications of Nanoparticles, Liverpool (UK), September 02-04, 2009

6. Direct *fct* FePt NPs Syntheses (# 1303498)

S. Chen, M.J. Muldoon, K. Anderson, P. André ; ACS 238th, Division of Colloid & Surface Chemistry (Fundamental Research in Colloid and Surface Science), Washington DC (USA), August 16-20, 2009

7. FePt magnetic Nanoparticles: Syntheses & Characterization

S. Chen, D. MacLaren, J. Chapman, D. Cole-Hamilton, S. Lee, P. André ; SUPA Annual Meeting, Glasgow (UK) June 24th, 2008